



# THE UNIVERSITY *of* EDINBURGH

This thesis has been submitted in fulfilment of the requirements for a postgraduate degree (e. g. PhD, MPhil, DClinPsychol) at the University of Edinburgh. Please note the following terms and conditions of use:

- This work is protected by copyright and other intellectual property rights, which are retained by the thesis author, unless otherwise stated.
- A copy can be downloaded for personal non-commercial research or study, without prior permission or charge.
- This thesis cannot be reproduced or quoted extensively from without first obtaining permission in writing from the author.
- The content must not be changed in any way or sold commercially in any format or medium without the formal permission of the author.
- When referring to this work, full bibliographic details including the author, title, awarding institution and date of the thesis must be given.

# First-Principles Calculations of Anharmonic Phonons in Diamond and Silicon at High Temperature and Pressure

Jonathan Hunt



Doctor of Philosophy  
The University of Edinburgh  
August 2023

# Abstract

Many *ab initio* approaches for calculating anharmonic phonon dispersion relations have recently been developed, taking advantage of improvements in computational power. In this thesis, anharmonic phonons in the diamond-type semiconductors silicon and diamond are studied using two of these recently developed *ab initio* techniques to better understand the role of anharmonicity in these materials at elevated temperatures and pressures. The two techniques are the *self-consistent phonon* method as implemented in the ALAMODE code and the *temperature dependent effective potential* approach implemented in the TDEP code. Both these approaches rely on *density functional theory* calculations to compute anharmonic phonon frequencies from first principles.

The renormalisation of the zone-centre optical phonon of silicon is calculated using both methods. The TDEP approach accurately reproduces the experimentally observed temperature dependence of the zone-centre phonon, whereas ALAMODE underestimates the renormalisation. This underestimation is determined to originate from the exclusion of certain phonon–phonon interaction processes in a series expansion central to the self-consistent phonon method. In particular, an interaction process involving three phonons is identified to contribute strongly to the anharmonic phonon renormalisation. An attempt was made to extend ALAMODE to include this interaction, which was, regrettably, unsuccessful.

The TDEP approach is then applied to diamond in the same manner as silicon. The zone-centre optical phonon is calculated and a comparison to available experimental data is made. The approach is again found to accurately reproduce the experimental data. Consequently, the TDEP approach is used to investigate the so-called quantum isotope effect in diamond. Deviations from the harmonic frequency ratio of the zone-centre phonons are used to investigate the anharmonic

nature of the interatomic potential, as well as to search for an experimentally suggested “inversion” of the quantum isotope effect at high pressure. No such inversion of the quantum isotope effect is observed in the calculations made here. A detailed comparison of the effect of different exchange–correlation functionals and pseudopotentials on the density functional theory calculations is made, ultimately recommending local density approximation as the most accurate predictor of phonon frequencies in diamond.

Finally, the Raman frequency of natural diamond is calculated at high temperature and pressure using the highly accurate TDEP method. Improvements are made to the stochastic sampling process, eliminating unwanted scatter from misaligned eigenvectors at degenerate points in the Brillouin zone and increasing the precision of the method. The calculated Raman frequency is used to suggest a calibration of the high-frequency edge of the Raman signal from a diamond anvil, which is used as a pressure marker in very-high-pressure experiments. The suggested calibration extends to pressures up to 1 TPa and temperatures up to 2000 K.

# Lay summary

At finite temperatures, the atoms in a crystal vibrate about some fixed position. These oscillations are coupled together in the form of waves that travel through the crystal; these waves are known as *phonons*. The frequencies of these waves determine the energy they carry, and consequently determine the thermal properties of the material. The calculation of these phonon frequencies is therefore of paramount importance to predicting a material's thermal properties.

To calculate the phonon frequencies, one must somehow describe the forces between the atoms. These forces are, in general, complicated, but one approximation that works well in the majority of cases is the so-called *harmonic approximation*: that the restoring force on an atom as it is displaced from its equilibrium position is linear in the magnitude of this displacement. This simple approximation is sufficient in many cases to compute the phonon energies and the dependent material properties. However, the simple model is not perfect; the discrepancy between the harmonic model and the observed frequencies is usually slight, but becomes more pronounced at high temperatures when atoms are displaced further from their equilibrium positions. To amend these discrepancies, one must include the non-linear, or *anharmonic*, contributions to the force.

Two methods of doing this are considered in this thesis: the temperature-dependent effective potential (TDEP), and ALAMODE. Chapter 5 compares these methods in silicon and, with comparison to experimental data, demonstrates that the TDEP method is far more accurate in calculating the anharmonic phonon frequencies at high temperature. The accuracy is then confirmed in diamond, a crystal with the same atomic structure as silicon.

The same approach is used in chapter 6 to investigate subtle effects in the frequencies that arise due to the changes in atomic mass. Several papers in the

literature have stated that the anharmonic terms in the forces cause unusual and counter-intuitive effects to appear in diamond at high pressure. By calculating the anharmonic phonon frequencies in two isotopes of diamond ( $^{12}\text{C}$  and  $^{13}\text{C}$ ) and comparing them, one may hope to find evidence of this unusual behaviour. No such evidence is found.

Finally, the anharmonic phonon frequencies are calculated again for diamond in an application that will prove useful to future experiments. The behaviour of materials at high pressure is of particular interest to many physicists, and is the focus of many experiments. In these experiments, one must create a high-pressure environment, and then have some way of determining the pressure in this environment. The high-pressure environment is often created by forcing two diamonds together; diamond's exceptional hardness makes it well-suited to this method. One way of measuring the pressure is to measure the pressure-dependent frequency of one of the phonons in the diamond. This frequency is calculated in chapter 7 at temperatures and pressures up to 2000 K and 1 TPa, respectively. These calculations are then used to suggest a calibration of the pressure scale across this entire range of temperature and pressure.

# Declaration

I declare that this thesis was composed by myself, that the work contained herein is my own except where explicitly stated otherwise in the text, and that this work has not been submitted for any other degree or professional qualification except as specified.

*(Jonathan Hunt, August 2023)*

# Acknowledgements

I would like to thank my supervisor Ingo Loa for his help and guidance throughout this PhD. The support and advice he has given me over the years has been invaluable, and I could not have completed this thesis without him.

I would also like to thank Olle Hellman, who made his TDEP code available to me and made almost all of the results in this thesis possible.

Thanks also to my parents, who have always believed in me and whose love and support has been constant.

Thank you to my partner, Elle, whose patience and kindness were unwavering throughout the writing process.

And finally I would like to thank all of my friends and colleagues for their friendship and companionship. They have been a source of happiness throughout my time as a PhD student that I am eternally grateful for.



# Contents

<b>Abstract</b>	i
<b>Lay summary</b>	iii
<b>Declaration</b>	v
<b>Acknowledgements</b>	vi
<b>Contents</b>	vii
<b>1 Introduction</b>	1
<b>2 Background</b>	4
2.1 Harmonic and anharmonic phonons.....	4
2.2 Computing anharmonic phonons.....	7
2.2.1 The quasiharmonic approximation.....	7
2.2.2 Self-consistent phonons .....	8
2.2.3 Temperature-dependent effective potential.....	10
2.2.4 Other methods.....	13

<b>3</b>	<b>Theory</b>	16
3.1	Lattice dynamincs .....	16
3.1.1	The crystal .....	16
3.1.2	The Brillouin zone .....	17
3.1.3	The potential.....	17
3.1.4	Harmonic phonons .....	19
3.1.5	Symmetries of the force constants.....	22
3.2	Green’s functions .....	28
3.3	Density functional theory.....	44
3.3.1	Density functional theory fundamentals .....	45
3.3.2	Plane wave density functional theory and pseudopotentials .	51
3.3.3	Approximations to the exchange–correlation functional .....	55
3.3.4	Forces in density functional theory .....	56
<b>4</b>	<b>Methods</b>	57
4.1	Finite displacement .....	57
4.2	The quasiharmonic approximation .....	58
4.3	Temperature dependent effective potential .....	60
4.4	Self-consistent phonons.....	66
<b>5</b>	<b>Temperature dependence of the Raman signal in silicon and diamond</b>	70
5.1	Background .....	70
5.1.1	Alamode.....	71
5.1.2	TDEP.....	72

5.2	Methods .....	74
5.2.1	Displacement magnitude testing.....	74
5.2.2	Self-consistent phonons (silicon).....	75
5.2.3	Temperature-dependent effective potential.....	77
5.3	Results .....	80
5.3.1	Silicon.....	80
5.3.2	Diamond .....	88
5.4	Improvements to the self-consistent phonon method.....	91
<b>6</b>	<b>Diamond and the quantum isotope effect</b> .....	<b>95</b>
6.1	Background .....	95
6.2	Methods .....	110
6.2.1	Quasiharmonic calculations.....	110
6.2.2	TDEP.....	111
6.3	Results .....	115
6.3.1	Quasiharmonic results.....	115
6.3.2	TDEP results .....	123
<b>7</b>	<b>The Diamond Edge Raman Scale</b> .....	<b>126</b>
7.1	Background .....	126
7.1.1	The diamond edge Raman scale .....	129
7.1.2	Requirements of the diamond edge pressure scale .....	133
7.2	Methods .....	139
7.2.1	TDEP calculations.....	140

7.2.2	Fitting .....	143
7.2.3	Temperature interpolation .....	147
7.3	Results .....	149
8	Conclusion .....	159
	Bibliography .....	162

# Chapter 1

## Introduction

How atoms move has been an important question in condensed matter physics since atoms were first discovered to move. In the case of solids, and particularly crystals, one answer to this question was proposed by Einstein, who suggested that the atoms in the crystal acted as independent quantum harmonic oscillators. This approximation became known as the Einstein model of lattice dynamics and was mostly successful in describing the heat capacity of a solid as the temperature was lowered. However, there was still some disagreement between the predictions of the Einstein model and the observations made from experiment; the Einstein model underestimates the heat capacity of a solid at low temperatures. This problem was solved by Debye, who suggested that the oscillators in the crystal were not independent, but coupled. The coupling of the oscillators changed the spectrum of the energy levels and the predicted heat capacity. Debye's model of coupled harmonic oscillators successfully reproduced the low-temperature dependence of the heat capacity and provided the basis on which all modern lattice dynamics is founded. It is from Debye's model that the concept of a *phonon* arises as a collective excitation of the crystal that may be considered as a quasiparticle.

One crucial assumption in Debye's model, and of the phonon picture that arises from it, is that the oscillators in the crystal are *harmonic*; it is this harmonicity that allows the phonons to be calculated. To go beyond this simple picture into the realm of anharmonic phonons requires careful thought.

Accurate calculation of anharmonic phonons from first principles is currently a barrier to predicting and understanding the thermal properties of many materials. This thesis will examine some different methods that currently exist for calculating anharmonic phonons and apply them to two test systems — silicon and diamond. These systems have been chosen to provide rigorous tests to each of the methods so the strengths and weaknesses of each approach are understood. Silicon is a material that has a large amount of experimental data available, making it a good candidate to test the abilities of the methods. Diamond also has an abundance of experimental data, but is also the subject of experiments that have produced counter-intuitive and in some cases contradictory results. Before discussing the methods in detail, however, something must first be said about the nature of anharmonic phonons and why they are deserving of study.

Anharmonic phonons are present in all materials, however close to the purely harmonic model they may be, but they are particularly conspicuous in materials with novel thermal properties such as negative thermal expansion, thermoelectrics, high temperature superconductors, multiferroelectrics, ultralow/high thermal conductors, and more [1]. In all of these research areas, the ability to calculate the thermal properties from first principles is crucial, both to understanding the physics underpinning a material’s unusual behaviour, and for guiding research to develop better and more efficient materials for a variety of applications.

This thesis shall test two promising methods for calculating anharmonic phonons from first principles and compare the results both to each other, and to experimental data. The first method is implemented in a software package called ALAMODE developed by Terumasa Tadano and Shinji Tsuneyuki and applies quantum field theory to derive the anharmonic phonons directly from the harmonic ones [2]. The second approach is known as the temperature dependent effective potential (TDEP) and uses a more pragmatic approach to determine the anharmonic phonons using stochastic sampling of the atomic forces. Its implementation is the original one by Olle Hellman and Nina Shulumba in the TDEP software package [3].

The structure of the thesis is as follows. After this introduction, chapter 2 will provide an overview of the current state of anharmonic phonon calculations, and the materials to which they have been applied, their successes, and their weaknesses. Chapter 3 will discuss the theory underpinning anharmonic

phonons, and the methods used to calculate them using density functional theory. Chapter 4 will describe how the theory in chapter 3 is implemented in the codes ALAMODE and TDEP. Chapter 5 will apply these approaches to silicon and diamond and compare the results of each method. It will also provide a detailed look at the reasoning behind the implementation details of each approach and how to accurately carry out the calculations. Chapter 6 will use the findings of chapter 5 to calculate the pressure dependence of the so-called quantum isotope effect in diamond. The TDEP method will be used to calculate the effect from first principles and the results will be compared to unusual behaviour reported in the literature. Chapter 7 will again apply the TDEP approach to diamond, this time aiming to calculate a calibration of the diamond edge Raman pressure scale to high temperatures and pressures. This scale is useful to high-pressure experiments and a first-principles calculation will be beneficial as static pressure experiments reach higher and higher pressures. Finally, chapter 8 will summarise each investigation and provide reflections on the work in this thesis and the future direction of first-principles anharmonic phonon calculations.

# Chapter 2

## Background

Over the last 30 years, the field of lattice dynamics has seen new ground broken in the area of *ab initio* calculations of anharmonic phonons. These explorations have been made possible by the increase in computational power available at high-performance computing centres, and the commensurate increase in the computing power of the researcher's own desktop. The ability to run more simulations, more quickly, more easily, and more accurately means that it is now possible to implement more sophisticated methods that had previously remained intractable. These new methods use a variety of approaches to achieve the same goal: calculation of the anharmonic phonon frequencies from first principles. This section will review the differences between harmonic and anharmonic phonons and highlight some of the systems where anharmonicity is most prominent before examining the ways in which anharmonic phonons can be calculated from first principles.

### 2.1 Harmonic and anharmonic phonons

Harmonic phonon theory underpins much of the field of lattice dynamics and is the first port of call for anyone attempting to describe the atomic motion in a crystal. The form of harmonic phonon theory commonly used today was introduced by Born and Huang, who presented a formalism for describing the interactions between the atoms in a crystal in terms of a Taylor expansion of the many-body



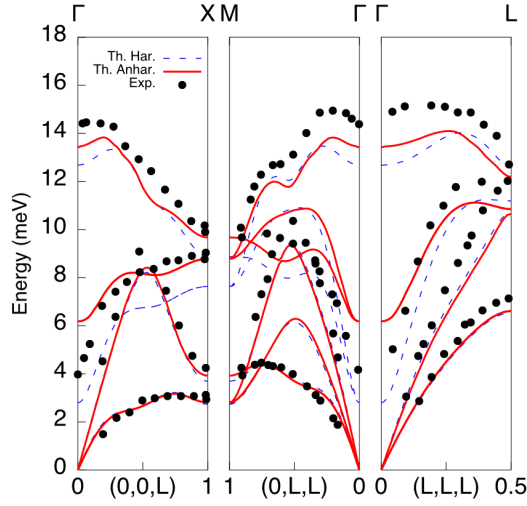


**Figure 2.1** *The calculated harmonic (blue, dashed) anharmonic (red, solid) phonon dispersions of PbTe compared with experimental inelastic neutron scattering measurements (black circles). Figure reproduced from [5].*

interatomic potential [4]. In the harmonic approximation, this Taylor expansion is truncated at second order. Treating the interatomic potential as strictly harmonic makes for a mathematically simple model that can be solved exactly. However, these harmonic calculations have several significant shortcomings that make more advanced theories necessary. Harmonic phonon theory fails to predict the correct thermal expansion in a material or the correct temperature dependence of the phonon frequencies and their dependent properties. These shortcomings are a result of the simplistic harmonic potential.

For example, the harmonic potential is symmetric, so the time-averaged position of an atom vibrating in a perfectly harmonic potential is always exactly in the centre of the potential, no matter the amplitude of vibration. As the temperature and the amplitude of vibration increase, the atom will always have the same average position relative to the potential, precluding the possibility of thermal expansion. An atom in a harmonic potential also keeps the same frequency of oscillation irrespective of the vibrational amplitude; increasing temperature will not change the phonon frequency, neither will increasing pressure.

Some systems are more appropriately described by the harmonic approximation than others. Materials with unusual thermal properties, dynamical instabilities, and superconductors are likely candidates for strong anharmonicity.

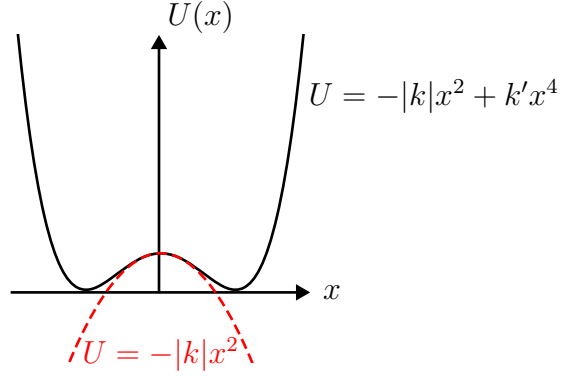


**Figure 2.2** *Schematic of an interatomic potential where the harmonic terms predict an imaginary frequency (negative eigenvalue) but higher order terms stabilise the potential.*

The case of lead telluride (PbTe) is well known for exhibiting large changes in the phonon frequencies when anharmonic effects are considered (see figure 2.1). PbTe is an efficient thermoelectric material — a material that produces an electric voltage when a thermal gradient is applied across the material. Such materials are important for reclaiming energy that would otherwise be lost to heat, or for using naturally occurring sources of heat to power electronic devices. An understanding of their thermal properties is therefore essential. A strongly anharmonic potential is common to many of the most promising thermoelectrics that are being studied currently; the anharmonicity in the potential encourages phonon–phonon scattering which lowers the thermal conductivity, making it easier to impose the required temperature gradient [6].

Dynamical instabilities are predicted when the energy of the crystal would be lowered by a static deformation of the crystal lattice. They occur when the energy of the crystal is lowered rather than raised by the displacement of the atoms from their static positions. Such instabilities are sometimes incorrectly predicted in the harmonic approximation and are found to be eliminated when higher-order terms are considered. An example of this is strontium titanate (SrTiO<sub>3</sub>) [2]. If one truncates the interatomic potential of cubic SrTiO<sub>3</sub> at the harmonic level, then one finds that the phonon frequencies are imaginary over large regions of the Brillouin zone. This would ordinarily indicate a dynamical instability. Dynamical instabilities often drive phase changes when the phonon frequency at a point in the Brillouin zone becomes imaginary. However, in the case of SrTiO<sub>3</sub>, the structure is found to be stable at temperatures and pressures where the harmonic theory predicts an instability. Higher-order terms in the interatomic potential stabilise

the structure, eliminating the instability. Figure 2.2 shows schematically how a potential may produce stable states only once higher-order terms are included. For potentials such as these a method of accurately computing the anharmonic phonon frequencies is required in order to describe its thermal properties.

## 2.2 Computing anharmonic phonons

A variety of techniques have been developed to calculate anharmonic phonons beyond the harmonic approximation, employing a range of theoretical principles. Most are still in their incipient stages having only been employed on a small selection of systems. The approaches are each characterised by their theory, implementation, and appropriacy to various systems or problems. Here, two of the approaches are discussed in detail: the self-consistent phonon (SCPH) approach implemented in ALAMODE and the temperature dependent effective potential (TDEP) approach implemented in the code of the same name [2, 3, 7, 8]. The section ends with a brief conspectus of the other approaches currently being developed.

### 2.2.1 The quasiharmonic approximation

The first treatment of the anharmonicity of crystals comes from Mie and Grüneisen in their papers in 1903 and 1908 [9, 10]. In these papers the authors consider a temperature-dependent lattice parameter of a cubic crystal  $a(T)$ , the potential energy is then also a function of  $T$ . At each temperature the interatomic potential is expanded to harmonic order and the phonon frequencies and eigenvectors are then found. This approximation is frequently referred to as the *quasiharmonic approximation (QHA)* and is the simplest treatment of anharmonicity, capturing only effects coming from the changing volume.

In spite of its simplicity, the QHA performs quite well in a large number of cases and is often sufficient to describe, for example, the thermal expansion. However, as the QHA was applied to an increasing number of systems, many of these systems were found to be poorly described by the quasiharmonic formalism, indicating the presence of strong anharmonicity. The QHA fails to accurately

model such materials because the underlying assumption that the phonons are harmonic at a particular volume is not accurate. To go beyond the QHA a method of including the so-called *pure anharmonicity* is needed.

### 2.2.2 Self-consistent phonons

The SCPH method for calculating anharmonic phonon frequencies relies on the calculation of the *self-energy*. The self-energy is the energy that a phonon (or other particle) has as a result of interactions with its environment. For phonons, this means the energy from interactions with other phonons. The self-energy is expressed through the equation

$$V_{jj'}^{\mathbf{k}} = \Lambda_{jj'}^{\mathbf{k}} + \Sigma_{jj'}^{\mathbf{k}}(\omega) , \quad (2.1)$$

where  $V_{jj'}$  is the matrix of renormalised phonon frequencies at wavevector  $\mathbf{k}$ , with  $j$  and  $j'$  being band indices,  $\Lambda_{jj'}^{\mathbf{k}}$  is the matrix of harmonic (non-interacting) phonons, and  $\Sigma_{jj'}^{\mathbf{k}}(\omega)$  is the self-energy matrix. This matrix is, in general, energy dependent.

As a result, the strength of these interactions depends on the energies of the phonons involved, a self-consistent approach is required to calculate it accurately. This is the approach taken by ALAMODE, which makes use of quantum field theory to calculate the phonon self-energy from the phonon propagators. The self-energy is calculated in the SCPH theory by including the effects of increasingly complex phonon-phonon interactions characterised by terms in a series expansion of Feynmann diagrams. Although the effect of any diagram can, in theory, be included, only one of the lowest order contributions is included in the basic SCPH approach taken by ALAMODE. The other contributions are neglected, not just on the basis that they are expected to contribute less to the renormalisation, but also on the difficulty of their computation.

The first application of ALAMODE was to the previously mentioned perovskite  $\text{SrTiO}_3$ , where the dynamical instabilities in the harmonic approximation are successfully removed to produce a stable phonon dispersion [7, 11].  $\text{SrTiO}_3$  was later revisited by the authors, and a temperature-induced structural phase transition was predicted [12]. Other authors have since applied the SCPH method

to  $\text{SrTiO}_3$  to calculate its electronic band gap [13], dielectric constants and their strain dependence [14, 15], and the thermal conductivity [16]. In addition to  $\text{SrTiO}_3$ , ALAMODE has been applied to a slew of other perovskites [14, 17–21] and antiperovskites [22].

The SCPH approach has also shown promise when applied to superconductors such as the high-temperature superconductor  $\text{H}_3\text{S}$ .  $\text{H}_3\text{S}$  is well known for having once had, by a significant margin, the highest known critical temperature,  $T_c$ , of any material, and refocussed the search for high- $T_c$  superconductors back to those of the conventional BCS type [23]. This move proved fruitful, as other superconductors with even higher  $T_c$ s have since been discovered, with recent claims of  $T_c$  above room temperature at ambient pressure [24–26], although these claims have been met with scepticism [27–29]. ALAMODE showed the importance of anharmonic phonon effects in determining the critical temperature of  $\text{H}_3\text{S}$ , demonstrating that anharmonicity lowered the superconducting transition temperature by 12% [30].

The high-temperature superconductors that have emerged from the renewed focus on the conventional type of superconductivity have all included large amounts of hydrogen, as the high phonon frequencies that come from such a light atom are a major hallmark of the high-temperature conventional superconductivity. In fact, pure hydrogen itself has been suggested as a candidate for room temperature superconductivity [31]. Recent calculations on a candidate structure for solid hydrogen have been made using ALAMODE that again suggest that anharmonicity plays an important role in determining the superconducting transition temperature by reducing the electron-phonon coupling, and thus  $T_c$  [32–34].

Although the standard version of the ALAMODE software package includes only one of the lowest order contributions, corresponding to a 4-phonon interaction process, the authors have made an attempt to include a second interaction process of the same order that corresponds to a 3-phonon process in a study on  $\text{ScF}_3$  [35]. The self-energy from the 4-phonon process is frequency independent; the renormalisation of an anharmonic phonon from the 4-phonon process is the same no matter the frequency of the phonon in question. For the 3-phonon process, this is not the case; the self-energy must be evaluated at the correct frequency of the phonon being renormalised. The authors elected to use the frequencies

from the renormalisation from the 4-phonon process only. It is not clear that this approach provides a better result than simply using the harmonic phonons to calculate the third order effects, as it is possible for the cubic and quartic effects to act antagonistically, as in the case of  $\text{ScF}_3$ . The inclusion of the third-order terms in  $\text{ScF}_3$  improved the quantitative agreement with the experimental results, highlighting their importance. The inclusion of third-order terms in this manner was not done using the ALAMODE software package directly and required additional calculations; the ability to calculate these terms is still not included in the standard ALAMODE software.

### 2.2.3 Temperature-dependent effective potential

While the SCPH approach derives the renormalised phonons as a correction to the harmonic phonons, the temperature dependent effective potential (TDEP) approach attempts to find the renormalised phonons directly from the forces and displacements, without an intermediate calculation of the harmonic phonons. The TDEP formalism is underpinned by the fact that the phonons, once renormalised, are non-interacting and must therefore be the solution of a Hamiltonian with an *effective* harmonic potential. The TDEP approach involves calculating the forces on atoms displaced from their static lattice positions in a way that mimics the displacements found in a real crystal at an elevated temperature and then asking the question: *What harmonic potential best describes this set of displacements and forces?* Once this effective harmonic potential is found, the renormalised phonons can be extracted from using exactly the same approach as for the true (non-effective) harmonic potential.

The TDEP method can be viewed as an extension of the self-consistent *ab initio* lattice dynamics (SCAILD) approach developed by Souvatzis and co-workers [36, 37]. SCAILD works on the idea that displacing all the atoms in a supercell according to some mean square displacement and calculating the phonon frequencies from the forces will provide new, slightly different phonon frequencies. These updated frequencies can, in turn, be used to calculate a new mean square displacement as the thermodynamic average of the phonon modes. Once a new mean square displacement is found, a new configuration of displaced atoms is created and the cycle continues until self-consistency is achieved.

SCAILD is very robust as it makes no statement about the form of the anharmonicity. In principle, the renormalised frequencies are found to all orders. There are, however, some assumptions made in the method. Firstly, the phonon polarisations are fixed throughout the self consistent cycle. This means that the renormalised phonons have the same polarisations as the initial harmonic ones. This need not be the case for strongly anharmonic systems. Secondly, the effect of finite phonon lifetimes is not taken into account and very short-lived phonons (caused by severe anharmonicity) will have an impact on the thermodynamic averages and therefore affect the final frequencies produced by the self-consistent cycle. Finally, as with most anharmonic phonon approaches, the calculations are performed at a fixed volume, so additional thought is required to include the effect of thermal expansion. Despite these assumptions, the SCAILD method will work well for many systems. Its main limitation is that it requires a new density functional theory (DFT) calculation upon every iteration, meaning that the computational expense can be quite large.

TDEP is different from SCAILD in the way the atoms are displaced from their equilibrium positions. In SCAILD, the atoms are displaced with some Gaussian distribution around the mean square displacement, whereas TDEP aims to produce a more physically meaningful distribution of atomic displacements. The implementation of the TDEP method used in this thesis is the stochastic TDEP, developed by Hellman *et al.* [3, 8], where the atomic configurations used to calculate the force-displacement fitting data are generated by stochastically populating the harmonic phonon modes in order to approximate the state of the real crystal at a finite temperature. An alternative is to use snapshots from a molecular dynamics simulation as the configurations for generating the force-displacement data. These two flavours of TDEP differ only in the way the configurations are generated and, indeed, both approaches require similar attention to convergence and sampling. As the two flavours differ only in the initial step of gathering the force-displacement data, the distinction between them will not be drawn, and hereafter references to TDEP will refer to the stochastic TDEP unless otherwise stated.

Applications of the TDEP method cover a wide range of materials. The method was debuted by Hellman and co-workers in 2011 when it was successfully applied to bcc Li and bcc Zr, managing to reproduce the experimentally observed phonon dispersion at 300 K and 1300 K respectively. This flavour of TDEP was the non-

stochastic flavour that took the force-displacement data from *ab initio* molecular dynamics snapshots.

The stochastic flavour of TDEP was developed later in 2017 in an application to the lead compounds PbSe, PbTe, and PbS [38]. As the stochastically generated configurations require the population of phonon modes, one must have some initial set of harmonic (or effective harmonic) force constants in order to generate them. In the study of the lead compounds, the authors generated an initial guess of the force constants from a simplistic pair potential. This initial guess was used to generate more accurate force constants, which were then in turn used to generate more configurations. This process continued until self-consistency was reached. In total it took just three iterations of this self-consistent cycle where 50 configurations, each with 250 atoms, were used in each iteration. It is worth noting that this was for a system that is known for large anharmonic effects and starting from a very crude approximation of the force constants. For a less anharmonic system, and from a more accurate starting guess, it is not necessary to perform this self-consistent cycle at all.

Beyond this, the TDEP approach has also been used to study a range of physical properties and phenomena. In addition to the direct calculation of the renormalised phonon frequencies [39–42], the thermal conductivity [43, 44], thermal expansion [40], elastic properties [45, 46], phase transitions [47–50], and magnetic materials [51] have also been studied. Of particular note is an application to silicon, where effective third-order force constants were used to capture the antisymmetric parts of the potential that cannot be captured by the effective harmonic term [8, 40]. As the effective harmonic potential is constrained to be symmetric, it cannot describe any antisymmetric parts of the interatomic potential. By extending the potential to include effective third-order force constants these antisymmetric terms may be included through the calculation of the self-energy from the 3-phonon interaction. Extensive use of this technique will be made throughout this thesis.

The importance of considering the third-order force constants was further demonstrated in a study of PbTe and SnTe, where an anomaly in the self-energy measured from inelastic neutron scattering measurements was explained through the consideration of the three-phonon scattering processes [39]. The authors found that the renormalisation of the phonon frequencies at the  $\Gamma$ -point was



large enough to create nesting (where large portions of the phonon spectrum are separated by a constant wavevector, i.e. both phonon bands have the same gradient) between the acoustic and optical branches. This nesting allowed for large amounts of scattering and hence short phonon lifetimes. This manifests itself as a peak in the imaginary part of the self-energy which, through the Kramers–Kronig relations, appears as an oscillation in the real part of the self-energy where two distinct peaks can be seen, one of which corresponds to the anomalous self-energy peak observed in experiment.

## 2.2.4 Other methods

Beyond ALAMODE and TDEP there are other methods for calculating anharmonic phonon frequencies. Already mentioned was SCAILD as a precursor to the TDEP approach. One method that has not been mentioned thus far is the frozen phonon approach. The frozen phonon approach is well established; it originated long before any of the other methods, even the finite displacement approach for calculating harmonic force constants, were established [52–54]. Developed in the 1970s and becoming ubiquitous in the 1980s, the frozen-phonon method is used to calculate the vibrational frequency of a single phonon mode [55].

A phonon describes a wave travelling through a crystal and hence, for a particular phonon mode, the atoms are displaced from their equilibrium positions in a periodic pattern. A frozen phonon calculation involves calculating the internal energy with the atoms displaced from their equilibrium positions in this manner. This in effect *freezes in* a particular phonon mode. The internal energy of the crystal is computed for a series of such distorted supercells with a range of displacement amplitudes. The force constant of the phonon mode is then computed through the second derivative of the energy–displacement curve.

The frozen-phonon method is typically performed using DFT to calculate the energies and is therefore restricted to phonon modes whose wavevector is commensurate with the supercell used to calculate it. Fortunately, it is frequently the phonons at the Brillouin zone boundaries (or centre) that are of interest, which have a wavelength equal to the lattice parameter. Unfortunately, it makes this method impractical for calculating thermodynamic properties that generally require sampling the phonon frequencies of the entire Brillouin

zone. Furthermore, the frozen-phonon approach requires several calculations of the distorted supercell which can be quite computationally expensive for the calculation of just one phonon mode. Calculations cannot be recycled for other phonon modes.

Despite these drawbacks, the frozen phonon approach is still used today. As the static crystal energy is calculated explicitly for a range of phonon amplitudes, the resulting energy—displacement curve describes the potential for the phonon mode inclusive of all anharmonicity and the energy levels of this potential can be found by solving the time-independent Schrödinger equation. The frozen phonon method therefore allows some insight into the anharmonicity of the crystal. However, by only considering a single mode, it does not provide any insight into the effect of phonon–phonon interactions.

Another method of computing the anharmonic phonon frequencies is the so-called stochastic self-consistent harmonic approximation (SSCHA) developed by Errea and co-workers [56]. The SSCHA attempts to find the renormalised phonon dispersions by finding a density matrix that minimises the anharmonic free energy. As it is not possible to trial all possible density matrices, the approach restricts itself to trial density matrices that represent a harmonic system. In this respect, the approach is similar to TDEP in asking which harmonic system best approximates the anharmonic one. As the name of the stochastic self-consistent harmonic approximation implies, the minimisation process involves the stochastic sampling of the Born-Oppenheimer potential energy surface. This is the most expensive part of the calculation and, while steps have been taken to considerably reduce the number of times it is necessary to perform such sampling, it still remains a very computationally expensive approach with each sample involving the generation of “... up to several hundreds or thousands of configurations” [56].

For this reason, and the fact that the code was only recently released in 2021, the SSCHA is not considered in this thesis, although a comparison to ALAMODE and TDEP would be valuable in order to assess in what cases the additional computing time is justified compared to the techniques discussed here.

Phonopy and its sister code, Phono3py, are both well-established packages for computing phonons and thermal properties [57, 58]. Phonopy is one of the most well-used software packages for computing harmonic phonons and has the capability to perform QHA calculations, which will be made use of in this thesis.

Phono3py uses third order force constants to compute thermal properties of a material. It does not, however, make use of the fourth-order and higher force constants necessary to accurately calculate the anharmonic phonon frequency renormalisation, leaving it outside the scope of this investigation.

Finally, although the most promising methods (at the current state of the field) for computing anharmonic phonons have been mentioned, one must also point out the other approaches that exist. HIPHIVE is another software package, still in its incipient stages, that aims to use machine learning to determine higher order force constants more efficiently [59]. The Kaldo code aims to solve the thermal transport equation using anharmonic force constants [60]. It is hoped that these methods will continue to be developed and will enrich the field of *ab initio* anharmonic phonon calculations in the years to come. Presently, however, this thesis will restrict itself to the discussion of the SCPH method and the TDEP method. Comparisons to other approaches are left for future studies.

# Chapter 3

## Theory

### 3.1 Lattice dynamincs

#### 3.1.1 The crystal

A periodic crystal is an arrangement of atoms in space with a spatially periodic structure. This spatial periodicity is described mathematically by a lattice, a grid of lattice points arranged such that the crystal is unchanged under a translation from one lattice point to another. The positions of these points are described by the vectors  $\mathbf{a}_1, \mathbf{a}_2, \mathbf{a}_3$ , which serve as the *translation vectors* of the lattice, and the set of lattice vectors  $\{\mathbf{R}\}$ , whose components are integers and describe the positions of the lattice points in terms of the basis vectors. The set of all lattice points is therefore described by

$$\mathbf{R} = h\mathbf{a}_1 + k\mathbf{a}_2 + l\mathbf{a}_3 \quad \text{with} \quad \{h, k, l\} \in \mathbb{Z} . \quad (3.1)$$

With the lattice defined, the positions of the atoms are described by the application of the *basis*. The basis describes the displacement from the lattice point to each atom associated with the lattice point. These basis vectors will be called  $\mathbf{s}_\mu$  where  $\mu$  is the index of the atom in the *unit cell* — the parallelepiped drawn out by the vectors  $\mathbf{a}_1, \mathbf{a}_2, \mathbf{a}_3$ .

### 3.1.2 The Brillouin zone

In addition to the real space lattice, it is typical to define the reciprocal lattice, a separate lattice associated with the real space lattice described by reciprocal lattice vectors  $\mathbf{G}$  and reciprocal translation vectors  $\mathbf{b}_1, \mathbf{b}_2, \mathbf{b}_3$  where

$$\mathbf{G} = h\mathbf{b}_1 + k\mathbf{b}_2 + l\mathbf{b}_3 \quad \text{with} \quad \{h, k, l\} \in \mathbb{Z} . \quad (3.2)$$

The reciprocal translation vectors are related to the real space translation vectors by

$$\mathbf{b}_1 = 2\pi \frac{\mathbf{a}_2 \times \mathbf{a}_3}{\mathbf{a}_1 \cdot \mathbf{a}_2 \times \mathbf{a}_3} \quad (3.3)$$

$$\mathbf{b}_2 = 2\pi \frac{\mathbf{a}_3 \times \mathbf{a}_1}{\mathbf{a}_2 \cdot \mathbf{a}_3 \times \mathbf{a}_1} \quad (3.4)$$

$$\mathbf{b}_3 = 2\pi \frac{\mathbf{a}_1 \times \mathbf{a}_2}{\mathbf{a}_3 \cdot \mathbf{a}_1 \times \mathbf{a}_2} . \quad (3.5)$$

Defining the reciprocal lattice vectors in this manner enforces the relation

$$\mathbf{a}_i \mathbf{b}_j = 2\pi \delta_{ij} , \quad (3.6)$$

where  $\delta_{ij}$  is the Kronecker delta, and consequently,

$$\mathbf{R} \cdot \mathbf{G} = 2\pi N \quad N \quad \text{with} \quad \in \mathbb{Z} . \quad (3.7)$$

Applying the Wigner-Seitz construction to the reciprocal lattice points, one can construct a uniquely defined reciprocal unit cell called the Brillouin zone. Points in the Brillouin zone are identified by a wavevector  $\mathbf{k}$ , which has units of reciprocal length.

### 3.1.3 The potential

At finite temperature, the atoms are in motion and are displaced from their equilibrium positions. The displacements are small and one can therefore consider the crystal potential as a Taylor expansion in the displacements around these

equilibrium positions,

$$U = U_0 + U_1 + U_2 + U_3 + U_4 + \dots \quad (3.8)$$

The term  $U_n$  is given by

$$U_n = \frac{1}{n!} \sum_{\{\mathbf{R}, \mu, i\}} \Phi_{i_1 \dots i_n}(\mathbf{R}_1 \mu_1; \dots; \mathbf{R}_n \mu_n) u_{i_1}(\mathbf{R}_1 \mu_1) \dots u_{i_n}(\mathbf{R}_n \mu_n) \quad (3.9)$$

where the rank- $n$  tensor  $\Phi$  is given by

$$\Phi_{i_1 \dots i_n}(\mathbf{R}_1 \mu_1; \dots; \mathbf{R}_n \mu_n) = \frac{\partial^n U}{\partial u_{i_1}(\mathbf{R}_1 \mu_1) \dots \partial u_{i_n}(\mathbf{R}_n \mu_n)} \quad (3.10)$$

and is called the matrix of *force constants*, and  $u$  are the displacements of the atoms from their equilibrium positions. Both  $\Phi$  and  $u$  are indexed by a set or sets of three indices  $\{\mathbf{R}, \mu, i\}$ :  $\mathbf{R}$  is the real space lattice vector,  $\mu$  is the atom number within the unit cell pointed to by  $\mathbf{R}$ , and  $i$  represents a cartesian direction. As a concrete example, the rank-two tensor corresponding to the harmonic potential is given by

$$\Phi_{i_1, i_2}(\mathbf{R}_1 \mu_1; \mathbf{R}_2 \mu_2) = \frac{\partial^2 U}{\partial u_{i_1}(\mathbf{R}_1 \mu_1) \partial u_{i_2}(\mathbf{R}_2 \mu_2)}. \quad (3.11)$$

The elements of this matrix describe the force on atom  $\mathbf{R}_1 \mu_1$  in the  $i_1$  direction as the result of the displacement of atom  $\mathbf{R}_2 \mu_2$  in the  $i_2$  direction. Recalling that force is the negative of the first derivative of the potential,

$$F_{i_1}(\mathbf{R}_1 \mu_1) = -\frac{\partial U}{\partial u_{i_1}(\mathbf{R}_1 \mu_1)} \quad (3.12)$$

$$\approx -\frac{\partial^2 U}{\partial u_{i_1}(\mathbf{R}_1 \mu_1) \partial u_{i_2}(\mathbf{R}_2 \mu_2)} u_{i_2}(\mathbf{R}_2 \mu_2) \quad (3.13)$$

$$\approx -\Phi_{i_1, i_2}(\mathbf{R}_1 \mu_1; \mathbf{R}_2 \mu_2) u_{i_2}(\mathbf{R}_2 \mu_2). \quad (3.14)$$

As all of the tensors and vectors are indexed by sets of three indices, a more compact notation using the stacked index  $\begin{pmatrix} \mathbf{R}_n \\ \mu_n \\ i_n \end{pmatrix}$  of Leibfried and Ludwig shall be introduced [61]. The top index describes the lattice vector of the unit cell, the middle index is the index of the atom within this unit cell, and the bottom index is the cartesian direction. Using this notation, the  $n^{\text{th}}$  order contribution to the

potential energy is written as:

$$U_n = \frac{1}{n!} \sum_{\{\mathbf{R}, \mu, i\}} \Phi \left( \begin{smallmatrix} \mathbf{R}_1 & \dots & \mathbf{R}_n \\ \mu_1 & \dots & \mu_n \\ i_1 & \dots & i_n \end{smallmatrix} \right) u \left( \begin{smallmatrix} \mathbf{R}_1 \\ \mu_1 \\ i_1 \end{smallmatrix} \right) \dots u \left( \begin{smallmatrix} \mathbf{R}_n \\ \mu_n \\ i_n \end{smallmatrix} \right). \quad (3.15)$$

### 3.1.4 Harmonic phonons

The typical treatment of phonons considers only the harmonic terms of the interatomic potential. Many treatments of harmonic phonons can be found, employing a variety of methods to derive their existence [61–64]. Many of these approaches make simplifications for pedagogical reasons; a reader interested in such an approach is directed to the cited texts. Here the phonon treatment of atomic vibrations will be derived from the force constant model for a general crystal with multiple atoms per unit cell, and without any reference to concepts beyond the interatomic potential, the periodicity of the crystal, and some basic linear algebra. Proceeding in this manner allows the derived results to be applied to a general crystal without alteration, and sets the foundation for the discussion of the higher-order anharmonic terms.

Considering only the harmonic terms in the potential,  $U = U_0 + U_2$  ( $U_1 = 0$  at equilibrium), and, in fact, neglecting the equilibrium energy,  $U_0$ , which has no effect on the forces, the only remaining term is  $U_2$  and the equation of motion becomes

$$M_\mu \ddot{u} \left( \begin{smallmatrix} \mathbf{R} \\ \mu \\ i \end{smallmatrix} \right) (t) = - \sum_{\{\mathbf{S}, \nu, j\}} \Phi \left( \begin{smallmatrix} \mathbf{R} & \mathbf{S} \\ \mu & \nu \\ i & j \end{smallmatrix} \right) u \left( \begin{smallmatrix} \mathbf{S} \\ \nu \\ j \end{smallmatrix} \right) (t). \quad (3.16)$$

This can be symmetrised as

$$\sqrt{M_\mu} \ddot{u} \left( \begin{smallmatrix} \mathbf{R} \\ \mu \\ i \end{smallmatrix} \right) (t) = - \sum_{\{\mathbf{S}, \nu, j\}} \frac{\Phi \left( \begin{smallmatrix} \mathbf{R} & \mathbf{S} \\ \mu & \nu \\ i & j \end{smallmatrix} \right)}{\sqrt{M_\mu M_\nu}} \sqrt{M_\nu} u \left( \begin{smallmatrix} \mathbf{S} \\ \nu \\ j \end{smallmatrix} \right) (t). \quad (3.17)$$

To decouple these equations, one transforms to the eigenbasis. The eigenvalues and eigenvectors are found by diagonalising  $\frac{\Phi \left( \begin{smallmatrix} \mathbf{R} & \mathbf{S} \\ \mu & \nu \\ i & j \end{smallmatrix} \right)}{\sqrt{M_\mu M_\nu}}$ . The secular equation is

$$\sum_{\{\mathbf{S}, \nu, j\}} \frac{\Phi \left( \begin{smallmatrix} \mathbf{R} & \mathbf{S} \\ \mu & \nu \\ i & j \end{smallmatrix} \right)}{\sqrt{M_\mu M_\nu}} C \left( \begin{smallmatrix} \mathbf{S} & \mathbf{k} \\ \nu & \rho \\ j & r \end{smallmatrix} \right) = \left[ \omega \left( \begin{smallmatrix} \mathbf{k} \\ \rho \\ r \end{smallmatrix} \right) \right]^2 C \left( \begin{smallmatrix} \mathbf{R} & \mathbf{k} \\ \mu & \rho \\ i & r \end{smallmatrix} \right), \quad (3.18)$$

where  $\omega^2$  are the eigenvalues and  $C$  is the unitary transformation which transforms to the eigenbasis (i.e. the matrix of eigenvectors). Applying this transformation one finds

$$\sqrt{M_\mu} u \begin{pmatrix} \mathbf{R} \\ \mu \\ i \end{pmatrix} (t) = \sum_{\{\mathbf{k}, \rho, r\}} C \begin{pmatrix} \mathbf{R} & \mathbf{k} \\ \mu & \rho \\ i & r \end{pmatrix} a \begin{pmatrix} \mathbf{k} \\ \rho \\ r \end{pmatrix} (t) , \quad (3.19)$$

where  $a \begin{pmatrix} \mathbf{k} \\ \rho \\ r \end{pmatrix} (t)$  is the normal mode indexed by a vector  $\mathbf{k}$ , an integer  $\rho$ , and a cartesian direction  $r$ .

Substituting equation 3.19 into equation 3.17 this becomes

$$\sum_{\{\mathbf{k}, \rho, r\}} C \begin{pmatrix} \mathbf{R} & \mathbf{k} \\ \mu & \rho \\ i & r \end{pmatrix} \ddot{a} \begin{pmatrix} \mathbf{k} \\ \rho \\ r \end{pmatrix} (t) = - \sum_{\{\mathbf{k}, \rho, r\}} \sum_{\{\mathbf{S}, \nu, j\}} \frac{\Phi \begin{pmatrix} \mathbf{R} & \mathbf{S} \\ \mu & \nu \\ i & j \end{pmatrix}}{\sqrt{M_\mu M_\nu}} C \begin{pmatrix} \mathbf{S} & \mathbf{k} \\ \nu & \rho \\ j & r \end{pmatrix} a \begin{pmatrix} \mathbf{k} \\ \rho \\ r \end{pmatrix} (t) , \quad (3.20)$$

and now using equation 3.18 one can derive the relation

$$\sum_{\{\mathbf{k}, \rho, r\}} C \begin{pmatrix} \mathbf{R} & \mathbf{k} \\ \mu & \rho \\ i & r \end{pmatrix} \ddot{a} \begin{pmatrix} \mathbf{k} \\ \rho \\ r \end{pmatrix} (t) = - \sum_{\{\mathbf{k}, \rho, r\}} \left[ \omega \begin{pmatrix} \mathbf{k} \\ \rho \\ r \end{pmatrix} \right]^2 C \begin{pmatrix} \mathbf{R} & \mathbf{k} \\ \mu & \rho \\ i & r \end{pmatrix} a \begin{pmatrix} \mathbf{k} \\ \rho \\ r \end{pmatrix} (t) . \quad (3.21)$$

Each term in the sum is now independent of the others and the differential equation can now be solved for  $a$  as

$$a \begin{pmatrix} \mathbf{k} \\ \rho \\ r \end{pmatrix} (t) = A \begin{pmatrix} \mathbf{k} \\ \rho \\ r \end{pmatrix} \exp \left[ -i \omega \begin{pmatrix} \mathbf{k} \\ \rho \\ r \end{pmatrix} t \right] , \quad (3.22)$$

where  $A \begin{pmatrix} \mathbf{k} \\ \rho \\ r \end{pmatrix}$  is some amplitude. The quantity  $\omega$  may now be identified as a frequency of vibration. This solution to the differential equation contains the temporal part of the solution, while the matrix  $C \begin{pmatrix} \mathbf{R} & \mathbf{k} \\ \mu & \rho \\ i & r \end{pmatrix}$  contains the spatial part. As the force constants  $\Phi$  are periodic in the lattice vectors, the eigenvectors are periodic also.

The eigenvectors may therefore be split into a spatially periodic wave, and a constant vector called the polarisation vector,

$$C \begin{pmatrix} \mathbf{R} & \mathbf{k} \\ \mu & \rho \\ i & r \end{pmatrix} = E \begin{pmatrix} \mathbf{R} & \mathbf{k} \\ \mu & \rho \\ i & r \end{pmatrix} \exp (i \mathbf{k} \cdot \mathbf{R}) . \quad (3.23)$$

Here  $E$  is the matrix of normalised polarisation vectors and  $\mathbf{k}$  is a wavevector.

If one substitutes this equation into the secular equation (equation 3.18), one



finds

$$\sum_{\{\mathbf{S}, \nu, j\}} \frac{\Phi\left(\begin{smallmatrix} \mathbf{R} & \mathbf{S} \\ i & j \end{smallmatrix}\right)}{\sqrt{M_\mu M_\nu}} \exp(i\mathbf{k} \cdot \mathbf{S}) E\left(\begin{smallmatrix} \mathbf{S} & \mathbf{k} \\ \nu & \rho \end{smallmatrix}\right) = \left[\omega\left(\begin{smallmatrix} \mathbf{k} \\ \rho \end{smallmatrix}\right)\right]^2 E\left(\begin{smallmatrix} \mathbf{R} & \mathbf{k} \\ i & \rho \end{smallmatrix}\right) \exp(i\mathbf{k} \cdot \mathbf{R}) . \quad (3.24)$$

Multiplying by  $\exp(-i\mathbf{k} \cdot \mathbf{R})$  this becomes

$$\sum_{\{\mathbf{S}, \nu, j\}} \underbrace{\frac{\Phi\left(\begin{smallmatrix} \mathbf{R} & \mathbf{S} \\ i & j \end{smallmatrix}\right)}{\sqrt{M_\mu M_\nu}} \exp(i\mathbf{k} \cdot (\mathbf{S} - \mathbf{R}))}_{=D\left(\begin{smallmatrix} \mathbf{R} & \mathbf{S} \\ i & j \end{smallmatrix}\right)} E\left(\begin{smallmatrix} \mathbf{S} & \mathbf{k} \\ \nu & \rho \end{smallmatrix}\right) = \left[\omega\left(\begin{smallmatrix} \mathbf{k} \\ \rho \end{smallmatrix}\right)\right]^2 E\left(\begin{smallmatrix} \mathbf{R} & \mathbf{k} \\ i & \rho \end{smallmatrix}\right) , \quad (3.25)$$

where the *dynamical matrix* has been defined,

$$D\left(\begin{smallmatrix} \mathbf{R} & \mathbf{S} \\ i & j \end{smallmatrix}\right) = \frac{\Phi\left(\begin{smallmatrix} \mathbf{R} & \mathbf{S} \\ i & j \end{smallmatrix}\right)}{\sqrt{M_\mu M_\nu}} \exp(i\mathbf{k} \cdot (\mathbf{S} - \mathbf{R})) . \quad (3.26)$$

It can now be seen that the lattice periodicity means that the problem becomes a diagonalisation problem of the dynamical matrix to find the frequencies and the polarisation vectors. The waves described by these frequencies and polarisation vectors are called *phonons*.

Now recalling equation 3.19,

$$\sqrt{M_\mu} u\left(\begin{smallmatrix} \mathbf{R} \\ i \end{smallmatrix}\right)(t) = \sum_{\{\mathbf{k}, \rho, r\}} a\left(\begin{smallmatrix} \mathbf{k} \\ \rho \end{smallmatrix}\right)(t) C\left(\begin{smallmatrix} \mathbf{R} & \mathbf{k} \\ i & \rho \end{smallmatrix}\right) \quad (3.27)$$

$$= \sum_{\{\mathbf{k}, \rho, r\}} a\left(\begin{smallmatrix} \mathbf{k} \\ \rho \end{smallmatrix}\right)(t) E\left(\begin{smallmatrix} \mathbf{R} & \mathbf{k} \\ i & \rho \end{smallmatrix}\right) \exp(i\mathbf{k} \cdot \mathbf{R}) , \quad (3.28)$$

which gives the displacement of atom  $\left(\begin{smallmatrix} \mathbf{R} \\ i \end{smallmatrix}\right)$  as

$$u\left(\begin{smallmatrix} \mathbf{R} \\ i \end{smallmatrix}\right)(t) = \frac{1}{\sqrt{M_\mu}} \sum_{\{\mathbf{k}, \rho, r\}} A\left(\begin{smallmatrix} \mathbf{k} \\ \rho \end{smallmatrix}\right) E\left(\begin{smallmatrix} \mathbf{R} & \mathbf{k} \\ i & \rho \end{smallmatrix}\right) \exp\left[i\mathbf{k} \cdot \mathbf{R} - i\omega\left(\begin{smallmatrix} \mathbf{k} \\ \rho \end{smallmatrix}\right)t\right] . \quad (3.29)$$

This result will be crucial in describing the atomic displacements in the stochastic TDEP method. So far the idea of phonons as normal modes has been introduced and their description both by frequencies and polarisation vectors (eigenvalues and eigenvectors of the dynamical matrix) and by the real-space displacement of

the atoms from their equilibrium positions in the form of a wave.

### 3.1.5 Symmetries of the force constants

In order to diagonalise the dynamical matrix and determine the phonon frequencies, one must first determine the interatomic force constants from which it is constructed. Many of these force constants are equivalent by symmetry. Following the approach of Leibfried and Ludwig, this section will detail these symmetries and the constraints that arise from them [61]. The number of independent force constants after applying these constraints is of great importance, as that is what will determine the complexity of the calculations of the anharmonic phonons.

#### Translation by a lattice vector

The crystal is invariant under translation by a lattice vector  $\mathbf{R}$  and therefore the force constants must be also. By adding a lattice vector  $\mathbf{H}$  to the force constants one finds

$$\Phi\left(\begin{smallmatrix} \mathbf{R} & \mathbf{S} \\ \mu & \nu \\ i & j \end{smallmatrix}\right) = \Phi\left(\begin{smallmatrix} \mathbf{R}+\mathbf{H} & \mathbf{S}+\mathbf{H} \\ \mu & \nu \\ i & j \end{smallmatrix}\right) = \Phi\left(\begin{smallmatrix} \mathbf{0} & \mathbf{S}-\mathbf{R} \\ \mu & \nu \\ i & j \end{smallmatrix}\right) = \Phi\left(\begin{smallmatrix} \mathbf{0} & \mathbf{S}' \\ \mu & \nu \\ i & j \end{smallmatrix}\right). \quad (3.30)$$

The vector  $\mathbf{H}$  has been set equal to  $-\mathbf{R}$ , and the last equality is simply a relabelling of the indices  $\mathbf{S} - \mathbf{R} \rightarrow \mathbf{S}'$ . Equation 3.30 shows that by considering the force constants for the atoms in a single unit cell, one can determine the force constants of the whole crystal.

#### Permutation of the indices

The interatomic force constants are defined as derivatives of the potential energy surface (equation 3.10). As differential operators are commutative, the force constants are unchanged under permutation of the indices in the derivatives,

$$\begin{aligned} \Phi\left(\begin{smallmatrix} \mathbf{R}_1 & \mathbf{R}_2 \\ \mu_1 & \mu_2 \\ i_1 & i_2 \end{smallmatrix}\right) &= \Phi\left(\begin{smallmatrix} \mathbf{R}_2 & \mathbf{R}_1 \\ \mu_2 & \mu_1 \\ i_2 & i_1 \end{smallmatrix}\right) \\ \Phi\left(\begin{smallmatrix} \mathbf{R}_1 & \mathbf{R}_2 & \mathbf{R}_3 \\ \mu_1 & \mu_2 & \mu_3 \\ i_1 & i_2 & i_3 \end{smallmatrix}\right) &= \Phi\left(\begin{smallmatrix} \mathbf{R}_2 & \mathbf{R}_1 & \mathbf{R}_3 \\ \mu_2 & \mu_1 & \mu_3 \\ i_2 & i_1 & i_3 \end{smallmatrix}\right) = \Phi\left(\begin{smallmatrix} \mathbf{R}_3 & \mathbf{R}_2 & \mathbf{R}_1 \\ \mu_3 & \mu_2 & \mu_1 \\ i_3 & i_2 & i_1 \end{smallmatrix}\right) = \dots \\ &\vdots \end{aligned} \quad (3.31)$$

## Crystal symmetry

The force constants must also be invariant under transformations that respect the symmetry of the underlying crystal structure. Each symmetry operation  $S$  of a crystal structure can be written as a rotation  $\Omega$  and a translation  $T$ . Applying this symmetry operation will transform the atomic positions  $X$  to an equivalent set as

$$\sum_j S_{ij} X\left(\begin{smallmatrix} \mathbf{R} \\ \mu \\ j \end{smallmatrix}\right) = \sum_j \Omega_{ij} X\left(\begin{smallmatrix} \mathbf{R} \\ \mu \\ j \end{smallmatrix}\right) + T_i = X\left(\begin{smallmatrix} \mathbf{R}' \\ \mu' \\ i \end{smallmatrix}\right) . \quad (3.32)$$

If the set of vectors  $\left\{ X\left(\begin{smallmatrix} \mathbf{R} \\ \mu \\ j \end{smallmatrix}\right) \right\}$  could be any of the atomic positions, then  $\left\{ X\left(\begin{smallmatrix} \mathbf{R}' \\ \mu' \\ i \end{smallmatrix}\right) \right\}$  must also describe the set of the atomic positions. The Taylor expansion in equation 3.15 must be the same whether it is made with respect to the original or transformed displacements,

$$\begin{aligned} \sum_{\{\mathbf{R}, \mu, i\}} \Phi\left(\begin{smallmatrix} \mathbf{R}_1 & \dots & \mathbf{R}_n \\ \mu_1 & \dots & \mu_n \\ i_1 & \dots & i_n \end{smallmatrix}\right) u\left(\begin{smallmatrix} \mathbf{R}_1 \\ \mu_1 \\ i_1 \end{smallmatrix}\right) \dots u\left(\begin{smallmatrix} \mathbf{R}_n \\ \mu_n \\ i_n \end{smallmatrix}\right) \\ = \sum_{\{\mathbf{R}', \mu', i'\}} \Phi\left(\begin{smallmatrix} \mathbf{R}'_1 & \dots & \mathbf{R}'_n \\ \mu'_1 & \dots & \mu'_n \\ i'_1 & \dots & i'_n \end{smallmatrix}\right) S_{i'_1 i_1} u\left(\begin{smallmatrix} \mathbf{R}'_1 \\ \mu'_1 \\ i'_1 \end{smallmatrix}\right) \dots S_{i'_n i_n} u\left(\begin{smallmatrix} \mathbf{R}'_n \\ \mu'_n \\ i'_n \end{smallmatrix}\right) . \end{aligned} \quad (3.33)$$

As the atomic displacements must be equivalent on each side, one can deduce the relation between the primed (transformed) force constants and the unprimed ones as

$$\sum_{\{\mathbf{R}, \mu, i\}} \Phi\left(\begin{smallmatrix} \mathbf{R}_1 & \dots & \mathbf{R}_n \\ \mu_1 & \dots & \mu_n \\ i_1 & \dots & i_n \end{smallmatrix}\right) = \sum_{\{\mathbf{R}', \mu', i'\}} \Phi\left(\begin{smallmatrix} \mathbf{R}'_1 & \dots & \mathbf{R}'_n \\ \mu'_1 & \dots & \mu'_n \\ i'_1 & \dots & i'_n \end{smallmatrix}\right) S_{i'_1 i_1} \dots S_{i'_n i_n} , \quad (3.34)$$

thereby demonstrating that the force constants are invariant under transformation of the crystal symmetry.

## Translational and rotational invariance of the potential energy

The potential energy  $U$  of the crystal is a scalar quantity and must therefore be invariant under translation and rotation. This constraint is true for *any* translation and rotation of the crystal lattice. This is distinct from the previous constraint which argued that the atomic positions were invariant under some

*specific* transformation that respected the crystal symmetry. The transformations considered here will be infinitesimal rotations and translations of the crystal lattice that need not respect any particular symmetry.

The constraints derived here do not directly equate one force constant with a symmetry equivalent one, as in the previous sections. Instead they place constraints on the entire set of force constants at once. As these constraints do not apply directly to any specific force constant, they will not lower the complexity of the anharmonic phonon calculations. Instead these constraints are applied when fitting a force constant model to a set of forces and displacements to ensure that the result is physically reasonable.

By considering a rotation of the crystal it will be demonstrated that different orders of force constant are not independent, and by considering a translation of the crystal a constraint will be placed on the sum of force constants that will ensure momentum is conserved.

For a general transformation,  $D$ ,

$$\sum_j D_{ij} X \begin{pmatrix} \mathbf{R} \\ \mu \\ j \end{pmatrix} = \sum_j \Omega_{ij} X \begin{pmatrix} \mathbf{R} \\ \mu \\ j \end{pmatrix} + T_i \quad (3.35)$$

where  $\Omega$  again represents the rotation, and  $T$  the translation, the force constants  $\Phi \begin{pmatrix} \mathbf{R}_1 & \mathbf{R}_n \\ \mu_1 & \dots & \mu_n \\ i_1 & & i_n \end{pmatrix}$  must transform as

$$\Omega \Phi = \sum_{j_1 \dots j_n} \Omega_{i_1 j_1} \dots \Omega_{i_n j_n} \Phi \begin{pmatrix} \mathbf{R}_1 & \mathbf{R}_n \\ \mu_1 & \dots & \mu_n \\ j_1 & & j_n \end{pmatrix} \quad (3.36)$$

under rotation, and are invariant under translation.

Applying this transformation to the potential energy yields

$$DU(\dots X \begin{pmatrix} \mathbf{R} \\ \mu \\ i \end{pmatrix} \dots) = U(\dots DX \begin{pmatrix} \mathbf{R} \\ \mu \\ i \end{pmatrix} \dots) = U(\dots X \begin{pmatrix} \mathbf{R} \\ \mu \\ i \end{pmatrix} \dots) \quad (3.37)$$

where the last equality is the condition for invariance under the transformation  $D$ . From here, a pure rotation  $\Omega$  without any translational part will be considered. The rotation  $\Omega$  may be with or without inversion.

The rotation  $\Omega$  may be considered as an active transformation, creating displacements from the original positions as the atoms are moved. If one takes

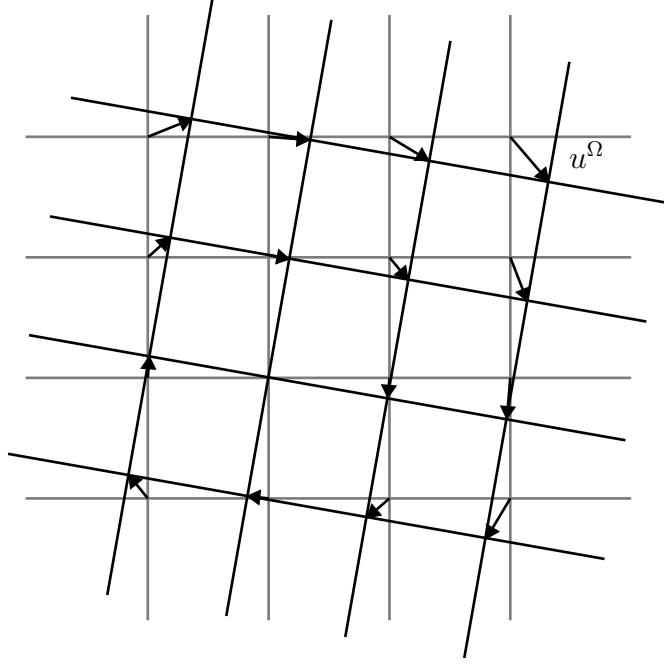


**Figure 3.1** *Rotation  $\Omega$  of the crystal structure, indicated by the grid of squares. For atomic positions on the corner of the squares, the displacements created by the small rotation are indicated by  $u^\Omega$ .*

the equilibrium positions (where the force constants are known to be well defined) to be the starting positions, then one can express the new positions as

$$\Omega X \begin{pmatrix} \mathbf{R} \\ \mu \\ i \end{pmatrix} = X \begin{pmatrix} \mathbf{R} \\ \mu \\ i \end{pmatrix} + (\Omega - 1) X \begin{pmatrix} \mathbf{R} \\ \mu \\ i \end{pmatrix} \quad (3.38)$$

$$= X \begin{pmatrix} \mathbf{R} \\ \mu \\ i \end{pmatrix} + u^\Omega \begin{pmatrix} \mathbf{R} \\ \mu \\ i \end{pmatrix}, \quad (3.39)$$

where  $u^\Omega \begin{pmatrix} \mathbf{R} \\ \mu \\ i \end{pmatrix}$  are the displacements created by applying the transformation  $\Omega$  and  $\mathbf{R}$  are the equilibrium positions. Rearranging equation 3.39, the displacements may be written as the difference between the transformed and the original displacements,

$$u^\Omega \begin{pmatrix} \mathbf{R} \\ \mu \\ i \end{pmatrix} = \sum_k (\Omega_{ik} - \delta_{ik}) X \begin{pmatrix} \mathbf{R} \\ \mu \\ k \end{pmatrix}. \quad (3.40)$$

The rotation  $\Omega$  and the displacements it creates are shown in figure 3.1.

To find the force constants at the displaced positions one may Taylor expand the force constants, defined at the original positions, in terms of the small displacement  $u^\Omega$ . As a force constant of order  $n$  is itself an  $n^{\text{th}}$ -order derivative of the crystal potential  $U$ , the coefficient of the  $m^{\text{th}}$  term in this expansion will be

the  $(n+m)^{\text{th}}$  derivative of  $U$  and thus will be an  $(n+m)^{\text{th}}$ -order force constant.

The force constants at the displaced positions are therefore

$$\begin{aligned} \Phi\left(\begin{smallmatrix} \mathbf{R}_1 \\ \mu_1 \\ i_1 \end{smallmatrix} \dots \begin{smallmatrix} \mathbf{R}_n \\ \mu_n \\ i_n \end{smallmatrix}\right)\Big|_{\{u^\Omega\}} &= \Phi\left(\begin{smallmatrix} \mathbf{R}_1 \\ \mu_1 \\ i_1 \end{smallmatrix} \dots \begin{smallmatrix} \mathbf{R}_n \\ \mu_n \\ i_n \end{smallmatrix}\right)\Big|_{\{u^\Omega=0\}} \\ &+ \sum_{\substack{\mathbf{R}_{n+1} \\ \mu_{n+1} \\ i_{n+1}}} \Phi\left(\begin{smallmatrix} \mathbf{R}_1 \\ \mu_1 \\ i_1 \end{smallmatrix} \dots \begin{smallmatrix} \mathbf{R}_{n+1} \\ \mu_{n+1} \\ i_{n+1} \end{smallmatrix}\right) u^\Omega\left(\begin{smallmatrix} \mathbf{R}_{n+1} \\ \mu_{n+1} \\ i_{n+1} \end{smallmatrix}\right) \\ &+ \sum_{\substack{\mathbf{R}_{n+1}, \mathbf{R}_{n+2} \\ \mu_{n+1}, \mu_{n+2} \\ i_{n+1}, i_{n+2}}} \Phi\left(\begin{smallmatrix} \mathbf{R}_1 \\ \mu_1 \\ i_1 \end{smallmatrix} \dots \begin{smallmatrix} \mathbf{R}_{n+2} \\ \mu_{n+2} \\ i_{n+2} \end{smallmatrix}\right) u^\Omega\left(\begin{smallmatrix} \mathbf{R}_{n+1} \\ \mu_{n+1} \\ i_{n+1} \end{smallmatrix}\right) u^\Omega\left(\begin{smallmatrix} \mathbf{R}_{n+2} \\ \mu_{n+2} \\ i_{n+2} \end{smallmatrix}\right) + \dots \end{aligned} \quad (3.41)$$

As both equation 3.36 and equation 3.41 are describing the transformed force constants, they must be equal. Consider now a rotation that is infinitesimal and antisymmetric,

$$\Omega_{ik} = \delta_{ik} + \omega_{ik} \quad \text{where} \quad \omega_{ik} = -\omega_{ki} . \quad (3.42)$$

As  $\omega$  is infinitesimal, only terms linear in  $\omega$  should be retained from equation 3.41.

Using this and equation 3.36 one arrives at the relation

$$\sum_{\lambda=1}^n \sum_{i'_\lambda} \omega_{i_\lambda i'_\lambda} \Phi\left(\begin{smallmatrix} \mathbf{R}_1 \\ \mu_1 \\ i_1 \end{smallmatrix} \dots \begin{smallmatrix} \mathbf{R}_\lambda \\ \mu_\lambda \\ i_\lambda \end{smallmatrix} \dots \begin{smallmatrix} \mathbf{R}_n \\ \mu_n \\ i_n \end{smallmatrix}\right) = \sum_{\substack{\mathbf{R}_{n+1} \\ \mu_{n+1} \\ i_{n+1}}} \Phi\left(\begin{smallmatrix} \mathbf{R}_1 \\ \mu_1 \\ i_1 \end{smallmatrix} \dots \begin{smallmatrix} \mathbf{R}_{n+1} \\ \mu_{n+1} \\ i_{n+1} \end{smallmatrix}\right) \omega_{i_{n+1} i} X\left(\begin{smallmatrix} \mathbf{R}_{n+1} \\ \mu_{n+1} \\ i \end{smallmatrix}\right) , \quad (3.43)$$

where

$$u^\Omega\left(\begin{smallmatrix} \mathbf{R} \\ \mu \\ i \end{smallmatrix}\right) = \sum_k (\Omega_{ik} - \delta_{ik}) X\left(\begin{smallmatrix} \mathbf{R} \\ \mu \\ k \end{smallmatrix}\right) = \sum_k (\omega_{ik} + \delta_{ik} - \delta_{ik}) X\left(\begin{smallmatrix} \mathbf{R} \\ \mu \\ k \end{smallmatrix}\right) = \sum_k \omega_{ik} X\left(\begin{smallmatrix} \mathbf{R} \\ \mu \\ k \end{smallmatrix}\right) \quad (3.44)$$

has been used.

Re-indexing  $i_{n+1} \rightarrow i'$  and using antisymmetry  $\omega_{ii'} = -\omega_{i'i}$  on the right hand side one finds

$$0 = \sum_{ii'} \omega_{ii'} \left[ \sum_{\substack{\mathbf{R}_{n+1} \\ \mu_{n+1}}} \Phi\left(\begin{smallmatrix} \mathbf{R}_1 \\ \mu_1 \\ i_1 \end{smallmatrix} \dots \begin{smallmatrix} \mathbf{R}_{n+1} \\ \mu_{n+1} \\ i' \end{smallmatrix}\right) X\left(\begin{smallmatrix} \mathbf{R}_{n+1} \\ \mu_{n+1} \\ i \end{smallmatrix}\right) + \sum_{\lambda=1}^n \sum_{i'_\lambda} \Phi\left(\begin{smallmatrix} \mathbf{R}_1 \\ \mu_1 \\ i_1 \end{smallmatrix} \dots \begin{smallmatrix} \mathbf{R}_\lambda \\ \mu_\lambda \\ i_\lambda \end{smallmatrix} \dots \begin{smallmatrix} \mathbf{R}_n \\ \mu_n \\ i_n \end{smallmatrix}\right) \delta_{ii_\lambda} \delta_{i' i'_\lambda} \right] . \quad (3.45)$$

As  $\omega$  was arbitrary except for the antisymmetry constraint, the only way to guarantee that the whole sum is zero in the general case is for the part in the square brackets to be symmetric in  $i \leftrightarrow i'$ ; for each  $ii'$  term an  $i'i$  term will cancel it.

The final constraint on the force constants is therefore that the expression

$$\sum_{\substack{\mathbf{R}_{n+1} \\ \mu_{n+1}}} \Phi \left( \begin{smallmatrix} \mathbf{R}_1 \\ \mu_1 \end{smallmatrix} \dots \begin{smallmatrix} \mathbf{R}_{n+1} \\ \mu_{n+1} \end{smallmatrix} \right) X \left( \begin{smallmatrix} \mathbf{R}_{n+1} \\ i \end{smallmatrix} \right) + \sum_{\lambda=1}^n \sum_{i'_\lambda} \Phi \left( \begin{smallmatrix} \mathbf{R}_1 \\ \mu_1 \end{smallmatrix} \dots \begin{smallmatrix} \mathbf{R}_\lambda \\ \mu_\lambda \end{smallmatrix} \dots \begin{smallmatrix} \mathbf{R}_n \\ \mu_n \end{smallmatrix} \right) \delta_{ii_\lambda} \delta_{i'_\lambda i'_\lambda} \quad (3.46)$$

is antisymmetric in  $i \leftrightarrow i'$ . This constraint relates the force constants of order  $n$  to those of  $n+1$ , and for a force constant model including terms up to order  $n_{\max}$ , the constraint applies to all orders:  $n = 0, 1, 2, \dots, n_{\max}$ .

Now considering the translational invariance, constraints on the force constants, known as the acoustic sum rules, are derived. One may repeat the procedure of considering the translation to be an active one and again expanding the force constants in terms of the resulting displacements.

The force constants at the displaced positions are

$$\begin{aligned} \Phi \left( \begin{smallmatrix} \mathbf{R}_1 \\ \mu_1 \end{smallmatrix} \dots \begin{smallmatrix} \mathbf{R}_n \\ \mu_n \end{smallmatrix} \right) \Big|_{\{u^T\}} &= \Phi \left( \begin{smallmatrix} \mathbf{R}_1 \\ \mu_1 \end{smallmatrix} \dots \begin{smallmatrix} \mathbf{R}_n \\ \mu_n \end{smallmatrix} \right) \Big|_{\{u^T=0\}} \\ &+ \sum_{\substack{\mathbf{R}_{n+1} \\ \mu_{n+1} \\ i_{n+1}}} \Phi \left( \begin{smallmatrix} \mathbf{R}_1 \\ \mu_1 \end{smallmatrix} \dots \begin{smallmatrix} \mathbf{R}_{n+1} \\ \mu_{n+1} \end{smallmatrix} \right) u^T \left( \begin{smallmatrix} \mathbf{R}_{n+1} \\ \mu_{n+1} \\ i_{n+1} \end{smallmatrix} \right) \\ &+ \sum_{\substack{\mathbf{R}_{n+1}, \mathbf{R}_{n+2} \\ \mu_{n+1}, \mu_{n+2} \\ i_{n+1}, i_{n+2}}} \Phi \left( \begin{smallmatrix} \mathbf{R}_1 \\ \mu_1 \end{smallmatrix} \dots \begin{smallmatrix} \mathbf{R}_{n+2} \\ \mu_{n+2} \end{smallmatrix} \right) u^T \left( \begin{smallmatrix} \mathbf{R}_{n+1} \\ \mu_{n+1} \\ i_{n+1} \end{smallmatrix} \right) u^T \left( \begin{smallmatrix} \mathbf{R}_{n+2} \\ \mu_{n+2} \\ i_{n+2} \end{smallmatrix} \right) + \dots \quad (3.47) \end{aligned}$$

(c.f. equation 3.41). This time the displacement comes from the translation  $u^T \left( \begin{smallmatrix} \mathbf{R} \\ \mu \\ i \end{smallmatrix} \right) = T_i$ . As the force constants are defined through derivatives of the atomic positions, adding a constant term has no effect and the force constants are invariant under this transformation,

$$\Phi \left( \begin{smallmatrix} \mathbf{R}_1 \\ \mu_1 \end{smallmatrix} \dots \begin{smallmatrix} \mathbf{R}_n \\ \mu_n \end{smallmatrix} \right) \Big|_{\{u^T\}} = \Phi \left( \begin{smallmatrix} \mathbf{R}_1 \\ \mu_1 \end{smallmatrix} \dots \begin{smallmatrix} \mathbf{R}_n \\ \mu_n \end{smallmatrix} \right) \Big|_{\{u^T=0\}}. \quad (3.48)$$

For an infinitesimal transformation  $T_i = t_i$  only terms linear in  $t$  need be

preserved, therefore

$$\sum_{\substack{\mathbf{R}_{n+1} \\ \mu_{n+1} \\ i_{n+1}}} \Phi \left( \begin{smallmatrix} \mathbf{R}_1 & \dots & \mathbf{R}_{n+1} \\ \mu_1 & \dots & \mu_{n+1} \\ i_1 & \dots & i_{n+1} \end{smallmatrix} \right) t_{i_{n+1}} = 0 . \quad (3.49)$$

Since this infinitesimal transformation is arbitrary, for the above to be generally true it must be the case that

$$\sum_{\substack{\mathbf{R}_{n+1} \\ \mu_{n+1} \\ i_{n+1}}} \Phi \left( \begin{smallmatrix} \mathbf{R}_1 & \dots & \mathbf{R}_{n+1} \\ \mu_1 & \dots & \mu_{n+1} \\ i_1 & \dots & i_{n+1} \end{smallmatrix} \right) = 0 . \quad (3.50)$$

As with the rotational invariance, in a force constant model considering terms up to  $n_{\max}$  the constraint of equation 3.50 must apply to all orders  $n = 0, 1, 2, \dots, n_{\max}$ . When  $n_{\max} = 2$  this becomes the familiar acoustic sum rule.

## 3.2 Green's functions

In the harmonic approximation, phonons do not interact with each other. The exact diagonalisation of the dynamical matrix establishes the harmonic phonons as the normal modes of the system, which are completely non-interacting. In reality, anharmonic terms in the potential introduce couplings between the normal modes of the harmonic system causing the phonons to interact. The coupling is described by the self-energy  $\Sigma$ . The self-energy is the energy a particle (in this case a phonon) has as a result of interactions with its environment. The self-energy corrects the harmonic phonon frequencies as

$$V_{ij}(\mathbf{k}) = \Lambda_{ij}(\mathbf{k}) + \Sigma_{ij}(\mathbf{k}) \quad (3.51)$$

where  $\Lambda_{ij}(\mathbf{k})$  is the diagonal matrix of harmonic phonon frequencies and  $\Sigma_{ij}(\mathbf{k})$  is a Hermitian matrix with complex elements. The self-energy is frequently expressed as  $\Sigma = \Delta + i\Gamma$  with  $\Delta$  and  $\Gamma$  being the real and imaginary parts. The imaginary part of the self-energy describes the phonon lifetimes, how long a phonon exists for before it scatters off another phonon, and the real part describes the renormalisation. When  $\Sigma$  is added to  $\Lambda$  the real part of  $\Sigma$  changes the phonon frequencies. This change, usually a lowering, is referred to as the renormalisation.



The elements of the self-energy are found through the Green's function formalism, which will be described here. This section will follow the approach of Reissland [62] in deriving the harmonic Green's function and the self-energy of the two lowest-order phonon–phonon interaction processes.

A Green's function, also called a propagator, describes the evolution of a system from a time  $t'$  to a time  $t$ . It is, therefore, a solution to the equation of motion which, in the quantum-mechanical case, is

$$i\hbar \frac{d\Psi(\mathbf{r}, t)}{dt} = \hat{H}\Psi(\mathbf{r}, t) \quad (3.52)$$

with a time-dependent solution of

$$\Psi(\mathbf{r}, t) = \sum_j C_j(t) \psi_j(\mathbf{r}) e^{-i\epsilon_j t/\hbar}. \quad (3.53)$$

Here  $\psi_j$  and  $\epsilon_j$  are the eigenstates and eigenvalues of the Hamiltonian  $\hat{H}$ , and  $C_j(t)$  are general, time-dependent coefficients. These coefficients are given by

$$C_j(t) = \int \psi_j^*(\mathbf{r}') \Psi(\mathbf{r}', t) e^{i\epsilon_j t/\hbar} d\mathbf{r}'. \quad (3.54)$$

Substituting this expression into equation 3.53 one finds

$$\Psi(\mathbf{r}, t) = \underbrace{\int \sum_j \psi_j^*(\mathbf{r}') \psi_j(\mathbf{r}) e^{-i\epsilon_j(t-t')/\hbar} \Psi(\mathbf{r}', t) d\mathbf{r}'}_{g(\mathbf{r}', t'; \mathbf{r}, t)}. \quad (3.55)$$

One may now identify the Green's function as

$$g(\mathbf{r}', t'; \mathbf{r}, t) = \sum_j \psi_j^*(\mathbf{r}') \psi_j(\mathbf{r}) e^{-i\epsilon_j(t-t')/\hbar}, \quad (3.56)$$

where  $g(\mathbf{r}', t; \mathbf{r}, t)$  is a function that relates the initial state  $\psi_j(\mathbf{r}')$  at  $t = t'$  to the final state  $\psi_j(\mathbf{r})$  at  $t$ . In order to preserve causality, the Green's function must be zero before the perturbation of the system at  $t'$ . To this end, it is usual to work with a modified form of  $g$  that simplifies the boundary conditions,

$$G(\mathbf{r}', t'; \mathbf{r}, t) = -i\eta(t - t')g(\mathbf{r}', t'; \mathbf{r}, t). \quad (3.57)$$

Causality is enforced by  $\eta(t - t')$ , the step function, which has the value 0 for  $t < t'$  and 1 for  $t > t'$ . With causality enforced one can now use the above equation to describe the propagation of a newly created phonon state at time  $t'$  to its destruction at time  $t$ . This creation and annihilation is indicated by the traditional operators:  $a^+(\mathbf{r}', t')$  and  $a(\mathbf{r}, t)$ .

The one-particle Green's function is therefore defined as

$$G(\mathbf{r}', t'; \mathbf{r}, t) = -i\eta(t - t')\langle a(\mathbf{r}, t)a^+(\mathbf{r}', t') \rangle \quad (3.58)$$

where  $\langle \dots \rangle$  denotes the thermodynamic average. There is also the possibility of a particle being *destroyed* at time  $t'$  and later created at  $t$  (i.e. the propagation of a hole). Considering this additional term, and choosing appropriate minus signs to indicate the direction of propagation, one can define the three basic Green's functions: retarded, advanced, and causal.

$$\begin{aligned} G_R(\mathbf{r}', t'; \mathbf{r}, t) &= -i\eta(t - t') (\langle a(\mathbf{r}, t)a^+(\mathbf{r}', t') \rangle - \langle a^+(\mathbf{r}, t)a(\mathbf{r}', t') \rangle) \\ &= -i\eta(t - t')\langle [a(\mathbf{r}, t), a^+(\mathbf{r}', t')] \rangle \end{aligned} \quad (3.59)$$

$$\begin{aligned} G_A(\mathbf{r}', t'; \mathbf{r}, t) &= i\eta(t' - t) (\langle a(\mathbf{r}, t)a^+(\mathbf{r}', t') \rangle - \langle a^+(\mathbf{r}, t)a(\mathbf{r}', t') \rangle) \\ &= i\eta(t' - t)\langle [a(\mathbf{r}, t), a^+(\mathbf{r}', t')] \rangle \end{aligned} \quad (3.60)$$

$$\begin{aligned} G_C(\mathbf{r}', t'; \mathbf{r}, t) &= -i\eta(t - t')\langle a(\mathbf{r}, t)a^+(\mathbf{r}', t') \rangle - i\eta(t' - t)\langle a^+(\mathbf{r}, t)a(\mathbf{r}', t') \rangle \\ &= -i\langle T\{a(\mathbf{r}, t)a^+(\mathbf{r}', t')\} \rangle \end{aligned} \quad (3.61)$$

The square brackets  $[\dots]$  are the standard commutation relations and the operator  $T$  is the time-ordering operator, which reorders the operators it acts upon such that they are time-ordered, e.g.

$$T\{A(t_1)B(t_2)C(t_3)\} = C(t_3)B(t_2)A(t_1) \quad \text{for } t_3 > t_2 > t_1. \quad (3.62)$$

In the case of phonons, the one-phonon Green's function may be written analogously to equation 3.61 with the appropriate indices to describe the phonon wavevector and band index inserted as

$$G(\mathbf{k}, j, t; \mathbf{k}', j', t') = i\langle T\{A_{\mathbf{k}j}(t)A_{\mathbf{k}'j'}^*(t')\} \rangle, \quad (3.63)$$

where  $A_{\mathbf{k}j}(t) = a_{-\mathbf{k}j}^+(t) + a_{\mathbf{k}j}(t)$ . With this definition, it is no longer necessary to

ascribe a time direction to the propagator as each term contains both  $\mathbf{k}$  and  $-\mathbf{k}$ .

### Temperature and imaginary time

It can be shown that the thermodynamic averages can be evaluated by taking the trace over the density matrix  $\rho$  which, for phonons, with zero chemical potential, is given by  $\rho = \frac{1}{Z}e^{-\beta\hat{H}}$ , where  $\beta = \frac{1}{k_B T}$  and  $Z$  is the partition function. For now assuming  $t' < t$ ,

$$\langle A_{\mathbf{k}j}(t)A_{\mathbf{k}'j'}^*(t') \rangle = \text{Tr}\{A_{\mathbf{k}j}(t)A_{\mathbf{k}'j'}^*(t')\rho\} . \quad (3.64)$$

Using the Heisenberg picture of quantum mechanics where the time dependence is ascribed to the operators,  $O(t) = e^{i\hat{H}t/\hbar}O(0)e^{-i\hat{H}t/\hbar}$ , this becomes

$$\langle A_{\mathbf{k}j}(t)A_{\mathbf{k}'j'}^*(t') \rangle = \text{Tr}\{\rho e^{i\hat{H}t/\hbar}A_{\mathbf{k}j}(0)e^{-i\hat{H}t/\hbar}A_{\mathbf{k}'j'}^*(t')\} \quad (3.65)$$

where  $\rho$  has been brought to the front using the cyclic property of the trace.

If  $t' > t$  then the time-ordering operator in equation 3.63 swaps the order of the operators and computing the trace yields

$$\langle A_{\mathbf{k}'j'}^*(t')A_{\mathbf{k}j}(t) \rangle = \text{Tr}\{A_{\mathbf{k}'j'}^*(t')A_{\mathbf{k}j}(t)\rho\} . \quad (3.66)$$

Again using the cyclic property of the trace,

$$\langle A_{\mathbf{k}'j'}^*(t')A_{\mathbf{k}j}(t) \rangle = \text{Tr}\{A_{\mathbf{k}j}(t)\rho A_{\mathbf{k}'j'}^*(t')\} . \quad (3.67)$$

Now considering the case of  $t = 0$  and inserting the expression for  $\rho$  and a factor of  $e^{-\beta\hat{H}}e^{+\beta\hat{H}} = 1$  one may derive

$$\langle A_{\mathbf{k}'j'}^*(t')A_{\mathbf{k}j}(0) \rangle = \frac{1}{Z}\text{Tr}\{A_{\mathbf{k}j}(0)e^{-\beta\hat{H}}A_{\mathbf{k}'j'}^*(t')\} \quad (3.68)$$

$$= \frac{1}{Z}\text{Tr}\{e^{-\beta\hat{H}}e^{+\beta\hat{H}}A_{\mathbf{k}j}(0)e^{-\beta\hat{H}}A_{\mathbf{k}'j'}^*(t')\} \quad (3.69)$$

$$= \text{Tr}\{\rho e^{\beta\hat{H}}A_{\mathbf{k}j}(0)e^{-\beta\hat{H}}A_{\mathbf{k}'j'}^*(t')\} . \quad (3.70)$$

It may now be observed that the right hand sides of equations 3.65 and 3.70 are

similar. By setting  $\beta = it/\hbar$  in equation 3.65 they can be made identical. One may therefore state

$$\langle A_{\mathbf{k}'j'}^*(t') A_{\mathbf{k}j}(0) \rangle = \langle A_{\mathbf{k}j}(\beta\hbar/i) A_{\mathbf{k}'j'}^*(t') \rangle, \quad (3.71)$$

drawing a formal equivalence between temperature and imaginary time. Now defining a second variable  $u$  with the same dimensions as  $\beta$  where  $-\beta < u < 0$ , it can then be shown that

$$G(\mathbf{k}, j, 0; \mathbf{k}', j', u) = i \langle A_{\mathbf{k}'j'}^*(0) A_{\mathbf{k}j}(u) \rangle \quad (3.72)$$

$$G(\mathbf{k}, j, 0; \mathbf{k}', j', u + \beta) = i \langle A_{\mathbf{k}j}(u + \beta) A_{\mathbf{k}'j'}^*(0) \rangle \quad (3.73)$$

$$= \frac{i}{Z} \text{Tr} \{ e^{(u+\beta)\hat{H}} A_{\mathbf{k}j}(0) e^{-(u+\beta)\hat{H}} A_{\mathbf{k}'j'}^*(0) e^{-\beta\hat{H}} \} \quad (3.74)$$

$$= \frac{i}{Z} \text{Tr} \{ e^{u\hat{H}} A_{\mathbf{k}j}(0) e^{-(u+\beta)\hat{H}} A_{\mathbf{k}'j'}^*(0) e^{-\beta\hat{H}} e^{\beta\hat{H}} \} \quad (3.75)$$

$$= \frac{i}{Z} \text{Tr} \{ e^{u\hat{H}} A_{\mathbf{k}j}(0) e^{-u\hat{H}} e^{-\beta\hat{H}} A_{\mathbf{k}'j'}^*(0) \} \quad (3.76)$$

$$= \frac{i}{Z} \text{Tr} \{ A_{\mathbf{k}'j'}^*(0) e^{u\hat{H}} A_{\mathbf{k}j}(0) e^{-u\hat{H}} e^{-\beta\hat{H}} \} \quad (3.77)$$

$$= i \langle A_{\mathbf{k}'j'}^*(0) A_{\mathbf{k}j}(u) \rangle \quad (3.78)$$

$$= G(\mathbf{k}, j, 0; \mathbf{k}', j', u) \quad (3.79)$$

where the Heisenberg representation of the operators, the expression for the density matrix,  $\rho = \frac{1}{Z} e^{-\beta\hat{H}}$ , and the cyclic property of the trace has been used. The one-phonon Green's function is therefore shown to be periodic in imaginary time with periodicity  $\beta$ ,

$$G(\mathbf{k}, j, 0; \mathbf{k}', j', u) = G(\mathbf{k}, j, 0; \mathbf{k}', j', u + \beta). \quad (3.80)$$

### The harmonic one-phonon Green's function

The one-phonon Green's function is defined as

$$G(\mathbf{k}, j, t; \mathbf{k}', j', t') = i \langle T \{ A_{\mathbf{k}j}(t) A_{\mathbf{k}'j'}^*(t') \} \rangle. \quad (3.81)$$

In the case of a Hamiltonian that does not explicitly depend on time, one may note that the propagator may depend only on the difference  $t - t'$  and the one-

phonon Green's function may be written

$$G(\mathbf{k}, j; \mathbf{k}', j'; t) = i \langle T \{ A_{\mathbf{k}j}(t) A_{\mathbf{k}'j'}^*(0) \} \rangle \quad (3.82)$$

where  $t - t' \rightarrow t$ .

Given that this function is periodic in imaginary time, define  $u = it/\hbar$  and expand as a Fourier series,

$$G(\mathbf{k}, j; \mathbf{k}', j'; u) = \sum_p G_{\mathbf{k}j\mathbf{k}'j'}(\omega_p) e^{i\hbar\omega_p u}, \quad (3.83)$$

where  $\omega_p = \frac{2\pi}{\beta\hbar}p$  are the so-called *Matsubara frequencies*, and the coefficients  $G_{\mathbf{k}j\mathbf{k}'j'}(\omega_p)$  are given by

$$G_{\mathbf{k}j\mathbf{k}'j'}(\omega_p) = \frac{1}{\beta} \int_0^\beta G(\mathbf{k}, j; \mathbf{k}', j'; u) e^{-i\hbar\omega_p u} du. \quad (3.84)$$

Although this function is only defined for the values of  $\omega_p$ , it can be analytically continued to a continuous variable  $G_{\mathbf{k}j\mathbf{k}'j'}(\omega)$ .

For a harmonic Hamiltonian,

$$\hat{H}_0 = \sum_{\mathbf{k}j} \left( a_{\mathbf{k}j}^+ a_{\mathbf{k}j} + \frac{1}{2} \right) \hbar\omega_{\mathbf{k}j} = \sum_{\mathbf{k}j} \left( n_{\mathbf{k}j} + \frac{1}{2} \right) \hbar\omega_{\mathbf{k}j}, \quad (3.85)$$

these Fourier coefficients may be determined as follows: by writing the operators  $A_{\mathbf{k}j}(t)$  and  $A_{\mathbf{k}j}^*(t)$  in full,

$$G^0(\mathbf{k}, j; \mathbf{k}', j'; t) = i \langle T \{ [a_{-\mathbf{k}j}^+(u) + a_{\mathbf{k}j}(u)] [a_{-\mathbf{k}'j'}(0) + a_{\mathbf{k}'j'}^+(0)] \} \rangle, \quad (3.86)$$

it can be seen the propagator will be zero unless  $k = k'$  and  $j = j'$ , and, furthermore, only terms where both operators act on the same wavevector will be non-zero in the thermodynamic average, resulting in an expression

$$G^0(\mathbf{k}, j; t) = \langle T \{ a_{-\mathbf{k}j}^+(u) a_{-\mathbf{k}j}(0) + a_{\mathbf{k}j}(u) a_{\mathbf{k}j}^+(0) \} \rangle. \quad (3.87)$$

Using the Heisenberg representation of the operators  $a_{-\mathbf{k}j}^+(u)$  and  $a_{\mathbf{k}j}(u)$  and

noting the time-ordering operator, one finds

$$G^0(\mathbf{k}, j; t) = \langle e^{\hat{H}_0 u} a_{-\mathbf{k}j}^+(0) e^{-\hat{H}_0 u} a_{-\mathbf{k}j}(0) + e^{\hat{H}_0 u} a_{\mathbf{k}j}(0) e^{-\hat{H}_0 u} a_{\mathbf{k}j}^+(0) \rangle \quad (3.88)$$

for  $u > 0$  and

$$G^0(\mathbf{k}, j; t) = \langle a_{-\mathbf{k}j}(0) e^{\hat{H}_0 u} a_{-\mathbf{k}j}^+(0) e^{-\hat{H}_0 u} + a_{\mathbf{k}j}^+(0) e^{\hat{H}_0 u} a_{\mathbf{k}j}(0) e^{-\hat{H}_0 u} \rangle \quad (3.89)$$

for  $u < 0$ .

For both of these cases, the exponentials may be expressed as a power series of the number operator  $n$ , and one may take advantage of the following:

$$a n^i = a n^{i-1} a^+ a \quad (3.90)$$

$$= (a a^+)^i a \quad (3.91)$$

$$= (1 + a^+ a)^i a \quad (3.92)$$

$$= (1 + n)^i a . \quad (3.93)$$

As each term in the series is transformed similarly,  $a f(n) = f(1 + n) a$ , where  $f$  is any function that can be represented as a power series in  $n$ . An analogous expression  $a^+ f(n) = f(n - 1) a^+$  can be derived for the creation operator. Consequently, for  $u > 0$ ,

$$G^0(\mathbf{k}, j; t) = \langle e^{n_{-\mathbf{k}j} \hbar \omega_{-\mathbf{k}j} u} e^{-(n_{-\mathbf{k}j}-1) \hbar \omega_{-\mathbf{k}j} u} a_{-\mathbf{k}j}^+(0) a_{-\mathbf{k}j}(0) + e^{n_{\mathbf{k}j} \hbar \omega_{\mathbf{k}j} u} e^{-(n_{\mathbf{k}j}+1) \hbar \omega_{\mathbf{k}j} u} a_{\mathbf{k}j}(0) a_{\mathbf{k}j}^+(0) \rangle \quad (3.94)$$

where the terms in equation 3.85 with wavevectors that do not equal  $\pm \mathbf{k}$  (as appropriate) commute and cancel in the exponentials, as do the  $\frac{1}{2} \hbar \omega_{\pm \mathbf{k}j}$  terms. Cancelling exponential factors and using the using  $a a^+ = 1 + n$  yields

$$G^0(\mathbf{k}, j; t) = \langle e^{\hbar \omega_{-\mathbf{k}j} u} n_{-\mathbf{k}j} + e^{-\hbar \omega_{\mathbf{k}j} u} (n_{\mathbf{k}j} + 1) \rangle . \quad (3.95)$$

A similar expression is derived for  $u < 0$ ,

$$G^0(\mathbf{k}, j; t) = \langle e^{-\hbar \omega_{-\mathbf{k}j} u} n_{-\mathbf{k}j} + e^{\hbar \omega_{\mathbf{k}j} u} (n_{\mathbf{k}j} + 1) \rangle . \quad (3.96)$$

For both  $u > 0$  and  $u < 0$  one finds

$$G^0(\mathbf{k}, j; t) = e^{\hbar\omega_{\mathbf{k}j}|u|}\bar{n}_{\mathbf{k}j} + e^{-\hbar\omega_{\mathbf{k}j}|u|}(\bar{n}_{\mathbf{k}j} + 1), \quad (3.97)$$

where  $\langle n_{\mathbf{k}j} \rangle = \bar{n}_{\mathbf{k}j}$  has been used.

Now finding the coefficients from equation 3.84,

$$G_{\mathbf{k}j}(\omega_p) = \frac{1}{\beta} \int_0^\beta (e^{\hbar\omega_{\mathbf{k}j}u}\bar{n}_{\mathbf{k}j} + e^{-\hbar\omega_{\mathbf{k}j}u}(\bar{n}_{\mathbf{k}j} + 1)) e^{-i\hbar\omega_p u} du \quad (3.98)$$

$$G_{\mathbf{k}j}(\omega_p) = \frac{1}{\beta\hbar} \left[ \left\{ \frac{\bar{n}_{\mathbf{k}j}e^{\hbar\omega_{\mathbf{k}j}u}}{\omega_{\mathbf{k}j} - i\omega_p} + \frac{(\bar{n}_{\mathbf{k}j} + 1)e^{-\hbar\omega_{\mathbf{k}j}u}}{-\omega_{\mathbf{k}j} - i\omega_p} \right\} e^{-i\hbar\omega_p u} \right]_0^\beta. \quad (3.99)$$

Substituting the limits and recalling the definition of  $\bar{n}_{\mathbf{k}j}(\omega) = \frac{1}{e^{\beta\hbar\omega} - 1}$  and that  $e^{-i\beta\hbar\omega_p} = 1$ , one arrives at an expression for the harmonic phonon propagator,

$$G_{\mathbf{k}j}(\omega_p) = \frac{2\omega_{\mathbf{k}j}}{\beta\hbar(\omega_{\mathbf{k}j}^2 + \omega_p^2)}. \quad (3.100)$$

This propagator is the starting point for calculating the self-energy of anharmonic phonons.

### Higher-order terms

To extend the above argument beyond the harmonic terms one continues the expansion of the Hamiltonian as

$$\hat{H} = \hat{H}_0 + \hat{H}' \quad (3.101)$$

where  $\hat{H}'$  is given by

$$\begin{aligned} \hat{H}' = \sum_{\{\mathbf{k}, j\}} V \begin{pmatrix} \mathbf{k}_1 & \mathbf{k}_2 & \mathbf{k}_3 \\ j_1 & j_2 & j_3 \end{pmatrix} A_{\mathbf{k}_1 j_1} A_{\mathbf{k}_2 j_2} A_{\mathbf{k}_3 j_3} \\ + \sum_{\{\mathbf{k}, j\}} V \begin{pmatrix} \mathbf{k}_1 & \mathbf{k}_2 & \mathbf{k}_3 & \mathbf{k}_4 \\ j_1 & j_2 & j_3 & j_4 \end{pmatrix} A_{\mathbf{k}_1 j_1} A_{\mathbf{k}_2 j_2} A_{\mathbf{k}_3 j_3} A_{\mathbf{k}_4 j_4}. \end{aligned} \quad (3.102)$$

The operators  $V(\mathbf{k}_1 \dots \mathbf{k}_n)$  are given by

$$V(\mathbf{k}_1 \dots \mathbf{k}_n) = \frac{1}{n!} \sqrt{\frac{\hbar}{2\omega_{\mathbf{k}_1 j_1}}} \dots \sqrt{\frac{\hbar}{2\omega_{\mathbf{k}_n j_n}}} \tilde{\Phi}(\mathbf{k}_1 \dots \mathbf{k}_n) . \quad (3.103)$$

The factors of  $\sqrt{\frac{\hbar}{2\omega_{\mathbf{k}_j}}}$  are there to ensure  $A_{\mathbf{k}j}$  are dimensionless; the tensors  $\tilde{\Phi}$ , a generalisation of the dynamical matrix, are given by

$$\begin{aligned} \tilde{\Phi}(\mathbf{k}_1 \dots \mathbf{k}_n) &= \frac{\Phi\left(\begin{smallmatrix} \mathbf{0} & \mathbf{R}_n \\ \mu_1 & \dots & \mu_n \\ i_1 & & i_n \end{smallmatrix}\right)}{\sqrt{M_{\mu_1} \dots M_{\mu_n}}} E\left(\begin{smallmatrix} \mathbf{0} & \mathbf{k}_1 \\ \mu_1 & j_1 \end{smallmatrix}\right) \dots E\left(\begin{smallmatrix} \mathbf{R}_n & \mathbf{k}_n \\ \mu_n & j_n \end{smallmatrix}\right) \\ &\quad \times \exp[i(\mathbf{k}_2 \cdot \mathbf{R}_2 + \dots + \mathbf{k}_n \cdot \mathbf{R}_n)] . \end{aligned} \quad (3.104)$$

The Green's function for such a perturbation has been derived by Maradudin and Fein [65]. It is given by

$$\begin{aligned} G(\mathbf{k}, j; \mathbf{k}', j'; u) &= \left\langle T\{\bar{A}_{\mathbf{k}j}(u) \bar{A}_{\mathbf{k}'j'}(0)\} \right. \\ &\quad \times \sum_{n=0}^{\infty} \frac{(-1)^n}{n!} \int_0^\beta d\beta_1 \dots \int_0^\beta d\beta_n \bar{H}'(\beta_1) \dots \bar{H}'(\beta_n) , \left. \right\rangle \end{aligned} \quad (3.105)$$

where the notation  $\bar{O}(u) = e^{\hat{H}_0 u} O(0) e^{-\hat{H}_0 u}$  has been introduced. Each term in this expansion may be represented by a series of Feynman diagrams describing the various phonon–phonon interaction processes of increasing complexity. Each term represents the set of distinct, connected diagrams with  $n$  vertices, where  $n$  is the order of the expansion term. The lines connecting the vertices represent the phonon propagator (i.e. a phonon).

The lowest order diagrams are the so-called bubble and loop diagrams shown in figure 3.2. The bubble diagram represents a single phonon splitting into two with wavevectors  $\mathbf{k}_1$  and  $\mathbf{k}_2$  before recombining into a single phonon with the same momentum as the original. The loop diagram shows the simultaneous creation and destruction of an “instantaneous” phonon through a single 4-phonon interaction. These two diagrams are contributions to the first term in the expansion in equation 3.105. Their contributions to the self-energy will be calculated and the phonon renormalisation as a result of these interaction processes will be found.



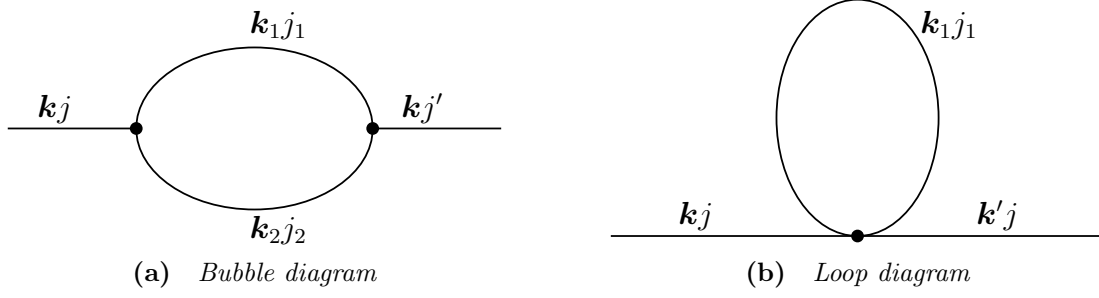


**Figure 3.2** *The lowest-order contributions to equation 3.105. The bubble diagram consists of two 3-phonon processes and the loop diagram consists of a single 4-phonon interaction.*

The effect of each interaction diagram can be found by taking the product of the interaction coefficients  $V\left(\begin{smallmatrix} \mathbf{k}_1 \\ j_1 \end{smallmatrix} \dots \begin{smallmatrix} \mathbf{k}_n \\ j_n \end{smallmatrix}\right)$ , a weighting factor that represents the number of possible ways the diagram can be connected, and a product of the harmonic phonon propagators  $G_{\mathbf{k}j}^0(\omega_p)$  — one for each line in the diagram — and summing the result over all the possible wavevectors  $\mathbf{k}$  and band indices  $j$  of the phonons involved.

The self-energies of these two diagrams are

$$\begin{aligned} \Sigma_p^{\text{bubble}}(\mathbf{k}j j') &= \frac{\beta \hbar^2}{16} \frac{1}{\sqrt{\omega_{\mathbf{k}j} \omega_{\mathbf{k}j'}}} \sum_{\substack{\mathbf{k}_1 \mathbf{k}_2 \\ j_1 j_2}} \frac{\tilde{\Phi}\left(\begin{smallmatrix} \mathbf{k} & -\mathbf{k}_1 & -\mathbf{k}_2 \\ j' & j_1 & j_2 \end{smallmatrix}\right) \tilde{\Phi}\left(\begin{smallmatrix} -\mathbf{k} & \mathbf{k}_1 & \mathbf{k}_2 \\ j & j_1 & j_2 \end{smallmatrix}\right)}{\omega_{\mathbf{k}_1 j_1} \omega_{\mathbf{k}_2 j_2}} \Delta(\mathbf{k} - \mathbf{k}_1 - \mathbf{k}_2) \\ &\quad \times \left\{ \frac{n_1 + n_2 + 1}{\omega_1 - i\omega_p + \omega_2} + \frac{n_2 - n_1}{\omega_1 - i\omega_p - \omega_2} \right. \\ &\quad \left. + \frac{n_2 - n_1}{\omega_1 + i\omega_p - \omega_2} + \frac{n_1 + n_2 + 1}{\omega_1 + i\omega_p + \omega_2} \right\} \quad (3.106) \end{aligned}$$

and

$$\Sigma_p^{\text{loop}}(\mathbf{k}j j') = \frac{\hbar^2}{8} \sum_{\mathbf{k}_1 j_1} \frac{2n_1 + 1}{\omega_{\mathbf{k}_1 j_1}} \tilde{\Phi}\left(\begin{smallmatrix} \mathbf{k} & \mathbf{k} & \mathbf{k}_1 & -\mathbf{k}_1 \\ j & j' & j_1 & j_1 \end{smallmatrix}\right) \quad (3.107)$$

where  $\Delta(\mathbf{K})$  is one if  $\mathbf{K}$  is a reciprocal lattice vector and zero otherwise, and the  $\mathbf{k}$ s and  $j$ s in the summations correspond to those in figure 3.2 [62]. The expression for the loop diagram is stated without proof, the bubble diagram will be derived in full in the following section.

## Evaluating the Bubble Diagram

This section will continue to follow the approach of Reissland [62]. Beginning from the expression for the bubble diagram in terms of the harmonic phonon propagators,

$$\begin{aligned} \Sigma_p^{\text{bubble}}(\mathbf{k}jj') &= 18\beta^2 \sum_{\substack{\mathbf{k}_1 \mathbf{k}_2 \\ j_1 j_2}} \sum_{\substack{p_1 \\ p_2}} V\left(\begin{smallmatrix} \mathbf{k} & -\mathbf{k}_1 & -\mathbf{k}_2 \\ j' & j_1 & j_2 \end{smallmatrix}\right) V\left(\begin{smallmatrix} -\mathbf{k} & \mathbf{k}_1 & \mathbf{k}_2 \\ j & j_1 & j_2 \end{smallmatrix}\right) \\ &\quad \times G_{\mathbf{k}_1 j_1}^0(\omega_{p_1}) G_{\mathbf{k}_2 j_2}^0(\omega_{p_2}) \delta(p - p_1 - p_2) , \end{aligned} \quad (3.108)$$

where  $\beta$  is the usual  $\frac{1}{k_B T}$ ,  $V$  are the third order interaction coefficients,  $G_{\mathbf{k}j}^0(\omega)$  is the harmonic phonon propagator, and  $\delta$  is the delta function; the  $p$ s are integers that index the Matsubara frequencies given by

$$\omega_p = \frac{2\pi}{\beta\hbar} p . \quad (3.109)$$

Focussing on the second line of equation 3.108 and substituting in the expression for  $G_{\mathbf{k}j}^0(\omega)$  (equation 3.100) gives

$$\frac{4\omega_1\omega_2}{\beta^2\hbar^2} \sum_{\substack{p_1 \\ p_2}} \frac{1}{\omega_{p_1}^2 - \omega_1^2} \times \frac{1}{\omega_{p_2}^2 - \omega_2^2} \times \delta(p - p_1 - p_2) . \quad (3.110)$$

Here the notation has been condensed somewhat so  $\omega_1 = \omega_{\mathbf{k}_1 j_1}$ , etc. The delta function imposes the restriction  $p_2 = p - p_1$  and therefore  $\omega_{p_2} = \omega_p - \omega_{p_1}$ . Using this one can rewrite the above expression as

$$\frac{4\omega_1\omega_2}{\beta^2\hbar^2} \sum_{p_1=-\infty}^{\infty} \frac{1}{\omega_{p_1}^2 - \omega_1^2} \times \frac{1}{(\omega_p - \omega_{p_1})^2 - \omega_2^2} . \quad (3.111)$$

Sums of this type can be solved by a contour integral, so at this point it is prudent to turn the two double poles into four simple poles,

$$\frac{4\omega_1\omega_2}{\beta^2\hbar^2} \sum_{p_1=-\infty}^{\infty} \frac{1}{(\omega_1 - i\omega_{p_1})} \frac{1}{(\omega_1 + i\omega_{p_1})} \frac{1}{(\omega_2 - i(\omega_p - \omega_{p_1}))} \frac{1}{(\omega_2 + i(\omega_p - \omega_{p_1}))} . \quad (3.112)$$

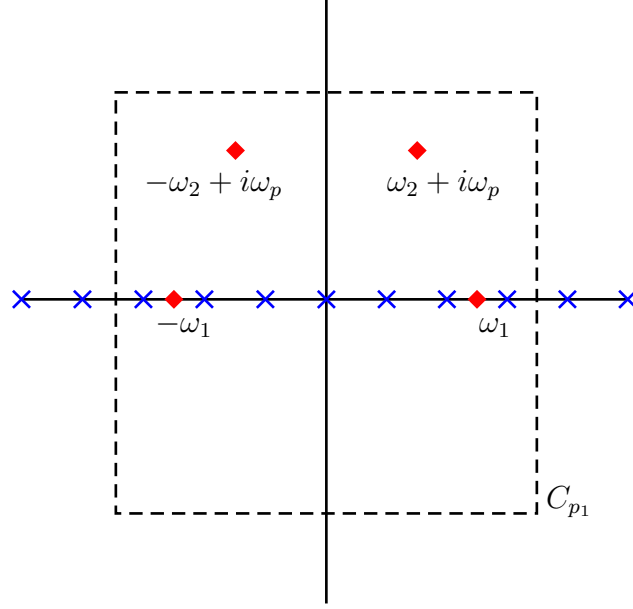


**Figure 3.3** *Complex plane of  $i\omega_{p_1}$  showing the contour  $C_{p_1}$  and poles of  $f(i\omega_{p_1})n(i\omega_{p_1})$ . Blue crosses indicate the poles of  $n(i\omega_{p_1})$ , red squares indicate the poles of  $f(i\omega_{p_1})$ .*

To evaluate a sum of the form

$$\sum_{p_1=-\infty}^{\infty} f(i\omega_{p_1})$$

one requires a function  $n(i\omega_{p_1})$  that has poles at the Matsubara frequencies, and has unit residue at these poles. Performing a contour integral of  $f(i\omega_{p_1})n(i\omega_{p_1})$  around all poles and recognising that it is equal to the sum of the residues allows one to draw a relation between the sum and the residues of  $f(i\omega_{p_1})$ .

The function that has the required properties is the Bose-Einstein distribution

$$\beta\hbar n(i\omega_{p_1}) = \beta\hbar \frac{1}{e^{i\beta\hbar\omega_{p_1}} - 1} \quad (3.113)$$

where the factor of  $\beta\hbar$  ensures the residue of the function at each of the poles is 1.

Now one integrates

$$\beta\hbar \oint_{C_{p_1}} f(i\omega_{p_1})n(i\omega_{p_1})d(i\omega_{p_1}) \quad (3.114)$$

over the contour  $C_{p_1}$  where  $C_{p_1}$  is the square drawn out by the points  $(\frac{2\pi p_1}{\beta\hbar} +$

$\frac{\pi}{\beta\hbar})(\pm 1 \pm i)$ . That is, it passes midway between the poles of  $n(i\omega_{p_1})$ . The contour and the poles of this integral are shown in figure 3.3. This integral goes to zero as  $p_1 \rightarrow \infty$ . Owing to the choice of contour,  $n(i\omega_{p_1})$  is a bounded function on the square  $C_{p_1}$ , and therefore

$$|n(i\omega_{p_1})| \leq M , \quad (3.115)$$

where  $M$  is some finite number. Additionally, one can see that the form of  $f(i\omega_{p_1})$  is such that  $zf(z) \rightarrow 0$  as  $|z| \rightarrow \infty$ . In other words,  $f(z)$  goes to zero faster than  $\frac{1}{R}$  where  $R = |z|$ . This is only true for sufficiently large  $R$ , beyond the poles of  $f$ . Therefore, for large  $R$ ,

$$|f(i\omega_{p_1})| \leq \frac{\epsilon}{R} \quad (3.116)$$

where  $\epsilon$  is a small number that goes to zero as  $R \rightarrow \infty$ .

The final relation to make use of is the fact that if  $|f(z)| \leq M$  at all points on the contour  $C_{p_1}$ , then the integral must be bounded as

$$\left| \int_{C_{p_1}} f(z) dz \right| \leq |Ml| \quad (3.117)$$

where  $l$  is the length of the contour. Putting all this together one can say

$$\lim_{p_1 \rightarrow \infty} \left| \oint_{C_{p_1}} \beta\hbar f(i\omega_{p_1}) n(i\omega_{p_1}) d(i\omega_{p_1}) \right| \leq \lim_{R \rightarrow \infty} \frac{\beta\hbar M l \epsilon}{R} = 0 , \quad (3.118)$$

as  $l \propto R$ . Therefore, the contour integral in equation 3.114 goes to zero as  $p_1$  goes to infinity.

The other way to compute this integral is by using the residue theorem. The integral is equal to  $2\pi i$  times the sum of the residues. There are simple poles at the Matsubara frequencies thanks to the Bose-Einstein distribution, and at the four poles in  $f(i\omega_{p_1})$ . Using the relation

$$\text{Res} \{f(z)g(z), z = z_f\} = g(z_f) \times \text{Res} \{f(z), z = z_f\} , \quad (3.119)$$

where  $z_f$  is a pole of  $f(z)$ , and recalling that the residue of  $\beta\hbar n(i\omega_{p_1})$  at the

Matsubara frequencies is 1, it can be written

$$\lim_{p_1 \rightarrow \infty} \oint_{C_{p_1}} \beta \hbar f(i\omega_{p_1}) n(i\omega_{p_1}) d(i\omega_{p_1}) = 2\pi i \left[ \sum_{p_1=-\infty}^{\infty} f(i\omega_{p_1}) + \beta \hbar \sum_{\omega_f} n(\omega_f) \text{Res} \{f(i\omega_{p_1}), i\omega_{p_1} = \omega_f\} \right] \quad (3.120)$$

where  $\omega_f$  are the poles of  $f(i\omega_{p_1})$ . Since the integral on the left-hand side goes to zero one can write

$$\sum_{p_1=-\infty}^{\infty} f(i\omega_{p_1}) = -\beta \hbar \sum_{\omega_f} n(\omega_f) \text{Res} \{f(i\omega_{p_1}), i\omega_{p_1} = \omega_f\} . \quad (3.121)$$

If desired, this can be written as a contour integral again as

$$\sum_{p_1=-\infty}^{\infty} f(i\omega_{p_1}) = -\frac{\beta \hbar}{2\pi i} \oint_C f(i\omega_{p_1}) n(i\omega_{p_1}) d(i\omega_{p_1}) , \quad (3.122)$$

where  $C$  this time only includes the poles of  $f(i\omega_{p_1})$  and not the poles of  $n(i\omega_{p_1})$ .

Returning to equation 3.112 and using equation 3.121 one finds the expression

$$-\frac{4\omega_1\omega_2}{\beta \hbar} \left\{ -\frac{n(\omega_1)}{2\omega_1} \frac{1}{(\omega_2 - i\omega_p + \omega_1)} \frac{1}{(\omega_2 + i\omega_p - \omega_1)} + \frac{n(-\omega_1)}{2\omega_1} \frac{1}{(\omega_2 - i\omega_p - \omega_1)} \frac{1}{(\omega_2 + i\omega_p + \omega_1)} - \frac{n(\omega_2)}{2\omega_2} \frac{1}{(\omega_1 - i\omega_p - \omega_2)} \frac{1}{(\omega_1 + i\omega_p + \omega_2)} + \frac{n(-\omega_2)}{2\omega_2} \frac{1}{(\omega_1 - i\omega_p + \omega_2)} \frac{1}{(\omega_1 + i\omega_p - \omega_2)} \right\} . \quad (3.123)$$

Using the relations

$$n(-\omega) = \frac{1}{e^{-\beta\hbar\omega} - 1} \quad (3.124)$$

$$= \frac{e^{\beta\hbar\omega}}{1 - e^{\beta\hbar\omega}} \quad (3.125)$$

$$= -\frac{e^{\beta\hbar\omega}}{e^{\beta\hbar\omega} - 1} \quad (3.126)$$

$$= -\frac{1 + e^{\beta\hbar\omega} - 1}{e^{\beta\hbar\omega} - 1} \quad (3.127)$$

$$= -\frac{1}{e^{\beta\hbar\omega} - 1} - \frac{e^{\beta\hbar\omega} - 1}{e^{\beta\hbar\omega} - 1} \quad (3.128)$$

$$n(-\omega) = -[n(\omega) + 1] \quad (3.129)$$

and

$$n(i\omega_p + \omega) = \frac{1}{e^{\beta\hbar(i\omega_p + \omega)} - 1} \quad (3.130)$$

$$= \frac{1}{e^{\beta\hbar i\omega_p} e^{\beta\hbar\omega} - 1} \quad (3.131)$$

$$= \frac{1}{e^{2\pi i} e^{\beta\hbar\omega} - 1} \quad (3.132)$$

$$= \frac{1}{e^{\beta\hbar\omega} - 1} \quad (3.133)$$

$$n(i\omega_p + \omega) = n(\omega) \quad (3.134)$$

and cancelling the minus signs, one arrives at the expression

$$\begin{aligned} -\frac{4\omega_1\omega_2}{\beta\hbar} \Bigg\{ & -\frac{n(\omega_1)}{2\omega_1} \frac{1}{(\omega_2 - i\omega_p + \omega_1)} \frac{1}{(\omega_2 + i\omega_p - \omega_1)} \\ & -\frac{n(\omega_1) + 1}{2\omega_1} \frac{1}{(\omega_2 - i\omega_p - \omega_1)} \frac{1}{(\omega_2 + i\omega_p + \omega_1)} \\ & -\frac{n(\omega_2)}{2\omega_2} \frac{1}{(\omega_1 - i\omega_p - \omega_2)} \frac{1}{(\omega_1 + i\omega_p + \omega_2)} \\ & -\frac{n(\omega_2) + 1}{2\omega_2} \frac{1}{(\omega_1 - i\omega_p + \omega_2)} \frac{1}{(\omega_1 + i\omega_p - \omega_2)} \Bigg\}. \end{aligned} \quad (3.135)$$

This can now easily be split into partial fractions and, using the notation  $n(\omega_1) =$

$n_1$  and  $n(\omega_2) = n_2$ , this becomes

$$\frac{1}{\beta\hbar} \left\{ \frac{n_1}{\omega_2 - i\omega_p + \omega_1} + \frac{n_1}{\omega_2 + i\omega_p - \omega_1} + \frac{n_1 + 1}{\omega_2 - i\omega_p - \omega_1} + \frac{n_1 + 1}{\omega_2 + i\omega_p + \omega_1} + \frac{n_2}{\omega_1 - i\omega_p - \omega_2} + \frac{n_2}{\omega_1 + i\omega_p + \omega_2} + \frac{n_2 + 1}{\omega_1 - i\omega_p + \omega_2} + \frac{n_2 + 1}{\omega_1 + i\omega_p - \omega_2} \right\}. \quad (3.136)$$

Summing like terms one finds

$$\frac{1}{\beta\hbar} \left\{ \frac{n_1 + n_2 + 1}{\omega_1 - i\omega_p + \omega_2} + \frac{n_2 - n_1}{\omega_1 - i\omega_p - \omega_2} + \frac{n_2 - n_1}{\omega_1 + i\omega_p - \omega_2} + \frac{n_1 + n_2 + 1}{\omega_1 + i\omega_p + \omega_2} \right\}. \quad (3.137)$$

One now transforms to a continuous variable where  $f(\omega) = f(i\omega_p)$  when  $\omega = i\omega_p$ . Formally, this is done by writing  $i\omega_p = \omega + i\epsilon$  where  $\epsilon \rightarrow 0$ . Applying this process to functions of the form  $\frac{1}{ix}$  gives

$$\lim_{\epsilon \rightarrow 0} \frac{1}{x \pm i\epsilon} = \frac{1}{(x)_{\mathbf{p}}} \mp i\pi\delta(x), \quad (3.138)$$

where  $\mathbf{p}$  indicates the principle part of the Laurent series. This can be proven as

$$\lim_{\epsilon \rightarrow 0} \frac{1}{x \pm \epsilon} = \lim_{\epsilon \rightarrow 0} \frac{x \mp i\epsilon}{x^2 + \epsilon^2} \quad (3.139)$$

$$= \lim_{\epsilon \rightarrow 0} \left\{ \frac{x}{x^2} \mp i \frac{\epsilon}{x^2 + \epsilon^2} \right\} \quad (3.140)$$

$$= \frac{1}{x} \mp i\pi\delta(x), \quad (3.141)$$

where the last step has been made by identifying the imaginary part as a Lorentz curve which becomes infinitely narrow in the limit  $\epsilon \rightarrow 0$ . An infinitely narrow Lorentz curve is the dirac delta function with the factor of  $\pi$  included for normalisation.

Applying this to the expression for the bubble self-energy and including the rest

of the terms from equation 3.108 one gets

$$\begin{aligned} \Sigma_p^{\text{bubble}}(\mathbf{k}jj') &= 18\beta^2 \sum_{\substack{\mathbf{k}_1 \mathbf{k}_2 \\ j_1 j_2}} V\left(\begin{smallmatrix} \mathbf{k} & -\mathbf{k}_1 & -\mathbf{k}_2 \\ j' & j_1 & j_2 \end{smallmatrix}\right) V\left(\begin{smallmatrix} -\mathbf{k} & \mathbf{k}_1 & \mathbf{k}_2 \\ j & j_1 & j_2 \end{smallmatrix}\right) \\ &\times \frac{1}{\beta\hbar} \left\{ \frac{n_1 + n_2 + 1}{\omega_1 - i\omega_p + \omega_2} + \frac{n_2 - n_1}{\omega_1 - i\omega_p - \omega_2} + \right. \\ &\quad \left. \frac{n_2 - n_1}{\omega_1 + i\omega_p - \omega_2} + \frac{n_1 + n_2 + 1}{\omega_1 + i\omega_p + \omega_2} \right\} . \quad (3.142) \end{aligned}$$

Adding the prefactors of equation 3.103 gives an extra factor of

$$\frac{1}{3! \times 3! \times 8} \frac{1}{\sqrt{\omega_{\mathbf{k}j}} \sqrt{\omega_{\mathbf{k}j'}}} \frac{1}{\omega_{\mathbf{k}_1 j_1} \omega_{\mathbf{k}_2 j_2}} ,$$

and the final result is

$$\begin{aligned} \Sigma_p^{\text{bubble}}(\mathbf{k}jj') &= \frac{\beta\hbar^2}{16} \frac{1}{\sqrt{\omega_{\mathbf{k}j} \omega_{\mathbf{k}j'}}} \sum_{\substack{\mathbf{k}_1 \mathbf{k}_2 \\ j_1 j_2}} \frac{\tilde{\Phi}\left(\begin{smallmatrix} \mathbf{k} & -\mathbf{k}_1 & -\mathbf{k}_2 \\ j' & j_1 & j_2 \end{smallmatrix}\right) \tilde{\Phi}\left(\begin{smallmatrix} -\mathbf{k} & \mathbf{k}_1 & \mathbf{k}_2 \\ j & j_1 & j_2 \end{smallmatrix}\right)}{\omega_{\mathbf{k}_1 j_1} \omega_{\mathbf{k}_2 j_2}} \Delta(\mathbf{k} - \mathbf{k}_1 - \mathbf{k}_2) \\ &\times \left\{ \frac{n_1 + n_2 + 1}{\omega_1 - i\omega_p + \omega_2} + \frac{n_2 - n_1}{\omega_1 - i\omega_p - \omega_2} \right. \\ &\quad \left. + \frac{n_2 - n_1}{\omega_1 + i\omega_p - \omega_2} + \frac{n_1 + n_2 + 1}{\omega_1 + i\omega_p + \omega_2} \right\} . \quad (3.143) \end{aligned}$$

This expression represents the real part of the self-energy arising from the bubble interaction process. It is used in the attempt to extend ALAMODE's SCPH algorithm to include the contribution from this process. The results of this are discussed in chapter 5. The corresponding expression for the loop diagram is already included in the standard SCPH algorithm as it will be described in the next chapter.

### 3.3 Density functional theory

Density functional theory (DFT) is one of the most commonly used methods for calculating the material properties of a solid from first principles. The implementation of DFT used in this thesis is that of the Vienna *ab-initio* simulation package (VASP) [66–68]. For the experienced reader it suffices



to say that VASP is a plane-wave pseudopotential DFT code that, in this investigation, made use of the projector augmented wave (PAW) pseudopotentials [69]. For readers not familiar with DFT, the fundamental theory of DFT common to all implementations will be discussed in section 3.3.1, the theory relevant specifically to VASP, namely the pseudopotential and PAW approach, is described in sections 3.3.2, approximations to the exchange–correlation functional are discussed in section 3.3.3, and finally the calculation of forces in DFT is discussed in section 3.3.4

### 3.3.1 Density functional theory fundamentals

Calculating material properties from quantum-mechanical first principles typically requires knowledge of the electronic many-body wavefunction. A direct solution of the Schrödinger equation is usually not possible due to the large number of degrees of freedom that are present. One simplification that is frequently made is the Born-Oppenheimer approximation, which assumes that the heavy nuclei can be considered static compared to the lighter and faster electrons. This simplifies matters, as one is left to solve only the electronic system, but it is not enough to turn the problem into one that is tractable. DFT is based on the principle that the complex, many-body wavefunction can be replaced with the much simpler electron density without losing any information about the system. It is underpinned firstly by the idea that the ground state electron density can be determined by minimising the energy with respect to the electron density, and secondly that the electron density that provides this ground-state electron density must be that of the the ground-state wavefunction. This is presented formally in the two Hohenberg-Kohn theorems.

#### The Hohenberg-Kohn theorems

Consider a system of  $N$  electrons under the influence of an external potential,  $V(\mathbf{r})$ , and the electron-electron coulomb interaction  $V_{ee}$  [70]. The Hamiltonian of such a system is

$$H = T + V(\mathbf{r}) + V_{ee} , \quad (3.144)$$

where  $T$  is the kinetic energy. The first Hohenberg-Kohn theorem states that the external potential,  $V(\mathbf{r})$ , is *uniquely* defined by the ground state electron density. The proof of this will be done in two parts; firstly it will be shown that there is a unique mapping between the potential and the ground-state wavefunction, and secondly that there is another unique mapping between the ground-state wavefunction and the ground-state electron density.

Beginning with the first part, consider two different potentials represented by operators  $V_A$  and  $V_B$  that give the same ground state wavefunction  $|\phi_0\rangle$ . The two associated Hamiltonians acting on the ground state gives two energies,  $E_A$  and  $E_B$ ,

$$H_A |\phi_0\rangle = (T + V_A + V_{ee}) |\phi_0\rangle = E_A |\phi_0\rangle \quad (3.145a)$$

$$H_B |\phi_0\rangle = (T + V_B + V_{ee}) |\phi_0\rangle = E_B |\phi_0\rangle . \quad (3.145b)$$

Subtracting 3.145b from 3.145a one finds

$$(V_A - V_B) |\phi_0\rangle = (E_A - E_B) |\phi_0\rangle \quad (3.146)$$

which can be rearranged as

$$V_A |\phi_0\rangle = V_B |\phi_0\rangle + (E_A - E_B) |\phi_0\rangle \quad (3.147)$$

$$V_A |\phi_0\rangle = [V_B + (E_A - E_B)] |\phi_0\rangle . \quad (3.148)$$

Assuming that the wavefunction is not zero and given that  $E_A - E_B$  is a scalar constant, the above equation implies that  $V_A$  and  $V_B$  are identical up to a constant. Two different potentials cannot therefore give the same ground state and the ground state  $|\phi_0\rangle$  *uniquely* defines the potential  $V(\mathbf{r})$ .

A similar argument relates the ground state,  $|\phi_0\rangle$ , to the electron density  $n(\mathbf{r})$ . Consider two different ground states  $|\phi_0^A\rangle$  and  $|\phi_0^B\rangle$  which, as has just been proven, must come from two different potentials  $V_A(\mathbf{r})$  and  $V_B(\mathbf{r})$ . Now imagine that these two ground states,  $|\phi_0^A\rangle$  and  $|\phi_0^B\rangle$ , have the same electron density  $n_0(\mathbf{r})$ . The ground-state energy of state  $|\phi_0^A\rangle$  in potential  $V_A(\mathbf{r})$  is

$$E_A = \langle \phi_0^A | H_A | \phi_0^A \rangle \quad (3.149)$$

where  $H_A = T + V_A + V_{ee}$  as before. The energy  $E_A$ , as it is the ground state

energy, must be less than the energy of the other state,  $|\phi_0^B\rangle$ , in the same potential,

$$E_A < \langle \phi_0^B | H_A | \phi_0^B \rangle . \quad (3.150)$$

Now using

$$H_A = T + V_A + V_{ee} \quad (3.151)$$

$$= T + V_A + V_B - V_B + V_{ee} \quad (3.152)$$

$$= H_B - V_B + V_A \quad (3.153)$$

and substituting 3.153 into 3.150,

$$E_A < \langle \phi_0^B | H_B - V_B + V_A | \phi_0^B \rangle \quad (3.154)$$

$$E_A < \langle \phi_0^B | H_B | \phi_0^B \rangle + \langle \phi_0^B | V_A - V_B | \phi_0^B \rangle \quad (3.155)$$

$$E_A < E_B + \int d^3\mathbf{r} [V_A(\mathbf{r}) - V_B(\mathbf{r})] n_0(\mathbf{r}) . \quad (3.156)$$

Using the same argument for the other potential one arrives at the same relation with subscripts  $A$  and  $B$  exchanged,

$$E_B < E_A - \int d^3\mathbf{r} [V_A(\mathbf{r}) - V_B(\mathbf{r})] n_0(\mathbf{r}) . \quad (3.157)$$

Summing 3.156 and 3.157 leads to the inequality

$$E_A + E_B < E_A + E_B . \quad (3.158)$$

This is clearly untrue, and therefore the assumption that both  $|\phi_0^A\rangle$  and  $|\phi_0^B\rangle$  have the same ground state electron density  $n_0(\mathbf{r})$  is also untrue.

So far it has been proven firstly that each ground-state wavefunction corresponds to a unique potential, and secondly that each ground-state electron density corresponds to a unique ground-state wavefunction. These statements can be combined to formally state the first Hohenberg-Kohn theorem.

**Theorem 1** *The external potential  $V(\mathbf{r})$  is a unique functional of the ground-state electron density  $n_0(\mathbf{r})$ .*

In other words, if one can find the ground-state electron density  $n_0(\mathbf{r})$ , one can find the external potential  $V(\mathbf{r})$ .

The question remains how one is to find the electron density of the ground state. The second Hohenberg-Kohn theorem states that the functional  $E[n(\mathbf{r})]$ , which gives the total energy of the system, is minimised only when the electron density is that of the true ground state,  $n(\mathbf{r}) = n_0(\mathbf{r})$ . If there was an electron density  $n(\mathbf{r})$  that was lower in energy than the ground state electron density  $n_0(\mathbf{r})$ , then

$$E[n(\mathbf{r})] < E[n_0(\mathbf{r})] . \quad (3.159)$$

It is known from the first Hohenberg-Kohn theorem that the external potential, and thus the Hamiltonian ( $H = T + V + V_{ee}$ ), is a unique functional of the ground-state electron density,

$$H[n_0(\mathbf{r})] = T[n_0(\mathbf{r})] + V[n_0(\mathbf{r})] + V_{ee}[n_0(\mathbf{r})] . \quad (3.160)$$

The ground-state wavefunction is also a unique functional of the ground-state electron density,

$$|\phi_0\rangle = |\phi_0[n_0(\mathbf{r})]\rangle . \quad (3.161)$$

Therefore, the Hamiltonian of the true ground-state electron density  $H[n_0(\mathbf{r})]$  (the actual Hamiltonian of the system) yields an actual ground-state energy of

$$E_0[n_0] = \langle \phi_0[n_0(\mathbf{r})] | H[n_0(\mathbf{r})] | \phi_0[n_0(\mathbf{r})] \rangle . \quad (3.162)$$

The energy of the same Hamiltonian in the “ground state” coming from the electron density that is posited to be lower in energy is

$$E_0[n] = \langle \phi_0[n(\mathbf{r})] | H[n_0(\mathbf{r})] | \phi_0[n(\mathbf{r})] \rangle , \quad (3.163)$$

and if  $E_0[n] < E_0[n_0]$ , then

$$\langle \phi_0[n(\mathbf{r})] | H[n_0(\mathbf{r})] | \phi_0[n(\mathbf{r})] \rangle < \langle \phi_0[n_0(\mathbf{r})] | H[n_0(\mathbf{r})] | \phi_0[n_0(\mathbf{r})] \rangle , \quad (3.164)$$

which is forbidden by the variational principle. This means any electron density  $n(\mathbf{r})$  that is not the ground state electron density  $n_0(\mathbf{r})$  will have a higher energy than that of the ground state, formally proving the second Hohenberg-Kohn

theorem.

**Theorem 2** *The functional of the electron density that gives the total energy is minimised only when the electron density is that of the ground state.*

This allows one to find the electron density of the ground state by minimising the energy functional  $E[n]$ . Once the ground-state electron density is found, the potential  $V(\mathbf{r})$  and thus the Hamiltonian can be determined. From the Hamiltonian the wavefunctions are calculated, from which all properties of the system can be derived.

### Kohn–Sham equations

The Hohenberg-Kohn theorems are promising, but a practical implementation is needed if one is to determine the ground state electron density. The second Hohenberg-Kohn theorem suggests that one should seek to find the electron density that minimises the energy, but doing this for a many-body system can be difficult.

To overcome this, the solution suggested by Kohn and Sham is commonly used [71]. The Kohn–Sham approach turns the many-body interacting system of electrons into a *fictitious* system of non-interacting electrons that has the same ground state electron density. One may be concerned that the first Hohenberg-Kohn theorem mentioned earlier demands that the potentials of these systems be the same, but this is not the case, as the real (interacting electrons) and fictitious (non-interacting electrons) potentials refer to different systems. The Hamiltonian acting on the full, many-body wavefunction,  $|\phi\rangle$ , is replaced by a fictitious, single-particle Hamiltonian acting on single-particle orbitals,  $|\psi\rangle$ .

$$H |\phi\rangle = (T + V + V_{\text{nuc}}) |\phi\rangle = E |\phi\rangle , \quad (3.165)$$

where  $V$  is the full electron-electron potential and  $V_{\text{nuc}}$  is the potential arising from the nuclei, becomes

$$H_S |\psi\rangle = (T_S + V_S + V_{\text{nuc}}) |\psi\rangle = E_S |\psi\rangle . \quad (3.166)$$

The subscript  $S$  indicates the single particle operators, and the original many-body wavefunction,  $|\phi\rangle$ , has been replaced by a single particle wavefunction of the fictitious system,  $|\psi\rangle$ .  $V_S$  can be further split into the Coulomb repulsion between electrons and the so-called “exchange–correlation” part,

$$V_S = V_{ee} + V_{xc} . \quad (3.167)$$

$V_{ee}$  is the Coulomb interaction from the other electrons in the system; it neglects quantum fluctuations, their correlations, and the exchange interaction that arises from the Fermionic nature of the electrons making it equivalent to the mean-field or Hartree approximation. This part of the potential can be calculated exactly. The neglected correlations are accounted for in the  $V_{xc}$  term. This term cannot be exactly calculated, however many approximations exist to estimate it. It is these approximations that make DFT inexact.

Correlations between electrons lower the energy. Quantum mechanical fluctuations in the electron density cause electrons to be instantaneously nearer or farther from each other than their average separation. If the electron density of one electron fluctuates such that the electron cloud is brought closer to another, the fluctuations of the second electron’s density will have an increased likelihood of being in a direction that will lower the energy of the electron pair. This also has an impact on the kinetic energy as a fluctuation of one electron density is likely to induce another to move, creating correlations in the velocities of the electrons. This creates a difference in the kinetic energy of the independent electrons and the interacting ones, hence  $T \rightarrow T_S$ . This difference in the kinetic energy is also included in  $V_{xc}$ .

The other effect included in the  $V_{xc}$  term is the exchange interaction. This is the interaction that occurs due to the Pauli exclusion principle, and the requirement for the wavefunction to be antisymmetric. This interaction causes a repulsion between the electrons of like spin which causes them to move apart and lowers the energy further.

In order to implement the Kohn–Sham approach to finding the ground state electron density, there are two main practical considerations that must be made. The first is that the Kohn–Sham orbitals of the fictitious non-interacting electrons must be represented in some manageable way; they must be expanded in some

basis,

$$|\psi_i(\mathbf{r})\rangle = \sum_j C_{ij} |\theta_j(\mathbf{r})\rangle , \quad (3.168)$$

where  $C_{ij}$  are the coefficients that express the state  $|\psi_i(\mathbf{r})\rangle$  in terms of the basis functions  $|\theta_j(\mathbf{r})\rangle$ .

The basis expansion used in VASP will be discussed in the next section. The second consideration is the approximation to the exchange–correlation functional  $V_{xc}$ . Approximations to this functional are discussed in section 3.3.3.

### 3.3.2 Plane wave density functional theory and pseudopotentials

There is a need for an expansion of the Kohn–Sham wavefunctions in some basis set. Two obvious choices present themselves: atomic orbitals, or plane waves. Representing the wavefunction as a superposition of atomic orbitals has the advantage of being physically motivated; a collection of independent atoms makes a good starting point for the interacting system. However, the drawback of such an approach is that the basis functions are difficult to manipulate mathematically. This makes the mathematical routines that the DFT codes rely on very slow and consequentially slows down the whole code.

The other approach is to use a mathematically simple basis and assume that the speedup in the manipulation of the basis functions offsets the hindrance of having to perform more of such operations. The basis chosen by VASP is plane waves. This also has a physical justification; delocalised electrons in metals, for example, lend themselves well to an expansion in plane waves, but the plane wave basis is less appropriate to electrons that are in the tightly bound core states where there is little hybridisation of the states and the electrons behave as in the isolated atom. In addition, it is difficult for plane waves to accurately describe the rapidly changing wavefunction close to the nucleus, where a large basis set would be required<sup>1</sup>. These rapid changes occur due to the constraint that the wavefunction of the valence electrons must be orthogonal to the wavefunctions of

---

<sup>1</sup>One may wonder whether it is possible to use both approaches, plane waves to describe the delocalised electrons and atomic orbitals to describe the core. Such approaches exist and are called augmented plane wave approaches.

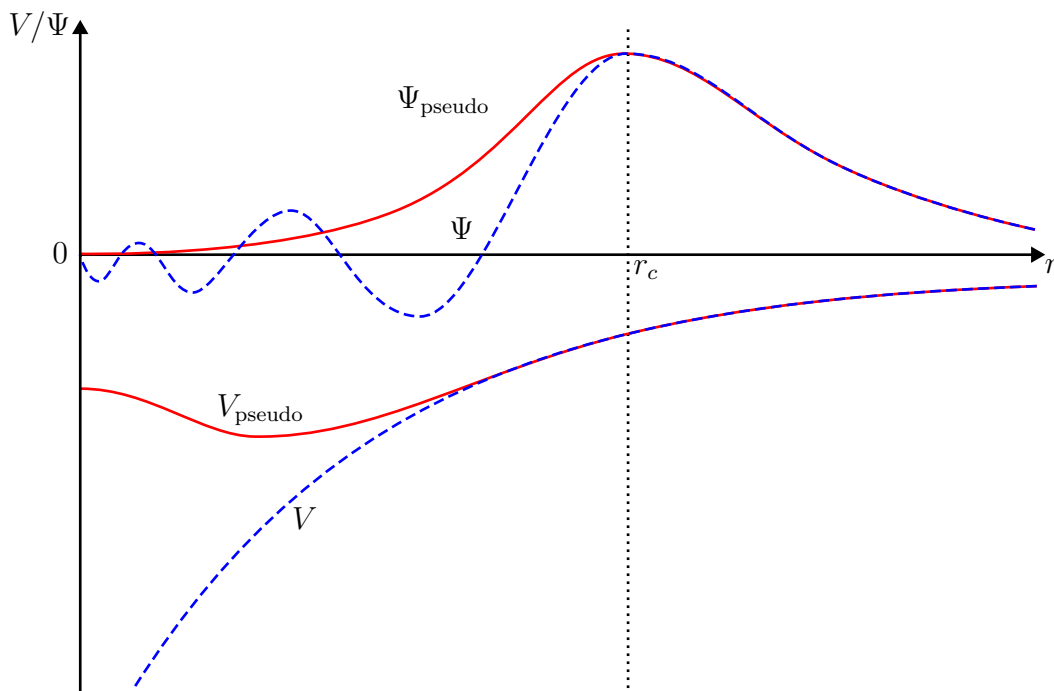


**Figure 3.4** *Comparison of the real (blue - dashed) potential and wavefunction and the pseudo (red - solid) potential and wavefunction as a function of distance from the nucleus  $r$ . Above some chosen cutoff radius  $r_c$ , the pseudo-wavefunction and potential exactly match their real counterparts.*

the core electrons.

To circumvent this problem, the idea of a pseudopotential is introduced. This replaces the real potential coming from the nucleus and the core electrons, which has little effect on the bonding, with a pseudopotential that is much smoother, and therefore requires fewer plane waves to describe than the true potential. The pseudopotential is designed so that the pseudowavefunction matches the true wavefunction outside some cutoff, but provide a smoother function inside this radius (see figure 3.4).

To obtain the greatest advantage from these pseudopotentials, one requires them to be as slowly varying as possible, so that the minimum number of Fourier coefficients is needed to describe them. This is referred to as the “softness” of the pseudopotential. Pseudopotentials that vary more slowly are softer than those that vary quickly. The softness of the pseudopotential is limited by the requirement that the number of electrons inside the core region should be conserved. This is equivalent to the statement that norm of the



pseudowavefunction must equal one electron, hence the name norm-conserving pseudopotential.

The condition of norm conservation can be relaxed, but doing so will mean that the Kohn–Sham wavefunctions will no longer be orthogonal and normalised. This is where the projector augmented wave (PAW) method is used. The PAW method does not require that the norm of the pseudowavefunctions is equal to that of the true Kohn–Sham wavefunctions, but does require that the two wavefunctions are related by a linear transformation,  $\mathcal{T}$ , as

$$|\psi\rangle = \mathcal{T} |\tilde{\psi}\rangle , \quad (3.169)$$

where  $|\psi\rangle$  is the true Kohn–Sham orbital, and  $|\tilde{\psi}\rangle$  is the pseudised version of this orbital.

Inserting this into the Schrödinger equation one finds

$$H\mathcal{T} |\tilde{\psi}\rangle = E\mathcal{T} |\tilde{\psi}\rangle \quad (3.170)$$

$$H |\tilde{\psi}\rangle = E\mathcal{T}^\dagger \mathcal{T} |\tilde{\psi}\rangle \quad (3.171)$$

$$H |\tilde{\psi}\rangle = ES |\tilde{\psi}\rangle . \quad (3.172)$$

The matrix  $S$  is the overlap matrix and describes the non-orthogonality of the pseudowavefunctions  $|\tilde{\psi}\rangle$ . Equation 3.172 can be identified as a generalised eigenvalue problem. This type of problem is slightly more complex to solve numerically, but the smaller basis set made possible by the PAW approach outweighs this drawback.

The form of  $\mathcal{T}$  must be that it leaves  $|\psi\rangle$  unchanged outside the cutoff radius, but applies a transformation inside this radius. The form

$$\mathcal{T} = \mathbb{I} + \hat{\mathcal{T}} \quad (3.173)$$

is therefore suggested, where  $\mathbb{I}$  is the identity matrix and leaves the wavefunctions unchanged and  $\hat{\mathcal{T}}$  represents the difference between the true Kohn–Sham wavefunction and the pseudowavefunction around the ionic core.

At this point it is useful to expand the pseudised Kohn–Sham wavefunctions in some basis functions as in equation 3.168. These basis functions are most

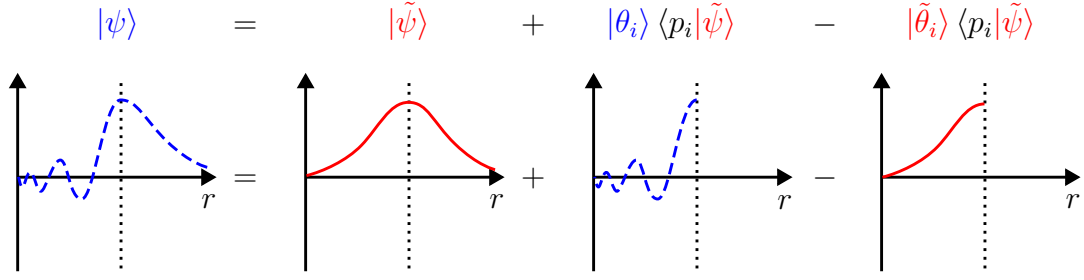


**Figure 3.5** *Schematic indicating how the true wavefunction is obtained from the pseudowavefunction through the use of projectors. The cutoff radius is indicated by the dotted line*

commonly chosen to be the solutions to the Kohn–Sham Schrödinger equation for an isolated atom,

$$|\tilde{\psi}\rangle = \sum_i C_i |\tilde{\theta}_i\rangle . \quad (3.174)$$

The coefficients  $C_i$  are determined by the projectors  $|p_i\rangle$  of the basis functions, defined by  $\langle p_i|\tilde{\theta}_j\rangle = \delta_{ij}$  and  $\sum_i |p_i\rangle \langle p_i| = \mathbb{I}$  as

$$C_i = \langle p_i|\tilde{\psi}\rangle . \quad (3.175)$$

The transformation  $\mathcal{T}$  can now be written out explicitly as

$$\mathcal{T} = \mathbb{I} + \sum_i (|\theta_i\rangle - |\tilde{\theta}_i\rangle) \langle p_i| . \quad (3.176)$$

This transformation is applied to the original Kohn–Sham wavefunction to transform it to the pseudised wavefunction,

$$|\psi\rangle = \mathcal{T} |\tilde{\psi}\rangle = |\tilde{\psi}\rangle + \sum_i |\theta_i\rangle \langle p_i|\tilde{\psi}\rangle - |\tilde{\theta}_i\rangle \langle p_i|\tilde{\psi}\rangle . \quad (3.177)$$

Equation 3.177 is shown schematically in figure 3.5.

It is now possible to work with the pseudowavefunctions,  $|\tilde{\psi}\rangle$ , and relate them back to the true wavefunctions,  $|\psi\rangle$ , through the projectors of the basis functions,  $|p_i\rangle$ . If an observable  $A$  is defined in the Kohn–Sham basis, then it can be expressed in the pseudobasis as

$$\tilde{A} = A + \sum_{ij} |p_i\rangle (\langle \theta_i|A|\theta_j\rangle - \langle \tilde{\theta}_i|A|\tilde{\theta}_j\rangle) \langle p_j| . \quad (3.178)$$

With this approach the requirement for norm-conservation in the pseudopotentials has been removed while still being able to compute observables of the system. The number of plane waves required to represent the pseudowavefunction is decreased and the computational efficiency is significantly improved, making more demanding calculations tractable as well as increasing the throughput of calculations.

### 3.3.3 Approximations to the exchange–correlation functional

DFT is an exact theory up to the point where the potential is split into the Coulomb part and the exchange and correlation part. Although the first Hohenberg-Kohn theorem states that the exchange–correlation functional exists, there is currently no exact form that is known — it must be approximated.

The simplest approximation that can be made is to assume that the true exchange–correlation energy density is equal point-by-point (locally) to that of the homogeneous electron gas of the same density. This approximation is known as the local density approximation (LDA) and was the approach proposed by Hohenberg and Kohn in their seminal paper [70]. The exchange–correlation energy in the LDA is given by

$$E_{\text{xc}}^{\text{LDA}}[n(\mathbf{r})] = \int d^3\mathbf{r} \, n(\mathbf{r}) \, \epsilon_{\text{xc}}^{\text{hom.}}(n)|_{n=n(\mathbf{r})} \quad (3.179)$$

where  $\epsilon_{\text{xc}}^{\text{hom.}}(n)|_{n=n(\mathbf{r})}$  is the exchange correlation energy of the homogeneous electron gas at the density  $n(\mathbf{r})$  corresponding to the volume element  $d^3\mathbf{r}$ . The function  $\epsilon^{\text{hom.}}$  has been determined exactly from Monte-Carlo simulations [72].

This approximation works well in many cases, but it is known to, in general, overestimate the bonding strength and perform poorly in certain situations [73, 74]. To correct this, the assumption that each volume element acts as a locally homogeneous system can be improved upon with the assumption that each volume element depends on the local density *and its gradients* in an approximation known as the generalised gradient approximation (GGA). Unlike LDA, which is determined entirely through first principles calculations and Monte-Carlo simulations, the GGA exchange–correlation functional must be parameterised somehow, and some parameters are fitted to reproduce experimentally observed

data. In this vein, the GGA functionals are not truly a first-principles approximation, but once the functional is made it is general enough that it can be applied to almost any system. There are many types of GGA functionals, some of which are designed for general use, and some that are designed to work well with specific systems or to accurately calculate a specific material property. Some common GGA functionals implemented in VASP are PBE [75], PBEsol [76], AM05 [77–79], and PW91 [80].

### 3.3.4 Forces in density functional theory

To calculate the dynamics of the atoms it will be necessary to calculate forces from DFT. These forces are calculated as the derivative of the potential energy with respect to the atomic position through the Hellmann–Feynman theorem [81, 82].

Although the Hellmann–Feynman theorem applies generally for any parameter on which the energy eigenvalue is dependent, it shall here be stated explicitly for one of the atomic coordinates  $X$ ,

$$F_X = -\frac{dE(X)}{dX} = -\left\langle \psi \left| \frac{dH}{dX} \right| \psi \right\rangle. \quad (3.180)$$

The wavefunctions  $|\psi\rangle$  are the Kohn–Sham wavefunctions. The above relation will be crucial to the phonon calculations performed in the following chapters which rely heavily on the calculation of the forces.

# Chapter 4

## Methods

### 4.1 Finite displacement

The methods for determining the force constants in this thesis are all variations of the finite displacement approach. The finite displacement approach involves displacing an atom from its static lattice position by some known displacement, computing the force on the atom using DFT, and then fitting the resulting force–displacement data to a system of equations of the form

$$F\left(\begin{smallmatrix} \mathbf{R} \\ \mu \\ i \end{smallmatrix}\right) = - \sum_{\{\mathbf{S}, \nu, j\}} \Phi\left(\begin{smallmatrix} \mathbf{R} & \mathbf{S} \\ \mu & \nu \\ i & j \end{smallmatrix}\right) u\left(\begin{smallmatrix} \mathbf{S} \\ \nu \\ j \end{smallmatrix}\right) , \quad (4.1)$$

where  $F$  is a vector of the forces computed from DFT,  $\Phi$  is the matrix of harmonic force constants, and  $u$  is the vector of atomic displacements. This approximates the derivative in the definition of the force constants as

$$\frac{\partial \mathbf{F}}{\partial u} = \frac{\Delta \mathbf{F}}{\Delta u} , \quad (4.2)$$

where  $\Delta u$  is chosen to be sufficiently small. This is the finite difference approximation — the *finite displacement* method of computing the force constants employs the *finite difference* approximation to the derivative.

The technique can be generalised to higher-order force constants; a force constant

model up to fourth order,

$$F\left(\begin{smallmatrix} R \\ \mu \\ i \end{smallmatrix}\right) = - \sum_{\{S,\nu,j\}} \Phi\left(\begin{smallmatrix} R & S \\ \mu & \nu \\ i & j \end{smallmatrix}\right) u\left(\begin{smallmatrix} S \\ \nu \\ j \end{smallmatrix}\right) - \sum_{\{S,\nu,j\}} \Phi\left(\begin{smallmatrix} R & S & T \\ \mu & \nu & \eta \\ i & j & k \end{smallmatrix}\right) u\left(\begin{smallmatrix} S \\ \nu \\ j \end{smallmatrix}\right) u\left(\begin{smallmatrix} T \\ \eta \\ k \end{smallmatrix}\right) \\ - \sum_{\{S,\nu,j\}} \Phi\left(\begin{smallmatrix} R & S & T & U \\ \mu & \nu & \eta & \tau \\ i & j & k & l \end{smallmatrix}\right) u\left(\begin{smallmatrix} S \\ \nu \\ j \end{smallmatrix}\right) u\left(\begin{smallmatrix} T \\ \eta \\ k \end{smallmatrix}\right) u\left(\begin{smallmatrix} U \\ \tau \\ l \end{smallmatrix}\right) , \quad (4.3)$$

is employed and a least-squares fit is performed to determine the optimal set of force constants.

In a finite displacement calculation, an atom or atoms are displaced in order to target certain force constants. The particular arrangement of displaced atoms will be referred to as a *displacement pattern*. Each element in the matrix  $\Phi$  relates a specific displacement pattern to a force created on an atom in a particular direction. Many of these force constants relate forces on different atoms, or in different directions, to the same displacement pattern, and many of the force constants and displacement patterns are equivalent by symmetry. Therefore the symmetry constraints of section 3.1.5 are used to determine some minimum set of displacement patterns needed to fit all force constants. Atoms are displaced along high-symmetry directions in the crystal, or along the cartesian axes (these coincide for the diamond structure considered in this thesis). In the diamond structure, only one displacement is necessary to deduce all independent harmonic force constants in the crystal.

## 4.2 The quasiharmonic approximation

Static crystal energies are computed through DFT, and the finite displacement method described above is used to compute the harmonic force constants and subsequently the dynamical matrix, from which harmonic phonon frequencies are calculated. All this is done without including any anharmonicity in the interatomic potential. To include this, the simplest approximation one can make is the quasiharmonic approximation (QHA), where the interatomic potential is still assumed to be harmonic, but the associated force constants are allowed to exhibit some volume dependence. As a consequence of this, the phonon

dispersions and the dependent properties also assume a volume dependence.

Quasiharmonic phonon calculations are performed as follows:

1. For a range of volumes covering the pressure range of interest, perform finite displacement calculations and obtain harmonic phonon frequencies on a sufficiently dense grid throughout the Brillouin zone. Also compute any phonon-frequency-dependent properties of interest, such as the zone-centre optical phonon frequency.

2. For each volume, determine the Helmholtz free energy at a temperature  $T$  as

$$F(T, V) = U(V) + F_{\text{ph}}(T, V) , \quad (4.4)$$

where  $U(V)$  is the static crystal energy calculated from DFT and the phonon contribution is given by

$$F_{\text{ph}}(T, V) = \frac{1}{N} \sum_{\mathbf{k}, j} \left\{ \frac{1}{2} \hbar \omega_{\mathbf{k}j}(V) + k_B T \ln \left( 1 - \exp \left[ \frac{\hbar \omega_{\mathbf{k},j}(V)}{k_B T} \right] \right) \right\} . \quad (4.5)$$

The sum in the above equation is a sum over the  $N$  phonons in the sampling grid indexed by their wavevector  $\mathbf{k}$  and their band index  $j$ .

3. Fit an *equation of state* to the free-energy–volume data. An equation of state is typically a function of the equilibrium free energy  $U_0$ , the zero-pressure bulk modulus  $B_0$ , its (first) derivative at zero pressure  $B'_0$ , and the zero-pressure unit cell volume  $V_0$ . An equation of state relating the volume to the free energy can be turned into an equation of state relating the volume to the pressure using the relation

$$P(V) = - \left. \frac{dF(T, V)}{dV} \right|_T . \quad (4.6)$$

4. Invert the  $P(V)$  equation of state to obtain a  $V(P)$  equation of state. This may need to be done numerically.
5. Use the  $V(P)$  equation of state to determine the volume at some pressure. Through an appropriate volume interpolation of the phonon-frequency-dependent property of interest from step 1,  $X(V)$ , one may now determine this property at any pressure as  $X(V(P))$ .

### 4.3 Temperature dependent effective potential

The TDEP approach to computing anharmonic force constants makes use of the fact that a set of non-interacting (i.e. renormalised) phonons must satisfy some fictitious harmonic potential. A TDEP calculation is performed by first generating a set of atomic displacements that mimics the actual displacements in the real crystal at some specified temperature. The forces on the atoms in these configurations are then calculated (from here, a “configuration” will refer to a particular arrangement of atoms within a supercell that have been randomly displaced from their equilibrium positions by some amount) and the resulting force–displacement data fitted to a harmonic force constant model,

$$F\left(\begin{smallmatrix} \mathbf{R} \\ \mu \\ i \end{smallmatrix}\right) = - \sum_{\{\mathbf{S}, \nu, j\}} \hat{\Phi}\left(\begin{smallmatrix} \mathbf{R} & \mathbf{S} \\ \mu & \nu \\ i & j \end{smallmatrix}\right) u\left(\begin{smallmatrix} \mathbf{S} \\ \nu \\ j \end{smallmatrix}\right) , \quad (4.7)$$

where  $\hat{\Phi}$  is some set of *effective* force constants. These effective force constants, and the effective potential they create, are chosen in such a way that the forces calculated from this effective potential are as close as possible to the forces from the DFT calculation in a least squares sense. The TDEP approach aims to minimise

$$\Delta F = \left\| F^{\text{TDEP}}\left(\begin{smallmatrix} \mathbf{R} \\ \mu \\ i \end{smallmatrix}\right) - F^{\text{DFT}}\left(\begin{smallmatrix} \mathbf{R} \\ \mu \\ i \end{smallmatrix}\right) \right\| , \quad (4.8)$$

where  $F^{\text{DFT}}\left(\begin{smallmatrix} \mathbf{R} \\ \mu \\ i \end{smallmatrix}\right)$  are the forces computed in the DFT calculations and  $F^{\text{TDEP}}\left(\begin{smallmatrix} \mathbf{R} \\ \mu \\ i \end{smallmatrix}\right)$  are calculated as in equation 4.7.

The effective harmonic potential is, in theory, able to capture anharmonicity to infinite order. However, as the potential is harmonic, it cannot account for any antisymmetric parts of the potential. To overcome this obstacle, effective third-order force constants can be found by fitting to the equation

$$F\left(\begin{smallmatrix} \mathbf{R} \\ \mu \\ i \end{smallmatrix}\right) - F^{\text{EFF. HARM.}}\left(\begin{smallmatrix} \mathbf{R} \\ \mu \\ i \end{smallmatrix}\right) = - \sum_{\{\mathbf{S}, \nu, j\}, \{\mathbf{T}, \eta, k\}} \hat{\Phi}\left(\begin{smallmatrix} \mathbf{R} & \mathbf{S} & \mathbf{T} \\ \mu & \nu & \eta \\ i & j & k \end{smallmatrix}\right) u\left(\begin{smallmatrix} \mathbf{S} \\ \nu \\ j \end{smallmatrix}\right) u\left(\begin{smallmatrix} \mathbf{T} \\ \eta \\ k \end{smallmatrix}\right) . \quad (4.9)$$

where  $F^{\text{EFF. HARM.}}\left(\begin{smallmatrix} \mathbf{R} \\ \mu \\ i \end{smallmatrix}\right)$  are the forces found from the effective harmonic part of the potential. In other words, the cubic force constants are fitted after the effective harmonic force constants to the residual forces. These effective cubic force constants are used to calculate the effect of 3-phonon and other odd-integer



phonon interactions on the phonon frequency. The leading contribution to these interactions is the bubble diagram in figure 3.2.

Inverse phonon lifetimes are commonly calculated from the imaginary part of the phonon self-energy as

$$\begin{aligned} \text{Im} [\Sigma_{jj'}(\mathbf{k}, \omega)] = & \frac{\pi \hbar}{16 \sqrt{\omega_{\mathbf{k}j} \omega_{\mathbf{k}j'}}} \sum_{\substack{\mathbf{k}_1 j_1 \\ \mathbf{k}_2 j_2}} \frac{\tilde{\Phi} \left( \begin{smallmatrix} -\mathbf{k} & \mathbf{k}_1 & \mathbf{k}_2 \\ j & j_1 & j_2 \end{smallmatrix} \right) \tilde{\Phi} \left( \begin{smallmatrix} \mathbf{k} & -\mathbf{k}_1 & -\mathbf{k}_2 \\ j & j_1 & j_2 \end{smallmatrix} \right)}{\omega_{\mathbf{k}_1 j_1} \omega_{\mathbf{k}_2 j_2}} \Delta(\mathbf{k}_1 + \mathbf{k}_2 - \mathbf{k}) \\ & \times \left[ (n(\omega_{\mathbf{k}_1 j_1}) + \omega_{\mathbf{k}_2 j_2} + 1) \delta(\omega_{\mathbf{k}_1 j_1} + \omega_{\mathbf{k}_2 j_2} - \omega) \right. \\ & - (n(\omega_{\mathbf{k}_2 j_2}) - n(\omega_{\mathbf{k}_1 j_1})) \delta(\omega_{\mathbf{k}_1 j_1} - \omega_{\mathbf{k}_2 j_2} + \omega) \\ & - (n(\omega_{\mathbf{k}_1 j_1}) + \omega_{\mathbf{k}_2 j_2} + 1) \delta(\omega_{\mathbf{k}_1 j_1} + \omega_{\mathbf{k}_2 j_2} + \omega) \\ & \left. + (n(\omega_{\mathbf{k}_2 j_2}) - n(\omega_{\mathbf{k}_1 j_1})) \delta(\omega_{\mathbf{k}_1 j_1} - \omega_{\mathbf{k}_2 j_2} - \omega) \right] , \end{aligned} \quad (4.10)$$

where  $\Delta(\mathbf{K})$  is 1 if  $\mathbf{K}$  is a reciprocal lattice vector and 0 otherwise, and  $n(\omega)$  is the Bose-Einstein distribution [62]. The imaginary part of the self-energy is an  $\omega$ -dependent function that produces something density-of-states-like. The real part of the self-energy can be found from equation 4.10 through the Kramers–Kronig relations, which state that for a complex function  $\Sigma(\omega)$

$$\text{Re} [\Sigma(\omega)] = \frac{1}{\pi} \int_{-\infty}^{\infty} \frac{\text{Im} [\Sigma(\omega')]}{\omega' - \omega} d\omega' \quad (4.11a)$$

$$\text{Im} [\Sigma(\omega)] = -\frac{1}{\pi} \int_{-\infty}^{\infty} \frac{\text{Re} [\Sigma(\omega')]}{\omega' - \omega} d\omega' . \quad (4.11b)$$

A representative example of this process is shown in figure 4.1. The imaginary part of the spectrum in the right-hand panel is calculated from equation 4.10 and the left-hand panel shows the real part of the spectrum calculated from equation 4.11a.

This allows one to estimate the frequency renormalisation from the 3-phonon processes. As the resulting real part of the self-energy is again a spectrum, one must evaluate it at the correct frequency,  $\omega$ , in order to obtain the correct renormalisation. This is, strictly speaking, a problem to be solved self-consistently, as the renormalised frequencies will give rise to a different

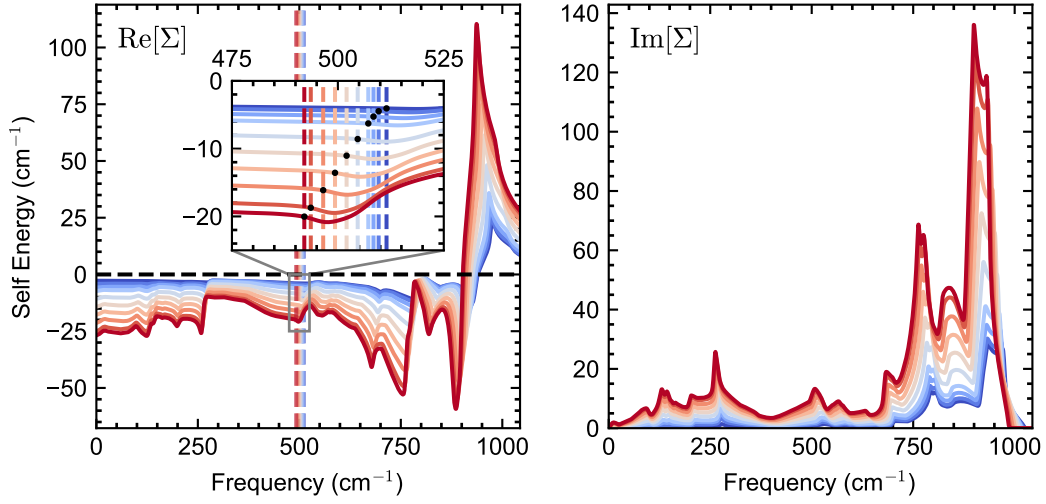


**Figure 4.1** *Calculation of the 3-phonon contribution in silicon at different temperatures. The real part of the self-energy (left) is found from the imaginary part (right) by the Kramers–Kronig relations. The renormalisation due to 3-phonon processes is given by the real part of the self-energy evaluated at the phonon frequency,  $\omega$ , at each temperature, indicated by the black dots at the intersection of the vertical dashed lines and  $\text{Re}[\Sigma]$ . Temperature indicated by the color of the lines from blue (0 K) to red (1000 K).*

imaginary part of the self-energy, which will, in turn, produce a different real part and therefore a different renormalisation. As it is not computationally feasible to iterate process to self-consistency, the assumption is made that the effective harmonic frequencies provide a close approximation to the self-consistent frequencies. In simple materials such as silicon and diamond this is likely to be approximately correct, in more complex ones, or materials where the real part of the self-energy has some pronounced features in region around the effective harmonic frequency, this approximation may not be true.

A TDEP calculation is therefore performed as follows:

1. Generate a set of configurations that represent snapshots of the crystal at finite temperature.
2. Perform DFT calculations on these configurations to determine the forces.
3. Fit the effective potential to the forces and displacements using equation 4.7.
4. Construct the dynamical matrix from the effective harmonic force constants

and calculate the phonon frequencies.

5. (Optionally) Compute the 3-phonon frequency correction from effective third-order force constants through the Kramers–Kronig relations.

## Generating configurations

Before continuing, the method for generating the configurations used in TDEP calculations must be explained. The success of the TDEP approach depends on how representative the set of configurations used to fit the effective potential are of the real crystal at the specified temperature. In order to find configurations of atoms that reflect the real crystal, one may perform molecular dynamics simulations and extract snapshots of the atoms at different times. This approach, however, comes with difficulties. The snapshots must be uncorrelated for accurate sampling of the  $N$ -body potential to occur, they must be taken from a molecular dynamics simulation that has been allowed to reach equilibrium from its starting configuration, and, perhaps most obviously, the method used to calculate the forces from timestep to timestep (DFT, interatomic potential, *etc.*...) must be sufficiently accurate to produce realistic snapshots. This last point may seem trivially obvious but it has the effect of making the generation of configurations for TDEP a very computationally intensive process.

In order to generate the configurations using the stochastic TDEP method, one must first create an initial set of force constants from which the phonon modes to be populated can be determined. This was done using a standard harmonic finite displacement calculation where atoms were displaced along the high-symmetry lines (see section 4.1) by 0.01 Å. From these harmonic force constants, phonon modes are calculated and then sampled as a canonical ensemble to populate the phonon modes in the TDEP configurations.

## Sampling the Canonical Ensemble

To produce a physically realistic distribution of the atomic displacements in the TDEP configurations, the phonon modes must be populated with an appropriate distribution. To determine the form of this distribution one may consider the equipartition theorem, which states that every degree of freedom in a system

contributes on average  $\frac{1}{2}k_B T$  to the total energy. Following from equation 3.29,

$$\left\langle \frac{1}{2} M_\mu \dot{u} \left( \frac{\mathbf{R}}{i} \right)^2 \right\rangle = \left\langle \frac{1}{2} M_\mu \omega_{\mathbf{k}j}^2 A_{\mathbf{k}j}^2 \sin^2(\omega_{\mathbf{k}j} t + \phi_{\mathbf{k}j}) \right\rangle = \frac{1}{4} M_\mu \omega_{\mathbf{k}j}^2 \langle A_{\mathbf{k}j}^2 \rangle = \frac{1}{2} k_B T, \quad (4.12)$$

where  $A_{\mathbf{k}j}$  is the amplitude of the normal mode, and  $\omega_{\mathbf{k}j}$  and  $\phi_{\mathbf{k}j}$  are respectively the frequency and phase of a mode with wavevector  $\mathbf{k}$  and band  $j$ . To go from the second to the third equality the identity

$$\langle \sin^2 x \rangle = \frac{1}{2\pi} \int \sin^2 x dx = \frac{1}{2}$$

has been used.

One possibility is to choose  $\langle A_{\mathbf{k}j} \rangle = \frac{1}{\omega_{\mathbf{k}j}} \sqrt{\frac{2k_B T}{M_\mu}}$  for all  $A_{\mathbf{k}j}$ . In this case, the energy of each mode (kinetic + potential) is  $k_B T$  and the condition of equipartition would be satisfied. However, a more physically reasonable approach is to assume a Boltzmann distribution for the energies of the modes  $E_{\mathbf{k}j}$ ,

$$\zeta_{\mathbf{k}j} = \frac{1}{k_B T} \int_0^{E_{\mathbf{k}j}} e^{-E/k_B T} dE, \quad (4.13)$$

where  $\zeta_{\mathbf{k}j}$  is a uniformly distributed random number between 0 and 1.

Evaluating the integral, one can determine the mode energies to be

$$\zeta_{\mathbf{k}j} = \left[ -e^{-E/k_B T} \right]_0^{E_{\mathbf{k}j}} \quad (4.14)$$

$$= 1 - e^{-E_{\mathbf{k}j}/k_B T}, \quad (4.15)$$

which can be rearranged to get

$$E_{\mathbf{k}j} = k_B T \ln(1 - \zeta_{\mathbf{k}j}). \quad (4.16)$$

Averaging this expression for the mode energies one finds

$$\langle E_{\mathbf{k}j} \rangle = -k_B T \langle \ln(1 - \zeta_{\mathbf{k}j}) \rangle \quad (4.17)$$

$$= -k_B T \left\{ \frac{1}{1-0} \int_0^1 \ln(1 - \zeta_{\mathbf{k}j}) \right\} \quad (4.18)$$

$$= -k_B T [(\zeta_{\mathbf{k}j} - 1) \ln(1 - \zeta_{\mathbf{k}j}) - \zeta_{\mathbf{k}j}]_0^1 \quad (4.19)$$

$$= k_B T , \quad (4.20)$$

demonstrating the equipartition principle still holds using this Boltzmann distribution for the energies. The normal mode amplitude can therefore be changed from  $A_{\mathbf{k}j} = \frac{1}{\omega_{\mathbf{k}j}} \sqrt{\frac{2k_B T}{M_\mu}}$  to  $A_{\mathbf{k}j} = \frac{1}{\omega_{\mathbf{k}j}} \sqrt{\frac{2k_B T}{M_\mu}} \sqrt{-\ln(1 - \zeta_{\mathbf{k}j})}$  and still satisfy equipartition.

This distribution of amplitudes can be used to determine the displacements of the atoms when the supercell is populated with phonons,

$$u\left(\begin{smallmatrix} \mathbf{R} \\ \mu \\ i \end{smallmatrix}\right)(t) = \sum_{\{\mathbf{k}, j\}} \frac{\sqrt{k_B T}}{M_\mu \omega_{\mathbf{k}j}} \sqrt{-2 \ln(\zeta_{\mathbf{k}j})} E\left(\begin{smallmatrix} \mathbf{R} & \mathbf{k} \\ \mu & j \end{smallmatrix}\right) \exp(i\omega_{\mathbf{k}j} t) . \quad (4.21)$$

The factor of  $\mathbf{k} \cdot \mathbf{R}$  does not appear in the exponential as it has been set equal to  $2\pi$  in order to consider only modes commensurate with the supercell size. Populating the supercell with modes not commensurate with the supercell will produce unrealistic configurations when periodic boundary conditions are imposed.

Since  $\zeta_{\mathbf{k}j}$  is a uniform random number between 0 and 1, it can be substituted for  $1 - \zeta_{\mathbf{k}j}$  with no effect. Now, in order to give the phonon a random phase one can either choose a random time, or give it a random phase offset. Both these operations can be expressed in a single random number as

$$u\left(\begin{smallmatrix} \mathbf{R} \\ \mu \\ i \end{smallmatrix}\right)(t) = \sum_{\{\mathbf{k}, j\}} \frac{\sqrt{k_B T}}{M_\mu \omega_{\mathbf{k}j}} \sqrt{-2 \ln(\zeta_{\mathbf{k}j})} E\left(\begin{smallmatrix} \mathbf{R} & \mathbf{k} \\ \mu & j \end{smallmatrix}\right) \exp(2\pi \xi_{\mathbf{k}j}) , \quad (4.22)$$

where  $\xi$  is again a uniform random number between 0 and 1.

It can be shown that, in the quantum case, the same expression for the energy distributions (equation 4.16) can be derived, and that the displacements of the atoms in the quantum regime can be found by replacing the classical expression

for the mode amplitude

$$\langle A_{\mathbf{k}j} \rangle = \frac{1}{\omega_{\mathbf{k}j}} \sqrt{\frac{2k_B T}{M_\mu}} \quad (4.23)$$

with the quantum

$$\langle A_{\mathbf{k}j} \rangle = \sqrt{\frac{\hbar(2n(\omega_{\mathbf{k}j}) + 1)}{M_\mu \omega_{\mathbf{k}j}}}, \quad (4.24)$$

where  $n$  is the Bose–Einstein distribution.

This quantum distribution of displacements,

$$u\left(\begin{smallmatrix} \mathbf{R} \\ \mu \\ i \end{smallmatrix}\right)(t) = \sum_{\{\mathbf{k}, j\}} \frac{1}{M_\mu} \sqrt{\frac{\hbar(2n(\omega_{\mathbf{k}j}) + 1)}{\omega_{\mathbf{k}j}}} \sqrt{-2 \ln(\zeta_{\mathbf{k}j})} E\left(\begin{smallmatrix} \mathbf{R} & \mathbf{k} \\ \mu & j \end{smallmatrix}\right) \exp(2\pi \xi_{\mathbf{k}j}), \quad (4.25)$$

is used to populate the phonon modes in this thesis, since all calculations will be at temperatures comparable with the Debye temperature.

A principle concern of investigations in subsequent chapters of this thesis is minimising the impact of the stochastic nature of the configuration generation process. When comparing two TDEP calculations, for example at two different temperatures, it is desirable to remove the stochastic error from the configuration generation process so that genuine changes in the phonon frequencies are not obscured by scatter in the frequencies. One obvious way of doing this is to use the same seed for the random number generator used to generate the sets of random numbers  $\zeta_{\mathbf{k}j}$  and  $\xi_{\mathbf{k}j}$ . This is satisfactory in some cases, but, in others, more laborious approaches are required which are described in the subsequent chapters as they are employed.

## 4.4 Self-consistent phonons

The self-consistent phonon approach implements the theory discussed in section 3.2. The method is used in the ALAMODE software package and is broadly implemented in the following manner. Firstly, force constants are determined up to fourth order by the finite displacement method described in section 4.1. The harmonic (second-order) force constants are used to determine a set of harmonic phonon frequencies on a dense,  $\Gamma$ -centred sampling grid across the Brillouin zone

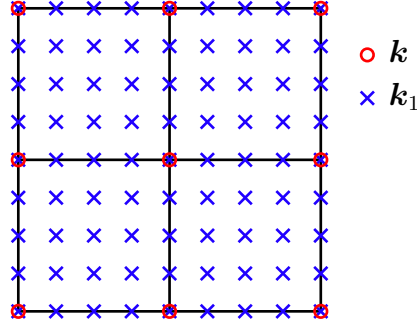


**Figure 4.2** *Grids used in the SCPH algorithm. The coarse  $\mathbf{k}$  grid indicated by the red circles is commensurate with the supercell size (here  $2 \times 2 \times 2$ ), the dense  $\mathbf{k}_1$  grid is used to compute the self energies and must be commensurate with the coarse  $\mathbf{k}$  grid.*

(indicated by blue crosses in figure 4.2). These harmonic phonon frequencies and the higher-order force constants are used to calculate the self-energy  $\Sigma_{jj'}$ , a correction to the harmonic dynamical matrix,  $\Lambda_{jj'}$ , on a coarser sampling grid across the Brillouin zone (red circles in figure 4.2). The correction is then applied to the harmonic dynamical matrix as

$$V_{jj'} = \Lambda_{jj'} + \Sigma_{jj'} , \quad (4.26)$$

and new, anharmonic phonons are calculated on the coarse grid by diagonalising the matrix  $V_{jj'}$ . Fourier interpolation of frequencies and eigenvectors is then used to determine the new phonons on the dense grid. These new phonons are then used to re-compute the self-energy, and the whole process is iterated until self-consistency is achieved.

In greater detail, SCPH approach as implemented by ALAMODE works as follows [2]:

1. Construct and diagonalise the dynamical matrix from the harmonic force constants. This gives the harmonic phonon frequencies  $\omega_{\mathbf{k}_1 j_1}^{[h]}$  and phonon eigenvectors  $e_{\mathbf{k}_1 j_1}^{[h]}$  on the dense  $\mathbf{k}_1$  grid.
2. Calculate the  $s \times s \times s \times s$  matrix  $\tilde{\Phi}(\frac{\mathbf{k}}{j} \frac{\mathbf{k}}{j'} \frac{\mathbf{k}_1}{j_1} \frac{-\mathbf{k}_1}{j_1})$ , where  $s$  is the number of bands, needed to compute the self-energy from the loop diagram (see equations 3.104 and 3.107) for each pair of  $\mathbf{k}$  points,  $\mathbf{k}$  and  $\mathbf{k}_1$ . The vector  $\mathbf{k}$  is restricted to the irreducible points that are commensurate with the size

of the supercell, and  $\mathbf{k}_1$  cover the whole  $\mathbf{k}$ -point grid (see figure 4.2).

3. Initialise the phonon frequencies as the harmonic frequencies  $\omega_{\mathbf{k}_1 j_1}^{[1]} = \omega_{\mathbf{k}_1 j_1}^{[h]}$ .
4. Construct the matrix

$$V_{jj'}^{[1]}(\mathbf{k}) = \left[ \omega_{\mathbf{k}_1 j}^{[h]} \right]^2 \delta_{jj'} + \frac{\hbar}{4} \sum_{\mathbf{k}_1 j_1} \frac{2n(\omega_{\mathbf{k}_1 j_1}^{[1]}) + 1}{\omega_{\mathbf{k}_1 j_1}^{[1]}} \times \tilde{\Phi}^{[1]} \left( \begin{smallmatrix} \mathbf{k} & \mathbf{k} & \mathbf{k}_1 & -\mathbf{k}_1 \\ j & j' & j_1 & j_1 \end{smallmatrix} \right),$$

where  $\tilde{\Phi}^{[1]} \left( \begin{smallmatrix} \mathbf{k} & \mathbf{k} & \mathbf{k}_1 & -\mathbf{k}_1 \\ j & j' & j_1 & j_1 \end{smallmatrix} \right)$  is the matrix constructed using the harmonic phonon eigenvectors.

5. Diagonalise the matrix  $V^{[1]}(\mathbf{k})$  as  $V^{[1]}(\mathbf{k}) = C^{[1]}(\mathbf{k})W^{[1]}(\mathbf{k})C^{[1]}(\mathbf{k})^\dagger$ . This yields a set of frequencies (as the eigenvalues) and a set of eigenvectors on the coarse grid  $\mathbf{k}$ . These eigenvectors are **not** the phonon eigenvectors. They are related to the phonon eigenvectors by a unitary transformation  $E^{[i]}(\mathbf{k}) = E^{[h]}(\mathbf{k})C^{[i-1]}(\mathbf{k})$ , where  $E(\mathbf{k})$  is the  $s \times s$  matrix of phonon eigenvectors, with the eigenvectors in the columns of  $E(\mathbf{k})$ .
6. Construct the new dynamical matrix

$$D^{[1]}(\mathbf{k}) = E^{[1]}(\mathbf{k})W^{[1]}(\mathbf{k})E^{[1]}(\mathbf{k})^\dagger = E^{[h]}(\mathbf{k})C^{[1]}(\mathbf{k})W^{[1]}(\mathbf{k})C^{[1]}(\mathbf{k})^\dagger E^{[h]}(\mathbf{k})^\dagger$$

for each irreducible  $\mathbf{k}$ .

7. Use the dynamical matrices calculated on the irreducible  $\mathbf{k}$ -points and the symmetries of the crystal to construct the dynamical matrices on the entire grid of  $\mathbf{k}$ . Recall that  $\mathbf{k}$  was limited to the points commensurate with the supercell size, and  $\mathbf{k}_1$  covered the entire  $N_1 \times N_2 \times N_3$   $\mathbf{k}$ -point grid.
8. Use Fourier interpolation to calculate the dynamical matrix on the denser  $\mathbf{k}_1$  grid from the  $\mathbf{k}$  grid.
9. From this dynamical matrix, find the phonon frequencies  $\omega_{\mathbf{k}_1 j_1}^{[1]}$  and the unitary transformation matrix  $C^{[1]}(\mathbf{k}_1)$  on the dense  $\mathbf{k}_1$  grid. The transformation matrix is needed for the next iteration of the SCPH cycle.
10. Update the matrix  $\tilde{\Phi} \left( \begin{smallmatrix} \mathbf{k} & \mathbf{k} & \mathbf{k}_1 & -\mathbf{k}_1 \\ j & j' & j_1 & j_1 \end{smallmatrix} \right)$  by applying the unitary transformations of  $C_{ij}(\mathbf{k}_1)$  as

$$\tilde{\Phi}^{[i]} \left( \begin{smallmatrix} \mathbf{k} & \mathbf{k} & \mathbf{k}_1 & -\mathbf{k}_1 \\ i & j & s & s \end{smallmatrix} \right) = \sum_{kl} \tilde{\Phi}^{[i-1]} \left( \begin{smallmatrix} \mathbf{k} & \mathbf{k} & \mathbf{k}_1 & -\mathbf{k}_1 \\ i & j & k & l \end{smallmatrix} \right) C_{sk}^{*[i-1]}(\mathbf{k}_1) C_{sl}^{[i-1]}(\mathbf{k}_1)$$



11. The first iteration of the SCPH cycle is now complete. Increment  $i$  and repeat the process. The equation for the  $i^{\text{th}}$  iteration of the cycle is<sup>1</sup>

$$V_{jj'}^{[i]}(\mathbf{k}) = \left[ \omega_{\mathbf{k}_1 j}^{[h]} \right]^2 \delta_{jj'} + \frac{\hbar}{4} \sum_{\mathbf{k}_1 j_1} \frac{2n(\omega_{\mathbf{k}_1 j_1}^{[i-1]}) + 1}{\omega_{\mathbf{k}_1 j_1}^{[i-1]}} \times \tilde{\Phi}^{[i-1]} \left( \begin{smallmatrix} \mathbf{k} & \mathbf{k} & \mathbf{k}_1 & -\mathbf{k}_1 \\ j & j' & j_1 & j_1 \end{smallmatrix} \right) .$$

12. Diagonalise the matrix  $V^{[i]}(\mathbf{k})$  as  $V^{[i]}(\mathbf{k}) = C^{[i]}(\mathbf{k})W^{[i]}(\mathbf{k})C^{[i]}(\mathbf{k})^\dagger$

13. Construct the new dynamical matrix

$$D^{[i]}(\mathbf{k}) = E^{[i]}(\mathbf{k})W^{[i]}(\mathbf{k})E^{[i]}(\mathbf{k})^\dagger = E^{[h]}(\mathbf{k})C^{[i]}(\mathbf{k})W^{[i]}(\mathbf{k})C^{[i]}(\mathbf{k})^\dagger E^{[h]}(\mathbf{k})^\dagger$$

for each  $\mathbf{k}$  in the coarse grid.

14. Construct the dynamical matrices on the entire grid of  $\mathbf{k}$  using the symmetry operations, as in step 7.
15. Use Fourier interpolation to calculate the dynamical matrix on the denser  $\mathbf{k}_1$  grid from the  $\mathbf{k}$  grid.
16. From these dynamical matrices find the phonon frequencies  $\omega_{\mathbf{k}_1 j_1}^{[i]}$  and the unitary transformation matrix  $C^{[i]}(\mathbf{k}_1)$ .
17. Check for self-consistency ( $\omega_{\mathbf{k} j}^{[i]} = \omega_{\mathbf{k} j}^{[i-1]}$  within some tolerance) on all irreducible  $\mathbf{k}$ -points. If it is achieved, print the resulting frequencies and eigenvectors and stop, else go to step 11.

To implement this approach, one must ensure that the fourth-order force constants are calculated and fitted accurately, the two grids  $\mathbf{k}$  and  $\mathbf{k}_1$  are dense enough to achieve convergence, and that the convergence criterion is sufficiently restrictive. A closer examination of these facets of the calculation, particularly the calculation and fitting of the force constants, is discussed in an application to silicon in the next chapter. The TDEP approach is also described in similar detail and the two approaches are compared.

---

<sup>1</sup>In actuality a mixing parameter is used here. This has been omitted for simplicity.

# Chapter 5

## Temperature dependence of the Raman signal in silicon and diamond

### 5.1 Background

The SCPH and TDEP approaches have each shown promise when applied to real systems [11, 30, 40, 43], but a direct comparison on the same system(s) will be instructive in highlighting the differences between the two approaches and the considerations that are necessary to employ each method effectively.

To assess the accuracy of each approach, a comparison to experimental data must be made. The systems chosen here are cubic silicon and cubic diamond, chosen in part for the abundance of high-quality experimental data available for comparison. The other reason for choosing these systems is to assess the performance of the two approaches when computing anharmonic effects in what are typically considered to be very harmonic materials, particularly diamond. The SCPH and TDEP approaches have been well applied to complex, strongly anharmonic systems, where capturing even some of the anharmonicity produces impressive results and deviations from the true experimental value are not unexpected [2, 30]. However, here a different approach is taken to investigate the ability of each approach to *precisely* calculate the anharmonic renormalisation of the phonon frequencies in simple systems, and fully account for any deviations from experimental data.

This section will look more closely at the technical details of the SCPH and TDEP methods and the effect such implementation details have on the calculated phonon frequencies. The chapter will begin with a brief outline of the existing applications of each technique before describing the details of their current application to silicon and diamond. The temperature dependence of the zone-centre Raman frequency for both silicon and diamond will be used to assess the accuracy of the calculations, and a comparison of the approaches will be made with recommendations for future studies.

### 5.1.1 Alamode

It was mentioned in chapter 2 that the first application of the SCPH method by ALAMODE was to strontium titanate,  $\text{SrTiO}_3$  [2]. This inaugural investigation used the finite displacement approach to determine the force constants, where the atoms are displaced from their equilibrium positions by an amount  $\Delta u$ . The authors note that “finding an optimal value of  $\Delta u$  is not a trivial task, especially when imaginary modes exist within the harmonic approximation”. A displacement magnitude of  $0.1 \text{ \AA}$  did not produce reliable fourth-order force constants. Instead, the force constants of third order and above were found from an *ab initio* molecular dynamics (AIMD) simulation, which used the harmonic force constants to calculate trajectories of the atoms. Snapshots were taken from the simulation, and an additional displacement of  $0.1 \text{ \AA}$  was added to each atom in a random direction to reduce the cross-correlation of the positions.

From this, it is apparent that care must be taken to determine the higher-order force constants. The instability of the fourth order force constants was attributed in this instance to the double-well nature of the interatomic potential; without *a priori* knowledge of the potential it may be difficult to determine the optimal  $\Delta u$  to use. The AIMD approach circumvents this problem and is resemblant of the TDEP method. The distinction between the two is that ALAMODE calculates *actual* force constants rather than effective ones.

The SCPH approach was subsequently applied to other perovskite systems by the same group of authors, who employed the same method to avoid the instability of the fourth order force constants. One application to a material unrelated to the perovskites is to  $\text{H}_3\text{S}$ , but by this time the AIMD approach had become the

standard approach the authors of the ALAMODE code used for creating the force-displacement sets, so the same method was used for  $\text{H}_3\text{S}$ . A study where the standard finite displacement method is used is not known, although for simple systems like silicon and diamond it should produce valid results.

### 5.1.2 TDEP

TDEP also has two ways in which the force-displacement data for the fitting process may be generated, which were discussed in chapters 2 and 4: from AIMD snapshots and from stochastically generated samples. As with ALAMODE, much of the existing literature makes use of expensive AIMD simulations to find realistic displacement configurations, but, unlike ALAMODE, success has been found with the latter, less computationally expensive approach. As new configurations need to be generated at every temperature and pressure, using a cheaper method to create them results in a significant reduction in the computational cost when performing calculations at a range of temperatures or pressures.

The stochastic TDEP approach used here, where configurations are generated by populating phonon modes (see section 4.3), has been applied to silicon, lead compounds (PbTe, PbSe, and PbS), and cementite ( $\text{Fe}_3\text{C}$ ), as well as others [38, 40, 46, 83]. In many of these applications, however, the number of configurations used is not reported. In a study of lead telluride and other lead compounds the authors used 50 snapshots of an AIMD simulation to ensure accurate frequencies [38], but this figure alone does not provide a full picture of the convergence with respect to the number of configurations, nor does it indicate how well the stochastic method will perform compared to the AIMD method. In some papers, it is almost suggested to be a single configuration of a single supercell, which the work in this thesis will show to be insufficient. Similarly, the number of snapshots from AIMD simulations is not reported. Despite this, it will be shown that TDEP is a robust method that can be well converged with a reasonable number of configurations.

Silicon has already been analysed using the TDEP approach by Hellman *et al.* in order to better understand the source of the negative thermal expansion at low temperatures [40]. In this investigation, it was found that the TDEP formalism described the thermal expansion even better than the quasiharmonic

approximation. Furthermore, it was found that the QHA is only so accurate due to fortunate cancellation of errors, where some modes are predicted too hard and some predicted too soft in such a manner that the total phonon free energy, the quantity that is central to the QHA, was correct on average. This is an encouraging showcase of TDEP's capability, which will be taken advantage of in this thesis.

## 5.2 Methods

### 5.2.1 Displacement magnitude testing

In the finite displacement approach to determining force constants, atoms are displaced from their equilibrium positions along high-symmetry directions in the crystal by a magnitude  $\Delta u$ . To determine an  $n^{\text{th}}$  order force constant,  $n - 1$  atoms must be displaced. In order to determine all symmetry-inequivalent force constants of a given order, there is a minimum number of displacement patterns that must be considered. In theory, one has complete freedom to choose  $\Delta u$  for each individual displacement of the atom(s) and for each displacement pattern. In practice, for well-behaved interatomic potentials, a single displacement magnitude can be used for all atoms in all displacement patterns for a given order  $n$ . The different orders of force constants should have different displacement magnitudes to probe the regions of the interatomic potential where each order of force constants is most significant. The harmonic force constants should have the lowest displacement, the cubic contributions to the potential become significant at slightly larger displacement, and the quartic contributions become noticeable at displacements that are larger still.

To implement the SCPH algorithm one requires force constants up to 4<sup>th</sup> order. It is therefore necessary to determine the tuple of displacement magnitudes,  $(u^{(2)}, u^{(3)}, u^{(4)})$ , that are optimal for determining the second-, third-, and fourth-order force constants, respectively. To do this, displacement patterns for cubic silicon were created for each order with  $\Delta u^{(i)}$  equal to 0.001 Å, 0.004 Å, 0.008 Å, 0.012 Å, 0.016 Å, and 0.020 Å for  $i = 2, 3, 4$ .

For each displacement pattern, the forces were computed using DFT in the manner described in section 3.3. The plane wave energy cutoff was 350 eV, and a  $3 \times 3 \times 3$   $\Gamma$ -centred k-point grid was used for the electronic integration. Self-consistency was deemed to be achieved at a difference in the energy of less than  $1 \times 10^{-8}$  eV between successive cycles. The Perdew-Berke-Ernzerhof exchange-correlation (XC) functional [75] was used and the so-called “Si” PAW-pseudopotential from the VASP library was used with the  $2s$  and  $2p$  orbitals as valence states (4 electrons per atom) [69]. Calculations were performed on a  $5 \times 5 \times 5$  supercell of the primitive unit cell containing 250 atoms.

Silicon has the so-called diamond structure, a face-centred cubic (fcc) lattice with atoms at  $\boldsymbol{\mu}_1 = (0, 0, 0)$  and  $\boldsymbol{\mu}_2 = (0.25, 0.25, 0.25)$  in the crystal basis. Only one displacement pattern is needed to determine all harmonic force constants in silicon (the atom at the origin displaced in the positive  $\boldsymbol{x}$  direction), 16 are needed for the cubic force constants, and 19 for the quartic, making 36 DFT calculations in total. These calculations were performed on a 64 core processor with a maximum and minimum computing time of 62 and 23 minutes per configuration and an average time of 47 minutes. The calculation time is determined primarily by the symmetry of the configuration, with high-symmetry harmonic and cubic configurations taking less time than the lower symmetry quartic configurations. The main limiting factor in the computation was memory availability; 64 GB of memory was required for the large supercell sizes.

A force constant model was fitted to the force–displacement data by least-squares fitting. The model considered all harmonic (two-atom) interactions in the 250 atom supercell, and cubic and quartic (three- and four-atom) interactions up to the second and first coordination shell, respectively. Two choices present themselves when fitting the force constant model; one may fit all orders of the model at the same time, or one may first fit the harmonic terms, then the cubic terms with harmonic terms fixed, and then the quartic terms with both harmonic and cubic terms fixed. Both methods were attempted and the results are presented in section 5.3.1.

## 5.2.2 Self-consistent phonons (silicon)

SCPH calculations were performed on silicon up to temperatures of 1000 K in increments of 100 K. Force constants up to fourth order were determined by the finite displacement method. The tuple of displacements  $(u^{(2)}, u^{(3)}, u^{(4)})$  described in section 5.2.1 was set to be  $(0.001 \text{ \AA}, 0.008 \text{ \AA}, 0.020 \text{ \AA})$ . The harmonic displacement is as low as possible to ensure that the potential is truly harmonic, the quartic displacement is chosen to match the mean square displacement at 1000 K, and the cubic displacement was chosen to minimise the fitting error. The force constants were fitted incrementally, starting with the harmonic force constants, then the cubic, then the quartic to ensure that each order of force constant did not pick up any contributions from higher orders. A full description of the reasoning behind these choices is presented later in section 5.3.1. The DFT

calculations were carried out in the manner described in the previous section

The SCPH calculations themselves were performed using an  $8 \times 8 \times 8$  k-point grid both to calculate the interaction coefficients (equation 3.104) and to solve the SCPH equation. The SCPH calculations converged sufficiently quickly that no interpolation was necessary, and the SCPH calculation could be solved on the dense grid directly. Considering the list of anharmonic phonon frequencies as a vector  $\mathbf{\Omega}$ , convergence was deemed to have been reached when  $\frac{1}{N}|\mathbf{\Omega}^{(i)} - \mathbf{\Omega}^{(i-1)}| < 1 \times 10^{-8}$  Ry, where  $N$  is the number of phonon modes and  $i$  is the iteration number.

At elevated temperatures, thermal expansion (generally) causes the interatomic spacing to increase and the phonon frequencies to change accordingly. This volume contribution to the phonon renormalisation was determined on the basis of experimental thermal expansion data from Okada and Tokumaru and Lyon *et al.* [84, 85], equation of state data from Anzellini *et al.* [86], and Raman data as a function of pressure from Weinstein and Piermarini [87]. Firstly, the thermal expansion data was integrated to determine a lattice parameter at an elevated temperature,

$$a(T) = a_0 \left[ \int_0^T \alpha(T') dT' + 1 \right] ; \quad (5.1)$$

secondly, the reported Vinet equation of state of Anzellini *et al.* was used to turn this volume fraction,  $\eta = \frac{V}{V_0}$ , into a pressure,

$$P(\eta) = 3B_0 \left( \frac{1 - \eta}{\eta^2} \right) e^{\frac{3}{2}(B'_0 - 1)(1 - \eta)} , \quad (5.2)$$

with  $B_0 = 101.5$  GPa and  $B'_0 = 3.43$ ; and finally a quadratic function fitted to the pressure–frequency data from Weinstein and Piermarini,

$$\frac{\omega(P)}{\omega_0} = \frac{(0.07 \text{ cm}^{-1}/\text{GPa}^2)P^2 + (5.2 \text{ cm}^{-1}/\text{GPa})P + 519.5 \text{ cm}^{-1}}{519.5 \text{ cm}^{-1}} , \quad (5.3)$$

was used to translate this pressure into a frequency, given a 0 K starting frequency  $\omega_0$  from the ALAMODE calculation.



### 5.2.3 Temperature-dependent effective potential

TDEP calculations were performed on silicon and diamond at 10 temperatures up to 1500 K. At each temperature, a number of displacement configurations must be generated by stochastically populating the phonon modes determined from a harmonic finite displacement calculation. Each configuration used a  $5 \times 5 \times 5$  supercell of the primitive unit cell with 250 atoms. Before performing a TDEP calculation one must first determine how many configurations are needed to achieve convergence of the phonon frequencies.

To establish this, 60 configurations were generated at 300 K, and DFT calculations were performed on each to determine the forces. A sample of size  $n$  was then drawn without replacement from these 60 configurations. Effective harmonic force constants were fitted to the displacements and forces from these  $n$  configurations, and the phonon frequencies were subsequently calculated. This process was repeated 30 times for each sample size  $n$ , and the standard deviation of the resulting 30 frequencies (for each band) was found to provide an estimate of the uncertainty in the phonon frequencies when  $n$  configurations are used.

Drawing a sample from the same 60 configurations each time reduced the computational expense considerably, but does introduce correlations between the samples as  $n$  becomes large; two samples of size  $n = 59$  will share 14,500 of the 14,750 force-displacement data (98%), and will therefore show very low amounts of scatter in the phonon frequencies regardless of the level of convergence. It was therefore decided to limit  $n$  to 30, so that on average only half of the data will be shared between any two samples. To completely eliminate the correlation between the samples would require an unfeasible number of DFT calculations to be performed. It was found in both silicon and diamond that 30 configurations were needed to achieve a scatter of less than  $1 \text{ cm}^{-1}$ , a result that was verified by splitting the 60 configurations into two and comparing the phonon frequencies from two completely independent samples, each of size  $n = 30$ .

30 configurations were therefore generated at each of the 10 temperatures up to 1500 K in both silicon and diamond. DFT calculations were performed for silicon on these configurations using the same parameters described in section 5.2.1, except that the k-point grid was replaced with a grid of the same density generated by the getKPoints utility for increased efficiency [88, 89]. At each temperature

effective harmonic force constants and the associated phonon frequencies were found; the correction from the three-phonon interaction was determined from the third-order force constants using the Kramers–Kronig relations. Calculations were this time performed using 128 cores and took approximately 30 minutes per configuration for silicon and, totalling 150 hours of computing time for all temperatures.

For diamond, a plane wave energy cutoff of 550 eV and a convergence criterion of  $1 \times 10^{-9}$  eV was used. The LDA XC functional was used and the “C” PAW-pseudopotential from the VASP library developed by G. Kresse, with 2s and 2p orbitals as the valence states (4 electrons), described the core regions of the potential [69]. Like with silicon, a  $5 \times 5 \times 5$  supercell of the primitive unit cell with 250 atoms was used for each configuration and a k-point grid from the getKPoints utility with a density equivalent to a  $5 \times 5 \times 5$  grid was used for the electronic integration [88, 89]. The diamond calculations were again calculated using 128 cores and took, on average, 41 minutes per configuration, totalling 205 hours of computing time.

The DFT calculations for TDEP must be done anew for each temperature. As such, unlike with the SCPH calculations, one may include the thermal expansion effects without incurring any additional computational cost. As DFT is a ground-state theory, the minimum-energy lattice parameter calculated by DFT excludes any expansion from the zero-point motion. An estimate of the experimental lattice parameter without zero-point expansion was found from thermal expansion data by extrapolating the linear (classical) regime to zero temperature. The ratio of the lattice parameters with and without zero point motion was then found ( $\frac{a_0^{ZP}}{a_0}$ ) and used to scale the minimum-energy lattice parameter from the DFT calculations to simulate the inclusion of the zero-point expansion. The thermal expansion data was then used to integrate this lattice parameter to finite temperatures. These lattice parameters were used for the TDEP calculations.

For silicon, the low-temperature thermal expansion data of Lyon *et al.* and the lattice parameter data of Okada and Tokumaru [84, 85] were used, and for diamond thermal expansion data from Jacobson and Stoupin [90] were used. Figure 5.1 shows in blue the extrapolation of the experimental linear regime to 0 K. The intercepts of the solid and dashed blue lines indicate the 0 K lattice parameter with and without zero-point expansion, respectively. The red lines in

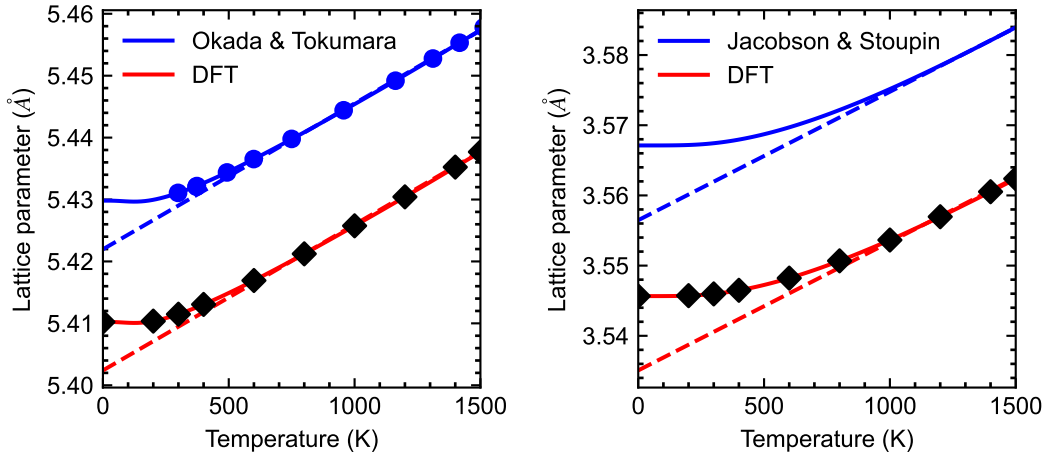


**Figure 5.1** *Lattice parameters for silicon (left) and diamond (right) from experimental data (blue) and an extrapolation of the linear regime to 0 K (dashed line). The red lines correspond to the blue lines scaled such that the intercept of the dashed red line is equal to the DFT minimum-energy lattice parameter. The black diamonds indicate the lattice parameters and temperatures at which the TDEP calculations were performed [84, 85, 90].*

figure 5.1 are (mathematically) similar to the blue lines, with the intercept of the dashed red line being the minimum-energy lattice parameter calculated from DFT. The black diamonds along the red line represent DFT lattice parameters inclusive of zero-point and thermal expansion.

## 5.3 Results

### 5.3.1 Silicon

The temperature dependence of the Raman signal was calculated both using the SCPH algorithm implemented by ALAMODE and by the TDEP formalism implemented by the code of the same name. In each case, the specifics of these calculations are reported and discussed to illustrate the reasoning behind the choices made and their effects. Finally, the results of the two approaches will be compared and recommendations made to readers interested in performing their own anharmonic phonon calculations.

#### Alamode

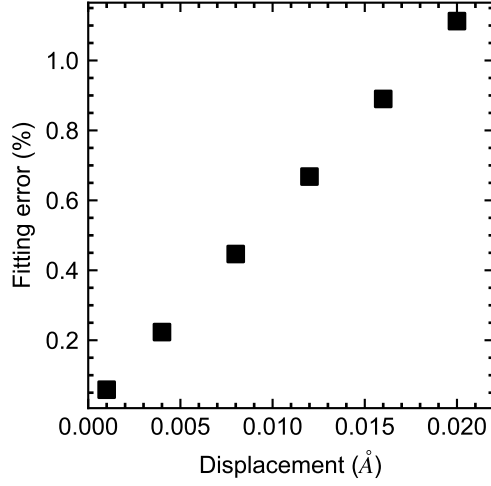
The process began with the displacement magnitude testing described in section 5.2.1. Each fit of the force constants to the force-displacement data from DFT calculations has an associated fitting error  $\sigma$  given by

$$\sigma = \sqrt{\frac{\sum_i (f_i^{\text{DFT}} - f_i^{\text{fit}})^2}{\sum_i (f_i^{\text{DFT}})^2}}. \quad (5.4)$$

This fitting error may be associated with fitting force constants of all orders simultaneously or incrementally, by fitting some particular order with lower orders held at fixed values. For the harmonic force constants there is, of course, no difference and the fitting error for the harmonic fitting at different displacements is shown in figure 5.2.

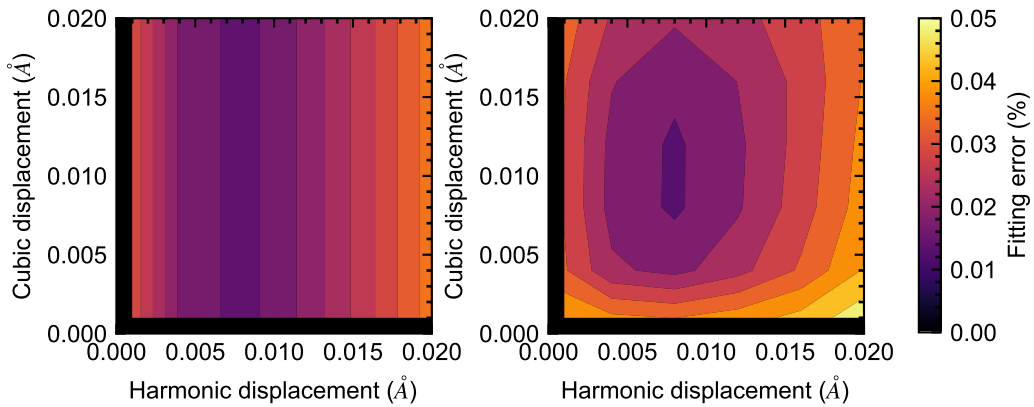
The fitting error is small — less than 1% — and increases linearly with increasing displacement magnitude, showing the deviation from the harmonic potential as atomic displacement increases. The small value of the fitting error indicates that, while there is some anharmonicity, silicon is overall modelled well by a harmonic model. To minimise the fitting error one must use the smallest displacement possible, where the atom is most firmly in the harmonic region of the potential and higher order terms have the smallest impact.

Figure 5.3 shows the fitting error from fitting the cubic force constant model to



**Figure 5.2** *Fitting error of the harmonic force constants in silicon as a function of displacement magnitude  $\Delta u^{(2)}$ .*

the forces and displacements, both by fitting harmonic and cubic terms together (left panel) and by fitting them incrementally (right panel). When both harmonic and cubic force constants are fitted simultaneously the fitting error is minimised when the harmonic displacement is 0.008 Å, but the cubic displacement has no influence on the fitting error. When the force constants are fitted incrementally, this is no longer the case. The minimum error still occurs when the harmonic displacement is 0.008 Å, but the cubic terms are now coupled to the harmonic displacement magnitude, and are minimised by a cubic displacement of 0.008 Å



**Figure 5.3** *Fitting error for the third-order force constants in silicon as a function of harmonic and cubic displacement magnitude ( $\Delta u^{(2)}$ ,  $\Delta u^{(3)}$ ) when they are fitted simultaneously (left) and incrementally (right).*

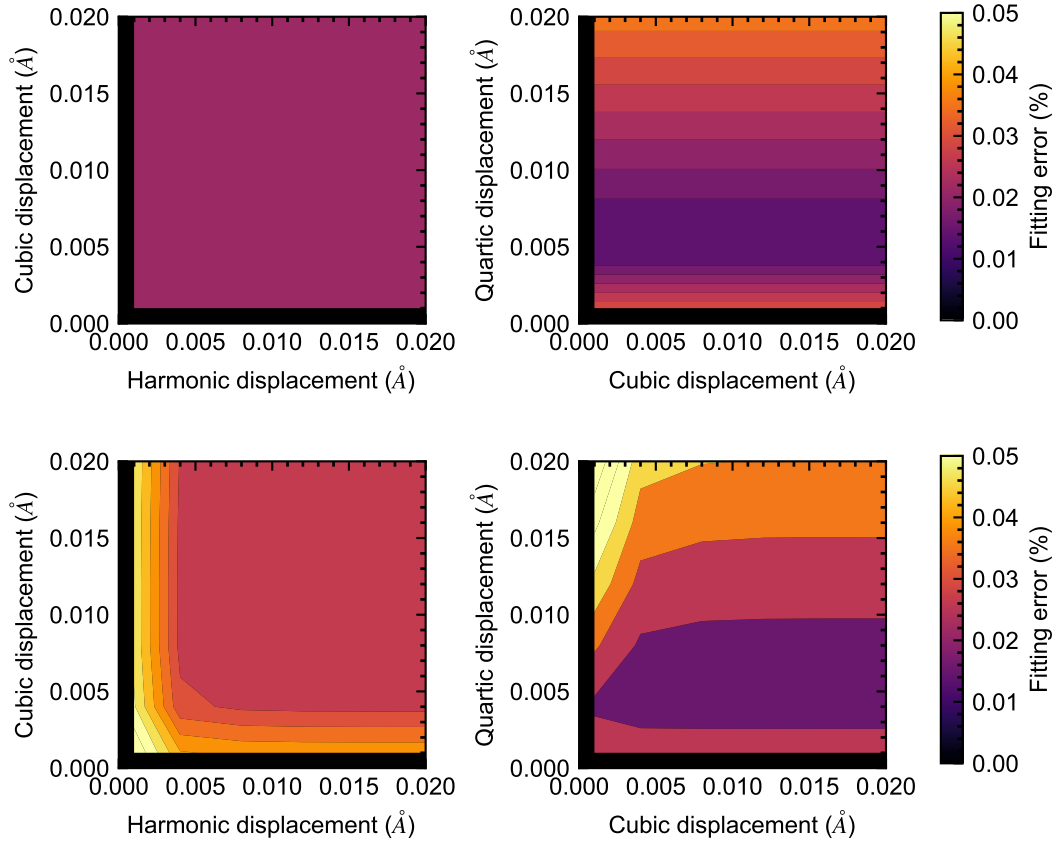


**Figure 5.4** *Slices through the displacement space  $(\Delta u^{(2)}, \Delta u^{(3)}, \Delta u^{(4)})$  for the fitting error of the fourth-order force constants in silicon when they are fitted simultaneously (top) and incrementally (bottom). Left-hand slices have fixed  $\Delta u^{(4)} = 0.012 \text{ \AA}$ , right-hand slices have fixed  $\Delta u^{(2)} = 0.008 \text{ \AA}$ .*

or  $0.012 \text{ \AA}$ .

It seems that, when fitting simultaneously, the harmonic and cubic force constants are correlated and can be adjusted together to produce an equally satisfactory fit for any value of the displacement magnitudes. When the freedom to fit both at once is removed, the cubic force constants can no longer adjust themselves so freely and a dependence on the cubic displacement is introduced. In other words, the harmonic and cubic force constants are correlated.

A similar story is present in the quartic force constants; when the cubic and quartic force constants are fitted simultaneously, the fitting error is minimised for a specific quartic displacement,  $0.004 \text{ \AA}$  (figure 5.4, top panels), but the cubic

displacement does not affect the fitting error, once again indicating that the third-order force constants allow the flexibility in the fit to minimise the fitting error regardless of the magnitude of the displacement. In this case, the harmonic and cubic force constants are completely uncorrelated.

When the force constants are fitted incrementally (figure 5.4, bottom panels), the cubic and quartic force constants are still largely decoupled, in that the cubic displacement does not have any effect on the fitting error. For all but the smallest displacements, the harmonic and cubic displacement magnitude may take any value without affecting the fitting error.

The conclusion of this, therefore, is that the cubic displacement magnitude may be chosen independently of the harmonic and quartic displacements, whether simultaneous or incremental fitting is used. The third-order terms would aim to fit the antisymmetric parts of the potential and therefore will not be affected by the choice of displacement for the symmetric harmonic and quartic terms. The flexibility in the fit provided by the simultaneous fitting is likely detrimental to establishing physically realistic force constants. More accurate force constants will be obtained by fitting the harmonic force constants first with the smallest possible displacement, as in figure 5.2. The quartic displacement should, on physical grounds, be larger than the harmonic and cubic ones; it should be large enough to sample the potential at the temperature(s) of interest, the quartic displacement should therefore be comparable to the root mean square displacement.

The recipe for choosing the displacement magnitudes without the kind of detailed investigation performed here is:

1. The harmonic displacement should be as small as possible without causing numerical issues.
2. The quartic displacement should be chosen to equal the root mean square displacement at the temperature of interest.
3. The cubic displacement is largely uncorrelated with the other two so should be chosen to lie somewhere in the middle of the harmonic and quartic displacements.

Since the investigation *was* done in the instance of silicon it was decided to use the

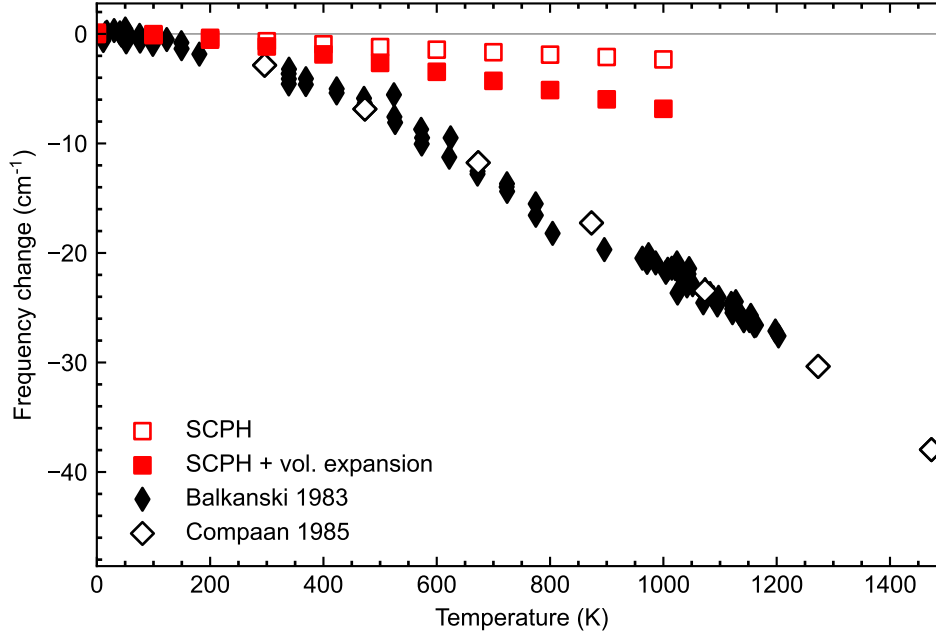


**Figure 5.5** *Temperature dependence of the  $\Gamma$ -point phonon frequency in silicon as a function of temperature calculated by the SCPH method. Filled and open black data are from Raman scattering experiments in references [92, 93].*

smallest possible displacement for the harmonic displacement,  $0.001 \text{ \AA}$ , a quartic displacement equal to the root mean square displacement at room temperature  $0.020 \text{ \AA}$  [91], and a cubic displacement between the two that minimised the fitting error,  $0.008 \text{ \AA}$ . The fitting was done incrementally to ensure that the higher order terms did not interfere with the fitting of the lower order terms, and to produce the most accurate force constants possible.

The temperature dependence of the zone-centre optical phonon calculated by the SCPH approach is shown in figure 5.5. The SCPH approach severely underestimates the phonon frequency renormalisation. At 1000 K the renormalisation from the pure anharmonic effects, without thermal expansion, is only around  $2 \text{ cm}^{-1}$ , compared to approximately  $22 \text{ cm}^{-1}$  observed in experiments. Including the thermal expansion contribution only accounts for a small additional amount, and is not enough to bring the calculated renormalisation close to the experimental value.

It will be argued later by comparison with the TDEP data, that this shortcoming



is due to the omission of 3-phonon effects and higher-order terms in the expansion of the self-energy. The fourth-order force constants being calculated incorrectly could cause an incorrect renormalisation of the phonons to be calculated, but the experiments show that there is a clear anharmonic contribution to the potential at 1000 K, which should be present in the quartic displacement patterns chosen to have a displacement matching the root mean square displacement at this temperature. The quartic force constants should therefore be adequately large to recreate this anharmonic potential. If anything, the quartic force constants may be overestimated due to the omission of terms higher than fourth order in the interatomic potential. This would cause the quartic force constants to include contributions from these other terms. Assuming the higher-order force constants act in the same way as the quartic force constants (to either stiffen or soften the potential), the inclusion of higher-order contributions in the quartic force constants will cause the magnitude of these quartic force constants to increase. Underestimation of the quartic force constants is therefore not thought to be the cause of the underestimation of the renormalisation.

## TDEP

Section 5.2.3 described the method used to determine the number of configurations needed to achieve convergence for a particular system. The standard deviations of the calculated phonon frequencies in silicon are shown in figure 5.6. From this figure it can be seen in the left panel that the  $\Gamma$ -point frequency has a larger scatter than the other points in the Brillouin zone, but at a sample size of 30 configurations the frequency is converged to  $\pm 1 \text{ cm}^{-1}$ ; the other points in the Brillouin zone are converged to well within  $\pm 0.4 \text{ cm}^{-1}$ .

The source of the increased scatter appears to be due to the longer wavelength of phonons in the centre of the Brillouin zone than those at the Brillouin zone boundary. The right panel of figure 5.6 shows the standard deviation decreases rapidly at a wavelength of  $0.2 \times 2a$ . This decrease occurs at the point where the supercell size becomes greater than half a wavelength. When the configurations are generated by populating modes in a supercell of dimension  $N$  in the direction of the phonon, a phonon at the Brillouin zone boundary will have  $\frac{N}{2}$  complete oscillations across the supercell, whereas a phonon close to the  $\Gamma$ -point will complete only a fraction of an oscillation, and therefore have a weaker signal

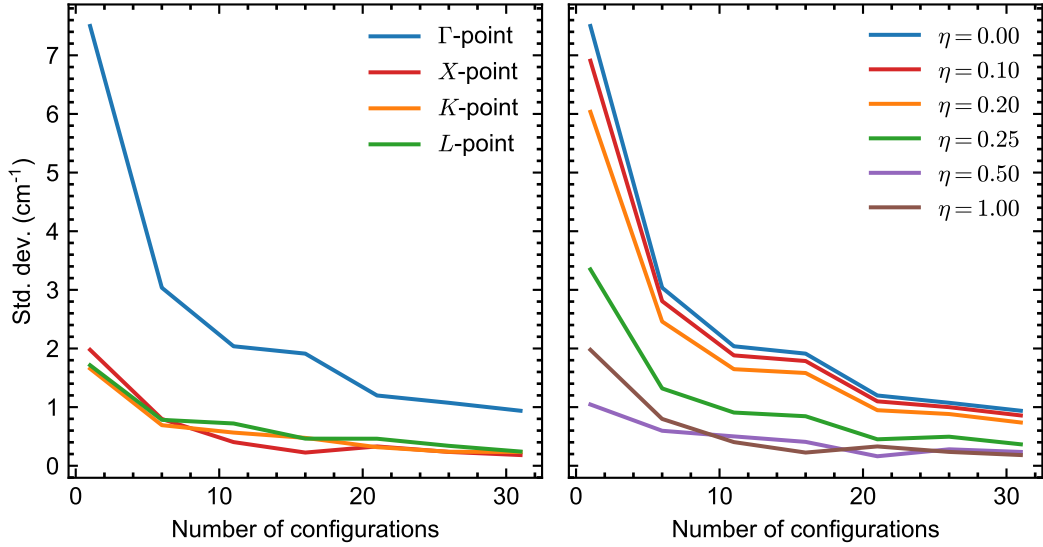


**Figure 5.6** Standard deviation of the phonon frequencies in silicon for different numbers of configurations used in the TDEP calculation. Left panel show special points in the Brillouin zone, right panel shows points along the  $\Gamma$ -X line  $\mathbf{k} = \frac{\pi}{a}(\eta, 0, 0)$ .

in the final displacement pattern.

To check the convergence was not due to the repetition of data between the different samples, the 60 configurations were split into two completely independent groups of 30 configurations each; the difference in the  $\Gamma$ -point frequency between the two groups was  $0.4 \text{ cm}^{-1}$ . The differences in the  $X$ -,  $K$ -, and  $L$ -point optical frequencies were  $0.5 \text{ cm}^{-1}$ ,  $0.6 \text{ cm}^{-1}$ , and  $0.5 \text{ cm}^{-1}$  respectively. On this basis, it can be said that the phonon frequencies are converged to within one wavenumber.

The temperature dependence of the  $\Gamma$ -point phonon frequency was then calculated using 30 configurations per temperature and a lattice parameter determined from the experimental data described in section 5.2.3. The result is shown in figure 5.7 with and without 3-phonon effects, along with the SCPH results. The TDEP calculations show much better agreement with the experimental data than the SCPH calculations, almost perfectly following the data of Compaa *et al.* and Balkanski *et al.* [92, 93].

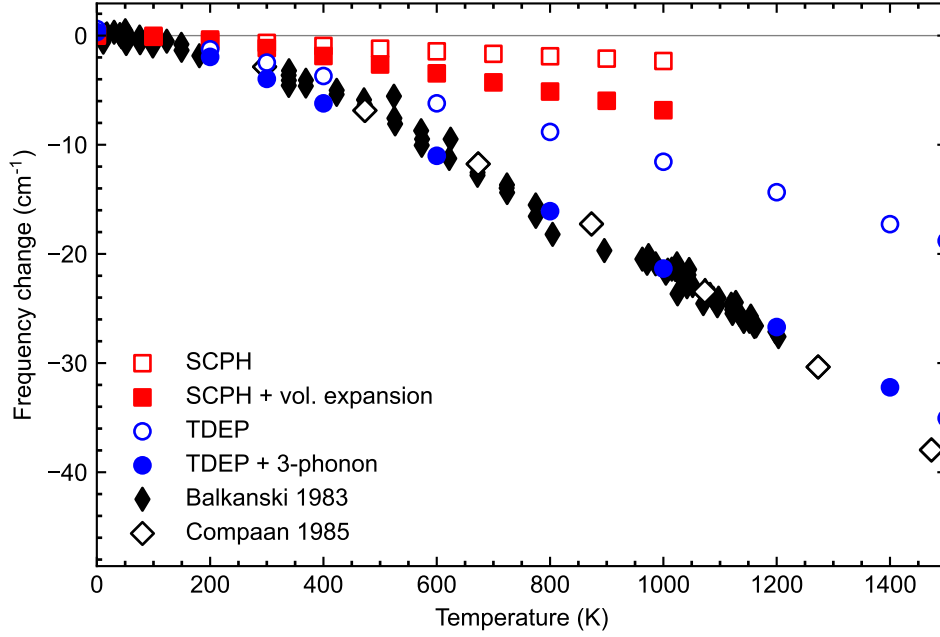


**Figure 5.7** *Temperature dependence of the  $\Gamma$ -point phonon frequency in silicon as a function of temperature calculated by both TDEP and the SCPH method. Both TDEP data include the thermal expansion from the data of references [84, 85]. Filled and open black data are from Raman scattering experiments in references [92, 93].*

The inclusion of the 3-phonon effects through the Kramers–Kronig relations is evidently important, and their omission from the SCPH calculations is likely to account for a large part of the underestimation of the renormalisation. The effect of thermal expansion (included in both TDEP results in figure 5.7) is also necessary to accurately reproduce the experimental temperature dependence of the zone-centre optical phonon frequency.

It is clear from figure 5.7 that TDEP is the better approach to take to accurately compute the anharmonic phonon frequencies in silicon. The success of ALAMODE in other materials such as strontium titanate and lead telluride may be due to the presence of anharmonicity strong enough to introduce significant effects from the 4-phonon interaction process, or simply due to a type of anharmonicity that happens to favour the 4-phonon process, since both 3- and 4-phonon processes are ostensibly same-order effects. It is not clear if it is possible to predict which systems would lend themselves well to the approach of ALAMODE, but perhaps

examining the density of states and making a Klemens-type assumption (where a phonon scatters into two or more phonons each with equal frequency) would be sufficient to predict whether a 4-phonon scattering process would have a strong influence.

The overwhelming success of TDEP and the comparatively poor performance of the SCPH approach suggests it is not practical to continue to use ALAMODE in its current form to calculate the anharmonic phonon frequencies. An attempt to extend the code to include the effect of the 3-phonon process was made and is described in section 5.4, but unfortunately the approach did not yield any useful results and had to be abandoned. Despite this setback, TDEP shows great promise in describing the behaviour of the phonons at elevated temperature. This suitability to the diamond-type semiconductors was next verified by applying the technique to diamond.

### 5.3.2 Diamond

The TDEP calculations were repeated for diamond, first verifying the convergence of the phonon frequencies with respect to the number of configurations. The standard deviation as a function of sample size is shown in figure 5.8. As before, the  $\Gamma$ -point shows a larger standard deviation than the other points in the Brillouin zone; again this is attributed to the long wavelength of the zone-centre phonons. The scale of convergence is similar to silicon in that the phonon frequencies are converged to within  $\pm 1 \text{ cm}^{-1}$ , although the zone-centre optical phonon frequency in diamond is over twice the zone-centre frequency in silicon —  $1332 \text{ cm}^{-1}$  compared to  $520 \text{ cm}^{-1}$  — resulting in a lower relative error. The 60 configurations were again split into two groups of 30 and the differences between the  $\Gamma$ -,  $X$ -,  $K$ -, and  $L$ -points were  $1.8 \text{ cm}^{-1}$ ,  $1.2 \text{ cm}^{-1}$ ,  $1.1 \text{ cm}^{-1}$  and  $1.5 \text{ cm}^{-1}$  respectively.

The overlap in data between different samples may have had a more pronounced effect in diamond than in silicon, or it may simply be that the two groups of 30 happened to have a difference in frequency that was more than a single standard deviation apart. With only two independent groups little can be said. Crucially, it may be noted from figure 5.8 that the standard deviation of the phonon frequencies is no longer decreasing significantly by 30 configurations, implying

that the limit of accuracy has been reached.

As with silicon, the temperature dependence of the zone-centre optical phonon was calculated and compared to experimental data. This comparison is shown with and without the 3-phonon interactions in figure 5.9. As before, the TDEP method of calculating anharmonic phonons accurately reproduces the experimental data when 3-phonon effects are included. The 3-phonon interaction process accounts for nearly half of the renormalisation at 1500 K. A full discussion of the various experiments used for comparison is deferred until chapter 7, where calculations of the  $\Gamma$ -point frequency are made at both high temperature and pressure. For now, it is sufficient to note that the TDEP calculations follow the majority of the experiments over the entire range of temperature shown.

It can therefore be said that TDEP works well to calculate the phonon frequencies in silicon and diamond, and reviewing the existing literature it can further be said that it is a method that works well across a range of different systems — both strongly and weakly anharmonic. Furthermore, the process undertaken here is

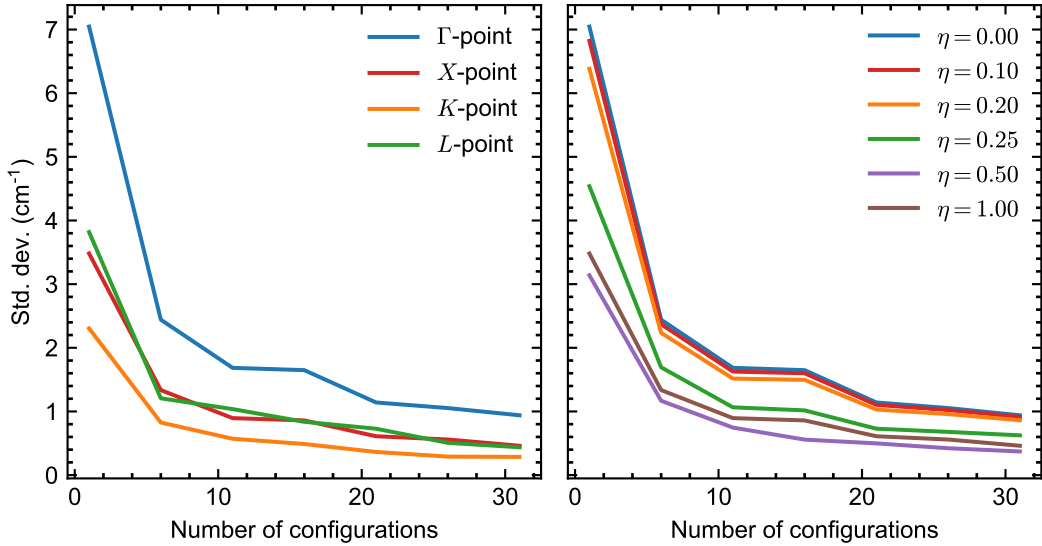


**Figure 5.8** *Standard deviation of the phonon frequencies in diamond for different numbers of configurations used in the TDEP calculation. The left panel shows special points in the Brillouin zone, the right panel shows points along the  $\Gamma$ -X line  $\mathbf{k} = \frac{\pi}{a}(\eta, 0, 0)$ .*

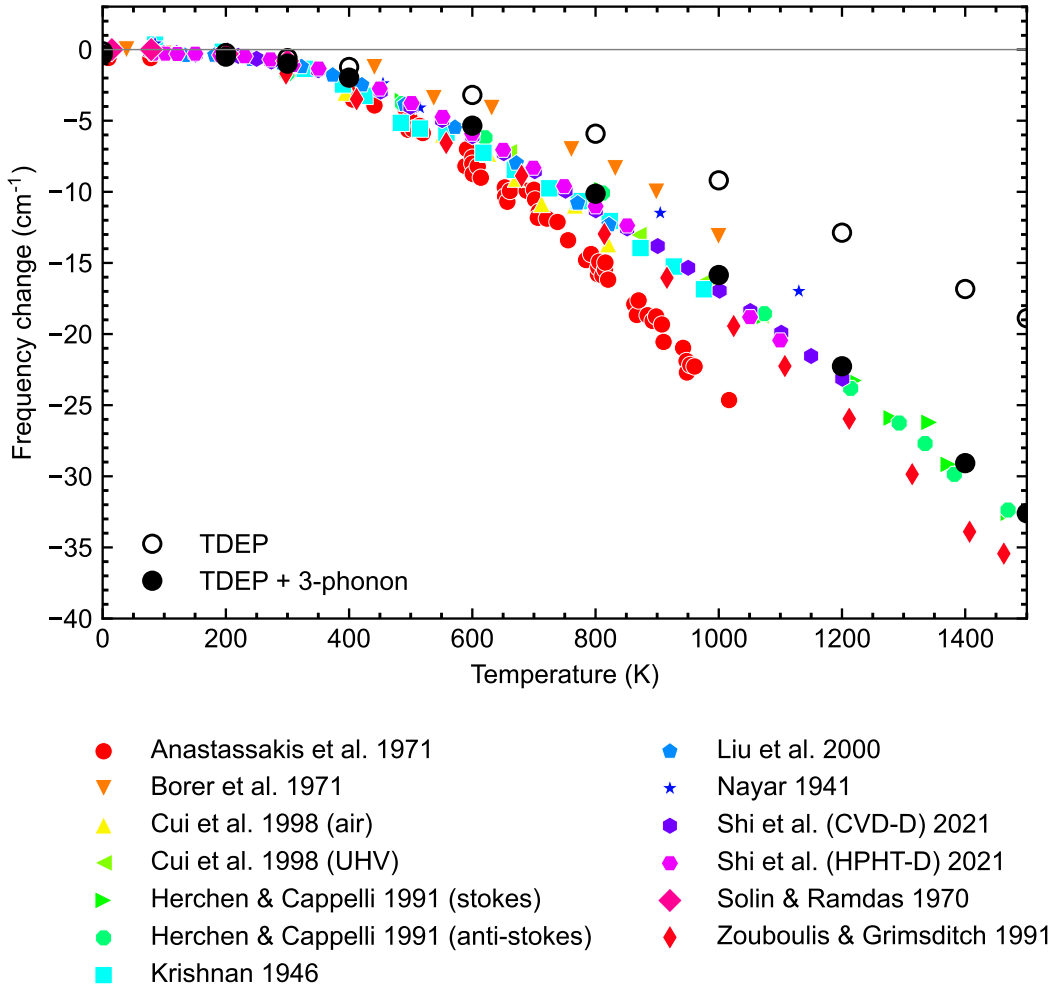


**Figure 5.9** *Temperature dependence of the  $\Gamma$ -point phonon frequency in diamond as a function of temperature calculated by TDEP. The effect of thermal expansion is included by choosing a different lattice parameter for each temperature. Experimental data are taken from references [94–103].*

robust, and can be applied easily to any system with little pre-existing knowledge required. In contrast, ALAMODE does not work well with the weakly anharmonic system of silicon, and the existing literature focusses primarily on the strongly anharmonic perovskite systems. For these systems it appears well suited, but the omission of 3-phonon effects makes it unsuitable for more weakly anharmonic systems such as the diamond-type semiconductors. If the 3-phonon interaction could be included, it could make ALAMODE a comparably successful method that would yield insight into the specific phonon–phonon interactions involved in the renormalisation.

## 5.4 Improvements to the self-consistent phonon method

The results of the previous section highlight the importance of the 3-phonon contribution to the renormalisation. On this basis, an attempt was made to include the effect of the bubble diagram in the SCPH algorithm that, regrettably, was not successful. Nevertheless, it shall be documented here for completeness and some comments on the reason for its failure will be made, as well as some thoughts on possible changes and difficulties that would need to be overcome to make it successful.

The SCPH algorithm in ALAMODE solves self-consistently the equation

$$V_{jj'}(\mathbf{k}, \omega) = \omega_{\mathbf{k}j}^{[h]} \delta_{jj'} - (2\omega_{\mathbf{k}j})^{\frac{1}{2}} (2\omega_{\mathbf{k}j'})^{\frac{1}{2}} \Sigma_{jj'}(\mathbf{k}, \omega) \quad (5.5)$$

on the irreducible points of a grid of k-points  $\mathbf{k}$ . The harmonic phonons  $\omega_{\mathbf{k}j}^{[h]}$  are renormalised by the self-energy  $\Sigma_{jj'}(\mathbf{k}, \omega)$ . When only the 4-phonon process (shown in the loop diagram on page 37 and in equation 3.107) is included, the self-energy does not have an explicit  $\omega$  dependence, and equation 5.5 is simplified as

$$V_{jj'}(\mathbf{k}) = \omega_{\mathbf{k}j}^{[h]} \delta_{jj'} - (2\omega_{\mathbf{k}j})^{\frac{1}{2}} (2\omega_{\mathbf{k}j'})^{\frac{1}{2}} \Sigma_{jj'}(\mathbf{k}) . \quad (5.6)$$

This equation must still be solved self-consistently as the self-energy depends on the anharmonic phonon frequencies, but the explicit  $\omega$  dependence has been removed.

The self-energy for the bubble diagram, which includes two 3-phonon processes, *does* depend explicitly on  $\omega$ ; the self-energy  $\Sigma_{jj'}(\mathbf{k}, \omega)$  describes a renormalisation that is dependent on the frequency of the phonon that is being renormalised. The attempted improvement to the SCPH algorithm relied on the principle that the SCPH equation may be solved mode-by-mode for a given k-point, and for each mode the frequency-dependent renormalisation could be accounted for. An improvement of this type would go beyond including just 3- and 4-phonon corrections, it would make it possible to include *any* frequency-dependent self-energy, theoretically allowing the inclusion of any interaction process.

The suggested update to the SCPH algorithm includes a second self-consistent

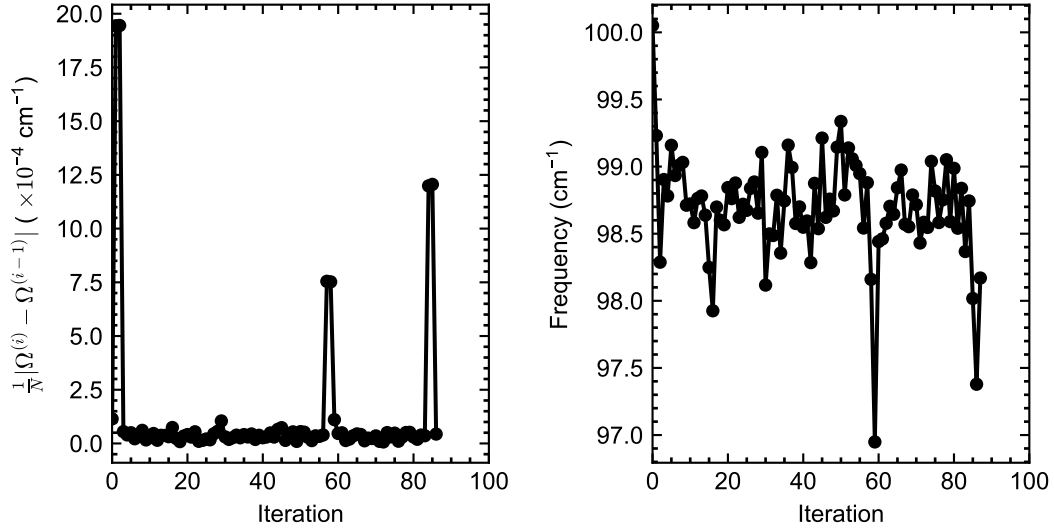


**Figure 5.10** *Convergence of the modified SCPH algorithm. The left panel shows the convergence criterion used in the outer self-consistent loop,  $\frac{1}{N} |\Omega^{(i)} - \Omega^{(i-1)}|$ , where  $\Omega$  is a vector of the renormalised frequencies. The right panel shows the frequency of a representative point in the Brillouin zone at each iteration. At the 88<sup>th</sup> iteration the algorithm returns not-a-number for one of the frequencies and stops.*

loop within the main loop to determine the self-energy at the frequency of the phonon in question. Step 11 of the method described on page 67 would be modified to include the frequency-dependent self-energy of the bubble diagram, and then steps 11 and 12 would be repeated until the square root of the eigenvalue of the matrix  $V_{jj'}(\mathbf{k}, \omega)$  (the anharmonic phonon frequency) was consistent with the frequency at which the self-energy was computed.

For reasons that are not fully clear, the above suggestion was not numerically stable; figure 5.10 shows the convergence of the new algorithm for some lead telluride sample data. The phonon frequencies do not tend towards convergence (as shown in the right panel of figure 5.10) and spikes in the convergence criterion can be seen in the left panel. The last spike seems to cause an instability that causes the algorithm to fail at the 88<sup>th</sup> iteration of the outer self-consistent loop. The inner self consistent loop, at any given iteration of the outer one and for any particular k-point and band, converges smoothly and in only a few iterations. This therefore suggests that the problem lies not in calculating the renormalisation of any particular k-point or band, but in assembling these



solutions into a complete set of phonon frequencies and eigenvectors. Some suggestions for why this should be the case are discussed below.

Although every effort was made to eliminate errors in the code, it cannot be ruled out that the numerical instability was simply due to a coding bug. However, there is some reason to think that the instability had more physical origins.

The eigenvectors of  $V_{jj'}(\mathbf{k}, \omega)$  describe the propagation of the anharmonic phonons and, as  $\Sigma_{jj'}(\mathbf{k}, \omega)$  is a Hermitian matrix, they are orthogonal. As the self-energy matrix is different for each  $\omega = \omega_{\mathbf{k}j}$ , the eigenvectors of  $V_{jj'}(\mathbf{k}, \omega)$  will be different also at each  $\omega$ . Therefore, when the self-energy is evaluated at different  $\omega$ , different sets of orthogonal eigenvectors will be found for each band. However, the eigenvector for anharmonic phonon  $j = 1$  will not necessarily be orthogonal to the eigenvector for the anharmonic phonon  $j = 2$ , and so on, resulting in a set of phonon eigenvectors that are not orthogonal.

Whether this poses a problem is not clear. Certainly it would require extending the algorithm further to deal with non-orthogonal eigenvectors, most likely through the introduction of an overlap matrix, but this is perhaps not impossible. Another question is the physical meaning of the non-orthogonal eigenvectors, since orthogonal eigenvectors arise from Hermitian operators, which represent physical observables. Would the phonon frequencies have any physical meaning if they were calculated in this way?

One other possibility for the instability of the algorithm is that a simple self-consistent cycle is not sufficient to find the solution to equation 5.5. A mixing parameter was introduced in an attempt to eliminate instability, but did not have the desired effect. The possibility remains that a more sophisticated root-finding algorithm may produce better results for the inner self-consistent loop.

Finally, there is the question of whether having an inner and outer self-consistent loop is sensible. When the update is split into the inner loop and the outer loop, the determination of the frequency at which to evaluate the self-energy and the update of the interaction coefficients are performed separately. It would be possible to perform both these operations at once. This was mimicked by setting the maximum number of iterations of the inner loop to one, but unfortunately this did not stabilise the algorithm.

Much of this section is speculative, but some things can be stated with certainty. The calculation of the bubble self-energy was implemented correctly. The expression for the bubble self-energy was carefully derived and reported in section 3.2; it was noticed that the expression in the paper detailing the original implementation of ALAMODE did not match that reported by Reissland [2, 62]. The expression reported in section 3.2 shows the correct symmetries and matches what is reported by Reissland, so is believed to be correct. Furthermore, the algorithm shows the expected behaviour when only the loop self-energy is considered. In this case, the inner self-consistent loop converges immediately, as one would expect from a self-energy that does not have a frequency dependence, and the results of each iteration of the outer loop exactly match that of the original algorithm.

It remains to be seen whether this approach can prove fruitful. It is the opinion of this author that further development of the method is worthwhile, although, due to time constraints and stalling progress, the decision was made to abandon the project. Nevertheless, some suggested next steps for the project are:

- Further investigate the non-orthogonality of the eigenvectors and attempt to account for this through the introduction of the overlap matrix.
- Try other, more sophisticated root finding methods for the inner self-consistent loop.
- Re-structure the code to allow for more targeted testing of each part. This would help eliminate bugs and coding errors; the code currently cannot easily be supplied with dummy data and despite significant changes already made, data is not encapsulated well in the current implementation.

It is sincerely hoped that these suggestions could produce a working algorithm that includes the bubble (and higher-order) self-energy contributions, but, in the interest of securing results, the rest of this thesis will focus on the TDEP method of computing anharmonic frequencies.

# Chapter 6

## Diamond and the quantum isotope effect

### 6.1 Background

Isotopic mass is known to affect the properties of a material. The differences exhibited under isotopic substitution may be used to assess the validity of a theoretical model that has some dependence on the atomic mass. Many of these differences occur due to changes in the phonon frequencies. Properties such as the heat capacity, thermal expansion, and thermal conductivity depend on the phonon dispersion, and changes in the phonon frequencies due to isotopic substitution will alter these properties also. Here, the change in the phonon frequencies and the dependent change in the atomic volume in diamond (carbon) will be studied. The change in the phonon frequencies arises simply from the dependence of an oscillator's frequency on its mass; the ensuing volume change arises from the change in the thermal pressure that comes from this change in the phonon frequencies. The exact nature of the isotope effect depends on the form of the interatomic potential.

There are two stable isotopes of carbon,  $^{12}\text{C}$  and  $^{13}\text{C}$ , with a mass ratio of 1.0836. A  $^{12}\text{C}$  diamond crystal contains lighter nuclei and therefore has the higher phonon frequency. The harmonic phonon theory in section [3.1.4](#) describes the harmonic phonon frequency to be inversely proportional to the square root of the mass

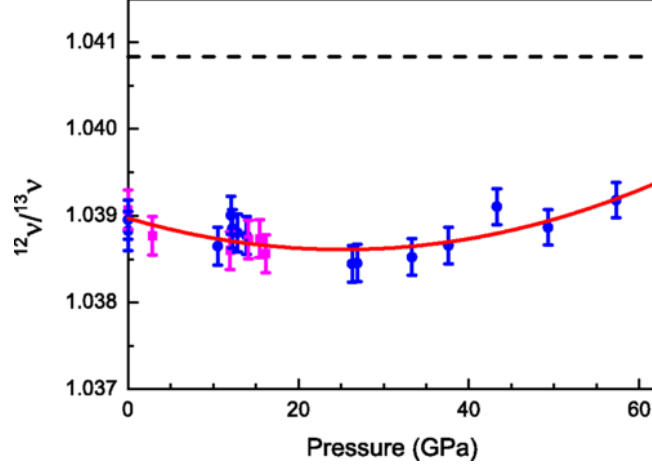


**Figure 6.1** Ratio of the  $^{12}\text{C}$  to  $^{13}\text{C}$  Raman frequencies ( $\frac{^{12}\nu}{^{13}\nu}$ ) of isotopically pure  $^{12}\text{C}$  and  $^{13}\text{C}$  diamond as a function of pressure as measured by Enkovich *et al.* [105]. Data are calculated from Raman measurements of a sample of each isotope placed in the same DAC. Blue data are taken at 300 K, pink data are collected at 80 K, the red curve is a quadratic fit to the data, the harmonic ratio is indicated by the dashed line. Figure reproduced from [105].

of the nuclei ( $\omega \sim m^{-\frac{1}{2}}$ ). The harmonic theory therefore predicts the ratio of the phonon frequencies in  $^{12}\text{C}$  and  $^{13}\text{C}$  diamond to be exactly  $\frac{\omega_{12}}{\omega_{13}} = \sqrt{\frac{m_{13}}{m_{12}}} = \sqrt{\frac{13.003355}{12.0}} = 1.040967299\dots$  at all temperatures and pressures. Deviation from this harmonic ratio is indicative of anharmonicity in the interatomic potential.

Attempts to measure this frequency ratio at high pressure have been made, but there is little agreement in the literature as to its behaviour. Muinov, Kanda, and Stishov performed experiments on natural diamond and isotopically enriched  $^{13}\text{C}$  diamond (up to 9%  $^{13}\text{C}$ ) up to 14 GPa and observed a decrease in the frequency ratio from the zero-pressure value [104]. A later study was performed by Enkovich *et al.* in 2016 [105]. The data, shown in figure 6.1, were much more extensive, but show unusual behaviour in the frequency ratio on increasing pressure. The authors report a minimum in the phonon frequency ratio at  $\approx 22$  GPa. Such a minimum would indicate a non-trivial dependence of the anharmonic parts of the interatomic potential on pressure. This unusual behaviour was attributed to quantum effects.

Unusual behaviour at high pressure in the *volume* isotope effect has also been observed by Fujihisa *et al.* [106]. These authors observed that, at high pressure, the  $^{12}\text{C}$  diamond had a smaller atomic volume than the  $^{13}\text{C}$  diamond, in

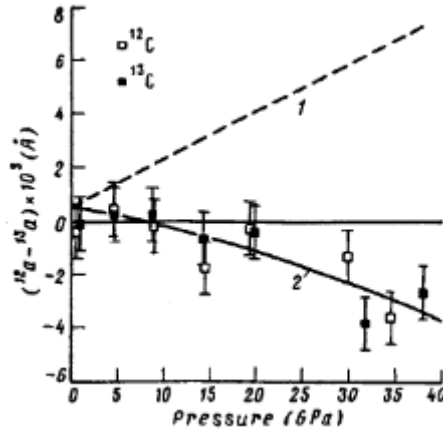


**Figure 6.2** *Difference in the lattice parameters for isotopically pure  $^{12}\text{C}$  and  $^{13}\text{C}$  diamond measured by Fujihisa et al. [106]. At zero pressure it is expected that the  $^{12}\text{C}$  diamond will have the larger volume. The dashed line (1) represents a prediction made by reference [104]. The solid line (2) is the difference between the fitted equations of state to the pressure–volume data. Filled and open circles indicate the difference between the experimental  $^{12}\text{C}$  points and the  $^{13}\text{C}$  equation of state and vice-versa. Figure reproduced from [106].*

opposition to what has been observed at ambient pressure, as well as what one would expect in the simple harmonic (or quasiharmonic) picture (see figure 6.2). This so-called inversion of the quantum isotope effect<sup>1</sup> was attributed to non-trivial behaviour of the quantum contribution to the lattice constants [106].

Beyond these studies, the majority of the existing research into isotope effects in diamond is focussed on isotopically mixed crystals. This is only tangentially related to the study at hand; many of the effects and processes involving isotopic disorder will not be observed in the isotopically pure crystals. Nevertheless, these studies offer insight into the behaviour of the pure crystals as the limiting case of a mixed crystal. The general case of isotopically mixed diamond will not be discussed in depth here, but the interested reader is directed to the review articles [108, 109].

<sup>1</sup>The isotope effect is dubbed quantum as, at low temperatures, it arises from the zero-point motion of the atoms [107].

## Frequency isotope effect

The aforementioned study of Enkovich *et al.* is distinguished from other studies by the inclusion of both  $^{12}\text{C}$  and  $^{13}\text{C}$  samples in the same diamond anvil cell (DAC) [105]. A chip of each isotope was placed in the DAC along with a helium pressure-transmitting medium and a chip of ruby. The DAC was pressurised, and the Raman spectrum of each sample was measured with a laser sufficiently focussed to measure each sample separately. This ensured that the two samples were at the same pressure (except for any pressure gradients within the sample chamber), allowing the authors to directly compare frequencies at a common pressure and compute a frequency ratio that was unaffected by uncertainty in the pressure calibration. Pressure gradients in the DAC were minimised, as helium was used as the pressure-transmitting medium. Helium is known to be the best pressure-transmitting medium, yet only remains truly hydrostatic up to  $\approx 20$  GPa [110]. Above this pressure a small amount of non-hydrostaticity is introduced, though significantly less than any other pressure-transmitting medium. Although 20 GPa is approximately the same pressure as the turnover in Enkovich's data, non-hydrostatic effects are not likely to be the cause of the turnover, as these effects are small in helium and other sources of uncertainty dominate the measured frequency ratio.

Difficulties distinguishing the sample Raman signal from the signal of the diamond anvils created pressure ranges where the Raman frequency was unable to be determined. Inspection of figure 6.1 shows the two lacunae to be between 3 GPa and 10 GPa, where the  $^{12}\text{C}$  signal could not be distinguished, and between 16 GPa and 25 GPa, where the  $^{13}\text{C}$  signal could not be distinguished. Outside these regions it was possible to determine the Raman frequencies of each isotope against the anvil background, and the ratio can therefore be confidently reported.

Aside from the high-pressure data of Enkovich *et al.*, measurements have been made of the frequency ratio at ambient pressure. A summary of the experimental data and theoretical predictions of the frequency ratio are shown in figure 6.3. Chrenko measured the Raman spectra of five synthetic diamonds with an isotopic composition ranging from 1.1% to 89%  $^{13}\text{C}$  [111]. Chrenko extrapolated the Raman frequency of these isotopically mixed crystals to their pure form and stated Raman frequencies of  $1333\text{ cm}^{-1}$  and  $1280\text{ cm}^{-1}$  for  $^{12}\text{C}$  and  $^{13}\text{C}$  respectively. This gives a frequency ratio of 1.041406. This is higher than the 1.040967... expected

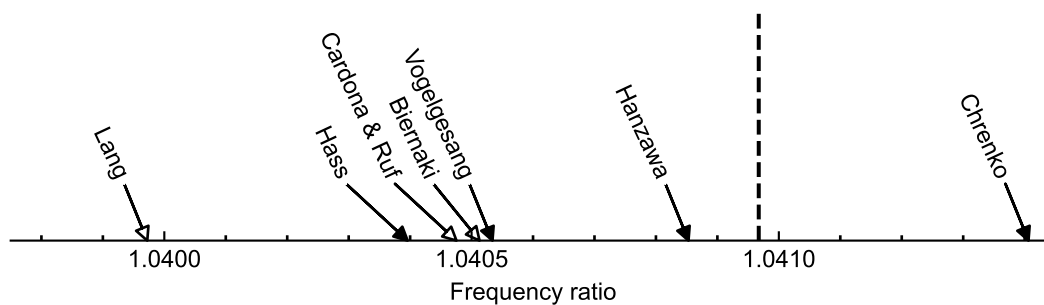


**Figure 6.3** Existing zero-pressure experimental data (solid arrowheads) and theoretical predictions (open arrowheads) of the frequency ratio in diamond. Data from [111–116]. The dashed black line represents the harmonic ratio.

from harmonic theory, a point which is not commented on by Chrenko due to the frequencies not being stated to sufficient accuracy. They are only reported to the nearest wavenumber; greater precision is required to determine the frequency ratio to a satisfactory precision.

The harmonic approximation can be used to make an estimate of the precision in the Raman frequencies required to accurately determine the frequency ratio. Assuming the  $^{12}\text{C}$  Raman frequency to be exactly  $1332\text{ cm}^{-1}$ , the  $^{13}\text{C}$  Raman frequency must be  $1279.579\text{ cm}^{-1}$ . An uncertainty on these figures of  $\pm 1\text{ cm}^{-1}$  results in an uncertainty in the frequency ratio of  $\pm 0.001$ . If the Raman frequencies are measured to a precision of  $\pm 0.1\text{ cm}^{-1}$  then this uncertainty in the ratio is reduced to  $\pm 0.0001$ . Examining figure 6.3 shows that if the Raman frequencies are reported only to the nearest wavenumber, then the harmonic ratio (and most other measurements) are within error. It can therefore be said that for an acceptably precise determination of the frequency ratio, the Raman frequencies should be determined to  $\pm 0.1\text{ cm}^{-1}$  or better.

Hass *et al.* performed a similar experiment to Chrenko with a larger range of isotopic compositions [112]. The authors again used five diamonds: one natural, one purified  $^{12}\text{C}$ , and three enriched with  $^{13}\text{C}$  to varying degrees. The highest concentration of  $^{13}\text{C}$  was 98.99%. The frequency–composition curve the authors report is the product of a force constant model and extensive numerical calculations, and is therefore not trivial to extrapolate to the pure crystals. However, their data were revisited by Vogelgesang *et al.* [113] who, with additional

data for natural diamond, fitted a polynomial,

$$\omega(x) = 1332.82 - 34.77x - 16.98x^2, \quad (6.1)$$

to Hass's data, where  $x$  is the fraction of  $^{13}\text{C}$  isotope. The frequency ratio found from the  $x = 0$  and  $x = 1$  values of this polynomial is 1.040396.

Vogelgesang and co-workers go beyond this and apply a theoretical model of an interatomic potential that contains a harmonic and cubic contribution to the bond stretching and to the bond bending [113]. In the end, the anharmonic bending terms cancel exactly. Applying this model to their own data, the authors alter slightly the extrapolation to the isotopically pure  $^{13}\text{C}$  crystal, and predict a frequency ratio of 1.040534. From this, and comparing with figure 6.3, one can start to see some agreement in the experimental data.

Hanzawa *et al.* also report a polynomial to describe the dependence of the Raman frequency on isotopic composition, however this polynomial was fixed to assume an exactly harmonic ratio of the Raman frequencies in the limiting case of the isotopically pure crystals [114]. Nevertheless, these authors report that the difference in frequency between their highest and lowest  $^{13}\text{C}$  concentrations (1.1% and 99%) was  $52.3 \text{ cm}^{-1}$ . The reported Raman frequency of the natural diamond crystal was  $1332.5 \text{ cm}^{-1}$ , which implies a frequency ratio for the highest and lowest  $^{13}\text{C}$  concentrations of 1.040853, only slightly below the harmonic ratio, and the values calculated from Hass's and Vogelgesang's data.

The fact that this is higher than most of the other reported values means that there must be some uncertainty in the data; it cannot be due to the fact that the data has not been extrapolated to the isotopically pure crystals. Given that the Raman frequency decreases monotonically as a function of the fraction of  $^{13}\text{C}$  isotope, a small amount of  $^{13}\text{C}$  impurity in the  $^{12}\text{C}$  crystal will lower the  $\omega_{12}$  Raman frequency, and a small amount of  $^{12}\text{C}$  impurity in the  $^{13}\text{C}$  crystal will raise the  $\omega_{13}$  Raman frequency. Any combination of these two effects will serve to lower the frequency ratio  $\frac{\omega_{12}}{\omega_{13}}$ .

Theoretical studies have also been made. From the phonon self-energy, considering only 3-phonon effects, Cardona and Ruf suggest that the renormalisation (the depression of the phonon frequency relative to the harmonic value) due to zero-point effects varies in proportion to  $M^{-1}$ , where  $M$  is the atomic



mass, and has been found to be  $16\text{ cm}^{-1}$  for natural diamond [115]. Assuming a renormalised phonon frequency of  $1332\text{ cm}^{-1}$  for  $^{12}\text{C}$ , this implies harmonic (non-renormalised) frequencies of  $1348.0\text{ cm}^{-1}$  for  $^{12}\text{C}$  and  $1294.9\text{ cm}^{-1}$  for  $^{13}\text{C}$ . The renormalised frequency for  $^{13}\text{C}$  is therefore  $1280.2\text{ cm}^{-1}$ , giving a frequency ratio of 1.040475. Lang *et al.* also suggest an  $M^{-1}$  dependence on the basis of density functional perturbation theory (DFPT) + frozen-phonon calculations [116]. Their calculations suggest a frequency ratio of 1.0399723. This difference in the ratio arises from Cardona and Ruf stating the renormalisation of natural diamond to be almost half what is stated by Lang *et al.*:  $16\text{ cm}^{-1}$  compared to  $31.6\text{ cm}^{-1}$ . This directly demonstrates that increasing anharmonic effects cause a greater deviation from the harmonic frequency ratio.

Biernaki studied the isotope effect in mixed crystals using a tight-binding model that used different force constants for  $^{12}\text{C}$ – $^{13}\text{C}$ ,  $^{12}\text{C}$ – $^{12}\text{C}$ , and  $^{13}\text{C}$ – $^{13}\text{C}$  bonds [117]. The tight-binding model had only a single free parameter to be fitted to experiment, the value of which is the same for the entire row of the periodic table and therefore is the same for both isotopes. The mass dependence is introduced through the Helmholtz free energy in a manner which is similar to the quasiharmonic calculations that will be presented later. The ratio of the  $^{12}\text{C}$ – $^{12}\text{C}$  and  $^{13}\text{C}$ – $^{13}\text{C}$  bond frequencies was calculated to be 1.040512, in agreement with the values from Hass’s data, as well as the self-energy argument made by Cardona and Ruf [112, 113, 115].

Path integral Monte Carlo (PIMC) simulations performed by Herrero employed a Tersoff potential to describe the interatomic potential in diamond, and produced good agreement with experimental data [118]. Herrero reports the ratio of the *total* vibrational energies per simulation cell (not just the zone-centre phonon but all vibrations) to be 1.039. This is lower than the values for the zone-centre phonon frequency ratio determined from Raman measurements and possibly indicates that the average frequency ratio across all phonons is lower than the ratio of the zone-centre optical phonon, and that the zone-centre phonon is particularly harmonic compared to other phonons in the Brillouin zone.

	$^{12}\text{C}$ (Å)	$^{13}\text{C}$ (Å)	Volume difference (Å <sup>3</sup> /atom)
Holloway <i>et al.</i> [119]	3.567 15(5)	3.566 62(5)	$2.528\,630(15) \times 10^{-3}$
Yamanaka <i>et al.</i> [120]	3.567 12(5)	3.566 59(7)	$2.528\,588(17) \times 10^{-3}$
Shikata <i>et al.</i> [121]	3.567 135(15)	3.566 658(17)	$2.275\,782(5) \times 10^{-3}$

**Table 6.1** Lattice parameters of  $^{12}\text{C}$  and  $^{13}\text{C}$  from different experimental studies.

## Volume isotope effects

In addition to the already mentioned study by Fujihisa *et al.*, which predicted an inversion of the isotope effect at high pressure, other authors have measured the change in the lattice parameter of diamond under isotopic substitution. Most of these studies have been at ambient pressure, with only a few at high pressure. The results of the zero-pressure measurements are shown in table 6.1.

As with the frequency isotope effect, much of the existing research is focussed on isotopically mixed crystals. Both Holloway *et al.* and Yamanaka *et al.* performed x-ray diffraction measurements on isotopically mixed crystals to determine the lattice parameter [119, 120]. Whereas Holloway *et al.* report a linear dependence of the lattice parameter on the fraction of  $^{13}\text{C}$  in the sample, Yamanaka *et al.* observed a curvature in their data (see figure 6.4). Yamanaka *et al.* point out that a linear relationship is unlikely as the two isotopes have different bulk moduli and Grüneisen parameters. Both of these quantities depend on the phonon frequencies, which vary non-linearly with isotope concentration. Yamanaka and Morimoto later revisited the question and attributed the non-linearity both to anharmonic phonon effects and differences in the valence electron density arising from electron–phonon coupling [122].

The effect of sample quality on the lattice parameter was investigated by Shikata *et al.* [121]. Various diamond samples were synthesised using different methods and their lattice parameters precisely measured. It was found that, with the exception of the doped samples and the  $^{13}\text{C}$  crystal, the lattice parameter was unchanged by the method of synthesis to within the error from the x-ray diffraction experiments. Poor sample synthesis is insufficient to account for the linear relation observed by Holloway *et al.* Isotopically mixed crystals (beyond the natural composition) were not considered, so no conclusions can be drawn on the

effect of uncertainty in the isotope fraction on the lattice parameter, although the isotope fraction would have to be very poorly determined to accidentally obtain a linear relation like Holloway *et al.*, and can therefore be discounted as its origin. However, it is interesting to note that Yamanaka *et al.* characterised their samples using a mass spectrometer, whereas Holloway *et al.* state that “uncertainties in composition are quite negligible by comparison with those arising from the measurements of lattice constant” [119].

Fujihiya *et al.* are the only authors to directly measure the volume isotope effect at high pressure. Other insights into its possible behaviour come from Gillet *et al.* [123], who measured the equation of state of both isotopes at high pressure; and indirect volume determinations from Enkovich *et al.* using their measured Raman frequencies and a Grüneisen model,  $\frac{V}{V_0} = \left(\frac{\omega}{\omega_0}\right)^{-0.97}$ , to determine the volume [105].

Gillet *et al.* reported tabulated volumes at high pressure for both isotopes along with fitted parameters for a Birch–Murnaghan equation of state. By finding the difference between the reported volumes of one isotope and the volume computed from the equation of state of the other, a volume difference can be found from Gillet’s data. Note that this is beyond what is attempted by the authors.

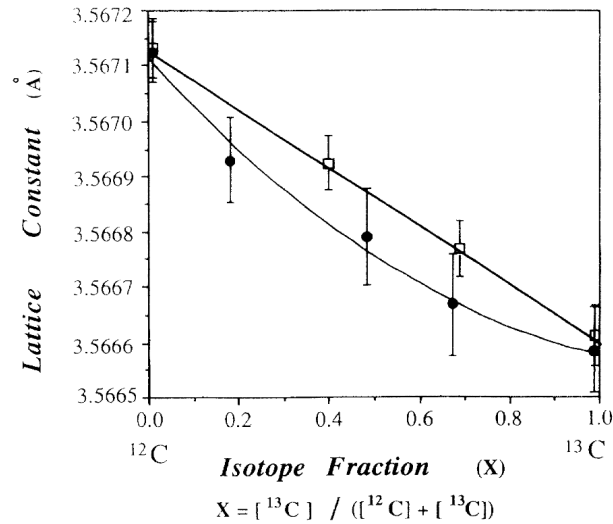


**Figure 6.4** Lattice constant of diamond with isotope concentration. Hollow squares are the data of Holloway *et al.* [119] and solid circles are the data of Yamanaka *et al.* [120]. Figure reproduced from reference [120].

This process relies on an equation of state to compute the volume difference between the isotopes at a common pressure. Gillet *et al.* reported several sets of parameters to the Birch–Murnaghan equation of state for the different isotopes and pressure-transmitting media, but the exact method used to perform the fitting is not clear. The authors state that “ $V(P)$  data . . . were fitted to a Birch–Murnaghan equation of state”, but the Birch–Murnaghan equation of state is a  $P(V)$  function that cannot be analytically inverted. Gillet *et al.*’s data were re-analysed by attempting to fit the  $V(P)$  data to a Birch–Murnaghan equation of state using numerical inversion. Unfortunately, this proved to be unstable and no reliable parameters could be found. An ordinary least-squares fit to the  $P(V)$  Birch–Murnaghan equation of state, using the errors in the unit cell volume as weights, was also performed, but the ensuing parameters did not match the values reported by Gillet *et al.* The authors also talk of “. . . taking into account the uncertainties in both pressures and cell volumes”, something which is not possible in ordinary least-squares fitting. To do this, something akin to orthogonal distance regression (ODR) is required.

The equation of state parameters reported by Gillet *et al.* along with the parameters found in the re-analysis are shown in table 6.2. The ordinary least-squares and the ODR fits omitted three data points from the tabulated values in reference [123]. These were two points that had been omitted from the author’s  $P$ – $V$  graph, suggesting them to be outliers — the highest pressure of the  $^{12}\text{C}$ ,  $\text{N}_2$  data set and the highest pressure of the  $^{13}\text{C}$ , Ar data set — and data at 0.46 GPa of the  $^{12}\text{C}$  methanol-ethanol-water (MEW) data set, where there is a typographical error. Including or amending these points did not cause the equation of state parameters from the re-analysis to match those reported by Gillet *et al.*

<sup>12</sup> C	Parameter	MEW data	N <sub>2</sub> data	Whole data set
Gillet <i>et al.</i> [123]	$V_0$ (Å <sup>3</sup> )	45.416(4)	45.414(4)	45.413(5)
	$B_0$ (GPa)	436(7)	445(7)	447(6)
	$B'_0$	6.5(2.9)	4 (fixed)	4 (fixed)
				5.3(1.6)
				4 (fixed)
				45.418(2)
				445(1)
				4 (fixed)
				1.4(0.4)
Ordinary least-squares	$V_0$ (Å <sup>3</sup> )	45.402(4)	45.410(2)	45.413(2)
	$B_0$ (GPa)	466(5)	452(1)	445(1)
	$B'_0$	2.1(0.7)	4 (fixed)	4 (fixed)
				45.402(3)
				469(4)
				4 (fixed)
				45.418(2)
				445(1)
				4 (fixed)
Orthogonal distance regression	$V_0$ (Å <sup>3</sup> )	45.413(3)	45.409(2)	45.413(2)
	$B_0$ (GPa)	439(8)	451(3)	447(2)
	$B'_0$	6.5(1.6)	4 (fixed)	4 (fixed)
				5.1(0.6)
				4 (fixed)
				45.411(1)
				443(4)
				4 (fixed)
				5.1(0.6)
<sup>13</sup> C	Parameter	MEW data	Ar data	Whole data set
Gillet <i>et al.</i> [123]	$V_0$ (Å <sup>3</sup> )	45.381(7)	45.381(7)	45.378(7)
	$B_0$ (GPa)	441(11)	440(11)	443(15)
	$B'_0$	3.8(2.0)	4 (fixed)	1.9(2.1)
				4 (fixed)
				45.383(6)
				438(8)
				4 (fixed)
				45.374(3)
				451(2)
Ordinary least-squares	$V_0$ (Å <sup>3</sup> )	45.389(16)	45.381(8)	45.382(10)
	$B_0$ (GPa)	422(33)	440(10)	436(17)
	$B'_0$	8.3(7.7)	4 (fixed)	6.3(2.5)
				4 (fixed)
				45.382(3)
				45.380(2)
				443(4)
				4 (fixed)
				8.2(2.6)
Orthogonal distance regression	$V_0$ (Å <sup>3</sup> )	45.383(3)	45.381(3)	45.378(7)
	$B_0$ (GPa)	425(13)	440(5)	450(5)
	$B'_0$	9.4(4.5)	4 (fixed)	4 (fixed)
				-0.5(5.8)
				4 (fixed)
				45.382(3)
				429(10)
				4 (fixed)
				8.2(2.6)

**Table 6.2** Reported equation of state parameters for diamond from Gillet *et al.* [123] and those found by ordinary least-squares and by orthogonal distance regression for a Birch–Murnaghan equation of state.

One may notice that, in many cases, the values reported by Gillet *et al.* match the values from the ODR, albeit with different errors, but this is not common to all fits; one cannot conclude that this was the approach used by Gillet *et al.*, especially since the publication date of 1999 pre-dates widespread use of the method. One possibility is that the authors used something *similar* but not identical to ODR. The differing errors could be attributed to an alternative method of determining them. It is also possible that whatever approach was used by the authors did not fully converge, resulting in values that are not the true best fit to the data.

Comparing the different fitting methods applied to different data sets little consensus on the correct values can be reached. All approaches agree that  $^{12}\text{C}$  has the larger unit cell volume, but there is disagreement as to which of the two isotopes has the larger bulk modulus. The most reliable values likely come from the consideration of the whole data set using the more sophisticated ODR fitting method. Given the limited compression of diamond over the small pressure range, the inclusion of  $B'_0$  as a fitting parameter provides little advantage, and in many cases is far from the accepted value of approximately 4 (later calculations in this chapter put the value between 3.47 and 3.81). Therefore the ODR fits with fixed  $B'_0 = 4$  are chosen here as the most accurate fits to the data reported by Gillet *et al.*, although in reality the data are not of sufficient quality to make any significant statements on the volume difference.

Nevertheless, a volume difference calculated from the tabulated volumes and these equation of state parameters is shown in figure 6.5. The scatter in the data is too great to make significant comment on the quantum isotope effect at zero pressure, and the data is not of sufficient quality to notice any trend on increasing pressure. The dashed blue line indicates the volume difference as a function of pressure calculated from the  $^{12}\text{C}$  and  $^{13}\text{C}$  Birch–Murnaghan equation of states and shows that the the volume difference increases as pressure increases.

This increase is a result of the bulk modulus of  $^{12}\text{C}$  being larger than that of  $^{13}\text{C}$  by 6 GPa. Ultrasonic measurements from Hurley *et al.* disagree with this and state  $^{13}\text{C}$  to have the larger bulk modulus. However, the authors state the difference to be 74.5 GPa — an increase of 17% [124]. This is far too high to be believable. Brillouin scattering measurements by Vogelgesang *et al.* also describe the bulk modulus of each isotope; the bulk modulus of pure  $^{12}\text{C}$  is

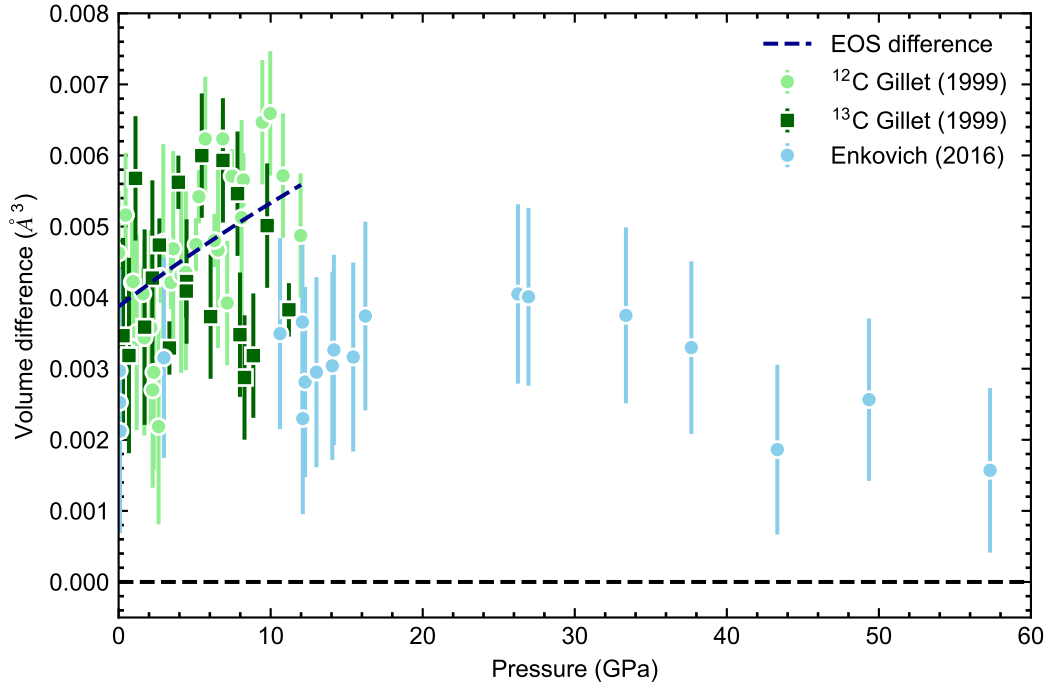


**Figure 6.5** *Experimental determinations of the volume difference per atom in diamond at high pressure. Light green circles are the difference between measured  $^{12}\text{C}$  volumes from Gillet *et al.* [123] and the volume calculated from the  $^{13}\text{C}$  equation of state fitted to the whole dataset using ODR and fixing  $B'_0 = 4$ , and vice versa for dark green squares. Light blue data are the reported volume differences obtained from the Grüneisen model and Raman frequencies in [105].*

reported as  $443.2 \pm 0.8$  GPa and the bulk modulus of their sample with the highest  $^{13}\text{C}$  concentration (99.2%) is reported to be  $442.9 \pm 1.2$  GPa. Although this superficially agrees with Gillet *et al.* in that  $^{13}\text{C}$  has the highest bulk modulus, the difference of only 0.3 GPa is far exceeded by the errors, and is an order of magnitude smaller than predicted by Gillet *et al.* It seems there is no experimental consensus on the bulk modulus of the pure isotopes.

The volume difference calculated using the Grüneisen model by Enkovich *et al.* is also shown in figure 6.5. It mirrors the unusual turnover observed in the Raman frequencies, and inherits all the problems in the measurement of these frequencies — namely the difficulty in discerning the sample signal from the anvil. It is unclear whether assuming a constant Grüneisen parameter for both isotopes and at high pressure is a valid assumption when considering effects of such small magnitude. The validity of Enkovich’s data is therefore held in question until the

Raman measurements can be verified.

The PIMC calculations of Herrero mentioned in the previous section were also used to calculate the volume isotope effect [118]. A volume difference of  $1.888 \times 10^{-3} \text{ \AA}^3/\text{atom}$  (at 0 K) was reported, which decreases with increasing pressure. At 500 GPa, the fractional volume change  $\frac{\Delta V}{V}$  had more than halved, which is attributed to a reduction of the zero-point lattice expansion due to an increasing bulk modulus. The tight-binding model of Biernacki calculates the length of the nearest-neighbour bond for each isotope, from which a volume difference of  $2.42 \times 10^{-3} \text{ \AA}^3$  at 0 K and  $1.16 \times 10^{-3} \text{ \AA}^3$  at 300 K can be deduced<sup>2</sup>. The zero temperature value agrees with the experimental values shown in table 6.1, which are results of room temperature measurements, whereas the 300 K value is too small by some 50%. It was suggested that this is due to the crudeness of the Einstein approximation in which the full phonon dispersion is replaced by a single frequency; by considering only one mode of vibration of a single bond this is, in effect, the assumption that has been made. This indicates the importance of considering the entire phonon spectrum, as is done in the quasiharmonic calculations presented later.

## Other works

Analogous studies have been done on silicon and germanium, also diamond-type semiconductors. Herrero, for example, repeated his PIMC calculations for silicon, and found a similar isotope effect in the vibrational energies of  $^{28}\text{Si}$  and  $^{30}\text{Si}$  as in diamond, albeit an order of magnitude smaller owing to the smaller relative mass difference between the isotopes [125, 126].

Enkovich repeated the high-pressure measurements of the Raman frequencies on silicon [127]. The frequency ratio between  $^{28}\text{Si}$  and  $^{30}\text{Si}$  shown in figure 6.6 appears completely flat, and does not deviate from the harmonic ratio at room temperature. Only at low temperature do the quantum effects play a role [128]. In germanium, where the mass ratio of the isotopes is even smaller, and the Debye temperature even lower, the quantum effects are even less apparent.

---

<sup>2</sup>A typographical error causes Biernacki to report the difference in the lattice parameter at 300 K to be  $1.1 \times 10^{-4} \text{ \AA}$  (volume difference  $6.1 \times 10^{-5} \text{ \AA}^3$ ). This does not affect the subsequent conclusions.



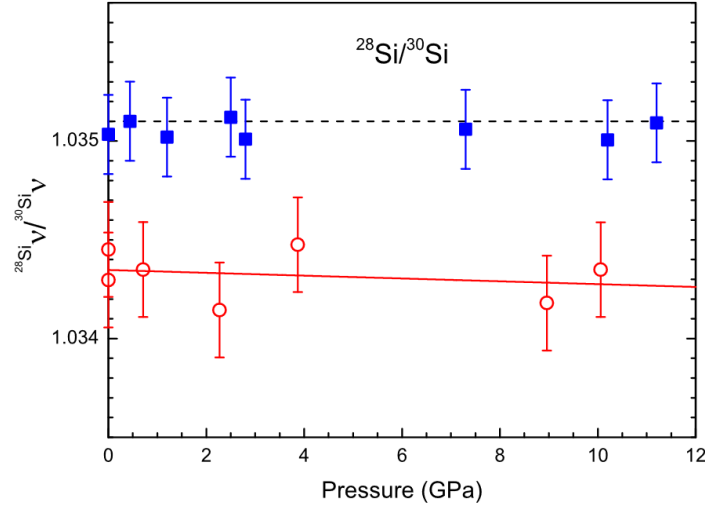


**Figure 6.6** Pressure dependence of the frequency ratio for  $^{28}\text{Si}$  and  $^{30}\text{Si}$ . Blue squares are data taken at 296 K and red circles are data taken at 80 K. The dashed line indicates the harmonic frequency ratio. Figure reproduced from [127].

In summary, it has been frequently reported that quantum contributions cause unusual behaviour in the isotope effect in diamond at high pressure. No similar effect is observed in silicon or germanium, which show no pressure dependence of the isotope effect, and in diamond there is disagreement in the literature as to the behaviour of these isotope effects at high pressure. The question of the high-pressure behaviour of the isotope effect in diamond has been frequently asked, yet so far no satisfactory answer has been found. This investigation will use anharmonic phonon calculations to provide an answer to this question from first principles.

## 6.2 Methods

### 6.2.1 Quasiharmonic calculations

The quantum isotope effect was investigated firstly with the QHA as described in section 4.2. The finite displacement method was used to calculate the harmonic phonon dispersions at 15 volumes covering the pressure range 0 GPa to 80 GPa.

Each of the finite displacement calculations was performed using a  $4 \times 4 \times 4$  supercell of the primitive unit cell, with the atom at the origin displaced 0.01 Å from its equilibrium position in the positive  $x$  direction. A  $4 \times 4 \times 4$  Monkhorst-Pack k-point grid was used for the electronic integration, and a stopping criterion of less than  $1 \times 10^{-8}$  eV between successive self-consistent cycles was used to halt the calculations once convergence was achieved. The effect of the XC functional and pseudopotential on the final results was investigated, and the above calculations were done once each using the LDA, PBE, and PBEsol XC functionals (using the so-called “C” pseudopotential) and once each using the C and C.h pseudopotential (using LDA). C and C.h are the standard and “hard” PAW pseudopotentials provided by VASP and constructed by G. Kresse with the  $2s$  and  $2p$  electrons as valence electrons [69, 70, 72, 75, 76, 129].

Density functional theory depends only on the electronic configuration and is therefore agnostic towards the masses of the nuclei. Consequently, the same DFT calculations were used to determine both the  $^{12}\text{C}$  and the  $^{13}\text{C}$  phonon free energies. The differing masses manifest only in the calculation of the phonon frequencies (which in the harmonic approximation follow the  $\omega \sim \frac{1}{\sqrt{m}}$  scaling). This change in the phonon frequencies in turn affects the phonon free energies, thus producing different equations of state for the two isotopes. The fitting of the phonon free energies in the QHA was performed using three energy–volume equations of state:

Murnaghan,

$$U(V) = U_0 + B_0 V_0 \left\{ \frac{1}{B'_0(B'_0 - 1)} \left( \frac{V}{V_0} \right)^{1-B'_0} + \frac{1}{B'_0} \frac{V}{V_0} - \frac{1}{B'_0 - 1} \right\}, \quad (6.2)$$

Birch–Murnaghan,

$$U(V) = U_0 + \frac{9B_0V_0}{16} \left\{ B'_0(\eta^{-2} - 1)^3 + (\eta^{-2} - 1)^2(6 - 4\eta^{-2}) \right\}, \quad (6.3)$$

and Vinet,

$$U(V) = U_0 + \frac{2B_0V_0}{(B'_0 - 1)^2} \times \left\{ 2 - [5 + 3B'_0(\eta - 1) - 3\eta] \times \exp \left[ \frac{3}{2}(B'_0 - 1)(1 - \eta) \right] \right\}, \quad (6.4)$$

where  $B_0$ ,  $B'_0$ , and  $V_0$  are the equilibrium bulk modulus, the pressure derivative of the bulk modulus at equilibrium, and the equilibrium volume respectively; and  $\eta = \left( \frac{V}{V_0} \right)^{\frac{1}{3}}$ .

## 6.2.2 TDEP

The frequency isotope effect was also investigated using the TDEP approach described in section 4.3. It was assumed that the frequency ratio was affected independently by the volume difference, the effects of which would be shown in the quasiharmonic calculations, and the pure anharmonicity of the zone-centre phonon optical frequency, which would be calculated by the TDEP calculations. Given that the volume difference between the two isotopes at a common pressure is very small, this approximation is expected to be reasonable; there will only be negligible changes in the anharmonicity of the potential between the two volumes at a common pressure. This assumption avoided the computational expense of calculating the fully-anharmonic phonon frequencies over the entire Brillouin zone necessary for the calculation of the fully anharmonic free energy. The pressure in the TDEP calculations was determined from the quasiharmonic calculations.

Nine lattice parameters were chosen corresponding to the average of the  $^{12}\text{C}$  and  $^{13}\text{C}$  lattice parameters at pressures over the range 0 GPa to 80 GPa in 10 GPa increments. At each of these lattice parameters, a harmonic finite displacement calculation was performed to determine the harmonic force constants necessary to create the TDEP configurations.

By using an averaged lattice parameter from both isotopes, the same harmonic

force constants were used to generate the configurations<sup>3</sup>. This alleviated a numerical problem where minutely different force constants lead to significantly different phonon eigenvectors at degenerate points in the Brillouin zone. At these degenerate points, the eigenvectors are not uniquely defined and are confined to a plane (or hyperplane) with a dimension equivalent to the degeneracy. Therefore, the small changes in the force constants that occur between the volumes of the two isotopes cause drastic changes in the orientation of eigenvectors at these degenerate points. As the eigenvectors are used to determine the direction in which the atoms should be displaced, atoms end up displaced in different directions in what should be similar configurations.

TDEP calculations were carried out at 300 K at the nine lattice parameters. Each TDEP calculation used 30 configurations of a  $5 \times 5 \times 5$  supercell of the primitive unit cell, resulting in a convergence of the zone-centre optical phonon frequency to within  $1 \text{ cm}^{-1}$ . The plane-wave energy cutoff for these calculations was increased to 550 eV to ensure accurate calculation of the forces; the convergence criterion was reduced to a difference of less than  $1 \times 10^{-9} \text{ eV}$  between successive self-consistent cycles; and the k-point grid was replaced with a grid generated by the getKPoints utility [88, 89] of equivalent density to the  $4 \times 4 \times 4$  grid used in the QHA calculations, for increased efficiency. The calculations were done using the LDA XC functional, as this best matched the experimental value for the Raman frequency, and the standard C pseudopotential, as the harder pseudopotential produced no advantage and required a higher energy cutoff to converge.

## Verifying the similarity of the configurations

After using the same harmonic force constants to generate the configurations, the resulting 30 configurations for the two isotopes were, as much as possible, scaled versions of one another. The displacements depend on the normal mode amplitudes, which in turn depend on the mass; the eigenvectors, which ultimately depend on the force constants; and the phonon frequencies, which depend on the mass and on the force constants. By using the same seed for the configuration generation and the same set of force constants for both isotopes, only the mass was left to affect the atomic configurations.

---

<sup>3</sup>The different displacement magnitudes for the  $^{12}\text{C}$  and  $^{13}\text{C}$  isotopes is retained through the mass-dependent normal mode amplitudes

The mass affects the displacements through the normal mode amplitudes which are

$$\langle A_{is} \rangle = \sqrt{\frac{\hbar(2n(\omega_s) + 1)}{2m_i\omega_s}} \quad (6.5)$$

in the quantum case, and

$$\langle A_{is} \rangle = \frac{1}{\omega_s} \sqrt{\frac{k_B T}{m_i}} \quad (6.6)$$

in the classical. Here  $\hbar$  is the reduced Planck's constant,  $n(\omega)$  is the Bose-Einstein distribution for frequency  $\omega$ ,  $m_i$  is the mass of atom  $i$ ,  $\omega_s$  is the frequency of mode  $s$ ,  $k_B$  is the Boltzmann constant, and  $T$  is the temperature.

As harmonic calculations are used for the configuration generation, the frequencies scale inversely with the square-root of the mass. The ratio of the normal mode amplitudes can therefore be found as

$$\frac{\langle A_{is}^{12} \rangle}{\langle A_{is}^{13} \rangle} = \sqrt{\frac{\omega_s^{12}}{\omega_s^{13}}} \sqrt{\frac{2n(\omega_s^{12}) + 1}{2n(\omega_s^{13}) + 1}} \quad (6.7)$$

in the quantum case, and

$$\frac{\langle A_{is}^{12} \rangle}{\langle A_{is}^{13} \rangle} = \frac{\omega_s^{13}}{\omega_s^{12}} \sqrt{\frac{m_i^{13}}{m_i^{12}}} = 1 \quad (6.8)$$

in the classical.

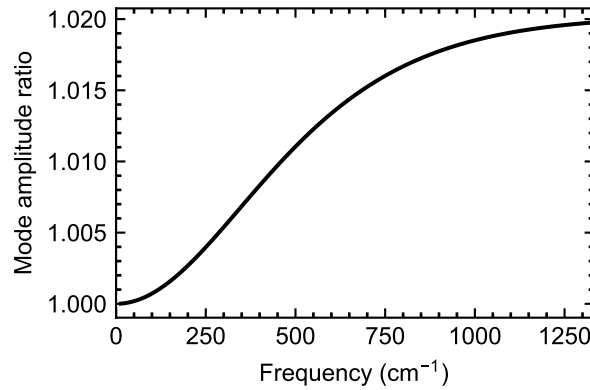


**Figure 6.7** Ratio of the  $^{12}\text{C}$  and  $^{13}\text{C}$  normal mode amplitudes  $\frac{\langle A \rangle(\omega_{12})}{\langle A \rangle(\omega_{13})}$  at 300 K. The frequency denoted on the x-axis is the  $^{12}\text{C}$  frequency,  $\omega_{12}$ . The  $^{13}\text{C}$  frequency,  $\omega_{13}$ , is given by  $\sqrt{\frac{12}{13.003355}} \times \omega_{12}$ .

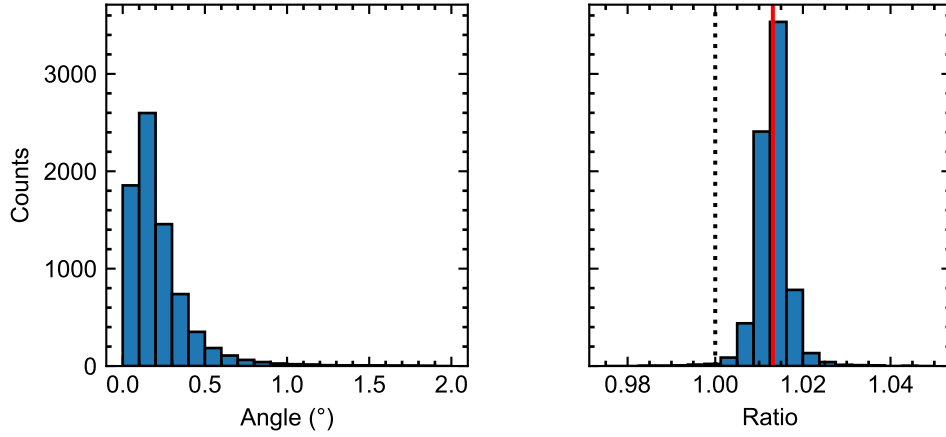


**Figure 6.8** *Angle (left) between corresponding atomic displacements in the  $^{12}\text{C}$  and  $^{13}\text{C}$  configurations and their magnitude ratio (right). The red line in the right panel indicates the average displacement ratio over all atoms and configurations.*

It is apparent that the isotope effect only exists in the quantum limit, where it depends on the frequency of the mode and the temperature (through the Bose-Einstein distribution). The mode amplitude ratio in the quantum limit is plotted in figure 6.7. The maximum ratio of the normal mode amplitudes in diamond is around 1.02 at  $1332\text{ cm}^{-1}$ ; a phonon mode at this frequency will produce an atomic displacement 2% larger in the  $^{12}\text{C}$  crystal than the  $^{13}\text{C}$  crystal. If the average frequency is roughly half the  $\Gamma$ -point frequency, then the average ratio of the normal mode amplitudes is roughly 1.01, and the atomic configurations for  $^{12}\text{C}$  are expected to have 1% larger displacements than the  $^{13}\text{C}$  configurations. The average ratio of the displacement magnitudes over all 250 atoms in all 30 configurations was found to be 1.0131 for the zero-pressure calculation.

Each atomic displacement in a  $^{12}\text{C}$  configuration has a corresponding displacement of the same atom the  $^{13}\text{C}$  configuration. The distributions of the magnitude ratio and the angle between these corresponding displacements are shown in figure 6.8. This figure demonstrates that, by and large, the atoms in the  $^{12}\text{C}$  and  $^{13}\text{C}$  configurations are displaced in the same direction by an amount that is on average 1.3% larger in  $^{12}\text{C}$  than  $^{13}\text{C}$ . Those with a larger angle between them are the small displacements where the stochastic nature of the configuration generation has the most pronounced effect. One configuration is clearly recognisable as a scaled version of the other.

## 6.3 Results

### 6.3.1 Quasiharmonic results

#### Equation of state fitting

The three equations of state were each fitted to the free-energy–volume data. The resulting parameters of these fits are shown in table 6.3. The values of  $B'_0$  for all isotopes are identical; between  $^{12}\text{C}$  and natural diamond there are only minute differences in the parameters, as expected. It can be seen that, for all three isotopes, the Murnaghan equation of state produces values which are out of line with the other two equations, and the Vinet and the Birch–Murnaghan equations agree with each other much better. Unless otherwise specified, the Vinet equation of state is chosen to present the results in this section; it will later be shown that the results do not depend on the choice of equation of state.

It was confirmed that the results of table 6.3 were not simply due to correlation effects between  $B_0$  and  $B'_0$  in the equation of state fitting process by repeating the fit with  $B'_0$  fixed at the average of the  $^{12}\text{C}$  and  $^{13}\text{C}$  values (using the full numerical precision of the fits). This procedure left the values in table 6.3 unchanged within

Isotope	Equation of state	$B_0$ (GPa)	$B'_0$	$V_0$ ( $\text{\AA}^3/\text{atom}$ )
Natural diamond	Vinet	452.18(4)	3.76(1)	5.5846(1)
	Murnaghan	454.56(5)	3.47(2)	5.5849(2)
	Birch–Murnaghan	452.73(3)	3.69(1)	5.5846(1)
$^{12}\text{C}$ diamond	Vinet	452.17(4)	3.76(1)	5.5846(1)
	Murnaghan	454.56(5)	3.47(2)	5.5849(2)
	Birch–Murnaghan	452.72(3)	3.69(1)	5.5847(1)
$^{13}\text{C}$ diamond	Vinet	452.57(3)	3.76(1)	5.5822(1)
	Murnaghan	454.90(5)	3.47(1)	5.5826(1)
	Birch–Murnaghan	453.10(3)	3.69(1)	5.5823(1)

**Table 6.3** *Values of the equilibrium bulk modulus  $B_0$ , the pressure derivative of the bulk modulus at zero pressure  $B'_0$  and the equilibrium volume  $V_0$  at 300 K for the Vinet, Murnaghan, and Birch–Murnaghan equations of state for natural diamond,  $^{12}\text{C}$  diamond, and  $^{13}\text{C}$  diamond from fitting energy–volume data calculated from the QHA calculations.*

the fitting uncertainty.

The values in table 6.3 should be compared with the experimental values of Gillet *et al.* [123]. The re-analysis of Gillet *et al.*'s data suggested an ODR fit to a Birch–Murnaghan equation of state with fixed  $B'_0 = 4$  produced the best results. The resulting values for  $B_0$ , and  $V_0$  in  $^{12}\text{C}$  diamond were 449 GPa and  $5.676 \text{ \AA}^3/\text{atom}$ ; and 443 GPa and  $5.673 \text{ \AA}^3/\text{atom}$  in  $^{13}\text{C}$  diamond. One notes that the experimental volume is larger, and the bulk modulus smaller, than any of the DFT results in table 6.3. This indicates the over-binding typical of the LDA exchange–correlation functional used in the DFT calculations — the material is calculated to be stiffer with a smaller volume. Comparing the experimental and calculated equilibrium volumes, the LDA can be said to over-bind by 1.6% for both isotopes.

It was mentioned previously that the bulk moduli from Gillet *et al.*'s data vary between the two isotopes by 6 GPa and the equilibrium volumes differs by  $0.004 \text{ \AA}^3$ , with  $^{12}\text{C}$  having the larger value in *both* cases. This is qualitatively and quantitatively different to the QHA results where the difference between the two

Isotope	XC functional	$B_0$ (GPa)	$B'_0$	$V_0$ ( $\text{\AA}^3/\text{atom}$ )
Natural diamond	LDA	452.17(4)	3.76(1)	5.5846(1)
	PBE	419.60(4)	3.81(1)	5.7595(3)
	PBEsol	436.74(4)	3.77(1)	5.6755(2)
$^{12}\text{C}$ diamond	LDA	452.17(4)	3.76(1)	5.5846(1)
	PBE	419.59(4)	3.81(1)	5.7595(3)
	PBEsol	436.74(4)	3.77(1)	5.6757(1)
$^{13}\text{C}$ diamond	LDA	452.57(3)	3.76(1)	5.5822(1)
	PBE	419.97(4)	3.81(1)	5.7570(3)
	PBEsol	437.12(4)	3.77(1)	5.6733(1)
DFT (static)	LDA	465.10(3)	3.74(1)	5.5202(1)
	PBE	432.20(4)	3.79(1)	5.6913(2)
	PBEsol	449.39(3)	3.75(1)	5.6098(1)

**Table 6.4** *Values of the equilibrium bulk modulus  $B_0$ , the pressure derivative of the bulk modulus at zero pressure  $B'_0$  and the equilibrium volume  $V_0$  at 300 K for the LDA, PBE, and PBEsol XC functionals for natural diamond,  $^{12}\text{C}$  diamond, and  $^{13}\text{C}$  diamond using the Vinet equation of state. The values for a static DFT calculation where the phonon-free energy has not been included in the fitting are also shown.*



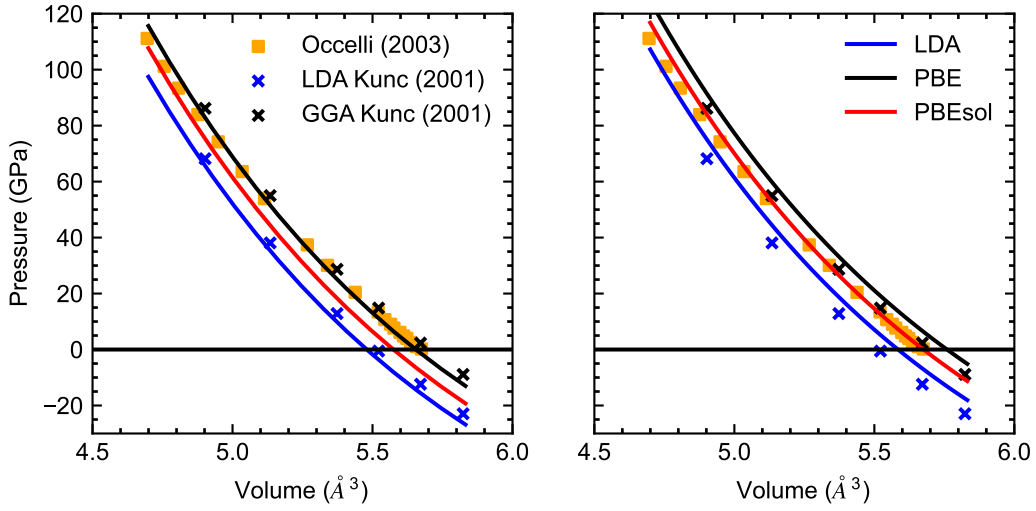


**Figure 6.9** *Static (left) and QHA (right) pressure–volume relation of diamond for different XC functionals. QHA data is for natural diamond using the Vinet equation of state. Legends in the figure apply to both panels. Blue and black crosses are LDA and GGA (PBEsol) data using PAW pseudopotentials from [132], orange squares are single-crystal x-ray diffraction data from [133].*

isotopes is just 0.4 GPa and  $0.0025 \text{ Å}^3$ , with  $^{12}\text{C}$  having the larger volume but the *smaller* bulk modulus. The QHA results are in reasonable agreement with a theoretical prediction made by Vogelgesang *et al.* on the basis of an interatomic potential including cubic terms, which predicts the relative increase of the bulk modulus between  $^{12}\text{C}$  and  $^{13}\text{C}$  to be 0.12%. Using the average  $^{12}\text{C}$  bulk modulus from table 6.3, this gives a difference of 0.54 GPa.

The effect of XC functional was investigated by repeating the QHA calculations for LDA with the PBE and PBEsol functionals [70, 72, 75, 76]. The values are shown in table 6.4, where the Vinet equation of state has been used for the fitting. Again, LDA exhibits the over-binding while PBE and PBEsol under-bind to varying degrees. The final three rows of the table show the result of a fit to the volumes and pressures calculated from the stress theorem [130, 131] and can be directly compared to the work of Kunc *et al.* [132], where similar calculations were performed. These static pressure–volume fits are shown in comparison with the data of Kunc *et al.* in figure 6.9.

The static LDA results of the present investigation shown in the left-hand panel of figure 6.9 lie below the LDA results of Kunc’s work due to a different plane-

wave energy cutoff. The cutoff used in Kunc *et al.*'s work was significantly higher as a result of the harder pseudopotential and the necessity of well-converged DFT pressures calculated by the stress theorem. Such highly converged pressures were not required for this investigation, which obtains pressures through the QHA, although increasing the cutoff does move the curves in figure 6.9 slightly closer to the data reported by Kunc *et al.* The left panel of figure 6.9 shows LDA to present the biggest underestimation of the volume in the static case, with PBE aligning most closely with experimental data. This agreement is altered by the inclusion of the phonon free-energy as shown in the right panel. When the phonon free energy is considered, PBEsol shows the most faithful representation of the experimental data.

### Pressure–frequency

Despite calculations using PBEsol showing best agreement with experimental volumes, LDA was shown to produce the closest agreement with the frequencies. The volumes at which the frequencies were calculated were translated into pressure through the fitted equation of state, and a quadratic function was fitted

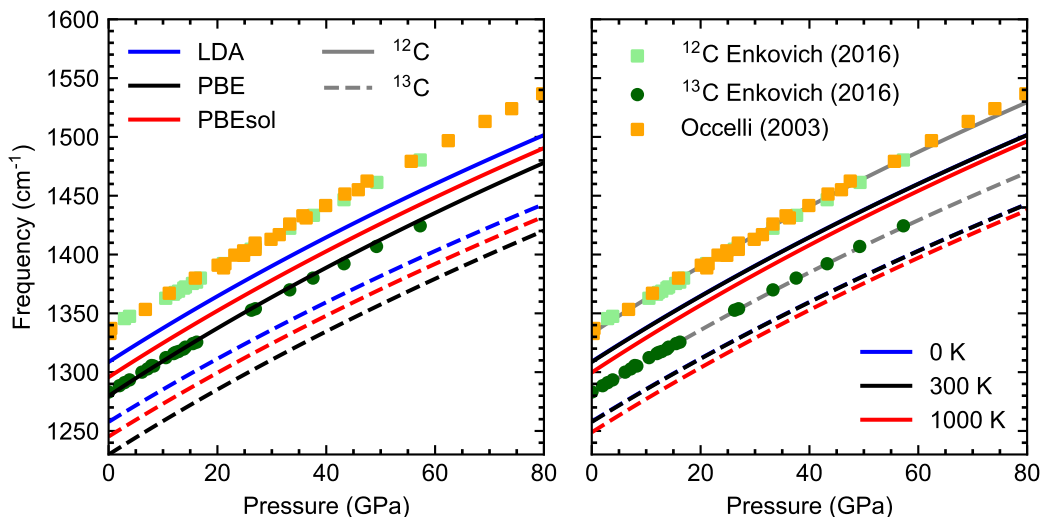


**Figure 6.10** *Frequency–pressure curves in diamond from the QHA using different XC functionals (left) and different temperatures (right). Solid and dashed lines indicate <sup>12</sup>C and <sup>13</sup>C data respectively. The 0 K data in the right panel (blue) is coincident with the black line. The grey lines in the right panel are the 300 K data scaled to match the experimental data at zero pressure.*

to the ensuing pressure–frequency data. The results of this for different XC functionals are shown in the left panel of figure 6.10. There is a noticeable spread between the different XC functionals with LDA being closest to the experimental data, but still being short by  $20\text{ cm}^{-1}$ . All three XC functionals follow the same trend, indicating that they differ only by a constant offset and not in any qualitative way.

The QHA results for different temperatures are shown in the right panel of figure 6.10. This figure indicates little difference between the 0 K and 300 K values; diamond has such a high Debye temperature that, compared to the Debye temperature, 300 K is still a very low temperature. The grey dashed and solid lines in figure 6.10 represent the 300 K results for both  $^{12}\text{C}$  and  $^{13}\text{C}$  scaled up by 1.86%. This scaling was chosen to align the 300 K results with the experimental data, and provides assurance that the frequency ratio results are not affected by the underestimation of the phonon frequencies by DFT.

## Volume difference

The volume difference between the two isotopes of diamond is shown in figure 6.11. It can be seen from this figure that the zero-pressure QHA result is in excellent agreement with the zero-pressure experimental data. The agreement is less good when compared with the experimental high-pressure data, yet there is reason to believe it is the experimental data that is in error. The data of Gillet *et al.* have already been discussed; it was determined that the upward trend in the volume difference was the result of the bulk modulus of  $^{12}\text{C}$  being higher than that of  $^{13}\text{C}$ , but that this result was sensitive to the type of fitting performed.

The highest-pressure data from Enkovich *et al.* agree with the QHA, as do the zero-pressure data from the same authors. Aside from these points, however, the QHA results do not reproduce the trend of Enkovich *et al.*'s results, as there is no maximum at 30 GPa. In contrast with the conclusions drawn by Enkovich, the volume difference calculated here demonstrates that quantum effects decrease steadily with increasing pressure. Increasing temperature also serves to lower the quantum contribution in line with the conclusions of Herrero [118].

The high-pressure experimental data presented in figure 6.11 should be treated with caution. The experiment performed by Gillet *et al.* did not have sufficient

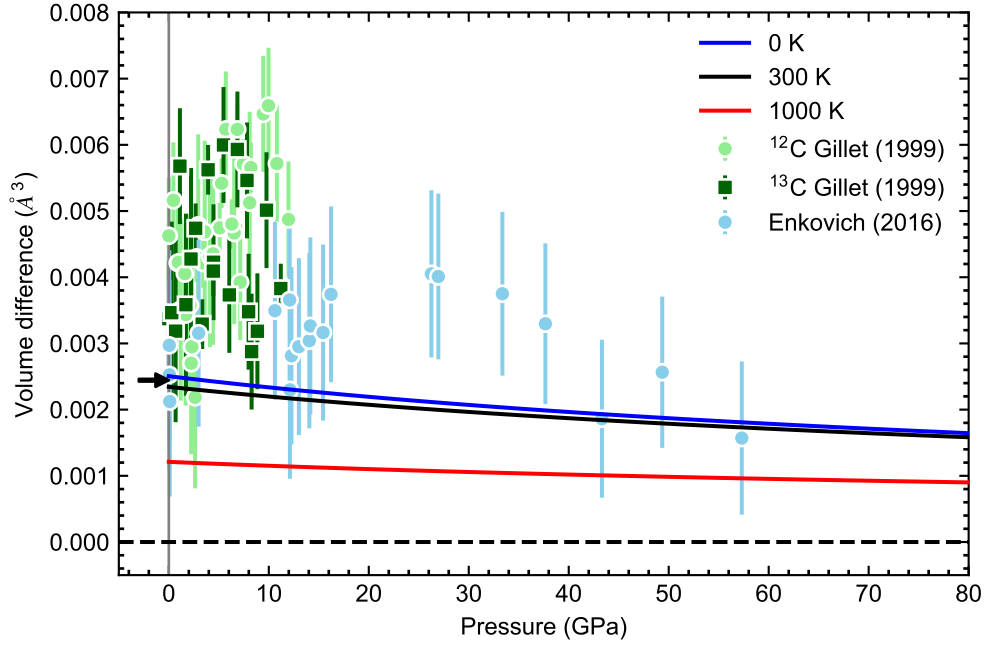


**Figure 6.11** Volume difference ( $V(^{12}\text{C}) - V(^{13}\text{C})$ ) per atom as a function of pressure as calculated by the QHA. The black arrow indicates an averaged volume difference from the experimental zero-pressure data in table 6.1. The experimental uncertainty on the black arrow is less than the line width of the arrow stem. Light blue data are obtained indirectly from Raman frequencies and a Grüneisen model [105]; Light and dark green data are from [123] and are found as the difference between the tabulated volumes of one isotope and the equation-of-state volumes of the other isotope, as in figure 6.5. The results of the QHA calculations are shown by the blue, black, and red lines.

precision to accurately deduce the volume difference (but recall that this is beyond what is attempted by the authors) and the volume data provided by Enkovich *et al.* is indirect, coming from the Grüneisen model applied to the measured Raman frequencies. Nevertheless, the QHA data is in excellent agreement with the zero-pressure data, which is believed to be very accurate, and there is no reason to suspect that the high-pressure QHA results are any less accurate than the zero-pressure results.

The QHA calculations are robust against changes in the XC correlation functional and pseudopotential used in the DFT calculations, as well as the equation of state used to describe the energy–volume (and subsequently pressure–volume)

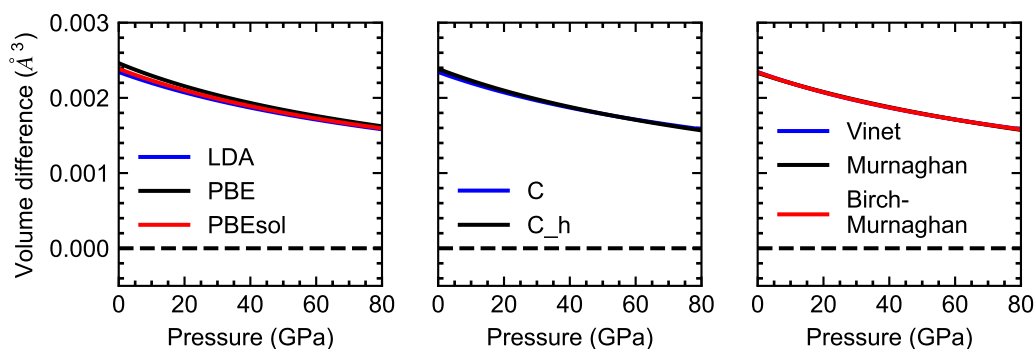


**Figure 6.12** QHA volume isotope effect in diamond for different XC functionals (left), pseudopotentials (centre), and equations of state (right).

relation. Figure 6.12 shows the volume difference computed for different XC functionals, pseudopotentials, and equations of state. From this figure it can be seen that the greatest uncertainty comes from the choice of XC functionals, with the uncertainty being greatest at zero pressure and diminishing at higher pressure. The choice of pseudopotential and the choice of equation of state do not show a noticeable change in the volume difference. Therefore the QHA can be said to accurately and robustly calculate the volume isotope effect in diamond, and its predictions at high pressure should be regarded as credible.

## Frequency ratio

The frequency isotope effect in diamond calculated by the QHA is shown in figure 6.13. The zero-pressure ratio is in best agreement with the experimental observations of Vogelgesang *et al.* [113] and the prediction of Cardona and Ruf, who suggested that the renormalisation varied as  $M^{-1}$  and had been found to be  $16 \text{ cm}^{-1}$  in natural diamond. The ratio found by Lang *et al.*, who also suggested a  $M^{-1}$  dependence of the renormalisation but that it was found to be  $31.6 \text{ cm}^{-1}$  in natural diamond, apparently overestimate the role of quantum effects in diamond.

The QHA calculations predict a much reduced role of quantum effects compared to the results of Enkovich *et al.* The disagreement between Enkovich's data and the quasiharmonic calculations, as well as the most credible zero-pressure experimental data, suggest that there are systematic errors introduced by the DAC in the high-pressure measurements. The QHA calculations also fail to produce any turnover or inversion of the quantum isotope effect, either in the

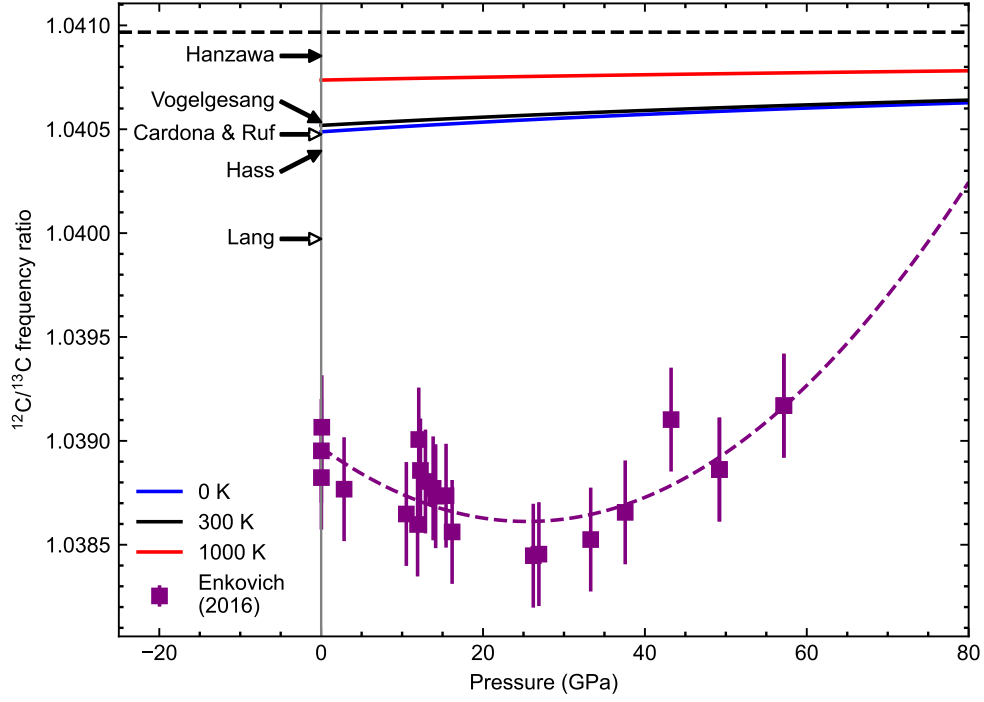


**Figure 6.13** *Frequency ratio as calculated by the QHA with the Vinet equation of state and LDA as the XC functional. The blue, orange, and green arrows indicate the frequency ratios reported by Hass, Vogelgesang, and Hanzawa [112–114]. The magenta and cyan arrows are the ratios reported by Lang et al. and Cardona and Ruf [115, 116]. Purple data and the associated curve are the data from [105] and a fitted quadratic. The dashed black line shows the harmonic frequency ratio.*

volume or frequency isotope effects. In both cases the quantum effects reduce smoothly and monotonically with increasing pressure. Increasing temperature also reduces the quantum effects, which is the expected behaviour as one approaches the Debye temperature.

As with the volume isotope effect, the frequency ratio calculations were shown to be robust with respect to the XC functional, the pseudopotential, and the equation of state. These aspects of the calculation were each varied and the results are shown in figure 6.14. The XC functional and the equation of state do not have any significant influence on the frequency ratio. The pseudopotential has the greatest effect with a difference in the ratio of  $2 \times 10^{-4}$  at zero pressure and

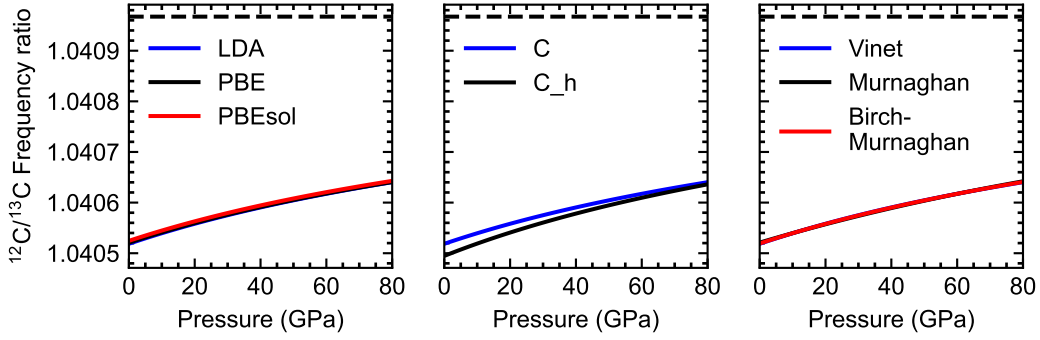


**Figure 6.14** QHA frequency isotope effect for different XC functionals (left), pseudopotentials (centre), and equations of state (right). The dashed line indicates the harmonic frequency ratio.

decreasing as pressure increases. Assuming this difference to be representative of of an error on the QHA calculations, the conclusions drawn from figure 6.13 are unchanged by an error of this magnitude.

### 6.3.2 TDEP results

The QHA accounts for some anharmonicity through the volume dependence of the interatomic potential, but cannot account for the so-called “pure” anharmonicity arising from terms in the potential higher than quadratic order. To investigate the effect of this pure anharmonicity on the phonon frequency ratio, TDEP calculations were performed. The TDEP approach splits the pure anharmonic contribution to the potential into an effective harmonic part, representing the even terms in the expansion (see equations 3.8 and 3.9), and an effective 3-phonon part deduced from the phonon linewidth and the Kramers–Kronig relations.

The volume effect, shown to be accurately accounted for by the QHA calculations, was included separately. The small volume difference between the two isotopes at a common pressure creates a small frequency difference. As described in section 6.2.2, the TDEP calculations were performed at the midpoint of these two volumes, and  $^{12}\text{C}$  and  $^{13}\text{C}$  anharmonic phonon frequencies were found. The QHA frequency effect was then added to the TDEP results by adding half the QHA frequency difference to the  $^{12}\text{C}$  frequency, and subtracting half from the  $^{13}\text{C}$  frequency, then taking the ratio. The results are shown in figure 6.15.

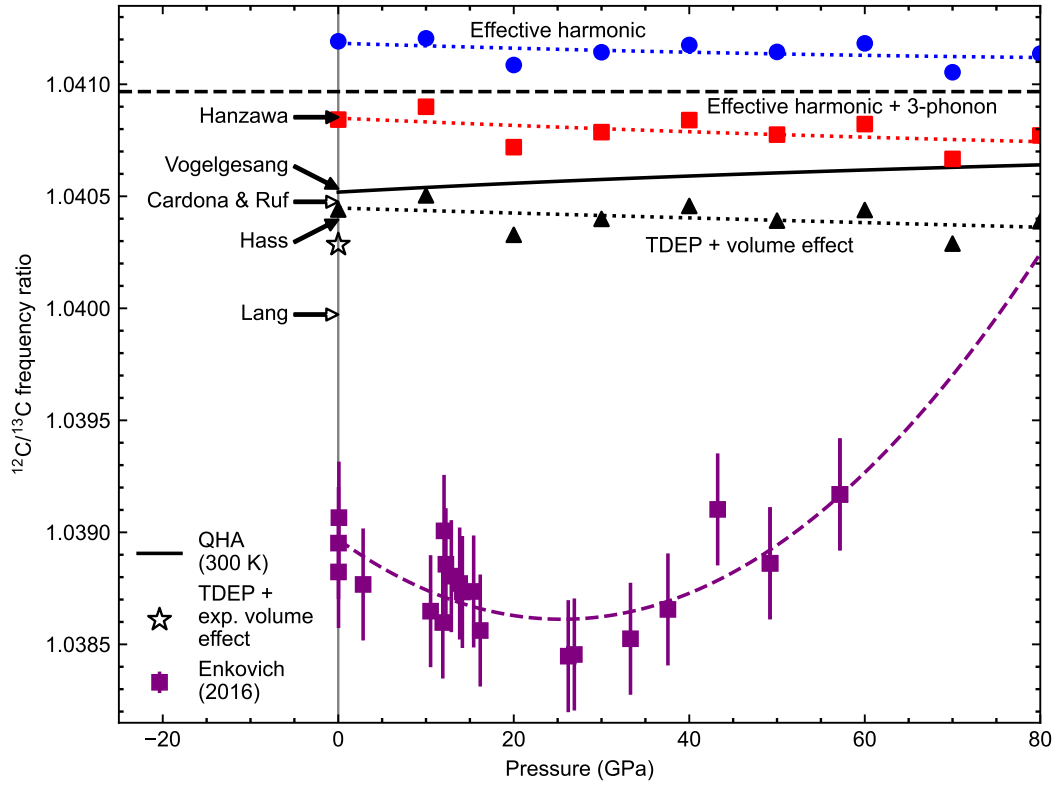


**Figure 6.15** *Frequency isotope effect in diamond calculated using the TDEP formalism for an effective-harmonic potential. The frequency ratio from an effective harmonic potential is indicated by the blue circles and the ratio from the effective-harmonic potential with 3-phonon effects is shown by the red squares. The black triangles indicate these effective harmonic + 3-phonon data with the contribution from the differing isotope volumes from QHA calculations included. The solid black line shows the ratio of the QHA calculation at 300 K. The open black star show the zero-pressure effective harmonic + 3-phonon ratio with a isotope volume contribution found from the experimental lattice parameters in table 6.1. Arrows indicate experimental (solid) and theoretical (open) frequency ratios from references [112–116]. Purple data and the associated curve are the data from [105] and a fitted quadratic. The dashed black line shows the harmonic frequency ratio.*

Strikingly, the effective harmonic potential shows a frequency ratio that is larger than the harmonic one, implying that the even (quartic and above) terms of the potential cause the potential to stiffen at greater atomic displacement. The lighter  $^{12}\text{C}$  atom, which more deeply probes this potential, therefore has a higher frequency than it would from the harmonic term only, and thus raises the frequency ratio. This effect is reversed in near equal magnitude by the



consideration of the 3-phonon corrections, which indicates that the potential, with all terms considered, *softens* with increasing atomic displacement. In addition to this, the inclusion of the volume effect lowers the frequency ratio again, indicating a softening of the potential as the lattice expands, as is common across materials.

A slight downward trend can be distinguished in all the TDEP results. The slope of this trend is so slight that it is flat to within the uncertainty of the fit; the pure anharmonic and volume effects combined produce a pressure-independent frequency ratio. This is in line with what has been seen in silicon [127]. It is striking that the volume and pure-anharmonic effects should cancel so exactly, but the calculations that account for the volume effect through the QHA and the pure anharmonicity through the TDEP calculations show that the quantum isotope effect is largely pressure independent, and provide no evidence for the reported inversion. The large disagreement between the frequency ratio reported by Enkovich *et al.* and both the zero-pressure experimental results and the *ab initio* calculations reported here suggests that Enkovich's experimental results are not reliable.

# Chapter 7

## The Diamond Edge Raman Scale

### 7.1 Background

Diamond is typically considered to be an exceptionally harmonic material; isotopically pure diamond has the highest known thermal conductivity of any material [134] indicating that there is very little phonon–phonon scattering. This, along with many other of the well-known superlative properties of diamond, is a result of the strong, highly directional covalent bonds that form between the carbon atoms.

Another, better known, property of diamond is its exceptional hardness. Its resistance to deformation makes it ideal for creating high-pressure environments in a DAC. A DAC consists of two opposing diamonds held in place by a metal casing. A diagram of a typical DAC is shown in figure 7.1. Between the diamonds there is a small chamber surrounded by a metal gasket containing the sample and a pressure-transmitting medium. When the screws in the casing are tightened, a force is created at the diamond tips that creates hydrostatic pressure in the sample chamber. The small surface area of the diamond tips coupled with the hardness of the diamonds creates pressures of up to 1 TPa [135, 136].

When experiments are performed using a DAC, the pressure in the cell must be measured in some way. One common approach is to use *ruby fluorescence* [138–140]. When a ruby is illuminated with a laser it produces a fluorescence,

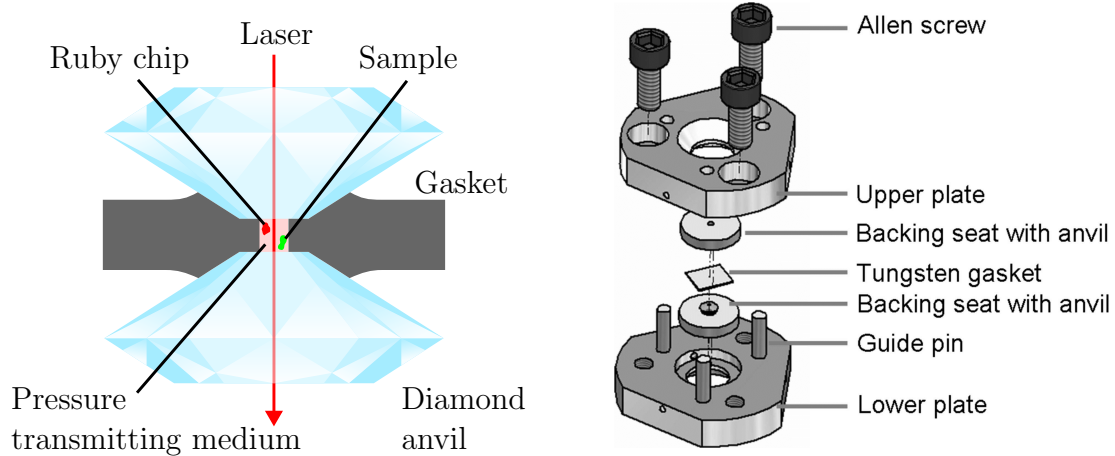


**Figure 7.1** *Schematic (left) and exploded diagram (right) of the diamond anvil cell using a ruby chip as a pressure marker. In the left figure, the sample (green) and the ruby pressure marker (red) are in the sample chamber which is filled with a pressure transmitting medium. The pressure in the sample chamber is increased by tightening the Allen screws. Optical measurements are taken through the aperture in the cell casing. Right diagram reproduced from [137].*

whose light has a specific frequency. This frequency changes with pressure, and by linking this change to a known pressure scale (for example the equation of state of a well-studied material) the pressure in the ruby can be determined.

Another common approach, used particularly at multi-megabar pressure where the ruby calibration is not as reliable, or where no ruby chip can be placed in the DAC, is to use the so-called diamond edge Raman scale. The Raman signal from a diamond under ambient conditions consists of a sharp peak at  $1333\text{ cm}^{-1}$  corresponding to the zone-centre optical phonon ( $T_{2g}$  mode) [141]. When the diamond is used as an anvil in a DAC, a pressure gradient from the table of the diamond to the tip is created. As a result, the sharp peak is spread out over a wide range of frequencies, with a defined edge at the highest frequency corresponding to the highest pressure at the tip of the diamond. If one knows the pressure dependence of this Raman edge, one can use this as a measure of the pressure inside the DAC.

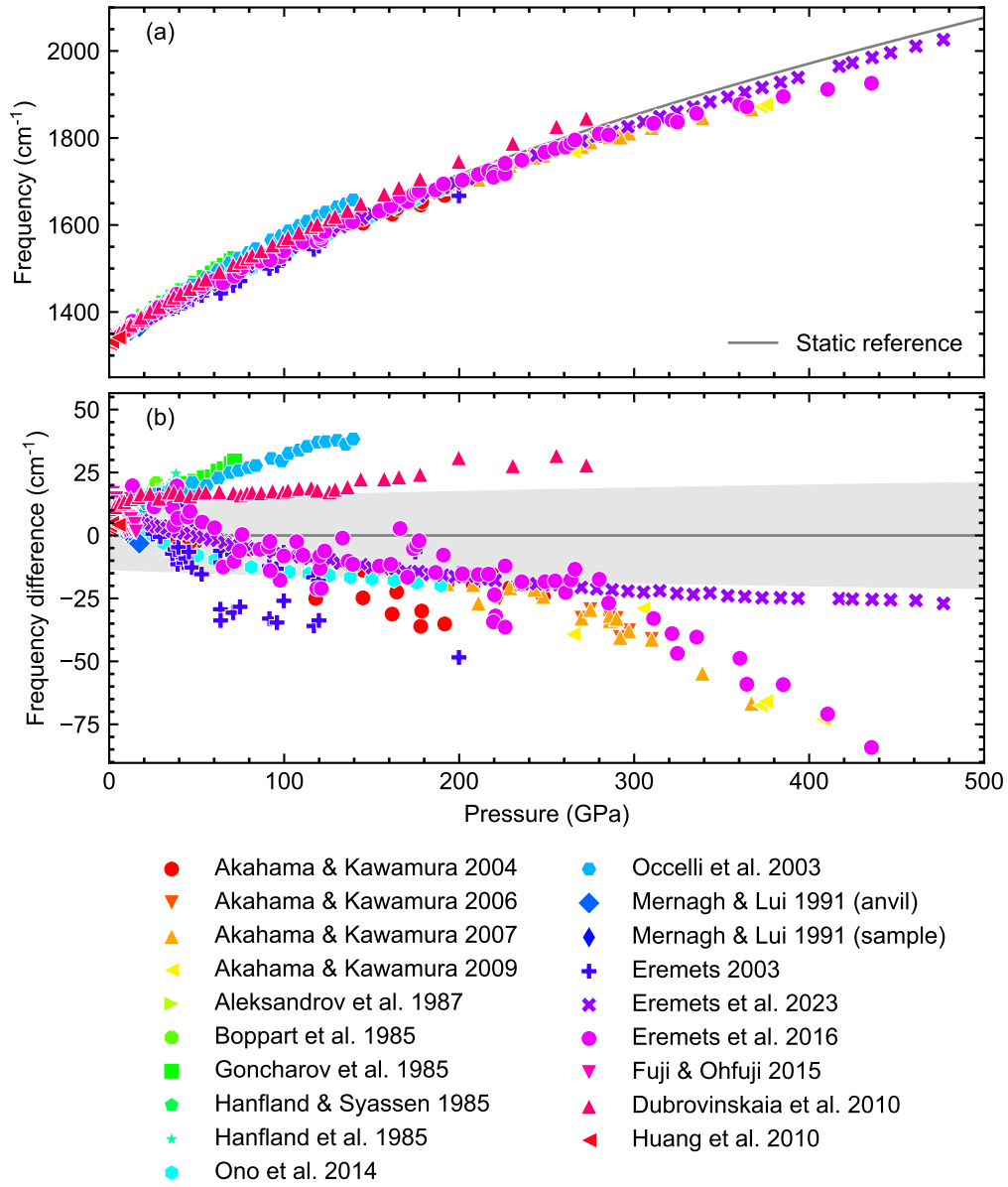


**Figure 7.2** *The Raman frequency of diamond as a function of pressure measured from various experiments on an absolute scale (a) and relative to a reference DFT calculation where the phonon frequency is calculated using harmonic finite displacement and the pressures are found from a Davis–Gordon equation of state fitted to the static crystal energies, with no consideration of the phonon free energy (grey line) (b). The grey region in the bottom panel indicates a  $\pm 1\%$  error of the reference DFT calculation. Experimental data from [133, 142–158].*

### 7.1.1 The diamond edge Raman scale

Hanfland and Syassen first proposed the idea of using the Raman signal from the diamond anvil itself as a pressure marker in 1985 [149]. In their experiment, a linear relation was found between the high-frequency edge of the Raman signal and the pressure. The relation was valid in the range 5 GPa to 30 GPa with a minimal deviation from this linear relationship at pressures below 5 GPa. This deviation was attributed to the plastic deformation of the gaskets under initial loading. This inaugural study positioned the Raman edge as a potentially viable method of determining the pressure inside a DAC, but further study was needed to establish the true calibration of the pressure scale and its transferability between experiments. Such studies have been performed by a number of researchers, and are still being improved upon and updated to this day.

Figure 7.2 shows diamond edge Raman measurements from many different authors. The top panel shows the data on an absolute scale and the bottom panel show the same data relative to a frequency–pressure curve calculated from DFT, where the frequency was calculated using harmonic finite displacement phonon calculations and the pressure found by fitting a Davis–Gordon equation of state to the static crystal energy as a function of volume (with no consideration of the phonon free energy). The same DFT reference curve is shown in the top panel as a grey line.

On the absolute scale, all the data show general agreement and attention must be directed to the bottom panel of figure 7.2 to see subtle variations in the gradients of the reported results. It is striking that, with one exception, the data fall into two distinct groups: one with a low-pressure gradient greater than the reference DFT calculation and one with a low-pressure gradient that is smaller. The exception to this is the data from Dubrovinskaia *et al.* [157] whose low-pressure gradient is close to the reference DFT calculation. If this outlier is removed, the resulting lacuna separates the data into a group that measured the Raman frequency of a sample of diamond suspended in a pressure transmitting medium inside a DAC and a group that measured the high-frequency edge of the Raman signal directly from the anvil. This can also be observed in table 7.1, which shows a summary of the various experiments.

Authors	Year	Pressure (GPa)	Anvil/ Sample	Peak position	Pressure scale	0 GPa Gradient ( $\text{cm}^{-1}/\text{GPa}$ )
Hanfland & Syassen [149]	1985	30	Anvil	HHM	Ruby R1 [139]	2.3(3)
Hanfland <i>et al.</i> [150]	1985	38	Sample	Peak	Ruby R1 [139]	2.90(5)
Boppart <i>et al.</i> [147]	1985	27	Sample	Peak	Ruby R1 [159]	2.87(10)
Goncharov <i>et al.</i> [148]	1985	72	Sample	Peak	Ruby R1 [159]	3.01(2)
Aleksandrov <i>et al.</i> [146]	1987	40	Sample	Peak	Ruby R1 [159]	2.91(3)
Tardieu <i>et al.</i> [160]	1990	15	Sample	Peak	Ruby R1 [139]	2.64(10)
Mernagh & Liu [152]	1991	17	Both	Peak	Ruby R1	1.9
Vohra <i>et al.</i> [161]	1994	250	Anvil	Unknown	Ruby <190 GPa Cu [162] >190 GPa	1.693
Markwell & Butler [163]	1995	6	Anvil	HHM	Raman frequency of $\text{NaNO}_3$ [164]	1.5
Eremets [153]	2003	200	Anvil	Peak	Ruby [165]	2.06
Occelli <i>et al.</i> [133]	2003	140	Sample	Peak	Ruby [159, 166, 167]	2.83(1)

Akahama & Kawamura [142]	2004	250	Anvil	Peak	Ruby [168] <100 GPa Pt [169] >190 GPa Re gasket	2.338(7)
Sun L. <i>et al.</i> [170]	2005	300	Anvil	Linewidth	Pt [169]	1.54(2)
Akahama & Kawamura [143]	2006	310	Anvil	Peak	Pt [169]	2.44(5)
Akahama & Kawamura [144]	2007	367	Anvil	Peak	Pt [169]	2.44(5)
Akahama & Kawamura [145]	2009	410	Anvil	Peak	Pt [169]	2.44(5)
Huang <i>et al.</i> [158]	2010	5	Sample	Peak	R1 Ruby [171]	3.04
Dubrovinskaia <i>et al.</i> [157]	2010	270	Sample	Peak	Ruby [172] <100 GPa Au [173]	2.610(21)
Ono <i>et al.</i> [151]	2014	100	Anvil	Peak	Au and NaCl	2.22(3)
Fujii & Ohfuji [156]	2015	20	Anvil	Peak	Ruby R1 [159]	1.71
Eremets <i>et al.</i> [155]	2016					2.17
Enkovich <i>et al.</i> [105]	2017	70	Anvil		Ruby R1	2.91(2)
Eremets <i>et al.</i> [154]	2023					2.58(2)

**Table 7.1** Summary of Raman edge experiments. The Pressure column indicates the maximum pressure achieved in the experiment; the anvil/sample column states whether the measurement was performed on a diamond sample placed into a DAC, or whether the measurement was performed on the diamond anvil directly; peak position is the method of determining the peak of the Raman spectrum (or high frequency edge if a measurement on the anvil). The peak is found by conventional peak fitting, indicated by “peak”, the height at half maximum (HHM), or by assuming a constant linewidth in the case of Sun *et al.* Pressure scale indicates the method used to determine the pressure; where known, the calibration of the pressure marker has been included as a reference. The final column indicates the zero-pressure gradient of the pressure dependence.

This discrepancy was evident from the beginning with the inaugural work of Hanfland and Syassen in 1985. Another publication in the same year by the same authors, along with three other contributors, performed a similar experiment using a sample of diamond inside a DAC [149, 150]. Both studies reported a linear relation between the Raman frequency and the ruby fluorescence line (and consequently the pressure), but the gradients of these lines were not the same. The experiment that used a diamond sample produced a gradient of  $2.90 \pm 0.05 \text{ cm}^{-1}/\text{GPa}$ , whereas the experiment that used the Raman edge produced a gradient of  $2.3 \pm 0.3 \text{ cm}^{-1}/\text{GPa}$ .

Mernagh and Lui explicitly addressed the discrepancy in the gradients by measuring the Raman frequency both from a sample of diamond in a DAC, and the Raman edge of the anvil. The findings corroborated what had been observed in the two papers by Hanfland and Syassen and coworkers in 1985. The authors observed significant scatter in the data, which they attributed to the uniaxial stress, and this leads the authors to conclude that the Raman edge was not suitable as a pressure marker.

However, the pressure achieved in this experiment was moderate, only 17 GPa, far below the pressures where the Raman edge pressure marker would be most advantageous. The first study to reach these high pressures was conducted by Vohra *et al.*, who observed the Raman edge up to a pressure of 250 GPa [161]. The authors achieved the pressures where the ruby fluorescence becomes unreliable and used x-ray diffraction of copper powder as the pressure marker above 190 GPa. These authors suggested their own calibration for the Raman edge, but one that only applies at pressures greater than 50 GPa.

This ushered in an age of calibrations of the Raman edge to pressures greater than 100 GPa. These were done chiefly by two groups: Akahama and Kawamura, and Eremets. Eremets started first in 2003, establishing a calibration up to 200 GPa [153], then Akahama and Kawamura published four papers over the course of the 2000s, each time increasing the maximum pressure and directing focus to a particular question concerning the universality and practicality of the scale [142–145]. After this, Eremets renewed his interest in the Raman edge with the intent of applying it to high-pressure research on hydrogen [155]. It is Eremets who has reported the highest pressure data for the scale at almost 480 GPa [154].



### 7.1.2 Requirements of the diamond edge pressure scale

In order for the Raman edge to be useful as a pressure marker it must have a universal calibration. The calibration should be independent of pressure transmitting medium, shape of the anvils, and transferable from one experiment to the next. There are three main things to consider when constructing a universal scale. Firstly, the existing pressure scale against which to calibrate the new scale. When calibrating the Raman edge the pressure must be determined accurately in order for the scale to be true. This is a problem common to all pressure markers and self-consistency between the different approaches is the only practical way to ensure they are accurate. The exception to this are *ab initio* calculations such as the ones presented here; these calculations will aid efforts to produce a universal scale, as they are able to determine the pressure independently of any existing pressure calibration. Secondly, the effect of anisotropic stresses in the anvils must be determined. While it is in principle possible to characterise the Raman signal from stressed diamonds, doing so requires knowledge of the exact nature of the stress distribution within the anvil. A scale that relies on a stressed diamond anvil will not be a universal scale, as the stress profile of different anvils could differ significantly [174, 175]. Finally, a consistent method of determining the position of the high-frequency Raman edge must be found, and one that accurately relates to the signal from the true highest pressure in the DAC.

#### Raman edge position

Two principal methods exist in the literature for determining the position of the edge. Firstly, one can find the edge using the minimum of the first derivative of the Raman signal; an example is shown in figure 7.3. The high-frequency edge appears as a minimum in the derivative of the spectrum that may be used to determine its position. The problem with this approach is that the pressure profile in the anvil is non-linear, slowly increasing from the table of the diamond towards the tip with a sharp increase at the end [149]. As a result, a smaller volume of the diamond is at high pressure than at low pressure, and the intensity of the signal at high pressure is reduced compared to the low frequency, zero pressure signal. At very high pressures the diamond tip may be producing a very weak signal compared to the bulk of the anvil meaning that the sharpness of

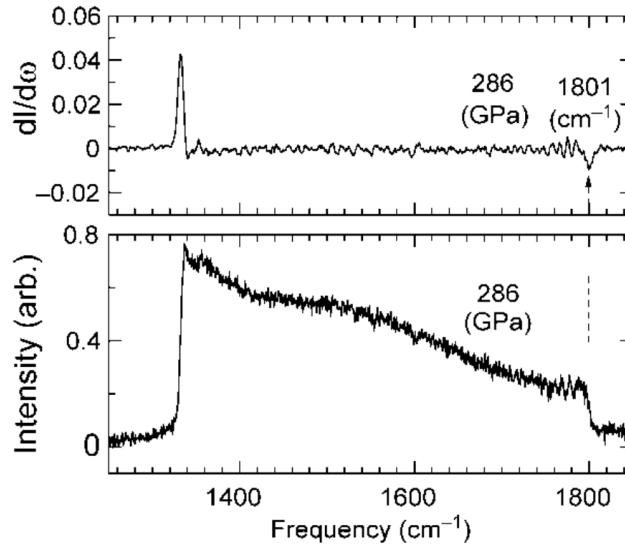


**Figure 7.3** *Raman spectrum of a diamond anvil under load (lower) and the differential spectrum  $\frac{dI}{d\omega}$  (upper). The local minimum in the differential spectrum indicated by the arrow corresponds to the high pressure edge of the anvil. Figure recreated from [144].*

the edge and its signature in the derivative of the spectrum is diminished. This is without considering the axial focussing of the Raman laser which can alter the shape of the observed signal considerably [142, 149]. When determining the position of the edge through the minimum of the first derivative, it is assumed that the laser is sufficiently focussed on the tip that the largest component of the signal comes from the diamond tip.

An alternative approach that does not make this assumption is to use the height at half-maximum treating the high frequency edge as a peak with a definite width [149, 163]. For a laser system that is not highly focussed on the tip, this accounts somewhat for the diminished intensity coming from the smaller volume of the diamond at high pressure. However, the accommodation is imprecise, and there is no guarantee that the height at half-maximum will correspond to the signal from the highest pressure. This method is again best suited to signals where the edge is sharply defined in the Raman spectrum.

A final approach, taken by Sun *et al.* [170], is to subtract the (half-)width of the zero-pressure signal from the highest frequency observed with non-zero intensity. If the linewidth of the Raman signal is constant under pressure (approximately true) then a volume element of diamond under hydrostatic conditions will produce

a Raman peak centred at some frequency with a fixed width. The peak of this signal will always be a fixed distance from the highest observed frequency, although the smooth nature of the peak makes it difficult to determine where this starts. Although Sun *et al.* use the full width at half maximum, it would perhaps be more appropriate to use the half width.

### Non-hydrostatic effects

The question of non-hydrostaticity was addressed directly by Akahama and Kawamura [144]. In non-hydrostatic conditions, the triply degenerate  $T_{2g}$  mode of diamond splits into either three singly-degenerate modes ( $\omega_1$ ,  $\omega_2$ ,  $\omega_3$ ) or one singly-degenerate mode and one doubly-degenerate mode ( $\omega_S$  and  $\omega_D$ ). The exact nature of the splitting depends on the orientation of the crystal. Akahama and Kawamura took advantage of this orientational dependency and, by using anvils of different crystallographic orientations together with appropriate polarisation filters, observed the different frequencies of the split modes. When both the anvil (loading) axis and the incident Raman laser are along the [001], [110], and [111] direction, the splittings are given by

$$F//[001] \quad \omega_S = \omega_H + \frac{2}{3}\Delta\omega_{[001]} \quad (7.1)$$

$$\omega_D = \omega_H - \frac{1}{3}\Delta\omega_{[001]} \quad (7.2)$$

$$F//[110] \quad \omega_1 = \omega_H - \frac{1}{3}\Delta\omega_{[001]} \quad (7.3)$$

$$\omega_2 = \omega_H + \frac{1}{6}\Delta\omega_{[001]} + \frac{1}{2}\Delta\omega_{[111]} \quad (7.4)$$

$$\omega_3 = \omega_H + \frac{1}{6}\Delta\omega_{[001]} - \frac{1}{2}\Delta\omega_{[111]} \quad (7.5)$$

$$F//[111] \quad \omega_S = \omega_H + \frac{2}{3}\Delta\omega_{[111]} \quad (7.6)$$

$$\omega_D = \omega_H - \frac{1}{3}\Delta\omega_{[111]} . \quad (7.7)$$

The magnitude of the splitting is determined by the  $\Delta\omega$ s and depends on the stress in each direction. One could, in theory, determine the hydrostatic pressure  $\omega_H$  by treating the above equations as a system of linear equations with unknowns, but this does not fully remove the need to consider stress effects, as the hydrostatic pressure in the diamond is *not* the pressure in the sample chamber. A typical edge

calibration experiment will use diamond anvils oriented such that the axial force is along the [001] direction. In the sample chamber there is a metal sample or ruby chip to determine the pressure suspended in a hydrostatic pressure-transmitting medium. The pressure of this medium, and thus the metal or ruby, will equilibrate with the *axial* stress at the tip of the diamond.

The Raman frequency will typically be measured in the back scattering geometry, focussing the laser at the very tip of the anvil. If the tip of the diamond is not under hydrostatic conditions, the triply degenerate  $T_{2g}$  mode of diamond will, for stress in the [001] direction, split into a singlet state and a doublet state whose frequencies  $\omega_S$  and  $\omega_D$  are related to the hydrostatic triplet frequency,  $\omega_H$ , by equations 7.1 and 7.2.

When the diamond anvil is compressed,  $\Delta\omega_{[001]}$  is negative, meaning  $\omega_S < \omega_H < \omega_D$ . In the back scattering geometry with [001] oriented diamonds, one does not observe the doublet state due to properties of the polarisation tensor. Therefore, the typical edge calibration experiment observes only the lower frequency singlet state and consequently underestimates the hydrostatic pressure at the diamond tip.

The magnitude of the splitting depends on the difference between the axial and radial stress ( $\sigma_z$  and  $\sigma_R$ , respectively). One may define the difference between the axial and the radial stress as

$$\tau = \sigma_z - \sigma_R . \quad (7.8)$$

Exactly how the axial–radial stress difference depends on the hydrostatic pressure will depend on the shape of the diamond and the construction of the DAC, but the data in figure 7.2, which shows many experiments from different anvil experiments to have a similar gradient, indicates it could be quite consistent. Nevertheless, one would expect a monotonic increase of  $\tau$  with pressure, meaning the magnitude of the splitting will also increase monotonically. Since  $\Delta\omega_{[001]}$  is negative, the observed singlet frequency falls further below the hydrostatic triplet frequency with increasing pressure, manifesting as a lower gradient for  $\omega_S$  than  $\omega_H$ . This explains the difference in gradients between the two groups in figure 7.2.

Ideally, one wishes to determine the axial stress  $\omega_z$  in some way. If both  $\omega_H$

and  $\omega_S$  were known then it would in principle be possible to obtain  $\tau$  from the difference between  $\omega_H$ , and  $\omega_S$ . As  $\omega_H$  is related to the hydrostatic component of the stress,  $\sigma_H$  (equivalently the average stress), it is also in principle possible to obtain  $\sigma_H$  from  $\omega_H$ .

The average stress is given by

$$\sigma_H = \frac{1}{3}(\sigma_z + 2\sigma_R) \quad (7.9)$$

If both  $\tau$  and  $\sigma_H$  are known, then one can determine  $\sigma_R$  and, crucially,  $\sigma_z$  as

$$\sigma_R = \sigma_H - \frac{1}{3}\tau \quad (7.10)$$

$$\sigma_z = \sigma_H + \frac{2}{3}\tau \quad (7.11)$$

The drawback of this method is that one cannot determine  $\omega_H$ , from a single, or even multiple, measurements of  $\omega_S$ . There are four possible solutions to this problem. Firstly, one may create a calibration of  $\omega_H$  and  $\omega_S$  against an external pressure scale and assume this scale is universal to all DAC experiments. This could be a viable approach given that there is some consistency in the gradients of Raman edge calibrations, indicating a consistent stress difference. However, the gradients are not completely uniform and there is some scatter in the data.

Another solution might be to use a transmission scattering geometry to observe both the singlet and the doublet state, from which  $\omega_H$  can be deduced, but this is in general not practical for diamond anvil experiments due to difficulties of discerning the weak Raman signal from the strong laser and reflections from each of the diamond surfaces weakening the signal. In high-pressure experiments the only commonly employed geometry for Raman experiments is the backscattering one.

A third solution is to follow the approach of Akahama and Kawamura and use an anvil oriented with the [110] direction as the direction of applied force. In this configuration, with appropriate polarisation filters, all three singlet states can be observed. From these three frequencies, the hydrostatic frequency and the axial-radial stress difference can be deduced. This is not the typical orientation for diamond anvils and, although pressures of 250 GPa were achieved, it is not clear how much higher this could be driven. Additionally, as a diamond is stressed

it becomes birefringent. Linearly polarised light such as the type needed to observe the three Raman frequencies of a  $[110]$  stressed anvil becomes elliptically polarised as it travels through the diamond. This makes it difficult to target certain selection rules and determine the individual frequencies. Akahama and Kawamura do not comment on their polarisation setup in detail.

Finally one may insert a chip of diamond into the sample chamber in a similar spirit to ruby fluorescence and current equation of state pressure markers. This eliminates the need to consider the axial–radial stress difference in the anvil, but a Raman experiment on a diamond chip in the sample chamber is marred by difficulties discerning the signal from the chip and the signal from the nearby anvil tip which is at a similar pressure, but it has been achieved by several authors [133, 146–148, 150, 160]. In this method one is guaranteed that the pressure of the diamond chip is very close to that of the sample.

In all of these possible approaches, the calibration of the hydrostatic Raman signal of diamond as a function of pressure is essential. It is to this end that the following investigation has been undertaken, to provide from first principles, and to the best accuracy allowed by current theory, a calibration of the Raman frequency of diamond as a function of temperature and pressure.

## 7.2 Methods

The calculation of the Raman frequency in diamond as a function of pressure was done using the TDEP formalism described in section 4.3. This section will detail the specifics of the application of the formalism to diamond as well as some extensions that were made to the standard approach.

The investigation was performed in three stages:

1. TDEP calculations were performed at temperatures from 0 K to 2000 K for a series of 17 volumes corresponding to pressures from 0 GPa to 1000 GPa, and the zone-centre phonon frequency and phonon free energies were computed for each case. The TDEP calculations require a harmonic finite-displacement calculation to generate the configurations; frequencies and phonon free energies were found for these calculations also.
2. An equation of state was fitted to the resulting free-energy–volume curve, and an extended mode Grüneisen model was fitted to the volume–frequency curve at each temperature.
3. At this stage it is possible to relate the pressure to a volume through the equation of state and the volume to a frequency through the extended mode Grüneisen model at the specific temperature of the TDEP calcs in step 1 and at any pressure. The results were generalised to an arbitrary temperature by interpolation of the fitting parameters.

This process allows the zone-centre optical phonon frequency in diamond to be evaluated at any temperature and pressure within the pressure and temperature ranges specified in step 1. Three levels of theory were used to compute the phonon free energies and phonon frequencies: the quasiharmonic from the finite difference calculations, the effective harmonic from the TDEP approach, and the effective harmonic with 3-phonon corrections included through the Kramers–Kronig relations. For each of these levels of theory the fitting and interpolation described in steps 2 and 3 was performed.

### 7.2.1 TDEP calculations

The harmonic force constants necessary to compute the phonon frequencies and eigenvectors used to generate the TDEP configurations were calculated using the finite displacement method on a  $5 \times 5 \times 5$  supercell of the primitive unit cell with the atom at the origin displaced  $0.1 \text{ \AA}$  in the positive  $x$  direction. The DFT calculations were performed using a 550 eV plane-wave energy cutoff, a convergence criterion of  $1 \times 10^{-9} \text{ eV}$ , and a k-point grid generated from the getKPoints utility with a density equivalent to a  $5 \times 5 \times 5$  Monkhorst-Pack grid [88, 89]. The LDA was used, as it was shown in the previous chapter that it most accurately reproduced the experimental phonon frequencies once the phonon free energy is accounted for. As demonstrated in the previous chapter, changing the XC functional creates a constant offset of the absolute phonon frequencies of up to  $30 \text{ cm}^{-1}$ , or 2%; relative changes in the phonon frequencies are unaffected. The standard “C” PAW pseudopotential developed by Kresse and provided by the VASP library with the  $2s$  and  $2p$  electrons as valence electrons was also used [69].

The TDEP calculations were performed by generating 30 configurations at each of the 17 volumes for 11 temperatures between 0 K and 2000 K, using the same seed for the random number generator in each case. An improvement to the method of generating the configurations, described below, allowed the scatter in the phonon frequency seen in the previous chapter to be almost completely eliminated. The TDEP DFT calculations used the same settings as the finite displacement calculations, except that the plane-wave energy cutoff was increased to 850 eV.

#### Generation of the configurations

The general method for creating the configurations used in TDEP is described in section 4.3, but for this investigation it was necessary to pay careful attention to the eigenvectors of the phonon modes used to generate the configuration. As with previous investigations in this thesis, an effort was made to reduce the random scatter in the phonon frequencies introduced by the stochastic generation of the configurations; this was, in part, achieved by using the same seed for the random number generator at each volume. However, it was observed that this alone was



insufficient to maintain similarity between the configurations at different volumes. It was found that the eigenvectors were changing dramatically from one volume to the next. In particular, the phonon eigenvectors at points in the Brillouin zone where the frequencies are degenerate are not uniquely defined, and were being assigned an almost random orientation whilst still being a valid diagonalisation of the dynamical matrix.

Recall that the eigenvectors of, for example, a doubly degenerate phonon mode are confined to a  $2D$ -plane, and it is valid to choose any pair of orthogonal eigenvectors in this plane to define the phonons. Changes in the force constants between the volumes manifested as small changes in the dynamical matrix, which caused the numerical diagonalisation routines to select completely different eigenvectors at the degenerate points. This is the same problem that occurred in the previous chapter and was overcome by using the same harmonic finite displacement calculation for both isotopes.

Although freedom in the definition of the eigenvectors was a problem most pronounced at points in the Brillouin zone where the phonons have degenerate frequencies, there are other freedoms in choosing the eigenvectors that produced similar problems, although less frequently, at non-degenerate points. One such problem was that the eigenvectors are defined only up to a complex phase, and a different phase could be chosen from one volume to the next. A second problem was that the assignment of band indices to the eigenvalues and eigenvectors is arbitrary. If phonons swapped band indices between volumes then the random weight assigned by the configuration generation process would be swapped also. Figure 7.4 shows how two eigenvectors may change between two volumes.

To correct these issues, the following procedure was employed. The dynamical matrix was computed over a small line in the Brillouin zone from the point  $(d_1, d_2, d_3)$  to  $(d_1, d_2, d_3) + (0.001, 0.002, 0.003)$ , and the real and imaginary components of the eigenvectors were extrapolated to the point  $(d_1, d_2, d_3)$  by cubic splines. At each point along the line it was necessary to re-index and align the phases of the eigenvectors such that the components of each eigenvector varied smoothly. The eigenvectors were aligned by taking one eigenvector at one point along the line as the reference eigenvector, and searching through the eigenvectors of the adjacent point for the candidate eigenvector with the largest absolute value of the dot product with the reference eigenvector. An eigenvector that is mostly

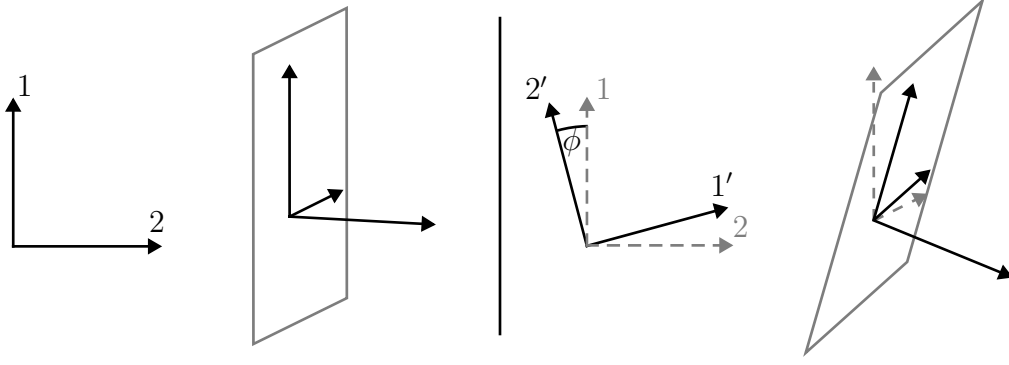


**Figure 7.4** *Diagram of eigenvectors at the same two-fold degenerate point in the Brillouin zone at two different volumes on the left and right of the centre line. The out-of-plane, non-degenerate eigenvector may move a small amount determined by the dynamical matrix. The in-plane eigenvectors are not constrained within the plane and may therefore be rotated by an arbitrary angle  $\phi$ . Note also that the labelling of the eigenvectors has been swapped between the left and right volumes.*

aligned with the reference eigenvector should have a dot product of approximately 1 (up to a complex phase) while the other, almost orthogonal, eigenvectors should be close to zero. Mathematically this is expressed as

$$\mathbf{e}_{\text{ref}} \cdot \mathbf{e}_{\text{cand}} \approx \begin{cases} 1 \times e^{i\theta} & \text{if aligned} \\ 0 & \text{otherwise.} \end{cases} \quad (7.12)$$

The appropriate candidate was then divided by  $e^{i\theta}$  to ensure the phases of the reference and candidate eigenvectors were similar, and then the candidate was accepted as the new reference and the process was repeated at the next point along the line.

Applying this approach to align the eigenvectors along the line in the Brillouin zone and extrapolating to the degenerate point allowed the eigenvectors at the degenerate points to be uniquely defined *up to a phase and labelling of the band indices*. To ensure that eigenvectors were aligned (and thus receiving the same random weighting when generating the configurations) across the different volumes, it was necessary to repeat the alignment process just described, this time using eigenvectors from two adjacent volumes as the reference and candidate eigenvectors.

### 7.2.2 Fitting

Step 2 of the process described at the start of the section illustrated the need to fit an equation of state to the free-energy–volume data to relate the pressure to the volume, as well as the need to fit the volume–frequency data to an extended mode Grüneisen model to relate the volume to a zone-centre optical phonon frequency.

#### Volume–Frequency fitting

The typical way to relate a change in volume to a change in phonon frequency is through the mode Grüneisen parameter  $\gamma$  defined as

$$\gamma = \frac{V_0}{\omega_0} \frac{d\omega}{dV} = \frac{d \ln(\omega/\omega_0)}{d \ln(V/V_0)}, \quad (7.13)$$

which, if  $\gamma$  is constant, describes a linear relation between the natural logarithm of the frequency and the natural logarithm of the volume. In the common case of  $\gamma \approx 1$  the phonon frequency is related to the volume as  $\omega \propto \frac{1}{V}$ . In this investigation, however, it was necessary to go beyond this simple relationship and extend the mode Grüneisen parameter to include higher order terms. The form of this expansion is derived as follows.

First, define variables  $x = \ln(V/V_0)$  and  $y = \ln(\omega/\omega_0)$ , and  $x_0 = \ln(V_0/V_0) = 0$  and  $y_0 = \ln(\omega_0/\omega_0) = 0$ , where  $\omega = \omega_0$  when  $V = V_0$ . One can describe the relationship between  $x$  and  $y$  through a Taylor expansion,

$$y = y(x_0) + \left. \frac{dy}{dx} \right|_{x=x_0} (x - x_0) + \frac{1}{2} \left. \frac{d^2y}{dx^2} \right|_{x=x_0} (x - x_0)^2 + \frac{1}{6} \left. \frac{d^3y}{dx^3} \right|_{x=x_0} (x - x_0)^3 + \dots \quad (7.14)$$

Transforming this back to the original variables this becomes

$$\begin{aligned}\ln(\omega/\omega_0) = \ln(\omega_0/\omega_0) &+ \left. \frac{d \ln(\omega/\omega_0)}{d \ln(V/V_0)} \right|_{V=V_0} (\ln(V/V_0) - \ln(V_0/V_0)) \\ &+ \frac{1}{2} \left. \frac{d^2 \ln(\omega/\omega_0)}{d [\ln(V/V_0)]^2} \right|_{V=V_0} [\ln(V/V_0) - \ln(V_0/V_0)]^2 \\ &+ \frac{1}{6} \left. \frac{d^3 \ln(\omega/\omega_0)}{d [\ln(V/V_0)]^3} \right|_{V=V_0} [\ln(V/V_0) - \ln(V_0/V_0)]^3 + \dots\end{aligned}\quad (7.15)$$

Defining

$$\gamma_n = \frac{1}{n!} \left. \frac{d^n \ln(\omega/\omega_0)}{d [\ln(V/V_0)]^n} \right|_{V=V_0} \quad (7.16)$$

one arrives at

$$\ln(\omega/\omega_0) = \gamma_1(\ln(V/V_0)) + \gamma_2[\ln(V/V_0)]^2 + \gamma_3[\ln(V/V_0)]^3 + \dots \quad (7.17)$$

where  $\gamma_1$  is the well-known linear mode Grüneisen parameter.

The frequency  $\omega$  is given by

$$\omega = \omega_0 \exp \left\{ \gamma_1(\ln(V/V_0)) + \gamma_2[\ln(V/V_0)]^2 + \gamma_3[\ln(V/V_0)]^3 + \dots \right\} \quad (7.18)$$

For this investigation the terms up to and including second order ( $\gamma_2$ ) were preserved. A comparison of the different orders of equation 7.18 on some representative frequency–volume data is shown in figure 7.5. The residual plot shows that the first-order mode Grüneisen model is insufficient to describe the frequency–volume relationship, and that higher orders cannot be meaningfully distinguished and that the series expansion had converged by second order. Including orders higher than second order was found to introduce overfitting in later stages of the process.

## Energy–Volume fitting

The phonon free energies and volumes calculated in step 1 may be related through an equation of state. There are many suggested analytic expressions for equations of state, although they are most commonly stated as relations between the pressure and the volume,  $P(V)$ , rather than the energy and the volume,  $E(V)$ .

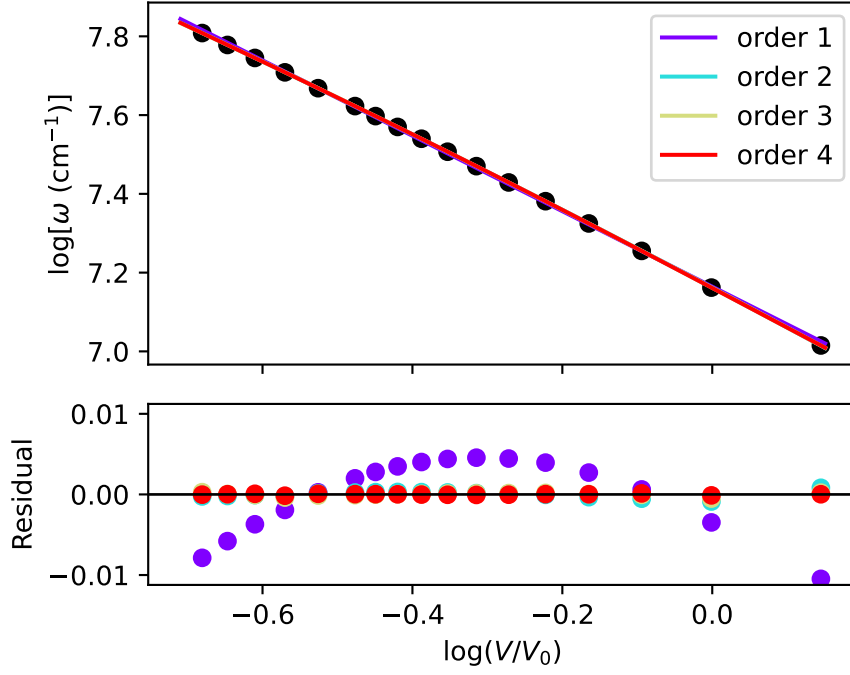


**Figure 7.5** *Frequency–volume fitting for different orders of  $\gamma_n$ . The frequencies are calculated using the effective harmonic potential with 3-phonon corrections included.*

These two forms are related through the expression

$$P(V) = -\frac{dE(V)}{dV} . \quad (7.19)$$

By integrating the pressure–volume relation one may obtain the energy–volume relation more useful to first-principles calculations, where the energy is more readily calculated. A library of such equations of state has been compiled by Karl Syassen in his program DatLab [176]. This program had the functionality of fitting multiple equations of state to energy–volume data and comparing the fitted parameters and goodness-of-fit for each. However, owing to the age of the program and its incompatibility with modern operating systems it was impractical to use for this investigation.

A small python package was therefore written to implement this functionality. The equations of state were transcribed from the DatLab manual, correcting some errors and validating the integrations of the pressure–volume relations. Each

Equation of state	$B_0$ (GPa)	$B'_0$	$V_0$ ( $\text{\AA}^3$ )	$\chi^2$
Davis-Gordon O3	455.3(5)	3.62(1)	5.5892(4)	$9.89 \times 10^{-7}$
Davis-Gordon	454.9(3)	3.632(3)	5.5892(4)	$1.07 \times 10^{-6}$
Modified True Strain	456.6(4)	3.1870(9)	5.5901(5)	$1.66 \times 10^{-6}$
Holzapfel-AP1	458.7(7)	3.508(4)	5.5904(8)	$5.29 \times 10^{-6}$
Modified Rydberg	452.2(7)	3.662(5)	5.5898(9)	$6.41 \times 10^{-6}$
Birch-3	452.8(6)	3.611(2)	5.5910(9)	$6.50 \times 10^{-6}$
Bardeen	463(1)	3.418(8)	5.591(2)	$2.20 \times 10^{-5}$
Rydberg-Vinet	446(2)	3.82(1)	5.589(2)	$4.41 \times 10^{-5}$
Murnaghan	487(5)	2.87(2)	5.593(7)	$4.14 \times 10^{-4}$

**Table 7.2** *Fitting parameters for some equations of state of diamond at 0 K for the harmonic energies.  $B_0$  is the zero-pressure bulk modulus,  $B'_0$  is the pressure derivative of the bulk modulus at zero-pressure, and  $V_0$  is the equilibrium volume.*

equation of state was fitted to the energy–volume data and the  $\chi^2$ ,

$$\chi^2 = \sum_i (E_i^{\text{fit}} - E_i^{\text{DFT}})^2, \quad (7.20)$$

was compared for each. A representative summary of the fitting for the quasiharmonic theory at 0 K is shown in table 7.2.

For all levels of theory at all temperatures, the equation of state that gave the lowest  $\chi^2$  was the third-order Davis-Gordon equation. This equation of state uses a higher-order expansion of the bulk modulus than the other equations which allows greater flexibility of the function. In the least-squares sense this function fits the data best, but it was found that the first and second pressure derivative of the bulk modulus were highly correlated. This caused the first and second derivative of the bulk modulus not to vary smoothly between fits at different temperatures, and made interpolation to an arbitrary temperature difficult. The decision was therefore made to discount the third order Davis-Gordon equation and use the second order Davis-Gordon equation as the energy–volume relation. The form of this equation of state is

$$U(V) = U_0 - B_0 \left[ (B'_0 - 2)V_0 \log \left( \frac{V}{V_0} \right) + \frac{1}{2}(B'_0 - 3)(V - V_0) + \frac{1}{2}(B'_0 - 1)V_0 \frac{V - V_0}{V} \right]. \quad (7.21)$$

The fitting parameters  $U_0$ ,  $B_0$ ,  $B'_0$ , and  $V_0$  are zero-pressure values for the internal energy, bulk modulus, pressure derivative of the bulk modulus, and volume per atom respectively. These same parameters (with the exception of  $U_0$ ) can then be used to relate the volume to the pressure as

$$P(V) = B_0 \frac{V_0 - V}{V} \left[ 1 + \frac{1}{2}(B'_0 - 1) \frac{V_0 - V}{V} \right] . \quad (7.22)$$

### 7.2.3 Temperature interpolation

The above fitting processes relate the phonon free energy calculated at a specific temperature to a volume, and a volume to a frequency calculated from a temperature-dependent effective potential. Using the fitted parameters from the energy–volume and volume–frequency fitting, one can determine the frequency of the zone-centre optical phonon at any pressure, but only at the specific temperatures which the TDEP calculations were performed at. To determine the frequency at *any* temperature one must interpolate the fitted parameters to find an appropriate set of values at intermediate temperatures. All the parameters show a similar dependence on the temperature: at low temperature the parameters are temperature independent with the gradient at 0 K being zero due to the third law of thermodynamics, then, at some temperature, the gradient smoothly becomes finite before the function ends up linear at high temperature. This smooth step in the gradient from zero to some constant value suggests that the fitting parameters of the energy– and frequency–volume relations should be fitted with the integral of a sigmoidal function. The function chosen was the logistic function resulting in a parameter  $X(T)$  being fitted to the function

$$X(T) = \int_{-\infty}^T \frac{L}{1 + e^{-k(T'-T_0)}} dT' + C \quad (7.23)$$

$$= \frac{L}{k} \ln [e^{k(T-T_0)} + 1] + C , \quad (7.24)$$

with each parameter of the energy– and frequency–volume relations having different values of  $L$ ,  $k$ ,  $T_0$ , and  $C$ .

In the logistic function,  $L$  describes the step height,  $k$  the width of the step, and  $T_0$  the step position. In the integrated form, these parameters determine the final linear gradient, the sharpness of the transition, and the position of the transition

respectively. The constant  $C$  determines the value of  $X$  at  $T = -\infty$ , which is approximately equal to the  $T = 0$  K value.



## 7.3 Results

The results of this investigation are, in effect, presented thrice, once for each level of phonon theory: “quasiharmonic”, in which the phonons are purely harmonic and the force constants are calculated as the second derivative of the interatomic potential at small finite displacement; “effective harmonic”, where the phonons are described using an *effective* harmonic potential at a specific temperature; and “effective harmonic with 3-phonon corrections”, where the phonon frequencies are determined with the same effective harmonic potential as previously, but with the antisymmetric parts of the potential accounted for by the 3-phonon interactions calculated using the Kramers–Kronig relations. Mention may also be made of the “static” case, where the phonon frequencies are calculated with the harmonic potential, but the phonon free energies are not accounted for and only the static crystal energy is used.

The previous section ended with a description of the interpolation process using an integrated logistic function to evaluate the zone-centre optical phonon frequency at any temperature and pressure. The fitted parameters of the equation of state and mode Grüneisen model, along with their interpolations, are shown in figure 7.6. Almost all the parameters show the same trend on increasing temperature: the parameters begin flat at low temperature before the gradient either increases or decreases to a linear relationship at high temperature. The parameter  $T_0$  gives a measure of the position about which the change in gradient is centred. Examination of table 7.3 shows that, except for the mode Grüneisen parameters for the quasiharmonic and effective harmonic cases, where the trend is not observed, the values lie between 250 K to 550 K. One may treat this range as the onset of finite temperature effects in diamond. Room temperature (300 K) is towards the lower end of this range, so finite temperature effects are likely to be small but noticeable. The other parameter that does not fall in this range is the equilibrium crystal energy  $U_0$ , but this parameter is not used in the calculation of the pressure–volume relation and is therefore not shown in figure 7.6.

The onset of finite-temperature effects is not the same for each parameter. The bulk modulus and its pressure derivative have the lowest values of  $T_0$ , indicating that the elastic properties are affected by temperature first, followed by the volume effects at around 530 K. The equilibrium volume as a function

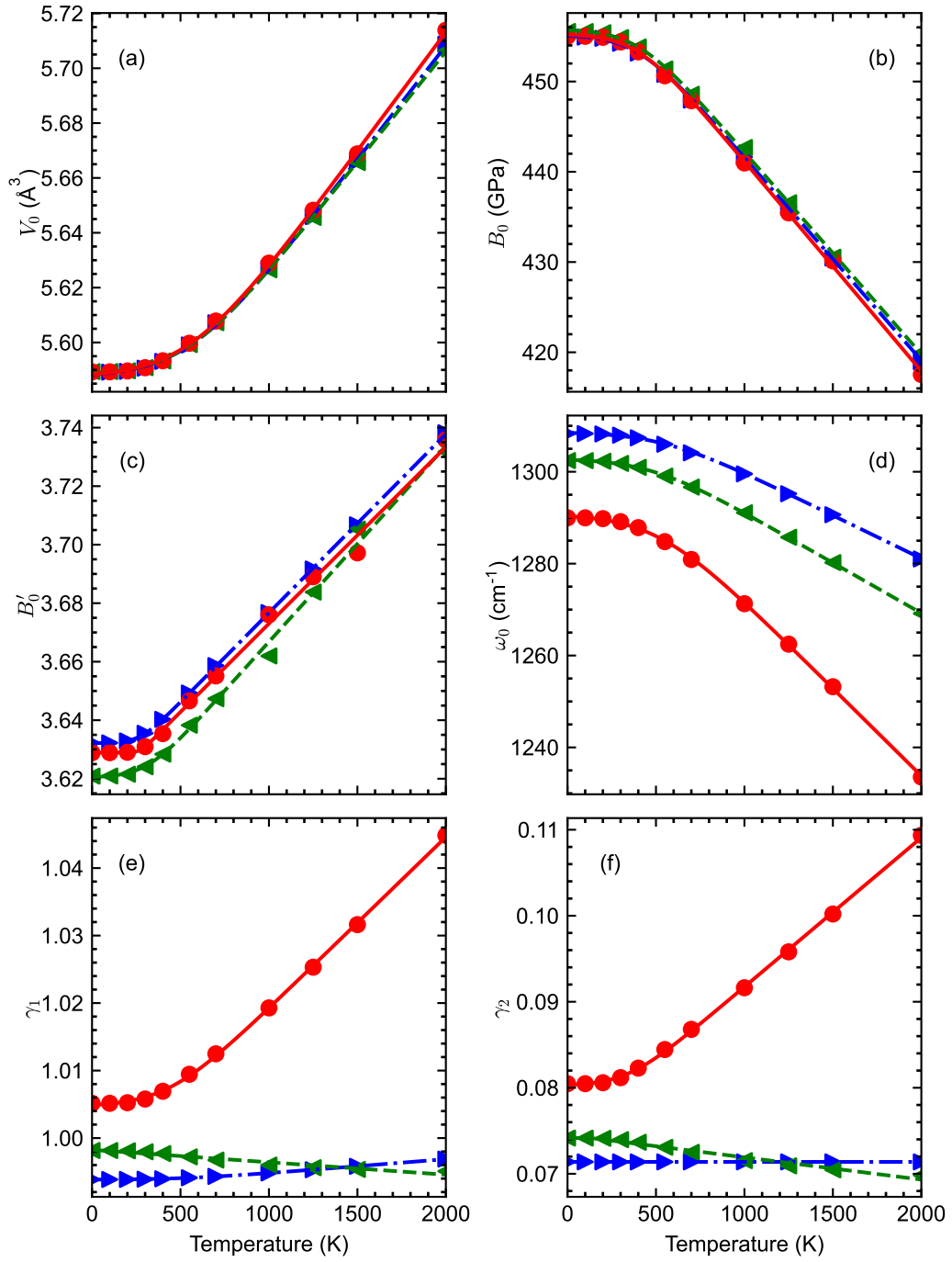


**Figure 7.6** *Calculated equation of state and frequency–volume parameters of diamond and the fitted integrated logistic function for each. Blue right triangles show the quasi-harmonic parameters, green left triangles indicate the effective harmonic parameters, and red circles indicate the effective harmonic parameters with 3-phonon scattering included.*

Parameter		$L$	$k$ (K <sup>-1</sup> )	$T_0$ (K)	$C$
Quasiharmonic	$U_0$	$-3.47(11) \times 10^4$	$3.6180(3) \times 10^2$	887(29)	-9.937(2)
	$V_0$	$8.31(14) \times 10^5$	$5.0930(5) \times 10^2$	545(16)	5.587(7)
	$B_0$	$-2.2476(2) \times 10^2$	$7.9(8) \times 10^3$	394(9)	455.2(2)
	$B'_0$	$6.110(24) \times 10^5$	$1.8(3) \times 10^2$	271(5)	3.6321(2)
	$\omega_0$	$-1.87(3) \times 10^2$	$5.33(5) \times 10^3$	530(14)	1308.7(2)
	$\gamma_1$	$2.08(3) \times 10^6$	$5.2(5) \times 10^3$	537(15)	0.99382(2)
	$\gamma_2$	$-1.90 \times 10^{11}$	$4 \times 10^2$	1669	0.07
Effective harmonic	$U_0$	$-3.5(1) \times 10^4$	$3.6(3) \times 10^3$	887(29)	-9.932(2)
	$V_0$	$8.1(1) \times 10^5$	$5.4(5) \times 10^3$	533(12)	5.5878(6)
	$B_0$	$-2.24(3) \times 10^2$	$8.2(16) \times 10^3$	393(16)	455.8(3)
	$B'_0$	$6.7(3) \times 10^5$	$1.1(9) \times 10^2$	307(47)	3.62(3)
	$\omega_0$	$-2.19(2) \times 10^2$	$5.7(5) \times 10^3$	466(11)	1302.9(2)
	$\gamma_1$	$-1.8422 \times 10^6$	$7.22 \times 10^2$	-685	0.99952
	$\gamma_2$	$-2.6(2) \times 10^6$	$1.5 \times 10^{01}$	135	0.07412(3)
Effective harmonic + 3-phonon	$U_0$	$-3.6(1) \times 10^4$	$3.6(3) \times 10^3$	888(28)	-9.939(2)
	$V_0$	$8.7(2) \times 10^5$	$5.0(6) \times 10^3$	548(18)	5.5873(10)
	$B_0$	$-2.32(4) \times 10^2$	$8.3(17) \times 10^3$	391(17)	455.3(3)
	$B'_0$	$6.0(2) \times 10^5$	$5.2(306) \times 10^2$	270(40)	3.629(2)
	$\omega_0$	$-3.81(6) \times 10^2$	$5.4(5) \times 10^3$	504(14)	1290.8(4)
	$\gamma_1$	$2.54(4) \times 10^5$	$6.5(9) \times 10^3$	428(15)	1.0046(3)
	$\gamma_2$	$1.74(2) \times 10^5$	$8.6(18) \times 10^3$	337(16)	0.0802(2)

**Table 7.3** *Parameters to interpolate the frequency–volume and energy–volume coefficients to arbitrary temperature.  $L$  is in units of  $[Q]/K$  and  $C$  is in units of  $[Q]$ , where  $[Q]$  is eV for  $U_0$ , Å<sup>3</sup> for  $V_0$ , GPa for  $B_0$ , cm<sup>-1</sup> for  $\omega_0$ , and dimensionless for  $B'_0$ ,  $\gamma_1$ , and  $\gamma_2$ .*

of temperature (figure 7.6, panel (a)) indicates the thermal expansion of the crystal. These data show that there is little thermal expansion below 500 K; this is supported by the results of Jacobson and Stoupin, whose integrated thermal expansion data showed little increase in the lattice parameter below 500 K [90]. The onset of finite temperature effects in the zone-centre phonon frequency  $\omega_0$  occurs between 466 cm<sup>-1</sup> and 530 cm<sup>-1</sup>. This broadly aligns with what has been seen in the previous chapters, particularly chapter 5.

The values of the parameter  $C$  in the interpolation function (equation 7.23) is, in most cases, largely unchanged between the different levels of theory. This parameter represents the value at  $T = -\infty$  and therefore one would not expect any anharmonic effects at all; agreement in this parameter across the levels of

theory indicates that all three levels agree on the low-temperature behaviour of the zone-centre phonon frequency.

The foremost aim of this investigation was to determine the pressure and temperature dependence of the zone-centre Raman frequency of diamond. The temperature dependence at ambient pressure and the pressure dependence at ambient temperature are shown in figures 7.7 and 7.8, respectively.

On an absolute scale, the calculated pressure dependence at 300 K follows the experimental data very well as evidenced by the top panel of figure 7.7. Only compared to the reference calculation in the bottom panel, where harmonic phonon frequencies from the finite displacement method are used as the reference calculation, and no consideration of the phonon free energy is made, can differences be seen clearly. All three levels of theory show a very similar trend, distinguished essentially by nearly constant offsets. Examination of the bottom panel in figure 7.7 shows that the gradients of the calculated lines fall in the gap between experiments that used a diamond sample and experiments that used the anvil, and even the most extreme outliers do not differ from the calculated values by more than a few percent.

One study that stands out as being closely aligned with the calculated results is the study by Eremets *et al.* [154]. This is the most recent calibration of the diamond edge Raman scale, published in February 2023. Although the low-pressure gradient follows the usual pattern of being below that of the reference calculation, at pressures of a few Mbar the gradient increases and becomes much more aligned with that of the TDEP calculations. Even on an absolute scale the data start to agree well with the effective harmonic calculations with 3-phonon effects included. This is an encouraging result and suggests that, despite the differences in the Raman signal between the diamond edge and hydrostatic diamond, the *ab initio* calculations presented here could be a better calibration of the diamond edge Raman scale at high pressures than expected. If this is true, then this is particularly useful at high temperatures, where no experimental calibrations exist. The results presented in the thesis thus far have shown that TDEP can accurately predict the temperature dependence of the zone-centre optical phonon frequency at ambient pressure, and figure 7.7 shows that it can predict the pressure dependence of the zone-centre optical phonon frequency at ambient temperature reasonably well also. It is therefore believable that

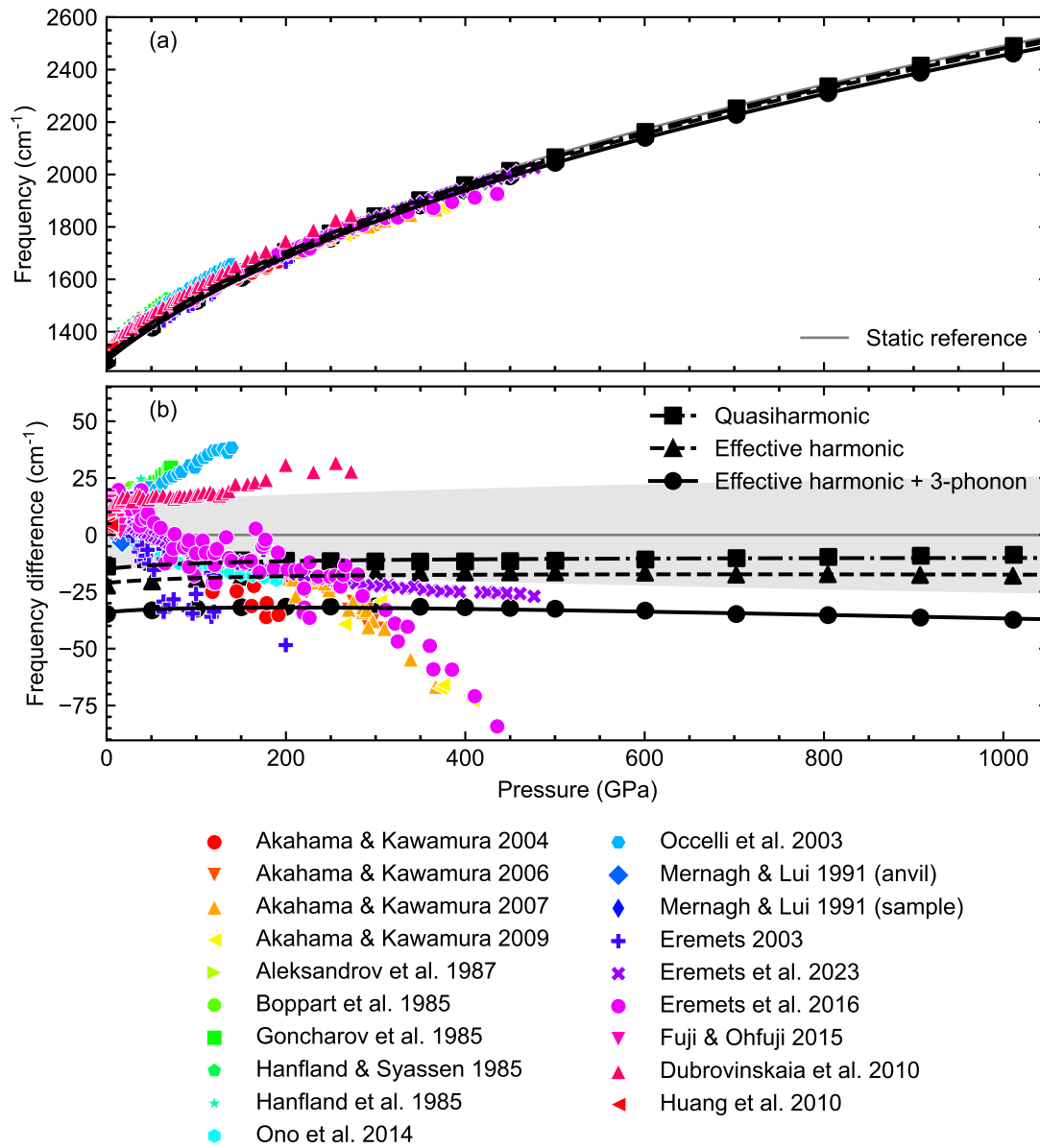


**Figure 7.7** The Raman frequency of diamond as a function of pressure measured from various experiments on an absolute scale (a) and relative to a reference DFT calculation where the phonon frequency is calculated using harmonic finite displacement and the pressures are found from a Davis–Gordon equation of state fitted to the static crystal energies, with no consideration of the phonon free energy (grey line) (b). The grey region in the bottom panel indicates a  $\pm 1\%$  error of the reference DFT calculation. Black squares, triangles, and circles represent the data calculated using the quasiharmonic, effective harmonic, and effective harmonic with 3-phonon formalisms, respectively. Experimental data from [133, 142–158].

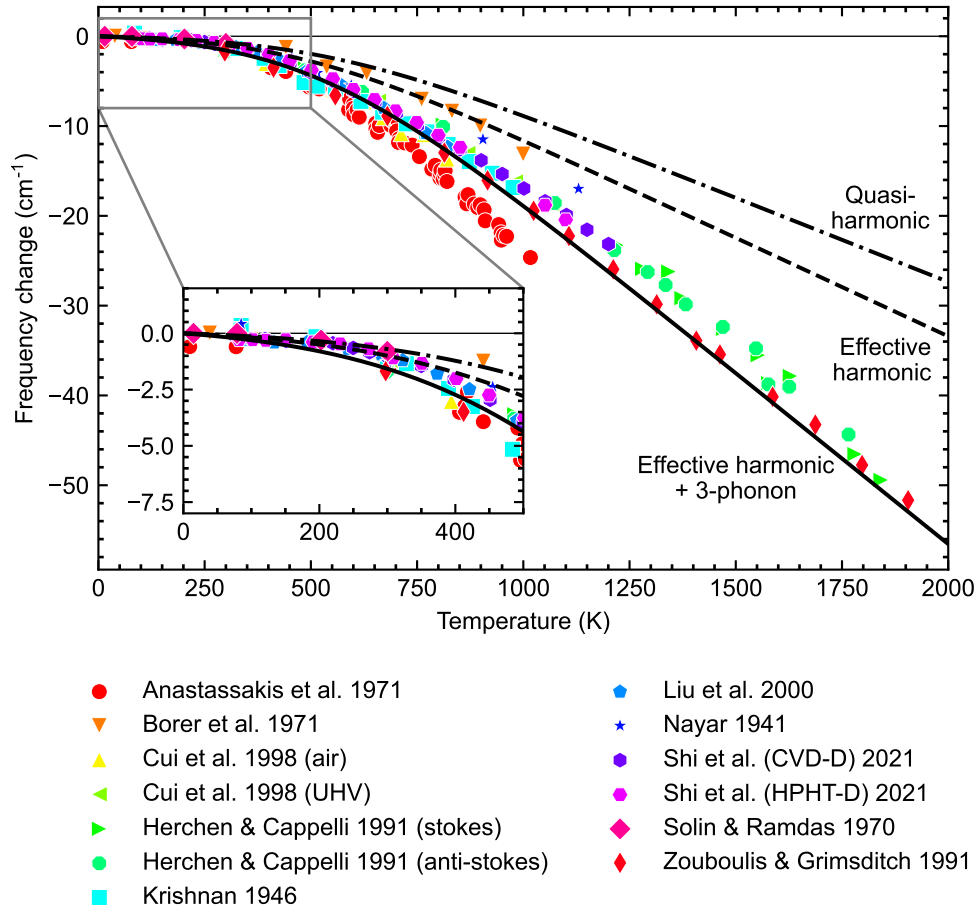


**Figure 7.8** *Temperature dependence of the Raman frequency of diamond at ambient pressure. Experimental data from [94–103].*

TDEP can predict the renormalisation of the zone-centre phonon at both high temperature and high pressure.

Nevertheless, as the calculations performed here are fully hydrostatic, one would ideally expect them to match the hydrostatic data in figure 7.8 — the group with the larger gradient. The calculated hydrostatic results show a slightly too low gradient compared to these data. A too-low gradient represents an increasingly underestimated phonon frequency at high pressure. As anharmonicity is considered here already and any other contributions to the phonon renormalisation tend to lower the frequency, it is unlikely that the phonon frequency that is in error. It therefore remains that differences between the DFT free-energy–volume relation and the true equation of state must be the cause of the underestimated gradient. One possibility is that there are additional

contributions to the free energy that are not considered in these calculations, such as the electronic free energy.

The temperature dependence at ambient pressure, shown in figure 7.8, agrees very well with experiment. The temperature dependence is more significantly affected by the level of anharmonicity considered, but the effective harmonic theory with 3-phonon effects demonstrates at high pressures an almost exact agreement with the data from Zouboulis and Grimsditch [103] and marginally underestimates the data from Herchen and Capelli and Shi *et al.* [97, 101]. The spread in the experimental data seen in figure 7.8 appears to be mostly due to the method of heating the sample and the measuring the temperature. The determination of the Raman frequency is expected to be very accurate even for the pre-laser experiments of Nayar and Krishnan [98, 100]. Sample heating methods ranged from furnaces [101, 177], to resistance heating of metal foil in contact with the sample [94, 97, 100].

The inset in figure 7.8 shows the calculation using the effective harmonic potential with 3-phonon effects included to lie slightly below the majority of the data between 0 K to 400 K and all three lines have a finite slope at zero temperature. This is thought to be an artifact of the interpolation process where the integrated logistic function was fitted to the equation of state and Grüneisen model parameters. It was mentioned previously that the parameter  $C$  in equation 7.23 gave the value at  $T = -\infty$ , where the function has zero slope; at  $T = 0$  K the slope is slightly non-zero, becoming more non-zero the closer  $T_0$  is to 0 K. If this artefact were remedied and the gradient of the interpolation function forced to be exactly zero at zero temperature then this underestimation may vanish.

At temperatures of 500 K to 1000 K the effective harmonic plus 3-phonon curve lies in the centre of all the available experimental data. This agreement with the experimental data verifies the accuracy of the TDEP approach in predicting the anharmonic phonon renormalisation and provides a basis for believing its predictions both at ambient conditions and at high-pressure-high-temperature conditions.

Figure 7.9 is analogous to figure 7.7b for a range of different temperatures. All three levels of theory exhibit a strong pressure dependence of the renormalisation at low pressures. It is especially noticeable that this pressure dependence is

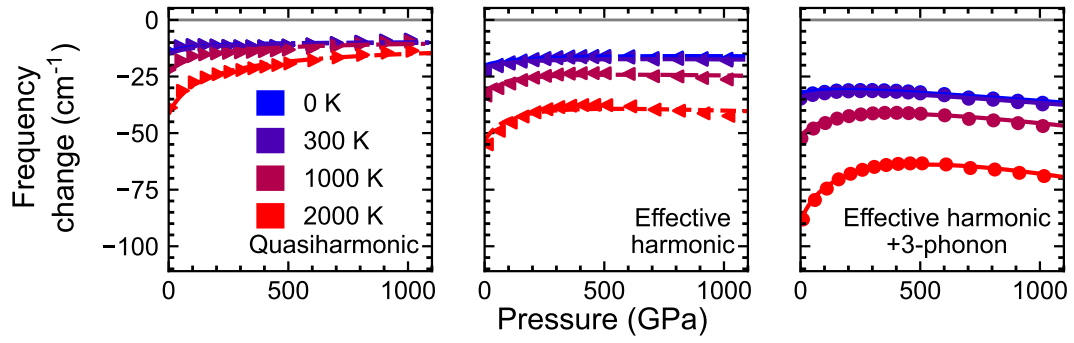


**Figure 7.9** *Pressure dependence of the frequency renormalisation in diamond for the quasiharmonic, effective harmonic, and effective harmonic with 3-phonon effects levels of theory.*

present in the quasiharmonic case, where there is no renormalisation arising directly from pure anharmonicity, rather the renormalisation is entirely due to the change in the volume incited by the temperature-dependent phonon free-energy. One can also note that the renormalisation in the quasiharmonic case tends to the same value at high pressure. From these observations, and by examining the free energies shown in figure 7.10, one can understand the origin of this effect and why this effect is most prominent at low pressures.

At low pressures the volume is closest to  $V_0$ , the minimum of the free energy curve, and the temperature-dependent phonon contribution to the free energy is largest relative to the temperature-independent static contribution. It is at these low pressures where the inclusion of the phonon contribution to the free energy has the greatest effect, and produces the greatest change in the volume of the crystal at a given temperature and pressure. Conversely, at high pressures, the free energy exhibits steep curvature and its volume-dependence is dominated by the temperature-independent static crystal energy, with the phonon contribution having little effect. One can therefore ascribe the low-pressure curvature of the renormalisation in figure 7.9 to the volume effects arising from changes in the phonon free-energy.

At high pressure, the pressure dependences in figure 7.9 are much diminished, but the nature of this slight pressure dependence is different for the quasiharmonic, effective harmonic, and effective harmonic with 3-phonon levels of theory. The quasiharmonic case has already been explained and show nothing remarkable at high pressure. Conversely, the TDEP results in the centre and right panels show



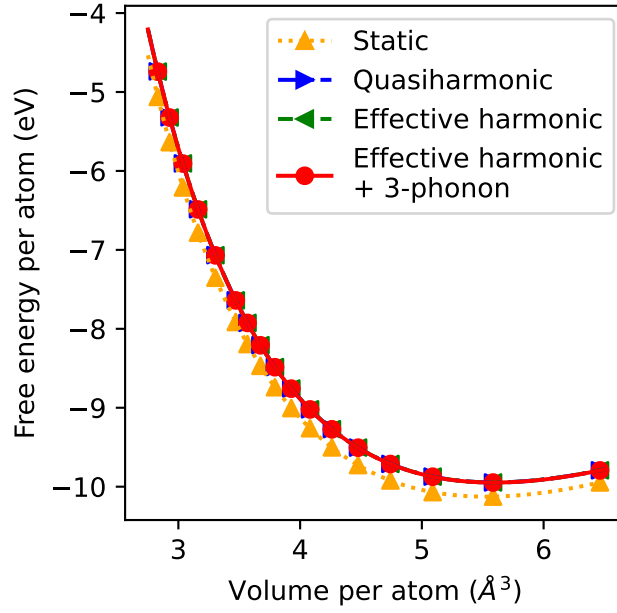


**Figure 7.10** *Free energy of diamond at 300 K as a function of volume for the static, quasiharmonic, effective harmonic, and effective harmonic plus 3-phonon cases. Lines indicate the Davis-Gordon equation of state fitted to the data.*

a turnover in the renormalisation at high pressure. This shows there is clearly some other contribution to the renormalisation whose contribution is greatest at high pressures. The absence of this effect in the quasiharmonic data, which is calculated from an interatomic potential that is only volume dependent, imply that this second contribution is caused by the pure anharmonicity of the potential directly — there is a volume contribution to the renormalisation that decreases with pressure and a temperature contribution that increases with pressure. The effect is most pronounced when 3-phonon effects are included, demonstrating the additional anharmonicity captured by their inclusion.

The temperature-dependence of the renormalisation at a series of pressures is shown in figure 7.11. The quasiharmonic case shows a decrease in the renormalisation all the way up to 1000 GPa, indicative of a potential that becomes increasingly harmonic at high pressures. In the case of the TDEP results, both with and without 3-phonon corrections, this decrease occurs mostly between pressures between 0 GPa and 300 GPa, resulting in a pressure-independent renormalisation at high pressure. This is simply another manifestation of the

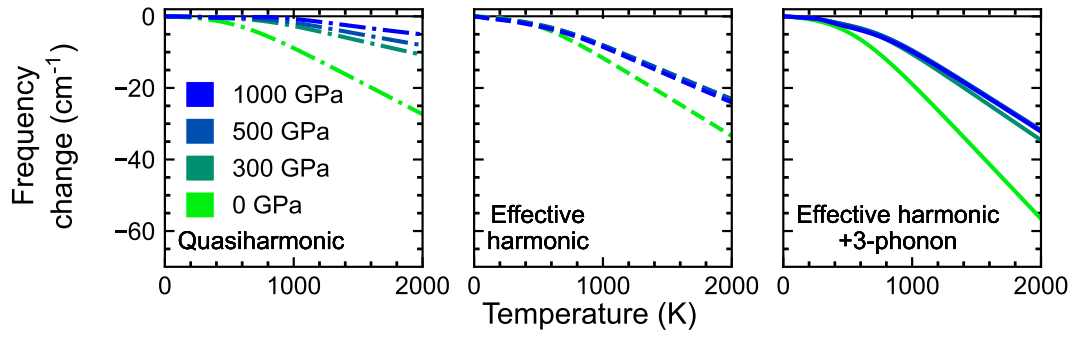


**Figure 7.11** *Temperature dependence of the frequency renormalisation for the quasiharmonic, effective harmonic, and effective harmonic with 3-phonon effects levels of theory.*

turnover described in the previous paragraphs. The shallow and extended nature of the turnover makes the pressure dependence appear almost flat. Nevertheless, from figure 7.11 it can be seen most clearly that the 3-phonon processes contribute most greatly at low pressure, and that at all pressures and temperatures they are significant enough that they must be included for an accurate determination of the Raman frequency of diamond.

In conclusion, the TDEP approach, where an effective harmonic potential is considered and 3-phonon effects are taken into account through the Kramers–Kronig relations, accurately predicts the renormalisation of the zone-centre Raman frequency of diamond both at ambient pressure as a function of temperature and at ambient temperature as a function of pressure. On this basis, it is asserted that the predictions of this method at elevated pressures and temperatures are to be believed, and that, through the parametrisations of the equation of state parameters and the Grüneisen parameters described in table 7.3, one can compute the Raman frequency of diamond at any temperature and pressure.

# Chapter 8

## Conclusion

First-principles calculations of anharmonic phonon frequencies is an area of physics where several new approaches are available to a researcher. This thesis has compared two of them, ALAMODE and TDEP, in applications to the diamond-type semiconductors silicon and diamond. The latter approach was found to be very accurate in calculating the temperature dependence of the zone-centre optical phonon frequency when applied to these systems. Consequently, it was applied to diamond to investigate the quantum isotope effect under pressure, and then to establish the behaviour of the Raman frequency in diamond at high temperature and high pressure, which may be used as a reference for the calibration of the diamond edge Raman scale. In both cases the accuracy of the method was confirmed using available experimental data, inspiring further confidence in its predictions. The poor performance of ALAMODE in silicon was discussed, and the omission of third-order terms was identified as being a significant factor in ALAMODE's shortcomings. A suggestion of how these third-order terms may be included was presented and an attempt was made to implement it. The attempt was unsuccessful, but the insights gained and some avenues for further development were discussed.

Chapter 5 served two purposes. Firstly, to compare ALAMODE and TDEP, but secondly to demonstrate in detail how each of these calculations should be performed. The higher-order finite displacement calculations used by ALAMODE to determine the force constants were described in detail and a recipe for choosing the magnitude of the displacements for each order was presented. Similarly, the

convergence of the phonon frequencies in the TDEP approach was discussed; it was demonstrated how one should determine the level of convergence using a reasonable number of DFT calculations. This chapter showed TDEP to be the most accurate method in silicon, and confirmed that it was accurate in diamond also.

Advantage was taken of this accuracy in chapter 6 to investigate the quantum isotope effect in diamond. The behaviour of the frequency and volume isotope effects at high pressure is disputed in the literature, but the quasiharmonic calculations presented in chapter 6 agreed well with the more accurate zero-pressure experimental data. The effect of pure anharmonicity in the frequency isotope effect was investigated using TDEP, and it was found that the effective harmonic part of the potential *raised* the frequency ratio, whereas the 3-phonon effects lowered it. The end result was that the pure anharmonicity did not significantly alter the predictions of the quasiharmonic model, and the unusual behaviour of the frequency isotope effect reported by Enkovich *et al.* at high pressure could not be reproduced [105], raising questions about its existence and the reliability of the reported experimental results.

Finally, chapter 7 addressed the diamond edge Raman scale and TDEP calculations were used to calculate the hydrostatic Raman frequency at pressures of up to 1 TPa and temperatures of 2000 K. These calculations may serve as a starting point for a calibration of the diamond edge Raman scale that accounts for the non-hydrostatic effects. This chapter also included an overview of the existing calibration experiments and discussed some of the key considerations that must be made in creating an accurate diamond edge Raman calibration. In the course of this investigation, special consideration was given to the manner in which the eigenvectors affected the generation of the TDEP configurations, and an effective method of reducing the vitiating effect misaligned eigenvectors had on the phonon frequencies was presented.

Beyond this thesis, there remain many unexplored areas of research in the field of anharmonic lattice dynamics, from further developing new or existing methods of calculating anharmonic phonon frequencies to applying these approaches to gain insight into the role of anharmonicity in various materials. Chapter 2 outlined some of the materials where anharmonicity is likely to play a large role, as well as some other approaches to computing anharmonic phonons that are currently in

development. Further work comparing these approaches to the methods discussed in this thesis would be instructive; the SSCHA has shown particular promise as being a highly-accurate way of computing anharmonic phonons.

Throughout this thesis, the effect of third-order terms in the phonon frequency renormalisation has been shown to be significant, often equal to that of the fourth-order terms. Further study into these effects would be of great benefit; the proposed extension to the SCPH method may still prove fruitful if the suggested modifications are made. Alternatively, one could use approaches taken in other areas of physics, such as particle or nuclear physics, to evaluate (or approximate) Feynman diagrams of the sort described in chapter 3 and apply them to phonons. Whatever explorations into the effects of anharmonic phonons are made in the coming years, it is hoped that the discussions, theory, and insight contained within this thesis proves in some way useful, and its contents will provide a useful contribution to the field of anharmonic lattice dynamics.

# Bibliography

- [1] B. Wei, Q. Sun, C. Li, and J. Hong, *Phonon anharmonicity: A pertinent review of recent progress and perspective*, *Sci. China Phys. Mech. Astron.* **64**, 117001 (2021).
- [2] T. Tadano and S. Tsuneyuki, *Self-consistent phonon calculations of lattice dynamical properties in cubic  $\text{SrTiO}_3$  with first-principles anharmonic force constants*, *Phys. Rev. B* **92**, 054301 (2015).
- [3] O. Hellman, I. A. Abrikosov, and S. I. Simak, *Lattice dynamics of anharmonic solids from first principles*, *Phys. Rev. B* **84**, 180301 (2011).
- [4] M. Born and K. Huang, *Dynamical Theory of Crystal Lattices*, 1st ed., edited by N. F. Mott, E. C. Bullard, and D. H. Wilkinson, International Series of Monographs on Physics (Clarendon Press, Oxford, 1954).
- [5] G. A. S. Ribeiro, L. Paulatto, R. Bianco, I. Errea, F. Mauri, and M. Calandra, *Strong anharmonicity in the phonon spectra of  $\text{PbTe}$  and  $\text{SnTe}$  from first principles*, *Phys. Rev. B* **97**, 014306 (2018).
- [6] J. P. Heremans, *The anharmonicity blacksmith*, *Nature Phys* **11**, 990 (2015).
- [7] T. Tadano, Y. Gohda, and S. Tsuneyuki, *Anharmonic force constants extracted from first-principles molecular dynamics: Applications to heat transfer simulations*, *J. Phys.: Condens. Matter* **26**, 225402 (2014).
- [8] O. Hellman and I. A. Abrikosov, *Temperature-dependent effective third-order interatomic force constants from first principles*, *Phys. Rev. B* **88**, 144301 (2013).
- [9] G. Mie, *Zur kinetischen Theorie der einatomigen Körper*, *Ann. Physik* **316**, 657 (1903).
- [10] E. Grüneisen, *Zusammenhang zwischen Kompressibilität, thermischer Ausdehnung, Atomvolumen und Atomwärme der Metalle*, *Ann. Physik* **331**, 393 (1908).

- [11] T. Tadano and S. Tsuneyuki, *First-Principles Lattice Dynamics Method for Strongly Anharmonic Crystals*, *J. Phys. Soc. Jpn* **87**, 041015 (2018).
- [12] T. Tadano and S. Tsuneyuki, *Ab Initio prediction of structural phase-transition temperature of  $\text{SrTiO}_3$  from finite-temperature phonon calculation*, *J. Ceram. Soc. Jpn.* **127**, 404 (2019).
- [13] Y.-N. Wu, W. A. Saidi, J. K. Wuenschell, T. Tadano, P. Ohodnicki, B. Chorpeneing, and Y. Duan, *Anharmonicity Explains Temperature Renormalization Effects of the Band Gap in  $\text{SrTiO}_3$* , *J. Phys. Chem. Lett.* **11**, 2518 (2020).
- [14] W. I. Choi, D. J. Yang, D. W. Jung, W.-J. Son, M. Shim, I. Jang, and D. S. Kim, *Ab-initio prediction of temperature-dependent dielectric constants and curie temperatures of cubic phase perovskite materials*, *MRS Commun.* **11**, 436 (2021).
- [15] W. I. Choi, J. S. An, I. Jang, and D. S. Kim, *Strain and temperature-dependent dielectric permittivity of cubic  $\text{SrTiO}_3$ : Self-consistent phonon theory calculations*, *Curr. Appl. Phys.* **29**, 78 (2021).
- [16] Q. Wang, Z. Zeng, and Y. Chen, *Revisiting phonon transport in perovskite  $\text{SrTiO}_3$  : Anharmonic phonon renormalization and four-phonon scattering*, *Phys. Rev. B* **104**, 235205 (2021).
- [17] J. Zheng, D. Shi, Y. Yang, C. Lin, H. Huang, R. Guo, and B. Huang, *Anharmonicity-induced phonon hardening and phonon transport enhancement in crystalline perovskite  $\text{BaZrO}_3$* , *Phys. Rev. B* **105**, 224303 (2022).
- [18] Y. Zhao, S. Zeng, G. Li, C. Lian, Z. Dai, S. Meng, and J. Ni, *Lattice thermal conductivity including phonon frequency shifts and scattering rates induced by quartic anharmonicity in cubic oxide and fluoride perovskites*, *Phys. Rev. B* **104**, 224304 (2021).
- [19] K. Ishioka, T. Tadano, M. Yanagida, Y. Shirai, and K. Miyano, *Anharmonic organic cation vibrations in the hybrid lead halide perovskite  $\text{CH}_3\text{NH}_3\text{PbI}_3$* , *Phys. Rev. Materials* **5**, 105402 (2021).
- [20] D. N. Sagatova, A. F. Shatskiy, N. E. Sagatov, and K. D. Litasov, *Phase relations in  $\text{CaSiO}_3$  system up to 100 GPa and 2500 K*, *Geochem. Int.* **59**, 791 (2021).
- [21] S. Kawano, T. Tadano, and S. Iikubo, *Effect of halogen ions on the low thermal conductivity of cesium halide perovskite*, *J. Phys. Chem. C* **125**, 91 (2021).

- [22] Y. Zhao, C. Lian, S. Zeng, Z. Dai, S. Meng, and J. Ni, *Quartic anharmonicity and anomalous thermal conductivity in cubic antiperovskites  $A_3BO$  ( $A=K,Rb$ ;  $B=Br,Au$ )*, *Phys. Rev. B* **101**, 184303 (2020).
- [23] Y. Yao and J. S. Tse, *Superconducting hydrogen sulfide*, *Chem. Eur. J.* **24**, 1769 (2018).
- [24] N. Dasenbrock-Gammon, E. Snider, R. McBride, H. Pasan, D. Durkee, N. Khalvashi-Sutter, S. Munasinghe, S. E. Dissanayake, K. V. Lawler, A. Salamat, and R. P. Dias, *Evidence of near-ambient superconductivity in a N-doped lutetium hydride*, *Nature* **615**, 244 (2023).
- [25] S. Lee, J.-H. Kim, and Y.-W. Kwon, *The first room-temperature ambient-pressure superconductor* (2023), [arxiv:2307.12008](#) .
- [26] S. Lee, J. Kim, H.-T. Kim, S. Im, S. An, and K. H. Auh, *Superconductor  $Pb_{10-x}Cu_x(PO_4)_6O$  showing levitation at room temperature and atmospheric pressure and mechanism* (2023), [arxiv:2307.12037](#) .
- [27] X. Ming, Y.-J. Zhang, X. Zhu, Q. Li, C. He, Y. Liu, T. Huang, G. Liu, B. Zheng, H. Yang, J. Sun, X. Xi, and H.-H. Wen, *Absence of near-ambient superconductivity in  $LuH_{2\pm x}N_y$* , *Nature* **620**, 72 (2023).
- [28] S. Sridhar, *True superconductivity at near ambient temperature has not been confirmed by Dasenbrock-Gammon et al. Nature, volume 615, pages 244–250 (2023)*, *J. Phys. Chem. Solids* **180**, 111381 (2023).
- [29] P. K. Jain, *Phase transition of copper (I) sulfide and its implication for purported superconductivity of LK-99* (2023), [arxiv:2308.05222](#) .
- [30] W. Sano, T. Koretsune, T. Tadano, R. Akashi, and R. Arita, *Effect of Van Hove singularities on high- $T_c$  superconductivity in  $H_3S$* , *Phys. Rev. B* **93**, 094525 (2016).
- [31] N. W. Ashcroft, *Metallic hydrogen: A high-temperature superconductor?*, *Phys. Rev. Lett.* **21**, 1748 (1968).
- [32] M. Dogan, S. Oh, and M. L. Cohen, *High temperature superconductivity in the candidate phases of solid hydrogen*, *J. Phys.: Condens. Matter* **34**, 15LT01 (2022).
- [33] M. Dogan, S. Oh, and M. L. Cohen, *Prediction of high-temperature superconductivity in C2/c-24 solid hydrogen*, *Phys. Rev. B* **105**, L020509 (2022).
- [34] M. Dogan, S. Oh, and M. L. Cohen, *Observed metallization of hydrogen interpreted as a band structure effect*, *J. Phys.: Condens. Matter* **33**, 03LT01 (2021).



- [35] Y. Oba, T. Tadano, R. Akashi, and S. Tsuneyuki, *First-principles study of phonon anharmonicity and negative thermal expansion in  $\text{ScF}_3$* , [\*Phys. Rev. Mater.\* \*\*3\*\*, 033601 \(2019\)](#).
- [36] P. Souvatzis, O. Eriksson, M. I. Katsnelson, and S. P. Rudin, *Entropy Driven Stabilization of Energetically Unstable Crystal Structures Explained from First Principles Theory*, [\*Phys. Rev. Lett.\* \*\*100\*\*, 095901 \(2008\)](#).
- [37] P. Souvatzis, O. Eriksson, M. Katsnelson, and S. Rudin, *The self-consistent ab initio lattice dynamical method*, [\*Comp. Mater. Sci.\* \*\*44\*\*, 888 \(2009\)](#).
- [38] N. Shulumba, O. Hellman, and A. J. Minnich, *Intrinsic localized mode and low thermal conductivity of  $\text{PbSe}$* , [\*Phys. Rev. B\* \*\*95\*\*, 014302 \(2017\)](#).
- [39] C. W. Li, O. Hellman, J. Ma, A. F. May, H. B. Cao, X. Chen, A. D. Christianson, G. Ehlers, D. J. Singh, B. C. Sales, and O. Delaire, *Phonon self-energy and origin of anomalous neutron scattering spectra in  $\text{SnTe}$  and  $\text{PbTe}$  thermoelectrics*, [\*Phys. Rev. Lett.\* \*\*112\*\*, 175501 \(2014\)](#).
- [40] D. S. Kim, O. Hellman, J. Herriman, H. L. Smith, J. Y. Y. Lin, N. Shulumba, J. L. Niedziela, C. W. Li, D. L. Abernathy, and B. Fultz, *Nuclear quantum effect with pure anharmonicity and the anomalous thermal expansion of silicon*, [\*Proc. Natl. Acad. Sci. USA\* \*\*115\*\*, 1992 \(2018\)](#).
- [41] L. Isaeva, O. Hellman, J. Lashley, I. Abrikosov, and O. Eriksson, *Dynamic stabilization of cubic  $\text{AuZn}$* , [\*Materials Today: Proceedings\* \*\*2\*\*, S569 \(2015\)](#).
- [42] J. Bouchet and F. Bottin, *Thermal evolution of vibrational properties of  $\alpha\text{-U}$* , [\*Phys. Rev. B\* \*\*92\*\*, 174108 \(2015\)](#).
- [43] A. H. Romero, E. K. U. Gross, M. J. Verstraete, and O. Hellman, *Thermal conductivity in  $\text{PbTe}$  from first principles*, [\*Phys. Rev. B\* \*\*91\*\*, 214310 \(2015\)](#).
- [44] A. L. Miranda, B. Xu, O. Hellman, A. H. Romero, and M. J. Verstraete, *Ab Initio calculation of the thermal conductivity of indium antimonide*, [\*Semicond. Sci. Technol.\* \*\*29\*\*, 124002 \(2014\)](#).
- [45] N. Shulumba, O. Hellman, L. Rogström, Z. Raza, F. Tasnádi, I. A. Abrikosov, and M. Odén, *Temperature-dependent elastic properties of  $\text{Ti}_{1-x}\text{Al}_x\text{N}$  alloys*, [\*Appl. Phys. Lett.\* \*\*107\*\*, 231901 \(2015\)](#).
- [46] L. Mauger, J. E. Herriman, O. Hellman, S. J. Tracy, M. S. Lucas, J. A. Muñoz, Y. Xiao, J. Li, and B. Fultz, *Phonons and elasticity of cementite through the Curie temperature*, [\*Phys. Rev. B\* \*\*95\*\*, 024308 \(2017\)](#).
- [47] F. C. Yang, J. A. Muñoz, O. Hellman, L. Mauger, M. S. Lucas, S. J. Tracy, M. B. Stone, D. L. Abernathy, Y. Xiao, and B. Fultz, *Thermally driven electronic topological transition in  $\text{FeTi}$* , [\*Phys. Rev. Lett.\* \*\*117\*\*, 076402 \(2016\)](#).

- [48] A. Dewaele, V. Stutzmann, J. Bouchet, F. Bottin, F. Occelli, and M. Mezouar, *High pressure-temperature phase diagram and equation of state of titanium*, [Phys. Rev. B](#) **91**, 134108 (2015).
- [49] J. D. Budai, J. Hong, M. E. Manley, E. D. Specht, C. W. Li, J. Z. Tischler, D. L. Abernathy, A. H. Said, B. M. Leu, L. A. Boatner, R. J. McQueeney, and O. Delaire, *Metallization of vanadium dioxide driven by large phonon entropy*, [Nature](#) **515**, 535 (2014).
- [50] I. A. Abrikosov, A. V. Ponomareva, A. Yu. Nikonov, A. Zharmukhambetova, I. Yu. Mosyagin, A. V. Lugovskoy, O. Hellman, H. Lind, A. I. Dmitriev, and S. A. Barannikova, *Theoretical description of pressure-induced phase transitions: A case study of Ti-V alloys*, [High Pressure Research](#) **35**, 42 (2015).
- [51] N. Shulumba, B. Alling, O. Hellman, E. Mozafari, P. Steneteg, M. Odén, and I. A. Abrikosov, *Vibrational free energy and phase stability of paramagnetic and antiferromagnetic CrN from ab initio molecular dynamics*, [Phys. Rev. B](#) **89**, 174108 (2014).
- [52] H. Wendel and R. M. Martin, *Theory of structural properties of covalent semiconductors*, [Phys. Rev. B](#) **19**, 5251 (1979).
- [53] D. W. Bullett, *Chemical pseudopotential approach to covalent bonding. II. Bond lengths and bond energies in diamond, silicon and graphite*, [J. Phys. C: Solid State Phys.](#) **8**, 2707 (1975).
- [54] D. J. Chadi and R. M. Martin, *Calculation of lattice dynamical properties from electronic energies: Application to C, Si and Ge*, [Solid State Commun.](#) **19**, 643 (1976).
- [55] M. T. Yin and M. L. Cohen, *Theory of lattice-dynamical properties of solids: Application to Si and Ge*, [Phys. Rev. B](#) **26**, 3259 (1982).
- [56] L. Monacelli, R. Bianco, M. Cherubini, M. Calandra, I. Errea, and F. Mauri, *The stochastic self-consistent harmonic approximation: Calculating vibrational properties of materials with full quantum and anharmonic effects*, [J. Phys.: Condens. Matter](#) **33**, 363001 (2021).
- [57] A. Togo and I. Tanaka, *First-principles phonon calculations in materials science*, [Scripta Mater.](#) **108**, 1 (2015).
- [58] A. Togo, *First-principles phonon calculations with Phonopy and Phono3py*, [J. Phys. Soc. Jpn.](#) **92**, 012001 (2023).
- [59] F. Eriksson, E. Fransson, and P. Erhart, *The Hiphive package for the extraction of high-order force constants by machine learning*, [Advanced Theory and Simulations](#) **2**, 1800184 (2019).

- [60] G. Barbalinardo, Z. Chen, N. W. Lundgren, and D. Donadio, *Efficient anharmonic lattice dynamics calculations of thermal transport in crystalline and disordered solids*, [J. Appl. Phys. \*\*128\*\*, 135104 \(2020\)](#).
- [61] G. Leibfried and W. Ludwig, in *Solid State Physics: Advances in Research and Applications.*, Solid State Physics, Vol. 12, edited by F. Seitz and D. Turnbull (Academic Press, New York, N.Y., 1961) pp. 275–444.
- [62] J. A. Reissland, *The Physics of Phonons* (Wiley, London, 1973).
- [63] C. Kittel, *Introduction to Solid State Physics*, 8th ed. (John Wiley & Sons, New Caledonia, 2005).
- [64] N. W. Ashcroft and N. D. Mermin, *Solid State Physics* (Brooks/Cole, 1976).
- [65] A. A. Maradudin and A. E. Fein, *Scattering of Neutrons by an Anharmonic Crystal*, [Phys. Rev. \*\*128\*\*, 2589 \(1962\)](#).
- [66] G. Kresse and J. Hafner, *Ab Initio molecular dynamics for liquid metals*, [Phys. Rev. B \*\*47\*\*, 558 \(1993\)](#).
- [67] G. Kresse and J. Furthmüller, *Efficiency of ab-initio total energy calculations for metals and semiconductors using a plane-wave basis set*, [Comp. Mater. Sci. \*\*6\*\*, 15 \(1996\)](#).
- [68] G. Kresse and J. Furthmüller, *Efficient iterative schemes for ab initio total-energy calculations using a plane-wave basis set*, [Phys. Rev. B \*\*54\*\*, 11169 \(1996\)](#).
- [69] G. Kresse and D. Joubert, *From ultrasoft pseudopotentials to the projector augmented-wave method*, [Phys. Rev. B \*\*59\*\*, 1758 \(1999\)](#).
- [70] P. Hohenberg and W. Kohn, *Inhomogeneous electron gas*, [Phys. Rev. \*\*136\*\*, 864 \(1964\)](#).
- [71] W. Kohn and L. J. Sham, *Self-consistent equations including exchange and correlation effects*, [Phys. Rev. \*\*140\*\*, A1133 \(1965\)](#).
- [72] D. M. Ceperley and B. J. Alder, *Ground state of the electron gas by a stochastic method*, [Phys. Rev. Lett. \*\*45\*\*, 566 \(1980\)](#).
- [73] M. Ernzerhof, J. P. Perdew, and K. Burke, *Coupling-constant dependence of atomization energies*, [Int. J. Quantum Chem. \*\*64\*\*, 285 \(1997\)](#).
- [74] P. Ziesche, S. Kurth, and J. P. Perdew, *Density functionals from LDA to GGA*, [Comp. Mater. Sci. \*\*11\*\*, 122 \(1998\)](#).
- [75] J. P. Perdew, K. Burke, and M. Ernzerhof, *Generalized gradient approximation made simple*, [Phys. Rev. Lett. \*\*77\*\*, 3865 \(1996\)](#).

- [76] J. P. Perdew, A. Ruzsinszky, G. I. Csonka, O. A. Vydrov, G. E. Scuseria, L. A. Constantin, X. Zhou, and K. Burke, *Restoring the density-gradient expansion for exchange in solids and surfaces*, [Phys. Rev. Lett. \*\*100\*\*, 136406 \(2008\)](#).
- [77] R. Armiento and A. E. Mattsson, *Functional designed to include surface effects in self-consistent density functional theory*, [Phys. Rev. B \*\*72\*\*, 085108 \(2005\)](#).
- [78] A. E. Mattsson, R. Armiento, J. Paier, G. Kresse, J. M. Wills, and T. R. Mattsson, *The AM05 density functional applied to solids*, [J. Chem. Phys. \*\*128\*\*, 084714 \(2008\)](#).
- [79] A. E. Mattsson and R. Armiento, *Implementing and testing the AM05 spin density functional*, [Phys. Rev. B \*\*79\*\*, 155101 \(2009\)](#).
- [80] J. P. Perdew, J. A. Chevary, S. H. Vosko, K. A. Jackson, M. R. Pederson, D. J. Singh, and C. Fiolhais, *Atoms, molecules, solids, and surfaces: Applications of the generalized gradient approximation for exchange and correlation*, [Phys. Rev. B \*\*46\*\*, 6671 \(1992\)](#).
- [81] H. Hellmann, *Einführung in Die Quantenchemie* (Deuticke, Leipzig, 1937).
- [82] R. P. Feynman, *Forces in Molecules*, [Phys. Rev. \*\*56\*\*, 340 \(1939\)](#).
- [83] N. Shulumba, O. Hellman, and A. J. Minnich, *Lattice thermal conductivity of polyethylene molecular crystals from first principles including nuclear quantum effects*, [Phys. Rev. Lett. \*\*119\*\*, 185901 \(2017\)](#).
- [84] Y. Okada and Y. Tokumaru, *Precise determination of lattice parameter and thermal expansion coefficient of silicon between 300 and 1500 K*, [J. Appl. Phys. \*\*56\*\*, 314 \(1984\)](#).
- [85] K. G. Lyon, G. L. Salinger, C. A. Swenson, and G. K. White, *Linear thermal expansion measurements on silicon from 6 to 340 K*, [Journal of Applied Physics \*\*48\*\*, 865 \(1977\)](#).
- [86] S. Anzellini, M. T. Wharmby, F. Miozzi, A. Kleppe, D. Daisenberger, and H. Wilhelm, *Quasi-hydrostatic equation of state of silicon up to 1 megabar at ambient temperature*, [Sci. Rep. \*\*9\*\*, 15537 \(2019\)](#).
- [87] B. A. Weinstein and G. J. Piermarini, *Raman scattering and phonon dispersion in Si and GaP at very high pressure*, [Phys. Rev. B \*\*12\*\*, 1172 \(1975\)](#).
- [88] P. Wisesa, K. A. McGill, and T. Mueller, *Efficient generation of generalized Monkhorst-Pack grids through the use of informatics*, [Phys. Rev. B \*\*93\*\*, 155109 \(2016\)](#).

- [89] Y. Wang, P. Wisea, A. Balasubramanian, and S. Dwaraknath, *Rapid generation of optimal generalized Monkhorst-Pack grids*, [Comp. Mater. Sci.](#) **187**, 110100 (2021).
- [90] P. Jacobson and S. Stoupin, *Thermal expansion coefficient of diamond in a wide temperature range*, [Diamond and Related Materials](#) **97**, 107469 (2019).
- [91] M. Ekman, K. Persson, and G. Grimvall, *Lattice dynamics and thermodynamic properties of the  $\beta$ -Sn phase in Si*, [Phys. Rev. B](#) **62**, 14784 (2000).
- [92] A. Compaan, M. C. Lee, and G. J. Trott, *Phonon populations by nanosecond-pulsed Raman scattering in Si*, [Phys. Rev. B](#) **32**, 6731 (1985).
- [93] M. Balkanski, R. F. Wallis, and E. Haro, *Anharmonic effects in light scattering due to optical phonons in silicon*, [Phys. Rev. B](#) **28**, 1928 (1983).
- [94] E. Anastassakis, H. C. Hwang, and C. H. Perry, *Temperature dependence of the long-wavelength optical phonons in diamond*, [Phys. Rev. B](#) **4**, 2493 (1971).
- [95] W. J. Borer, S. S. Mitra, and K. V. Namjoshi, *Line shape and temperature dependence of the first order Raman spectrum of diamond*, [Solid State Commun.](#) **9**, 1377 (1971).
- [96] J. B. Cui, K. Amtmann, J. Ristein, and L. Ley, *Noncontact temperature measurements of diamond by Raman scattering spectroscopy*, [J. Appl. Phys.](#) **83**, 7929 (1998).
- [97] H. Herchen and M. A. Cappelli, *First-order Raman spectrum of diamond at high temperatures*, [Phys. Rev. B](#) **43**, 11740 (1991).
- [98] R. S. Krishnan, *Temperature variations of the Raman frequencies in diamond*, [Proc. Indian Acad. Sci. A](#) **24**, 45 (1946).
- [99] M. S. Liu, L. A. Bursill, S. Prawer, and R. Beserman, *Temperature dependence of the first-order Raman phonon line of diamond*, [Phys. Rev. B](#) **61**, 3391 (2000).
- [100] P. G. N. Nayar, *Temperature variation of the Raman frequency of diamond*, [Proc. Indian Acad. Sci. \(Math. Sci.\)](#) **13**, 284 (1941).
- [101] Z. Shi, Q. Yuan, Y. Wang, K. Nishimura, G. Yang, B. Zhang, N. Jiang, and H. Li, *Optical properties of bulk single-crystal diamonds at 80-1200 K by vibrational spectroscopic methods*, [Materials](#) **14**, 7435 (2021).
- [102] S. A. Solin and A. K. Ramdas, *Raman spectrum of diamond*, [Phys. Rev. B](#) **1**, 1687 (1970).

- [103] E. S. Zouboulis and M. Grimsditch, *Raman scattering in diamond up to 1900 K*, [Phys. Rev. B \*\*43\*\*, 12490 \(1991\)](#).
- [104] M. Muinov, H. Kanda, and S. M. Stishov, *Raman scattering in diamond at high pressure: Isotopic effects*, [Phys. Rev. B \*\*50\*\*, 13860 \(1994\)](#).
- [105] P. V. Enkovich, V. V. Brazhkin, S. G. Lyapin, H. Kanda, A. P. Novikov, and S. M. Stishov, *Quantum effects in diamond isotopes at high pressures*, [Phys. Rev. B \*\*93\*\*, 014308 \(2016\)](#).
- [106] H. Fujihisa, V. A. Sidorov, K. Takemura, H. Kanda, and S. M. Stishov, *Pressure dependence of the lattice constant of diamond: Isotopic effects*, [JETP Letters \*\*63\*\*, 83 \(1996\)](#).
- [107] A. K. Ramdas, S. Rodriguez, M. Grimsditch, T. R. Anthony, and W. F. Banholzer, *Effect of isotopic constitution of diamond on its elastic constants:  $^{12}\text{C}$  diamond, the hardest known material*, [Phys. Rev. Lett. \*\*71\*\*, 189 \(1993\)](#).
- [108] V. G. Plekhanov, *Isotope effects on the lattice dynamics of crystals*, [Materials Science and Engineering: R: Reports \*\*35\*\*, 139 \(2001\)](#).
- [109] M. Cardona and M. L. W. Thewalt, *Isotope effects on the optical spectra of semiconductors*, [Rev. Mod. Phys. \*\*77\*\*, 1173 \(2005\)](#).
- [110] S. Klotz, J. C. Chervin, P. Munsch, and G. Le Marchand, *Hydrostatic limits of 11 pressure transmitting media*, [J. Phys. D: Appl. Phys. \*\*42\*\*, 075413 \(2009\)](#).
- [111] R. M. Chrenko,  *$^{13}\text{C}$ -doped diamond: Raman spectra*, [J. Appl. Phys. \*\*63\*\*, 5873 \(1988\)](#).
- [112] K. C. Hass, M. A. Tamor, T. R. Anthony, and W. F. Banholzer, *Lattice dynamics and Raman spectra of isotopically mixed diamond*, [Phys. Rev. B \*\*45\*\*, 7171 \(1992\)](#).
- [113] R. Vogelgesang, A. K. Ramdas, S. Rodriguez, M. Grimsditch, and T. R. Anthony, *Brillouin and Raman scattering in natural and isotopically controlled diamond*, [Phys. Rev. B \*\*54\*\*, 3989 \(1996\)](#).
- [114] H. Hanzawa, N. Umemura, Y. Nisida, H. Kanda, M. Okada, and M. Kobayashi, *Disorder effects of nitrogen impurities, irradiation-induced defects, and  $^{13}\text{C}$  isotope composition on the Raman spectrum in synthetic Ib diamond*, [Phys. Rev. B \*\*54\*\*, 3793 \(1996\)](#).
- [115] M. Cardona and T. Ruf, *Phonon self-energies in semiconductors: Anharmonic and isotopic contributions*, [Solid State Commun. \*\*117\*\*, 201 \(2001\)](#).



- [116] G. Lang, K. Karch, M. Schmitt, P. Pavone, A. P. Mayer, R. K. Wehner, and D. Strauch, *Anharmonic line shift and linewidth of the Raman mode in covalent semiconductors*, [Phys. Rev. B](#) **59**, 6182 (1999).
- [117] S. W. Biernacki, *Lattice parameter and Raman spectra of isotopically mixed diamond*, [Phys. Rev. B](#) **56**, 11472 (1997).
- [118] C. P. Herrero, *The isotopic mass and lattice parameter of diamond; a path-integral simulation*, [J. Phys.: Condens. Matter](#) **13**, 5127 (2001).
- [119] H. Holloway, K. C. Hass, M. A. Tamor, T. R. Anthony, and W. F. Banholzer, *Isotopic dependence of the lattice constant of diamond*, [Phys. Rev. B](#) **44**, 7123 (1991).
- [120] T. Yamanaka, S. Morimoto, and H. Kanda, *Influence of the isotope ratio on the lattice constant of diamond*, [Phys. Rev. B](#) **49**, 9341 (1994).
- [121] S. Shikata, T. Tanno, T. Teraji, H. Kanda, T. Yamada, and J.-I. Kushibiki, *Precise measurements of diamond lattice constant using Bond method*, [Jpn. J. Appl. Phys.](#) **57**, 111301 (2018).
- [122] T. Yamanaka and S. Morimoto, *Isotope effect on anharmonic thermal atomic vibration and  $\kappa$  refinement of  $^{12}\text{C}$  and  $^{13}\text{C}$  diamond*, [Acta Cryst. B](#) **B52**, 232 (1996).
- [123] Ph. Gillet, G. Fiquet, I. Daniel, B. Reynard, and M. Hanfland, *Equations of state of  $^{12}\text{C}$  and  $^{13}\text{C}$  diamond*, [Phys. Rev. B](#) **60**, 14660 (1999).
- [124] D. C. Hurley, R. S. Gilmore, and W. F. Banholzer, *Ultrasonic phase velocity and elastic modulus in isotopically enhanced manufactured diamonds*, [J. Appl. Phys.](#) **76**, 7726 (1994).
- [125] C. P. Herrero, *Quantum atomistic simulations of silicon and germanium*, [J. Mater. Res.](#) **16**, 2505 (2001).
- [126] C. P. Herrero, *Dependence of the silicon lattice constant on isotopic mass*, [Solid State Commun.](#) **110**, 243 (1999).
- [127] P. V. Enkovich, V. V. Brazhkin, S. G. Lyapin, A. P. Novikov, A. V. Gusev, V. A. Gavva, M. F. Churbanov, and S. M. Stishov, *Quantum effects in silicon isotopes at low temperatures under normal and high pressures*, [J. Phys. Commun.](#) **1**, 055005 (2017).
- [128] P. V. Enkovich, V. V. Brazhkin, S. G. Lyapin, and S. M. Stishov, *Quantum isotope effect in silicon at low temperatures*, [J. Exp. Theor. Phys.](#) **128**, 207 (2019).
- [129] P. E. Blöchl, *Projector augmented-wave method*, [Phys. Rev. B](#) **50**, 17953 (1994).

- [130] O. H. Nielsen and R. M. Martin, *First-principles calculation of stress*, [Phys. Rev. Lett. \*\*50\*\*, 697 \(1983\)](#).
- [131] O. H. Nielsen and R. M. Martin, *Quantum-mechanical theory of stress and force*, [Phys. Rev. B \*\*32\*\*, 3780 \(1985\)](#).
- [132] K. Kunc, I. Loa, and K. Syassen, *Equation of state and phonon frequency calculations of diamond at high pressures*, [Phys. Rev. B \*\*68\*\*, 094107 \(2003\)](#).
- [133] F. Occelli, P. Loubeyre, and R. LeToullec, *Properties of diamond under hydrostatic pressures up to 140 GPa*, [Nature Mater. \*\*2\*\*, 151 \(2003\)](#).
- [134] D. R. Lide, ed., *Handbook of Chemistry and Physics*, 85th ed. (CRC Press, Boca Raton, 2004).
- [135] G. Shen and H. K. Mao, *High-pressure studies with x-rays using diamond anvil cells*, [Rep. Prog. Phys. \*\*80\*\*, 016101 \(2016\)](#).
- [136] N. Dubrovinskaia, L. Dubrovinsky, N. A. Solopova, A. Abakumov, S. Turner, M. Hanfland, E. Bykova, M. Bykov, C. Prescher, V. B. Prakapenka, S. Petitgirard, I. Chuvashova, B. Gasharova, Y.-L. Mathis, P. Ershov, I. Snigireva, and A. Snigirev, *Terapascal static pressure generation with ultrahigh yield strength nanodiamond*, [Sci. Adv. \*\*2\*\*, e1600341 \(2016\)](#).
- [137] S. A. Moggach, D. R. Allan, S. Parsons, and J. E. Warren, *Incorporation of a new design of backing seat and anvil in a Merrill–Bassett diamond anvil cell*, [J. Appl. Cryst. \*\*41\*\*, 249 \(2008\)](#).
- [138] R. A. Forman, G. J. Piermarini, J. D. Barnett, and S. Block, *Pressure measurement made by the utilization of ruby sharp-line luminescence*, [Science \*\*176\*\*, 284 \(1972\)](#).
- [139] G. J. Piermarini, S. Block, J. D. Barnett, and R. A. Forman, *Calibration of the pressure dependence of the  $R_1$  ruby fluorescence line to 195 kbar*, [J. Appl. Phys. \*\*46\*\*, 2774 \(1975\)](#).
- [140] K. Syassen, *Ruby under pressure*, [High Pressure Res. \*\*28\*\*, 75 \(2008\)](#).
- [141] C. Ramaswamy, *The Raman effect in diamond*, *Indian J. Phys.* **5**, 97 (1930).
- [142] Y. Akahama and H. Kawamura, *High-pressure Raman spectroscopy of diamond anvils to 250 GPa: Method for pressure determination in the multimegabar pressure range*, [J. Appl. Phys. \*\*96\*\*, 3748 \(2004\)](#).
- [143] Y. Akahama and H. Kawamura, *Pressure calibration of diamond anvil Raman gauge to 310 GPa*, *J. Appl. Phys.* **100**, 043516 (2006).



- [144] Y. Akahama and H. Kawamura, *Diamond anvil Raman gauge in multimegabar pressure range*, [High Pressure Res. \*\*27\*\*, 473 \(2007\)](#).
- [145] Y. Akahama and H. Kawamura, in *Journal of Physics: Conference Series*, Vol. 215 (IOP Publishing, Tokyo, Japan, 2009) p. 012195.
- [146] I. V. Aleksandrov, A. F. Goncharov, A. N. Zisman, and S. M. Stishov, *Diamond at high pressures: Raman scattering of light, equation of state, and high-pressure scale*, *Zh. eksp. teor. Fiz.* **93**, 680 (1987).
- [147] H. Boppart, J. van Straaten, and I. F. Silvera, *Raman spectra of diamond at high pressures*, [Phys. Rev. B \*\*32\*\*, 1423 \(1985\)](#).
- [148] A. F. Goncharov, I. N. Makarenko, and S. M. Stishov, *Raman scattering from a diamond at pressures up to 72 GPa*, *JETP Lett.* **41**, 184 (1985).
- [149] M. Hanfland and K. Syassen, *A Raman study of diamond anvils under stress*, [J. Appl. Phys. \*\*57\*\*, 2752 \(1985\)](#).
- [150] M. Hanfland, K. Syassen, S. Fahy, S. G. Louie, and M. L. Cohen, *Pressure dependence of the first-order Raman mode in diamond*, [Phys. Rev. B \*\*31\*\*, 6896 \(1985\)](#).
- [151] S. Ono, K. Mibe, and Y. Ohishi, *Raman spectra of culet face of diamond anvils and application as optical pressure sensor to high temperatures*, [J. Appl. Phys. \*\*116\*\*, 053517 \(2014\)](#).
- [152] T. P. Mernagh and L.-G. Liu, *Pressure dependence of Raman phonons of some group IVA (C, Si, and Ge) elements*, [J. Phys. Chem. Solids \*\*52\*\*, 507 \(1991\)](#).
- [153] M. I. Erements, *Megabar high-pressure cells for Raman measurements*, [J. Raman. Spectrosc. \*\*34\*\*, 515 \(2003\)](#).
- [154] M. I. Erements, V. S. Minkov, P. P. Kong, A. P. Drozdov, S. Chariton, and V. B. Prakapenka, *Universal diamond edge Raman scale to 0.5 terapascal and implications for the metallization of hydrogen*, [Nat. Commun. \*\*14\*\*, 907 \(23\)](#).
- [155] M. I. Erements, I. A. Troyan, and A. P. Drozdov, [Low temperature phase diagram of hydrogen at pressures up to 380 GPa. A possible metallic phase at 360 GPa and 200 K \(2016\), arxiv:1601.04479 \[cond-mat\]](#) .
- [156] T. Fujii and H. Ohfuji, *Pressure estimation using the ‘diamond Raman scale’ at low pressures in diamond anvil cell experiments using a highly confocal Raman system*, [Meas. Sci. Technol. \*\*26\*\*, 025501 \(2015\)](#).

- [157] N. Dubrovinskaia, L. Dubrovinsky, R. Caracas, and M. Hanfland, *Diamond as a high pressure gauge up to 2.7 Mbar*, [Appl. Phys. Lett.](#) **97**, 251903 (2010).
- [158] E.-P. Huang, E. Huang, S.-C. Yu, Y.-H. Chen, J.-S. Lee, and J.-N. Fang, *High-temperature and pressure Raman spectroscopy of diamond*, [Mater. Lett.](#) **64**, 580 (2010).
- [159] H. K. Mao, P. M. Bell, J. W. Shaner, and D. J. Steinberg, *Specific volume measurements of Cu, Mo, Pd, and Ag and calibration of the ruby  $R_1$  fluorescence pressure gauge from 0.06 to 1 Mbar*, [J. Appl. Phys.](#) **49**, 3276 (1978).
- [160] A. Tardieu, F. Cansell, and J. P. Petitet, *Pressure and temperature dependence of the first-order Raman mode of diamond*, [J. Appl. Phys.](#) **68**, 3243 (1990).
- [161] Y. K. Vohra, S. McCauley, G. Gu, and S. S. Vagarali, in [AIP Conference Proceedings](#), Vol. 309 (AIP, Colorado Springs, Colorado (USA), 1994) pp. 515–518.
- [162] W. J. Nellis, J. A. Moriarty, A. C. Mitchell, M. Ross, R. G. Dandrea, N. W. Ashcroft, N. C. Holmes, and G. R. Gathers, *Metals physics at ultrahigh pressure: Aluminum, copper, and lead as prototypes*, [Phys. Rev. Lett.](#) **60**, 1414 (1988).
- [163] R. D. Markwell and I. S. Butler, *On the use of diamond as a pressure calibrant for near-infrared FT-Raman microspectroscopy at high pressures*, [Can. J. Chem.](#) **73**, 1019 (1995).
- [164] D. D. Klug and E. Whalley, *Nitrite and nitrate ions as infrared pressure gauges for diamond anvils*, [Rev. Sci. Instrum.](#) **54**, 1205 (1983).
- [165] J. H. Eggert, F. Moshary, W. J. Evans, K. A. Goettel, and I. F. Silvera, *Ruby at high pressure. III. A pumping scheme for the  $R$  lines up to 230 GPa*, [Phys. Rev. B](#) **44**, 7202 (1991).
- [166] C.-S. Zha, H.-K. Mao, and R. J. Hemley, *Elasticity of MgO and a primary pressure scale to 55 GPa*, [Proc. Natl. Acad. Sci. U.S.A.](#) **97**, 13494 (2000).
- [167] F. Datchi, R. LeToullec, and P. Loubeyre, *Improved calibration of the  $SrB_4O_7:Sm^{2+}$  optical pressure gauge: Advantages at very high pressures and high temperatures*, [J. Appl. Phys.](#) **81**, 3333 (1997).
- [168] H. K. Mao, J. Xu, and P. M. Bell, *Calibration of the ruby pressure gauge to 800 kbar under quasi-hydrostatic conditions*, [Journal of Geophysical Research: Solid Earth](#) **91**, 4673 (1986).

- [169] N. C. Holmes, J. A. Moriarty, G. R. Gathers, and W. J. Nellis, *The equation of state of platinum to 660 GPa (6.6 Mbar)*, [J. Appl. Phys. \*\*66\*\*, 2962 \(1989\)](#).
- [170] L. Sun, A. L. Ruoff, and G. Stupian, *Convenient optical pressure gauge for multimegabar pressures calibrated to 300GPa*, [Appl. Phys. Lett. \*\*86\*\*, 014103 \(2005\)](#).
- [171] A. F. Goncharov, J. M. Zaug, J. C. Crowhurst, and E. Gregoryanz, *Optical calibration of pressure sensors for high pressures and temperatures*, [J. Appl. Phys. \*\*97\*\*, 094917 \(2005\)](#).
- [172] A. D. Chijioke, W. J. Nellis, A. Soldatov, and I. F. Silvera, *The ruby pressure standard to 150 GPa*, [J. Appl. Phys. \*\*98\*\*, 114905 \(2005\)](#).
- [173] Y. Fei, A. Ricolleau, M. Frank, K. Mibe, G. Shen, and V. Prakapenka, *Toward an internally consistent pressure scale*, [Proc. Natl. Acad. Sci. U.S.A. \*\*104\*\*, 9182 \(2007\)](#).
- [174] S. Merkel, R. J. Hemley, and H.-k. Mao, *Finite-element modeling of diamond deformation at multimegabar pressures*, [Appl. Phys. Lett. \*\*74\*\*, 656 \(1999\)](#).
- [175] W. C. Moss and K. A. Goettel, *Finite element design of diamond anvils*, [Appl. Phys. Lett. \*\*50\*\*, 25 \(1987\)](#).
- [176] K. Syassen, DatLab software (1998).
- [177] N. V. Surovtsev and I. N. Kupriyanov, *Temperature dependence of the Raman line width in diamond: Revisited*, [J. Raman. Spectrosc. \*\*46\*\*, 171 \(2015\)](#).